A multi-scale approach to dynamic processes at the oil-water interface in surfactant enhanced oil recovery

A thesis submitted in partial fulfilment of the requirements for the degree of Doctor of Philosophy in the University of Durham by,

Marie-Capucine C. A. Pope

Department of Chemistry

University of Durham

September 2017

Abstract

Surfactant enhanced oil recovery (EOR) is used to increase production from oil reservoirs where, after conventional water-flooding processes, typically 60-70% of oil remains trapped by capillary forces. Enhanced recovery processes are important because of the reduction of easily accessible new reservoirs and increasing global demand for energy. This thesis describes studies on the visualisation of the oil-water interface during surfactant flooding enabling investigation of the underpinning mechanisms of surfactant EOR. The results will aid design systems for more efficient oil recovery and improve oil recovery models.

The thesis describes a multi-scale approach to the study of dynamic processes at the oil-water interface. The conventional approach to surfactant EOR depends upon equilibrium/continuum approach. However, behaviour at the interface depends on transport processes, local geometries, local concentrations, local oil-water ratio, and local wettability. These factors affect the local phase behaviour at the moving oil front, which in turn impacts oil mobilisation. Such factors cannot be described based on bulk analysis and equilibrium phase behaviour.

A pore-scale study demonstrated that the efficiency of a flood could be maintained at much reduced surfactant concentration, giving potential for substantial cost reduction. Furthermore, solubilisation of oil in a middle phase was shown not to be essential for complete oil desaturation from a pore network. Non-uniform adsorption at the oil-water interface in a hydrophilic pore network was suspected to be responsible for the mobilisation of oil blobs in the direction opposite to the flood direction. At the fracture scale, long-lasting self-induced convective flows were triggered by an interfacial tension gradient of less than 1% of the equilibrated interfacial tension. These two novel and captivating phenomena have not been reported previously. Finally, this thesis proposed a method development to monitor the formation of microemulsion at the oil-water interface by ellipsometry under convective and diffusive transport processes.

Contents

List of Tables

List of Figures

Abbreviations

ACN	Actual Carbon Number
AOT	Aerosol-OT, Di-octyl sodium sulfosuccinate
ButOH	Butan-1-ol
CFD	Computational Fluid Dynamics
CT	Computerised Tomography
cmc	Critical Micellar Concentration
DPD	Dissipative Particle Dynamics
DOSY	Diffusion-Ordered NMR SpectroscopY
EACN	Equivalent Alkane Carbon Number
EOR	Enhanced Oil Recovery
FT-IR	Fourier-Transform Infra-Red
GC	Gas Chromatography
HSV	Hue Saturation Value
IPA	Isopropyl Alcohol
microCT	Micro Computed Tomography
MRI	Magnetic Resonance Imaging
NA	Numerical Aperture
NaCl	Sodium Chloride
ND	Neutral Density
NMR	Nuclear Magnetic Resonance
OOIP	Oil Originally In Place
PEGMA	Poly(ethylene glycol) methacrylate

PMT	Photo-multiplier
PS	Polystyrene
PSD	Phase-Sensitive Detector
PV	Pore Volume
RI	Refractive Index
rpm	Round per minute
RGB	Red Green Blue
RT	Room Temperature
SDS	Sodium Dodecyl Sulfate
SEM	Scanning Electron Microscope

Glossary of Symbols

$\delta(t)$	Time varying phase shift
$\Delta\rho$	Density difference
ϵ	Dielectric constant
η_B	Ellipsometric parameter
η^R	Roughness contribution to the ellipsometric parameter
η_D^L	Thickness contribution to the ellipsometric parameter
η_A^L	Anisotropy contribution to the ellipsometric parameter
ζ_q	Amplitude of a wavevector q of a surface mode
θ	Angle of incidence
θ_B	Brewster angle
γ	Interfacial tension
γ	Mass fraction of surfactant and cosurfactant
μ	Viscosity
ρ	Density
ρ	Ratio of the Fresnel reflectivity coefficients of the p- and s-polarised light, respectively
$\overline{\rho}$	Coefficient of ellipticity
$\overline{\rho}^R$	Roughness contribution to the coefficient of ellipticity
ω_o	Modulation frequency
C	Concentration

Ca	Capillary number
D	Diffusion coefficient
D_{app}	Apparent diffusion coefficient
E	Electric field amplitude
g	Gravity acceleration
K	Rigidity coefficient of the interface
k_B	Boltzman's constant
L	Lenght of a pore
n	Refractive index
p	Pressure
p_c	Capillary pressure
q	Wave vector of a surface mode
Q	Flow rate
r	Reflection coefficient
r	Radius of a particle
r	Pore radius
T	Temperature
v	Velocity

Copyright notice

Acknowledgements

I am thankful to my supervisor, Prof. Colin Bain, for the support and guidance over the course of my PhD. I would like to thank Dr. Andrew Clarke for his help with Comsol and guidance during this project and for making my visits at Schlumberger enjoyable whilst productive. Thank you also to EPSRC and the Schlumberger Gould Research Center for financially supporting the project. I would like to express my gratitude to Dr. Andrew Howe for his advice, encouragement and guidance during the course of my PhD and over the years. I would like to thank Dr. Anderson McKeague for his help with coding at the early stages of this project. I appreciated the help of the mechanical workshop who supplied me with the flow cell. Thank you to Dr. Juan Aguilar-Malavia for the diffusion NMR measurements and the fruitful discussions on the technique.

I would also like to thank the members of the Bain group and friends from the chemistry department who have made my years at Durham an exciting and memorable experience. I would like to mention particularly Céline, Andy, Mario, Fanny, Anne and Brunella.

I am grateful for the love and support of all my family, who have not failed to encourage me throughout the years. A special thank you must go to Nikos for his patience, support and encouragement at all the stages of this adventure.

To my father

Chapter 1

Introduction

1.1. Motivation and thesis structure

Surfactant enhanced oil recovery (EOR) is one of the tertiary recovery methods used to exploit mature oil reservoirs, where 60 to 70% of the oil is still in place, and much of which is trapped by capillary forces. Our constant need for energy and the reduction of easily accessible new reservoirs explain the renewed interest in research covering surfactant EOR. Studying the underpinning mechanisms of surfactant EOR provides a stepping stone to design systems for more efficient recovery and more accurate models of oil recovery. Surfactant screening in petroleum chemistry is based on the criterion that the surfactant mixture suitable to recover left-behind oil blobs after a water flood can form a bicontinuous microemulsion with the oil. This test is undertaken at the macroscopic scale and under static conditions. However, characteristics of oil/water/surfactant systems may differ under flowing conditions. Furthermore, local concentrations, phase behaviours and flows near the oil-water interface during oil recovery differ from equilibrium and may depend on local surfactant depletion, local oil-brine ratio and local geometry.

Recently, a few pore-scale studies have shed some light on local oil displacement process during surfactant EOR, e.g. [Howe et al., 2015]. However the choice of surfactant concentration was based upon macroscopic and static phase behaviour. Smaller-scale study was proposed by Unsal et al. to look at microemulsion formation

under flow at the oil-water interface [Unsal et al., 2016]. The study, however, was not coupled with oil displacement study to exploit the role of microemulsion formation in the recovery of additional oil. For a clear picture of the mechanisms underpinning oil recovery, it is important to couple macroscopic phase behaviour study to pore-scale oil displacement, and molecular assessment of the oil-water interface. In addition, the variation of surfactant concentration would allow one to explore the impact of surfactant depletion and reflect the local concentrations at the moving oil front which may be significantly lower than bulk concentrations. Furthermore, both convective and diffusive transport are relevant in surfactant EOR and both situations should be explored. Finally, rocks are heterogeneous natural material with a range of wettability and porosity, which may affect the mechanisms by which oil is displaced.

This thesis thus took a multi-scale approach to reflect the diversity of environments and scenarios encountered in a rock during surfactant flooding. In addition, experiments were carried out under convection and diffusion as both transports are relevant to surfactant EOR. This work set out to aid the description of the displacement of oil during surfactant EOR by looking at non-equilibrium scenarios and designing a tool capable of analysing dynamically the formation of a microemulsion at the oil-water interface. These observations are used to highlight favourable conditions and dynamic processes leading to additional oil recovery. In this thesis, the complexity of natural crude oil and surfactant mixtures used in the oil industry is reduced to its minimum by using a simple model oil (alkane), and one pure surfactant and a co-surfactant for the surfactant system. This thesis focuses on water-soluble surfactant and no chemical reaction occurs between the aqueous and oil phases.

In this chapter, the fundamental concepts of surfactant EOR are introduced, including the definition of enhanced oil recovery, capillary number and microemulsions. The main literature contributions of oil displacement during surfactant EOR are reviewed and the flow regimes in reservoirs during flooding are discussed.

Chapter 2 describes the principles of operations of the instruments used in this thesis.

Chapter 3 investigates the phase behaviour of the surfactant-cosurfactant-brine-oil system chosen to represent surfactant EOR of crude oil in a continuum approach, to find its optimal salinity. The location of the cosurfactant is studied to determine its role in the formation of microemulsions.

Chapter 4 illustrates the early stage of diffusive surfactant transport in a millimetric fracture. A non-wetting oil drop is placed in a confined space filled with a brine solution of surfactant and cosurfactant with no external flow. The complex fluid motions observed are tracked and key variables (oil drop volume, butan-1-ol concentration and alkane chain length) are investigated. The rationalisation of the novel phenomenon and its potential in oil recovery are discussed.

Chapter 5 concentrates on oil displacement under steady-state flow in microfluidic devices, representative of pore networks. Floods at high and low surfactant concentrations, in hydrophobic and hydrophilic micromodels are presented. The mechanisms of oil displacement at the pore scale are discussed.

Chapter 6 proposes ellipsometry as a tool to monitor, at the molecular level, the evolution of the oil-water interface during surfactant flooding. Methodology is developed and preliminary results are presented. Qualities and limitations of the design are discussed.

Chapter 7 summarises the findings of this thesis and their implications for oil displacement by surfactant flooding. Future development are discussed.

1.2. Enhanced oil recovery

The extraction of crude oil from a reservoir takes place in a number of steps. In a nutshell, each step consists in injecting a fluid (flood solution) in the reservoir to displace the oil in place towards a production well. Recovery strategies are often tailored to the reservoir specificities, e.g. reservoir structure, rock and crude oil types [Al-Adasani and Bai, 2010]. For the large majority of reservoirs, the recovery

of crude oil is scheduled according the following steps: after a relatively small proportion of the original oil in place (OOIP) is recovered from a natural pressure drive, the reservoir is successively flooded with one or two surfactant-free fluids; at this stage only one third of OOIP is recovered. Finally, fluids containing surfactants are injected in the reservoir to displace and recover the oil which stayed in place. Crude oil is a complex fluid with high variability from site to site which contains a wide spectrum of molecules with respect to molecular weight and polarity. During primary and secondary oil recoveries, emulsion droplets can form between crude oil and the surfactant-free flooding fluid (e.g. brine) which are are stabilised by a rigid film formed from the heavy components of crude oil [Kokal, 2005]. These types of emulsions do not improve the displacement of trapped oil and on the contrary, can lead to production lost [Kokal, 2005].

Enhanced oil recovery encompasses all processes carried out to recover additional oil from a reservoir after it has been water-flooded. Enhanced oil recovery is also named tertiary oil recovery because it usually takes place after natural pressure drive recovery and water-flood recovery.

1.3. Capillary number

About 60 to 70% of the OOIP is still in the reservoir after a water-flood (secondary recovery) because of oil entrapment which is caused by capillary forces. During water flooding, as the oil is displaced through the pore network of the reservoir rock, it becomes disconnected into "pockets" of different scales, named ganglia (see Figure 1.1). Once oil becomes disconnected from a continuous oil bank, it cannot be further mobilised by the water flood: it is trapped by the capillary forces which are not overcome by the viscous forces of the flood. In addition, entire portions of the reservoir filled with oil may be by-passed by the primary and secondary recoveries because of their lower permeabilities and consequently larger capillary pressures.

The ratio of viscous and capillary forces competing on an oil ganglion is given by the capillary number, Ca, a non-dimensional number extensively used in the oil

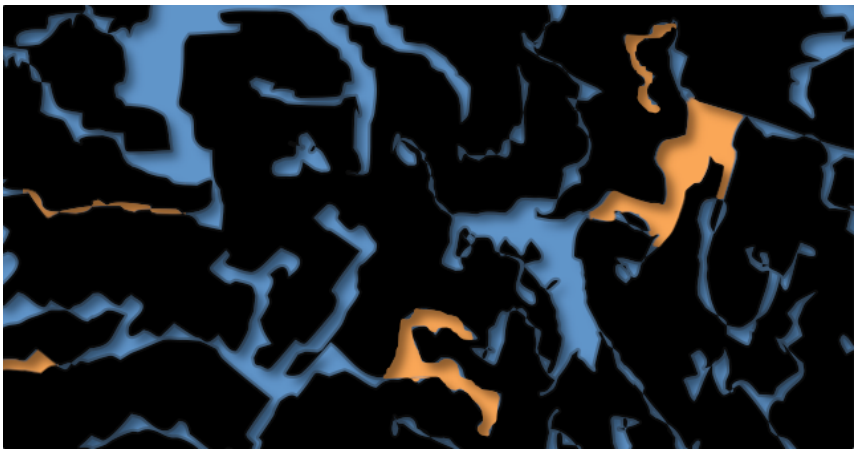

Figure 1.1: Representation of a water-flooded reservoir. Black: rock, blue: water, orange: residual oil.

industry. One simple expression of the capillary number is

$$Ca = \frac{\mu \times v}{\gamma} \tag{1.1}$$

where μ is the viscosity of the flood solution, v is its velocity and γ is the interfacial tension between the flood solution and oil. Mobilisation of oil (or oil desaturation) is found to occur at a critical capillary number of circa 10^{-5} to 10^{-3} depending on reservoir characteristics [Clarke et al., 2015]. This critical capillary number is typically determined from a capillary desaturation curve (see Figure 1.2). A capillary desaturation curve is made up from a series of core-flood experiments. Each run consists in pushing the flood solution through a core of the reservoir rock pre-saturated with crude oil, at a known pressure or velocity, and monitoring the oil recovery. Figure 1.2 shows two capillary desaturation curves, one of an oil-wet reservoir and one of a water-wet reservoir. The wettability of oil reservoirs depends on the nature of the rock, and on the crude oil. Precipitation of the less soluble fractions of crude oil (asphaltenes) onto the pore walls can modify the wettability from water-wet to oil-wet. Furthermore, the wettability can vary within the pore network of one reservoir. These types of reservoirs are said to have a mixed-wetting character. In Figure 1.2, the initial residual oil saturation, i.e. after water-flooding, is higher in the case of the water-wet reservoir. In a reservoir, the wetting phase

imbibes first the smaller pore spaces. Consequently, in water-wet reservoirs, pores with the smallest throats are invaded first and residual oil tends to stay trapped in the larger pores. Conversely, in oil-wet resevoirs, pores having the largest pore throats are invaded first by the water flood, resulting in a lower residual oil saturation after water flood. The critical capillary number, i.e. the capillary number above which additional oil is recovered, is generally between 10^{-5} and 10^{-3}.

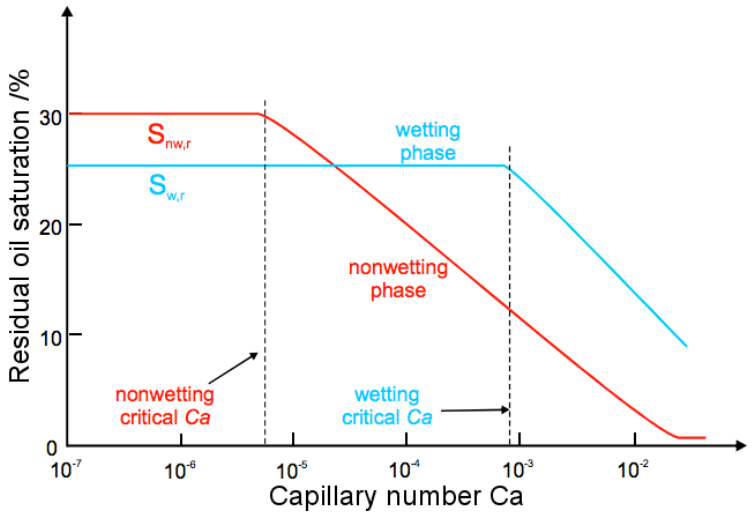

Figure 1.2: Two capillary desaturation curves: residual oil saturation of an oil-wet (blue line) and water-wet (red line) reservoir as a function of the capillary number. Reproduced from [Cense and Berg, 2009].

The critical capillary number is an experimental threshold value which is counter-intuitive because mobilisation would be anticipated to occur for capillary numbers greater than or equal to one. The difference of several orders of magnitude finds its root in the simple, and widely used, definition of the capillary number presented in Equation (1.1) which "assumes that the viscous forces and the capillary forces act over the same length scale" [Armstrong et al., 2014]. In reality, the capillary pressure acts over the length scale of a pore diameter, typically of the orders of a few tens of microns, while the viscous shear is applied to the entire oil ganglion, which can extend over many pore throats. Armstrong et al. found experimentally the more intuitive critical capillary pressure value for oil desaturation of one, by measuring local capillary pressures and ganglion lengths to obtain averaged overall figures [Armstrong et al., 2014]. This careful statistical approach was possible

using micro-tomography. Generally, the critical capillary number is accepted to be between 10^{-5} and 10^{-3}, keeping in mind that the definition of the capillary number used ignores a length different scale ratio, which is not easily accessible experimentally [Clarke et al., 2015].

In the conditions of a water flood where v is equal to a foot a day ($3{\times}10^{-6}$ m.s^{-1}), a figure commonly accepted in the oil industry [Sheng, 2010], the viscosity of the flood is close to that of water $\mu = 1 \times 10^{-3}$ Pa.s and the interfacial tension between crude oil and water is $\gamma = 30 \times 10^{-3}$ N.m^{-1}, the capillary number, as defined in Equation (1.1), is of the order of 10^{-7}. There is thus an increase of four orders of magnitude to attain a critical capillary number of 10^{-3} and mobilise disconnected oil ganglia. The viscous forces imposed by the pumping rates of the flood solution are capped due to engineering constraints and the possibility of fracturing the rock. The increase in capillary number can thus not be achieved by increasing the velocity of the flood, nor the viscosity, but by lowering the interfacial tension. A four orders of magnitude decrease from the interfacial tension value between oil and brine without surfactant, i.e. an interfacial tension of 0.01 mN.m^{-1} or less, allows to reach the critical capillary number and recover additional oil after a water flood. Such low interfacial tensions are termed ultra-low interfacial tensions (ULIFT).

The wettability of the rock can also alter the capillary number, so a lesser extent. In Equation 1.1 the rock was considered completely water-wet, giving $\gamma \times cos\theta = \gamma \times 1$. This hypothesis is used because snap-off of oil ganglia during water flood is more likely in water-wet regions.

1.4. Microemulsions

ULIFT underlies the formation of microemulsions. Their phase behaviours have been the subject of many publications since the foundation work of Winsor [Winsor, 1948]. A microemulsion is a system of oil, water and amphiphiles which forms a thermodynamically-stable single phase. The phase behaviour of microemulsion can be altered by changing the temperature or the ionic strength,

depending on if the amphiphiles in the system are non-ionic or ionic surfactants. The phase behaviours of a microemulsion are the following:

- an L1 system consists of an oil-in-water microemulsion in equilibrium with excess oil,
- an L2 system consists of a water-in-oil microemulsion in equilibrium with excess water, and
- an L3 system consists of a bicontinuous microemulsion (also named middle phase) in equilibrium with excess water and excess oil.

In bicontinuous microemulsion, there is no distinction between a continuous and a dispersed phase: both oil and water domains are continuous on a macroscopic scale in the middle phase. In addition, for L3 systems, the excess oil - excess water interfacial tension must be less than the sum of the middle phase - water plus the middle phase - oil interfacial tensions.

For systems containing ionic surfactants, an increase in salt concentration leads to a minimum in IFT (see Figure 1.3), as the microemulsion passes from an L1 system to an L3 system. A further salinity increase triggers a L3-to-L2 transition.

The interfacial tensions of microemulsions are the lowest in L3 systems and the ability of surfactant mixtures to form a middle phase with crude oil at the reservoir conditions of salinity, temperature and pressure thus became a criterion of selection for flood formulations in surfactant EOR. Furthermore, in the exploitations of oil reservoirs, L2 systems are unfavourable because the surfactant injected is lost to the oil.

Surfactant mixtures are screened for surfactant EOR applications by looking at their phase behaviours. Typically, surfactant mixtures are mixed with crude oil and brines of increasing salinity in test tubes. The empirical equation of Chun, which links the solubilisation power of the surfactant to the interfacial tension [Chun, 1979], is used to quickly measure the interfacial tension between the microemulsion phase and the excess phase(s) formed in the tubes. The larger the solubilisation power of a surfactant, measured through its solubilisation factor defined as the ratio by

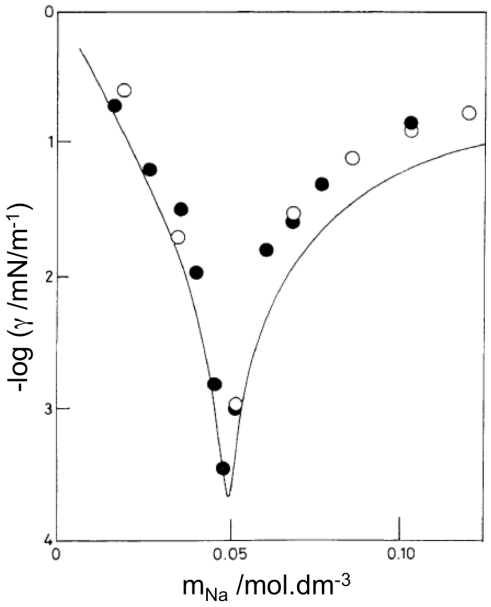

Figure 1.3: Variation of interfacial tension between aqueous phase and heptane with salt concentration at 25°C. AOT concentration is above the critical micellar concentration. Filled points are for non pre-equilibrated phases; empty points are for equilibrated phases. Reproduced from [Aveyard et al., 1986].

volume of water (or oil) to surfactant in the microemulsion phase, the lower the interfacial tension. In surfactant EOR, selected surfactants have a solubilisation factor of at least 10, corresponding to an interfacial tension of 0.003 $mN.m^{-1}$ or less [Sheng, 2010]. Other criteria of selection include low-viscosity microemulsion, low retention on the rock and cost.

Once a surfactant mixture is selected based on its solubilisation power, the formulation of the surfactant flood is usually tested for oil recovery during a core-flood experiment.

1.5. Visualisation of displacement during surfactant EOR

1.5.1. Non-optical assessment of oil displacement

The visualisation of the displacement of oil during oil recovery offers a more detailed in-sight of the recovery process, which is valuable to generate more accurate

models of oil recovery in order to improve prediction of field-scale performance [Mitchell et al., 2013]. Rock cores are however optically opaque materials, making the direct visualisation of oil displacement within the pore structure impossible. Non-optical techniques such as X-ray computed tomography (CT) and NMR imaging have been applied to core analysis. The following section outlines key studies.

Computed tomography

Computed tomography (CT) has been applied to geology from the end of the 80's, early 90's ([Wellington and Vinegar, 1987], [Orsi et al., 1994]). Projections of an object illuminated by an X-ray source are taken at many angles and 2D-section images of the object are reconstructed using algorithms. Micro-tomography or micro computed tomography (microCT) was introduced ten years later. The resolution was reduced from a typical CT resolution of 60 µm × 60 µm × 1 mm to 10 µm × 10 µm × 10 µm, by reducing the spot size of the X-ray source [Van Geet et al., 2000]. The increased resolution allowed for detailed reservoir appraisal. CT is used to map the microstructure of the rock, to evaluate interconnected porosity. Mapping of fluid distribution requires doping agents, such as cesium chloride ([Armstrong and Dorthe, 2012]) or iodine ([Li et al., 2015]), to alter the X-ray attenuation between fluids and rock, and improve contrast.

A large number of microCT studies investigates oil displacement by water flood, and the effect of different factors such as wettability ([Singh et al., 2016], [Scanziani et al., 2017]), fracture, salinity. Armstrong et al. offered an interesting study where capillary numbers of floods were calculated based on local measurements of pore-scale cluster lengths and pore-scale capillary pressures, [Armstrong et al., 2014]. With this careful local statistical approach, they validated a definition of the capillary number leading to a critical capillary number of one. This result is more intuitive than the value of the critical capillary number obtained with the classic definition of the capillary number, see discussion in section 1.3..

Fewer CT studies investigate surfactant EOR. They can be categorised between

static and dynamic studies. In the former category, studies focus on the residual oil mapping after surfactant flood or surfactant imbibition by measuring residual oil saturation, ganglia size, wettability alteration, etc. [Bataweel et al., 2011], [Alvarez et al., 2014], [Li et al., 2015]. An example is the study of Li et al. investigating the spontaneous imbibition of surfactant solution in a low-permeability reservoir core plug [Li et al., 2015]. Micro-CT scans were recorded daily after the rock was fully immersed in the surfactant solution for two days. The study thus did inform on the efficiency of the oil displacement by the surfactant flood, but the dynamic mechanisms by which the displacement occurred could not be revealed because of the static approach to the recording of the micro-CT scans. The temporal resolution of CT studies has been limited until recently by the long acquisition time of the technique. In 2011, ultra-fast microCT was demonstrated by Mokso et al. [Mokso et al., 2011]. The temporal resolution of micro-CT was improved from several minutes ([Armstrong and Dorthe, 2012]) down to sub-seconds, allowing the visualisation of dynamic, individual pore-scale displacements. To date, few studies applied ultra-fast microCT to the study of surfactant EOR. Youssef et al. investigated the surfactant flooding of a water-wet sandstone core saturated at 32% with oil, after water-flooding, with this technique [Youssef et al., 2014]. The scans were taken every three seconds and the spatial resolution was 5 µm. The surfactant solution was a 4% w/v potassium iodide brine solution of 0.025 wt% dodecyl benzene sulfate and 5 wt% isobutyl alcohol. The oil phase was decane. Unfortunately, the phase behaviour of mixtures of the surfactant solution and the oil phase was not reported. The interfacial tension between the two phases was measured to be 0.3 $mN.m^{-1}$; the injection flow rate was increased every 30 seconds during the surfactant flood from 0.05 $mL.min^{-1}$ up to 4 $mL.min^{-1}$, to cover a capillary number range between 10^{-4} and 10^{-2}. They observed coalescence and break-up of oil ganglia during the surfactant flood. No solubilisation of oil in the surfactant flood was reported. This technique generates rapidly a large amount of raw data (projections). Youssef et al. had to free the camera memory every 45 seconds. During the transfer time, which lasted 30 minutes, the sample was

maintained under steady state condition.

NMR imaging technique

NMR imaging technique, or magnetic resonance imaging (MRI), is readily used in petrophysics to scope the properties of the rock and fluids near the bore hole of a reservoir. The spatial resolution of MRI of rocks is intrinsically limited by the magnetic susceptibility contrast between the rock and the fluid (i.e. the difference of degree of magnetisation of the rock and the fluid in response to an applied magnetic field). For technical reasons, the use of high-field magnets, which would allow higher imaging resolutions, are impractical for the imaging of rocks because of a lack of quantification (for a more detailed discussion, see review of Mitchell et al. [Mitchell et al., 2013]). Low to very-low fields are used for the imaging of rocks and the spatial resolution is typically of 1 mm [Mitchell et al., 2013]. The spatial resolution may not allow the visualisation of local pore-scale events but is sufficient to map fluid saturation and fluid transport. In addition, the temporal resolution of the method allows to image the displacement of oil by an aqueous flood at velocities typically found in reservoirs far from the boreholes, i.e. one feet per meter. The chemical differentiation between fluids results from a compromise between high-resolution chemical spectra coupled with low-spatial resolution images, and low-resolution chemical spectra coupled with high-spatial resolution images. Alternatively, brine is commonly deuterated so the detection of ^{1}H only originates from the oil. With careful NMR experimental method, the water signal can be suppressed completely without the need of deuteration [Mitchell et al., 2015].

One challenge of MRI imaging for the study of surfactant EOR is the distinction between oil phase (considering that the brine phase is deuterated) and surfactant-rich phase or microemulsion. Howe et al. observed an oil-saturation shadow behind the moving oil front with 1D NMR scans of a core plug during a surfactant flood [Howe et al., 2015]. The shadow could be attributed to the formation of a middle phase between the oil bank and the flood solution from the direct optical observation of the flood in a microfluidic device. Theoretically,

the formation of a middle phase could be assessed by NMR imaging technique by tracking the location of the surfactant. In practice, NMR signals between oil and surfactant overlap and the NMR signal is obtained almost exclusively from the oil phase [Howe et al., 2015].

1.5.2. Optical assessment of oil displacement

Optical assessment of oil displacement is a powerful tool to study dynamic processes underpinning oil recovery. Microfluidic devices offer a highly tailorable means to visualise directly the oil-water interface during oil recovery. Their construction is relatively simple and the set-up does not involve more specialised equipment than an homogeneous light source and a camera. Local oil saturation, size of oil ganglia can be automatically retrieved with a simple imaging software. Although microfluidics are simplified representations of a rock, they have become an accepted methodology to screen EOR chemistry and investigate physical-chemistry processes during oil recovery (see the recent review of Lifton [Lifton, 2016]). The following section highlights the capabilities of microfluidics to represent pore networks and looks at key studies of surfactant EOR using microfluidics.

The geometry of pores can be tailored to represent the diversity of porosity of reservoir rocks. The pattern of channels can be periodic network patterns (triangles, rectangles, hexagons, etc.) or random networks (e.g. based on Voronoi diagrams) [Xu et al., 2014]. The width, length and height of channels can be varied to access a large spectrum of aspect ratios; distances vary typically from a few hundreds of micrometers (e.g. [Howe et al., 2015]) to less than ten micrometers (e.g. [He et al., 2015]). Dead-end pores can be included in the pattern. More realistic micromodels were produced by using adapted high-resolution SEM images of porous rock for the mask-making of microfluidics [Buchgraber et al., 2012]. The wettability of microfluidics depends on the starting material of the devices (e.g. PDMS, calcite, glass). In addition, the original wettability of a micromodel can be altered by chemical treatment. The homogeneity of the wettability of microfluidic devices contrasts with the mixed wettability of natural rocks. Wettability difference

can be designed more easily into single-channel devices than in pore networks. For example, Sinz et al. designed a single-channel device with hydrophilic bumps onto a hydrophobic substrate [Sinz et al., 2013] for the study of surfactant flood. The most common injection pattern into a microfluidic device is linear (e.g. from left to right), but designs of axisymmetric injections exist (e.g. [Cuenca et al., 2012]). Finally, microfluidics can sustain high pressure and temperatures making studies closer to field conditions [Song et al., 2014].

Studies of oil displacement with surfactant cover high interfacial tension systems and low, to very low, interfacial tension systems. In the latter surfactant systems, oil may be solubilised by the surfactant flood, forming microemulsions. The impact of pore geometry on the efficiency of oil recovery, with and without surfactant, was investigated by Xu et al. [Xu et al., 2014]. The oil was a light mineral oil and the surfactant flood was a 0.5 wt% solution of ethoxylated alcohol. The surfactant lowered the interfacial tension between the oil and the flood solution to 3.6 $mN.m^{-1}$, i.e. orders of magnitude higher than surfactant systems used to promote ultra-low interfacial tension. Surfactant improved the oil recovery by lowering the capillary pressure. The oil was displaced more efficiently in micromodels with smaller coordination numbers. Impact of emulsifying properties of surfactants on the efficiency of oil displacement was quantified by [He et al., 2015] using micromodels representing low-permeability reservoirs. The interfacial tension between the surfactant flood and the oil was 2.3 and 2.0 $mN.m^{-1}$ for the non-emulsifying and weakly emulsifying surfactants, respectively. The oil-water emulsions promoted by the surfactants were short-lived, less than 10 minutes in the case of the weakly emulsifying surfactant. These systems are therefore very different from surfactant systems commonly used in surfactant EOR to promote the formation of microemulsions, which are thermodynamically stable microemulsions. Improved oil recovery was obtained with weakly emulsifying surfactant compared to non-emulsifying surfactant. The efficacy was attributed to the capacity of weakly emulsifying surfactants to temporarily solubilise oil.

Surfactant flooding of micromodels with commercially available surfactants used

in surfactant EOR was undertaken by Howe et al. [Howe et al., 2015]. The surfactant flood consisted of a brine solution of the surfactant mixture (1 wt%) composed of C12, C13 alcohol-propoxy-sulfate and C20-24 internal olefin sulfonate, produced under the trade name of ENORDET, and butan-2-ol (8 wt%). The oil was decane. The brine salinity was varied to change the phase behaviour of equilibrated solutions from water-continuous microemulsion (L1 behaviour) to bicontinuous microemulsion (L3 behaviour). The interfacial tension between the microemulsion phase and the excess phase was 0.10 and 0.02 $mN.m^{-1}$ for the L1 and L3 behaviour, respectively. The optical assessment of the floods was coupled with an NMR imaging study of the floods in core plugs. The use of surfactant enhanced the oil recovery. The flood front of the lower salinity flood (corresponding to L1 behaviour at equilibrium) was rougher and moved faster than in the case of the higher salinity flood (corresponding to L3 behaviour at equilibrium). Left-behind patches were mobilised and solubilised at a distance from the flood front with the higher salinity flood. Solubilisation was the primary mechanism of oil recovery. Unsal et al. investigated the time and length scales at which microemulsions formed under dynamic conditions using a T-junction capillary geometry [Unsal et al., 2016]. The oil phase (decane) was brought into contact with a brine solution of surfactant (olefin sulfonate surfactant). The system did not contain a cosolvent. A solvatochromatic fluorescent dye gave spatially resolved compositional information. Results were compared with equilibrium phase behaviour. The impact of flow rate, salinity and surfactant concentration on the dynamic behaviour was investigated. The interfacial tensions between middle phase and excess aqueous phase were 0.5×10^{-3} to 0.5×10^{-2} $mN.m^{-1}$. Snap-off events were eliminated with higher flow rates; flow regimes affected the microemulsion formation. The three salinity concentrations investigated corresponded to L3 behaviour at equilibrium, which limited the scope of comparison between the static and dynamic behaviour. The formation of microemulsions was orders of magnitude faster than the equilibrium times in the static phase behaviour study. The numerical modeling of the study highlighted that the predicted flow behaviours based on characteristics of the equilibrium solutions

did not reflect the experimental dynamic flow behaviour.

Micromodels are also used to explore specific problems which can shed some light on EOR recovery processes. Sinz et al. showed that the transport of surfactant along discontinuous oil-water interface with no external flow is order of magnitude faster than diffusion because of self-induced Marangoni flows [Sinz et al., 2013]. In a one channel microfluidic device filled with dodecane, drops of ethylene glycol were deposited and maintained apart on hydrophilic islands created by chemical surface patterning. A drop of surfactant in oil (Triton X-15) was introduced at one end of the channel. The spreading of the surfactant was followed optically using a dye in the surfactant solution. This mechanism can enhance transport of surfactant in low-permeability reservoirs or dead-end pores and eventually improve oil displacement.

1.6. Fluid-flow regimes during surfactant EOR

1.6.1. Turbulent and laminar flows

In most cases, fluid flow through the porous network of an oil reservoir is creeping (laminar), i.e. the Reynolds number Re, defined as the ratio of inertial to viscous forces, is very small of the order of $< 10^{-2}$ [Andrade et al., 1999]. Locally, high Reynolds number can contribute to irreversible displacement events such as Haines jumps, where the non-wetting phase (e.g. oil) passes from a pore neck into a wider pore cavity. Berg et al. observed that only 39% of the displacement of oil by water in a core plug occurred through the filling of pore throats by laminar, reversible, flow [Berg et al., 2013]. Haines jumps were observed with microCT to cascade through 10 to 20 pores per event. Velocities during these non-reversible events, Haines jumps or snap-off, can be 10 orders of magnitude higher than the average reservoir velocity [Armstrong and Berg, 2013]. However, these events are less likely to occur in surfactant flooding as the decrease of interfacial tension between the oil and the flood solution allows oil ganglia to deform and pass more easily through pore throats without snapping-off.

1.6.2. Convective and diffusive flows

The relative ratio of viscous to capillary forces is assessed with the Péclet number Pe:

$$Pe = \frac{lv}{\mathcal{D}} \tag{1.2}$$

where l is a typical length scale, v is the velocity of the fluid and $\mathcal{D}$ is the diffusion coefficient of the solute of interest. If $Pe < 1$, diffusive regime is predominant; convective regime is predominant if $Pe > 1$. Transport regime is mixed diffusive-convective when $Pe \approx 1$. Equation (1.2) is a simple definition of the Péclet number. More thorough definitions may include the permeability and porosity of the rock, the entry capillary pressure [Hammond and Pearson, 2010]. Papers do not always quote the definition of the Péclet number they use (e.g. [Liu et al., 2008]), rendering the comparison of studies more difficult.

The velocity of a foot a day is frequently used and commonly accepted, to describe the fluid flow in field applications for EOR far from the bore hole. This value is an average velocity corresponding to a displacement of about a pore per second. Considering this velocity in Equation (1.2) of the Péclet number, a diffusion coefficient of surfactant in the aqueous phase of 4.8×10^{-10} $m^2.s^{-1}$ (self-diffusion coefficient of SDS monomer in water [Misselyn-Bauduin et al., 2001]) and a typical length scale of 10 µm, the Péclet number is 61. This rapid calculation would indicate that transports are dominated by convection.

Equation (1.2) shows that two factors influence the Péclet number: the typical length scale and the velocity in the pore network. The typical length scale depends of the porosity of the rock. The velocity of laminar flow in a porous medium can be described by Darcy's velocity:

$$v = -\frac{k}{\mu}\frac{\partial P}{\partial x} \tag{1.3}$$

where k is the permeability of the rock, μ is the viscosity of the fluid and $\frac{\partial P}{\partial x}$ is the pressure gradient. The lower the permeability of a rock (how easily a fluid flows through the rock), the lower the velocity. During oil recovery, two phases coexist in the pore network, complicating the picture of fluid transport. The relative ratio

of convective to diffusive flows thus also depends on relative phase mobility. These factors (porosity, permeability, and relative mobility) are easily modified in fluid transport simulations to study floods under convective, diffusive or intermediate regimes (e.g. [Hammond and Pearson, 2010]). In reality, all three regimes may be relevant during the flood of a single reservoir. Rocks are heterogeneous natural materials which present variation in their porosity and permeability. Certain types of reservoirs are also more likely to be fractured, e.g. carbonate reservoirs, resulting in dual porosity. Finally, the wettability of reservoirs affects the entry capillary pressure of fluids and their relative mobility. The wettability of reservoirs is now generally accepted to be mixed-wet [Al-Mjeni et al., 2010], i.e. two distinctive wetting conditions (water-wet and oil-wet) coexist, at different levels, in one reservoir. Relative fluid mobility may thus change within a reservoir. This complexity explains why a large spectrum of Péclet numbers is quoted in the literature of oil recovery.

In addition, under diffusive conditions, convective flows can be self-induced by compositional gradient leading to Marangoni flows (e.g. [Sinz et al., 2013]).

In conclusion, the flow regime during surfactant EOR is laminar. Both convective, diffusive and convective-diffusive flow transports are relevant in the study of surfacant EOR.

Chapter 2

Methods

2.1. Introduction

In this chapter, the principles of operations of the instruments used in this thesis are described. Described here are: tensiometry, refractometer, density measurements and ellipsometry. In the case of ellipsometry, the principle of operation is introduced by a section on polarised light to facilitate the comprehension of the principle of operation of the instrument.

2.2. Tensiometer

In this thesis, interfacial tension was measured by the drop-shape analysis. The shape of a drop results from the competition between two forces of opposing effects. The interfacial tension along the interface pulls the surface to minimise its surface area. Gravitational force in the case of pendant drop tensiometer, and centrifugal force in the case of spinning drop tensiometer, compete with interfacial tension.

A curved surface can be described by two radii of curvature as illustrated in Figure 2.1.

The pressure difference, ΔP, across a curved surface is expressed by the Laplace equation,

$$\Delta P = \gamma \times (\frac{1}{R_1} + \frac{1}{R_2}) \tag{2.1}$$

where γ is the interfacial tension and R_1 and R_2 are the principle radii of curvature.

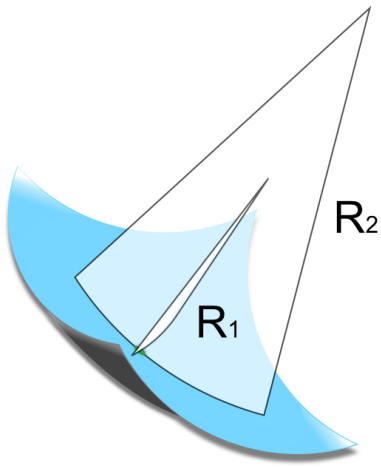

Figure 2.1: Representation of a curved surface (in blue) and two orthogonal planes. The intersections of the planes with the curved surface are two arcs characterised by their radii of curvature R_1 and R_2.

Figure 2.1 illustrates a small portion of a surface area. In the case of a drop, the radii of curvature vary along the surface of the drop. The pressure gradient ΔP thus needs to be defined *locally* $(x,\ y,\ z)$, as in Equation (2.2).

$$\Delta P(x, y, z) = \gamma \times (\frac{1}{R_1(x, y, z)} + \frac{1}{R_2(x, y, z)}) \tag{2.2}$$

Equation (2.2) can be considered for surface shapes that are experimentally relevant for the determination of γ by the drop-shape analysis. The axial symmetry of these shapes simplifies the mathematical expression of the Laplace equation.

Figure 2.2 shows respectively a pendant drop, a sessile drop, and a spinning drop with the coordinate systems commonly adopted in drop-shape analysis [Drelich et al., 2002]. For pendant and sessile drops, the origin of the axes is placed at the apex of the drop. By convention the origin of the axes for spinning drops is placed at the intersection of the axis of symmetry and the z-axis. The profiles of

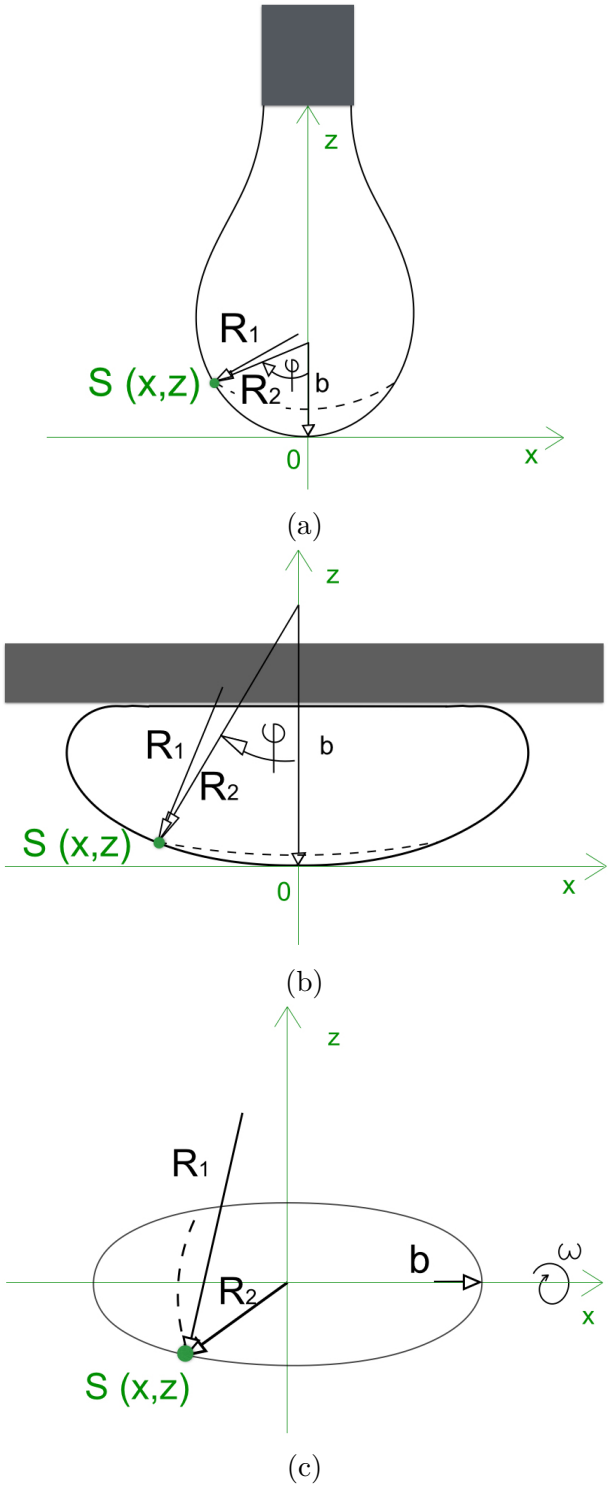

Figure 2.2: System of coordinates in (a) a pendant drop, (b) a sessile drop, and (c) a spinning drop. S is a point on the profile of the drop of coordinates x and z. The grey blocks represent the supporting surface for the drop, (a) a needle and (b) a flat surface. ω is the rotational velocity at which the drop spins. S is a point of Cartesian coordinates x and z. R_1, R_2 are the radii of curvature. b is the radius of curvature at the apex of the drop. ϕ is the angle between the axis of symmetry and R_2. The dotted line describes the profile outside the sheet of paper.

the drops are in the plane of the sheet of paper and represented by continuous lines. The surfaces of the drops are obtained by revolving the profiles around the axes of symmetry of the drops (the z-axis for pendant and sessile drops and the x-axis for spinning drops). The radius of curvature R_1 is in the plane of the sheet of paper. It describes the curvature of the profile at the point S of Cartesian coordinates x and z. R_2 is the radius of curvature in a plane that is perpendicular to R_1. The hoop radius of rotation describes the profile outside of the plane of the sheet of paper, represented with the dotted line, when it rotates around the axis of symmetry of the drop and tends to zero at the apex. b is the radius of curvature at the apex of the drop. The two radii of curvature are equal to each other at the apex of pendant and sessile drops (at the tip for spinning drops) ($R_1 = R_2 = b$) because of the axial symmetry of the drops. This symmetry simplifies the expression of the Laplace equation. For pendant and sessile drops, ϕ is defined as the angle between the axis of symmetry and R_2.

The equations used in drop-shape analysis for droplets deformed by gravity or centrifugal force are detailed in the following relevant sections.

2.2.1. Pendant drop tensiometer

The pressure inside a droplet P_a, deformed by gravity (pendant or sessile drop) can be expressed relatively to the pressure at the apex of the drop, see Equation (2.3).

$$P_a = P_{a,0} + \rho_a g z \tag{2.3}$$

where $P_{a,0}$ is the pressure at the apex inside the drop, ρ_a is the density of the drop, g is the acceleration due to gravity and z is the coordinate as defined in Figures 2.2. Similarly the pressure outside the drop P_b is expressed as

$$P_b = P_{b,0} + \rho_b g z \tag{2.4}$$

where $P_{b,0}$ is the pressure at the apex inside the drop and ρ_b is the density outside the drop. The pressure difference at point S, ΔP_S, becomes

$$\Delta P_S = \Delta P_0 + \Delta \rho g z \tag{2.5}$$

where ΔP_0 is the pressure difference at the apex and $\Delta\rho$ is the density difference between the two phases ($\Delta\rho = \rho_a - \rho_b$).

As noted previously, a pendant or sessile drop is axially symmetric around the z-axis. Thus at the apex of the drop (for S(0,0)), the two radii of curvature are equal and the pressure difference at the apex ΔP_0 is equal to $2\gamma/b$. The pressure difference in S becomes

$$\Delta P_S = \frac{2\gamma}{b} + \Delta \rho g z. \tag{2.6}$$

Replacing Equation (2.6) in the Laplace Equation (2.2), one obtains

$$\gamma(\frac{1}{R_1} + \frac{sin\ \phi}{x}) = \frac{2\gamma}{b} + \Delta \rho g z \tag{2.7}$$

where R_2 is expressed as $x/sin\ \phi$.

It is common to normalise the distances in Equation (2.7) relatively to the radius at the apex to obtain the dimensionless Bashforth-Adams equation [Bashforth and Adams, 1883],

$$(\frac{1}{R_1/b} + \frac{sin\phi}{x/b}) = 2 + \beta\frac{z}{b}, \tag{2.8}$$

$$\text{with } \beta = \frac{\Delta\rho g b^2}{\gamma}.$$

Equation (2.9) gives the expression of R_1 in the system of coordinates defined in Figure 2.2 (a) [Bashforth and Adams, 1883].

$$\frac{1}{R_1} = \frac{d^2z/dx^2}{[1 + (dz/dx)^2]^{3/2}} \tag{2.9}$$

Equation (2.8) is thus a differential equation in x and z with a numerical solution.

Bashforth and Adams computed theoretical drop profiles by solving the equation for values of β between 0.125 and 100 and of ϕ between 0 and 180 degrees.

Principle of operation

An image of an experimental drop is taken with a frame grabber and an optical set-up minimising image distortion. The profile of the drop is then compared with theoretical profiles (i.e numerical solutions of Equation (2.8)). A value of β is retained for the best matching profile. As noted previously, $\beta = \Delta\rho g b^2/\gamma$. The radius of curvature at the apex b is not known with accuracy if estimated from the image. Instead the coordinate x of a point S on the drop profile can be measured easily and accurately. For the value of β matching the drop profile, the value of x/b for $\phi = 90^o$ is recovered from the numerical solution used to create the theoretical profile. $x_{\phi=90^o}$ is the maximal distance between the axis of symmetry and the drop edge, i.e. the maximal radius of the drop profile. b is calculated from the ratio of the measured distance $x_{\phi=90^o}$ to the known value x/b and consecutively $\gamma = \Delta\rho g b^2/\beta$ is known.

Operating procedure

In this thesis, a First Ten Ångstroms F-100 tensiometer placed onto an anti-vibration stage and equipped with a high resolution WAT-902B camera supplied by Watec was used to measure interfacial tensions of pendant and sessile drops. Pendant drops were dispensed with Hamilton gas tight syringes. The needle diameters depended on the range of interfacial tensions measured. Gravitational and interfacial forces must be of the same order of magnitude to have stable pendant drops and measure their interfacial tensions by drop-shape analysis, i.e. the Bond number (see Equation (2.10)) must be close to 1.

$$Bo = \frac{\Delta\rho g L^2}{\gamma} \tag{2.10}$$

where $\Delta\rho$ is the density difference, g is the acceleration of gravity, L is the characteristic drop length and γ is the interfacial tension. In practice, 18-gauge

needles were used for $\gamma > 10$ mN.m^{-1}, 22-gauge needles for $10 \leqslant \gamma \leqslant 1$ mN.m^{-1} and 33-gauge needles for $\gamma < 1$ mN.m^{-1}. Needles were sourced from Hamilton.

Glassware used for tensiometric measurements, and syringes and plungers, were sonicated 15 minutes in 1% aqueous solution of Neutracon (neutral-pH mixture of surfactants sourced from Decon Laboratories Limited) and rinsed thoroughly with Milli-Q water. The glassware was considered clean if the interfacial tension of Milli-Q water did not drift by more than 0.3 mN.m^{-1} after 20 minutes. For sessile droplets, the tilt angle of the supporting surface was adjusted with a two-screw tilt stage (ThorLabs). The magnification of the tensiometer was calibrated either with a 3-mm-diameter sapphire ball or a 50-µm graticule or the outer diameter of the dispensing needle for higher magnifications.

Interfacial tension measurements were carried out at room temperature (RT) (20 ± 2^oC). The interfacial tension of Milli-Q water was measured at the beginning of each series of measurements and each series was attributed a correcting factor equal to $\gamma_{water,20^oC}/\gamma_{water,RT}$. The variation of interfacial tension with the temperature variation experienced in the lab was assumed to be small and similar for all measured liquids (oil and aqueous phases). The same correction factor was thus applied to all liquids. Interfacial tensions were multiplied by the correcting factor of their series to account for the variation of room temperature between two series of measurements. Interfacial tension was assumed to vary linearly over the temperature variation recorded in room temperature.

2.2.2. Spinning drop tensiometer

Principle of operation

The expression of the interfacial tension of a spinning drop was expressed by Vonnegut by considering a spinning drop as a cylinder of length L and radius R terminated by two hemispherical caps, [Vonnegut, 1942]. The total energy of the drop has two sources: the rotation of the drop and the interfacial tension at the drop interface. The energy caused by rotation is equal to the pressure difference ΔP (Equation 2.11) caused by rotation integrated over the volume of the drop V.

$$\Delta P = \frac{\omega^2 z^2 \Delta\rho}{2} \tag{2.11}$$

where ω is the rotational velocity, z is the distance from the axis of rotation, and $\Delta\rho$ is the density difference between the drop and the continuous phase. The interfacial tension is the work required to create a portion of surface dA and thus the contribution of interfacial tension to the energy of the drop is equal to the product of the interfacial tension and the total area of the drop. The expression of the energy of the drop is thus

$$E = \int \Delta P dV + \gamma(2\pi RL + 4\pi R^2), \tag{2.12}$$

which leads to the expression of the interfacial tension as a function of R and L, see Equation 2.13.

$$\gamma = \frac{\rho\omega^2 R^3}{4}(1 + \frac{2R}{3L}). \tag{2.13}$$

With sufficient rotational speed ($\omega >> 0$), the length of the spinning drop becomes large compare to its radius, and the interfacial tension becomes

$$\gamma = \frac{\rho\omega^2 R^3}{4}, \tag{2.14}$$

known as the Vonnegut equation [Vonnegut, 1942]. Equation 2.14 is a specific case of the Laplace equation expressed for the spinning drop schematically represented in Figure 2.2 (c) [Viades-Trejo and Gracia-Fadrique, 2007].

Operating procedure

Interfacial tension measurements of low to ultra-low interfacial-tension systems were made using a SITE100 Krüss tensiometer at 21.0 ± 0.2^{o}C. A drop of the light phase in suspension in the heavy phase contained in a glass capillary was deformed by rotation of the tube along its long axis. At high rotational speed, the drop was a cylinder and the interfacial tension was measured only from the radius of the cylinder. The interfacial tension was measured on full drops or half drops. The

glass capillary was immersed into an oil of matching refractive index to avoid the distortion of the image through the capillary wall. When the drop was a cylinder the measured interfacial tension was independent of rotational speed and drop length. Measured interfacial tensions were the means of measurements made on at least three drops. Typical standard error was equal to 3%.

2.3. Refractometer

2.3.1. Principle of operation

Light travels at different speeds in different media. The refractive index (RI), expressed in Equation (2.15), is a measure of the reduction of the speed of light which characterises a medium.

$$n_D = \frac{\text{speed of light in vacuum}}{\text{speed of light in medium}} \tag{2.15}$$

where n_D is the refractive index of the medium.

The speed of light in a medium depends on its wavelength. RI values are often measured at 589 nm, which is the wavelength of the "D-lines" of the emission spectrum of sodium. The subscript D indicates that the RI was measured at this wavelength. The speed of light also depends on temperature because it modifies the density of the medium through which the light propagates.

For an interface, there is a critical incident angle θ_c, see Equation (2.16), above which all the light is reflected at the interface, i.e. no light is refracted.

$$\theta_c = arcsin\frac{n_2}{n_1} \tag{2.16}$$

where θ_c is the critical angle defined as the angle formed between the axis orthogonal to the interface and the beam of incident light; n_1 and n_2 are the refractive indexes of the media on each side of the interface with the incident light propagating in medium 1 of refractive index n_1.

Digital refractometers and Abbé refractometers have the same principle of

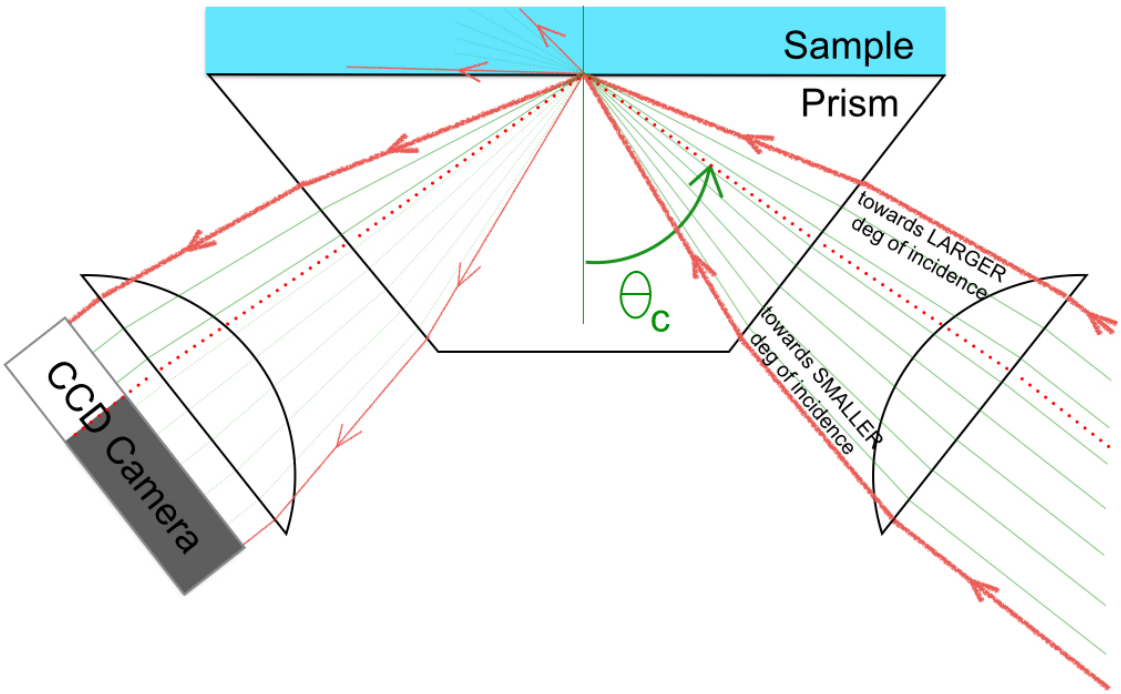

Figure 2.3: Schematic representation of a digital refractometer to illustrate its principle of operation. The direction of propagation of the light is indicated by arrows on the contours of the cone of light (continuous red lines). The green lines are a representation of rays of light above and below the critical angle (θ_c). The ray of light at the critical angle is highlighted by the dotted red line. The reflected and refracted rays below the critical of incidence are represented in lighter green to indicate that they are less intense than the incident light.

operation: the RI of a substance is deduced from the measurement of the critical angle of the interface formed by the substance of interest and a reference surface, a prism for example. A schematic representation of a digital refractometer is presented in Figure 2.3. The sample, of unknown RI, is placed onto the prism. The monochromatic light source passes through a lens to focus the cone of light at the prism-sample interface. Towards small angles of incidence, the light propagates into the sample, and is reflected back into the prism from the sample-prism interface. On the other hand, at larger angles of incidence, no light is refracted at the interface into the sample and only reflection occurs. In absence of absorption, the sum of intensities of reflected and refracted light is equal to the intensity of the incident light. Thus, because there is no refraction at larger angles of incidence, the reflected light is more intense. The border line between intense and less intense reflected light indicates the position of the critical angle. In digital refractometer, the position of the border line is established with a CCD camera. The refractive index is then calculated from the measured critical angle and indicated digitally to the operator. In Abbé refractometers, the sample is placed between two prisms. Above the critical angle, the refracted light propagates into the sample and onto the second prism towards the eyepiece. The operator assesses visually the border line and reads the refractive index on a scale which is paired with the position of the borderline.

2.3.2. Instrument and operating procedure

In this thesis, refractive indexes were measured at 20 $\pm$ 0.02^{o}C with a digital Bellingham & Stanley refractometer RFM-970 with Peltier temperature control. The prism onto which the sample was placed was artificial sapphire and the light source was a diode LED (589 nm). The instrument was calibrated sequentially with water (RI=1.33299 [Lide, 1993]) and dodecane (RI=1.42160 [Lide, 1993]). Measurements were carried out on 500-µL samples. The instrument returned a RI value once three consecutive measures were equal to each other within 0.00003. When re-measuring RI on a given solution, the RI value was equal to the first measurement undertaken on the solution within 0.00002.

The RI values of the substances used in this thesis were taken from CRC Handbook of Chemistry and Physics 74^{th} edition [Lide, 1993], unless stated otherwise.

2.4. Density

Densities (ρ) were measured at room temperature (RT) (20.0 $\pm$ 2.0^{o}C) with 1.04 $\pm$ 0.01 mL pycnometers supplied from Klaus Hofmann GmbH. The density of Milli-Q water was measured at the beginning of each series of measurement and each series was attributed a correcting factor equal to $\rho_{water,20^oC}/\rho_{water,RT}$. The same correction factor was applied to all liquids because it was assumed that over the small temperature variation experienced in the lab, coefficients of thermal expansion were small and similar for all liquids. The densities were multiplied by the correcting factor of their series to account for the variation of room temperature between two series of measurements. Density was assumed to vary linearly for the temperature variation recorded in room temperature. The mass of the liquids were measured with Mettler Toledo microbalance with a precision of 0.0001 g. The measured density of a liquid was the mean of three measurements. The error on the volume and the mass gave a typical standard error of 3%.

2.5. DOSY ^{1}H NMR

2.5.1. Principle of operation

DOSY NMR combines an NMR pulse sequence with a magnetic field gradient pulse sequence. As a result, the frequency of nuclear precession is dependent on the molecules position along the magnetic field gradient. The molecules are then allowed to diffuse for time (t) before a refocusing pulse is applied. Refocusing can only be achieved if the molecules have not diffused too far along the magnetic field gradient. Therefore, the intensity of the refocusing signal is inversely proportional to the diffusion distance. The measurement is then repeated with increasing field

gradients; the stronger the gradient the more spatially sensitive the refocusing signal. Diffusion coefficients can then be inferred from the decay of the peak intensities with increasing gradient strength. In this thesis, the DOSY was used to measure the apparent diffusion coefficients of the species constituting the microemulsions in order to indirectly study size domains and thus the structure of microemulsion phases (water-continuous or bicontinuous).

2.5.2. Instrument and operating procedure

Samples were measured at 25^{o}C on a 600 MHz Agilent spectrometer equipped with a probe with a z-gradient coil. The Oneshot45 pulse sequence ([Botana et al., 2011]) was used to acquire datasets in ten minutes with sixteen gradient amplitudes ranging from 2 to 48 G.cm^{-1} in equal steps of gradient squared, using eight transients, 32768 complex data points, a total diffusion-encoding gradient duration of 2.0 ms, and a diffusion time of 200 ms.

Microemulsion phases were transferred into NMR tubes with Pasteur pipettes and left in the sealed tubes at room temperature for 12 hours prior to the measurements. The solutions were clear.

2.6. Polarised light and Ellipsometry

2.6.1. Polarised light: Definitions and notations

Light is an electromagnetic wave oscillating "sinusoidally with time, at all points in space" [Azzam and Bashara, 1977]. It is composed of an electric and a magnetic field which always oscillate in perpendicular planes. Only one of the two fields is considered to describe a light beam, conventionally the electrical field. The direction of propagation of light is given by the wavevector, which is perpendicular to the oscillation planes of the electric and magnetic fields.

Light can be described by its polarisation. Light can be linearly-, circularly- or elliptically-polarised. These terms refer to the shape described by the trace of the electric field in time, at the intersection of a plane fixed in space and perpendicular

to the direction of propagation. An example of linearly-polarised light is represented in Figure 2.4. The point of intersection of the electric field represented in Figure 2.4 with the plane perpendicular to the direction of propagation oscillates with time on a vertical line. The trace of the electric field on this plane describes a line, thus the light is said to be linearly-polarised. At the point of intersection of the electric field onto the plane, a vector can describe the electric field. The starting point of the vector is the point of intersection of the field with the plane when the amplitude of the field is nil. The length of the vector is proportional to the amplitude of the electric field and its direction reflects the direction of the oscillation of the electric field.

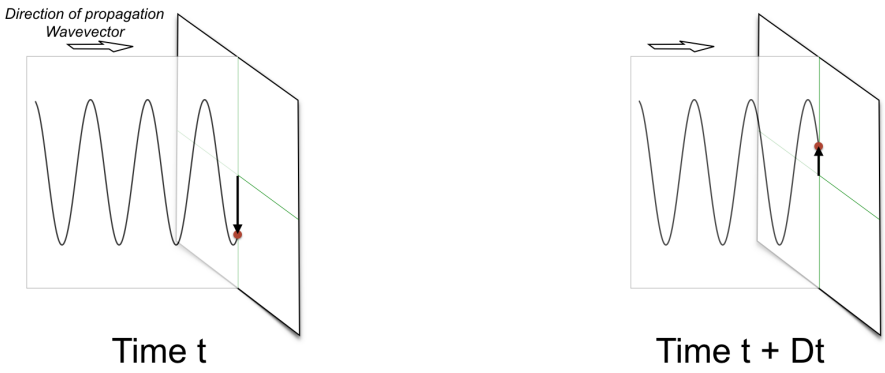

Figure 2.4: Schematic representation of the electrical field of linearly polarised light at two consecutive times, t (left) and t+Dt (right). The intersection of the field with a plane perpendicular to the direction of propagation is highlighted by a red dot. The electric field vector is represented by a black arrow on the plane.

Any polarisation can be expressed as a linear combination of its p- and s-components represented in Figure 2.5. p- and s-polarised light have their electrical field oscillating respectively in the plane parallel and perpendicular to the plane of incidence. They are called eigenpolarisations because the polarisation of an incident light purely p- or s-polarised propagating in an isotropic medium remains unchanged as it goes through, or is reflected by, an optically-isotropic medium. Linearly-polarised light is a linear combination of p- and s-polarised light oscillating in phase. Two waves are in phase when they reach their extrema at the same time. If the p- and s-polarised lights are out of phase but have the same amplitude, the

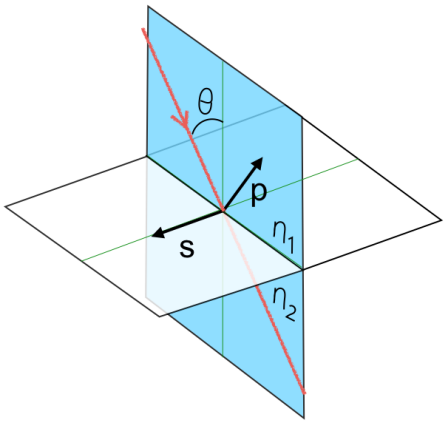

Figure 2.5: Schematic representation of light (red line) propagating in the incident plane (in blue). The polarisation of light can be expressed as a combination of its p- and s-polarisation components, respectively parallel and perpendicular to the plane of incidence.

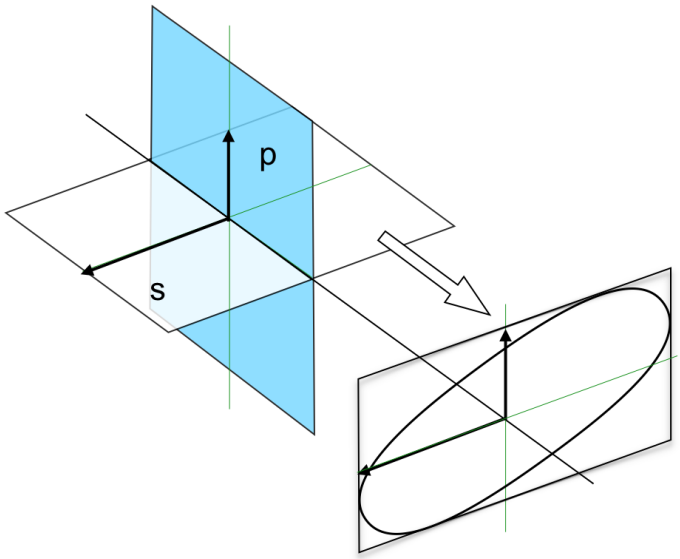

Figure 2.6: The combination of p- and s-polarised light oscillating out of phase and with different amplitude describes an elliptically polarised light. The white arrow is the wavevector.

resulting light is circularly-polarised. If the p- and s-polarised lights are out of phase and do not have the same amplitude, the resulting light is elliptically-polarised (see Figure 2.6).

The polarisation of light can be defined with the geometric description of the trace of the electric field in a reference frame. An example is given for elliptically polarised light in Figure 2.7, where the ellipticity angle Ψ is the angle between the major axis a and the minor axis b of the ellipse and the azimuthal angle θ is the angle between the major angle of the ellipse and the reference axis x. An elliptically polarised light can thus be described with

- the azimuthal angle θ, with $-\frac{1}{2}\pi \leqslant \theta < \frac{1}{2}\pi$,
- the ellipticity angle [Azzam and Bashara, 1977] Ψ with $tan\Psi = b/a$, and $-\frac{1}{4}\pi \leqslant \Psi \leqslant \frac{1}{4}\pi$,
- the amplitude of the ellipse vibration $A = (a^2 + b^2)^{1/2}$, and
- the phase shift Δ, with $-\pi \leqslant \Delta < \pi$.

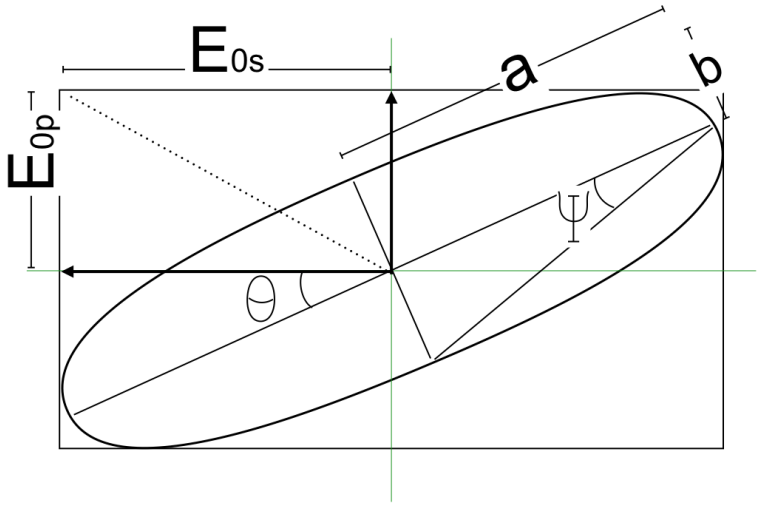

Figure 2.7: Geometric representation of elliptically polarised light.

2.6.2. Reflectivity at an interface

In this thesis, the conventions represented in Figure 2.5 are used: medium 1, where the incident and reflected light propagate, has a refractive index n_1 and the transmitted light propagates in medium 2 of refractive index n_2. The angle of incidence θ is the angle between the normal to the interface between media 1 and 2 and the direction of propagation of light. The wavevector, p- and s-polarised waves form a right-handed vector system. The refractive index n or the dielectric constant ϵ of a medium are used interchangeably using the relation $n = \epsilon^{1/2}$.

Reflection ellipsometry measures the polarisation variation of light upon reflection at an interface, measuring the ratio ρ, see Equation (2.17). The change in polarisation of light upon reflection at an interface can be described with the reflection coefficients of the interface or using the geometric description of the polarisation of the reflected light.

In the first case, ρ is expressed as

$$\rho = \frac{r_p}{r_s} \tag{2.17}$$

where r_p and r_s are the Fresnel reflectivity coefficients of the p- and s-polarised light, respectively.

The reflectivity coefficients r_s and r_p of a medium are not equal. Thus when a polarised incident light is reflected by this medium, the reflected waves have a different state of polarisation than the incident light. The modulus of the reflectivity coefficient of s- (p-) polarised light is equal to the amplitude ratio of the reflected to the incident electric field vectors, in the s- (p-) plane, see Equations (2.18).

$$|r_s| = \frac{|E_s^r|}{|E_s^i|} \tag{2.18a}$$

$$|r_p| = \frac{|E_p^r|}{|E_p^i|} \tag{2.18b}$$

where $|E|$ is the amplitude of the electric field vector. The subscripts s and p refer to the s- and p-components of the wave, respectively. The superscripts i and r refer

to the incident and reflected waves, respectively. Hence, $|E_s^r|$ is, for example, the amplitude of the reflected electric field in the s-plane, i.e. the plane perpendicular to the plane of incidence.

Reflection coefficients can be expressed as complex numbers:

$$r_s = |r_s|\, e^{i(\delta_s^r - \delta_s^i)} = \frac{|E_s^r|}{|E_s^i|}\, e^{i(\delta_s^r - \delta_s^i)} \tag{2.19a}$$

$$r_p = |r_p|\, e^{i(\delta_p^r - \delta_p^i)} = \frac{|E_p^r|}{|E_p^i|}\, e^{i(\delta_p^r - \delta_p^i)} \tag{2.19b}$$

where δ is the phase of the wave. The notations of Equations (2.18) apply and δ_s^r is, for example, the phase of the reflected wave in the s-plane.

ρ is thus a complex number, with a real part $Re(\rho)$ and an imaginary part $Im(\rho)$. The modulus of the ellipticity $|\rho|$ is $\sqrt{(Re(\rho)^2 + Im(\rho)^2}$. The imaginary part of ρ, $Im(\rho)$ is called the ellipticity coefficient $\overline{\rho}$, or ellipticity for short.

For dielectric materials, there is an angle of incidence defined in Equation 2.20 called the Brewster angle θ_B, for which none of the p-polarised light is reflected, i.e. $r_p = 0$.

$$\theta_B = arctan(\frac{n_2}{n_1}) \tag{2.20}$$

where n_1 and n_2 are the refractive indexes of transparent dielectrics 1 and 2 respectively, forming the interface at which the light is reflected. For a perfect interface, at the Brewster angle, the ratio ρ should vanish. At real interfaces, only the real part of ρ is equal to zero and its imaginary part is not zero. The interface is *real* and the imaginary part of ρ measured at the Brewster angle is a straight forward measure of the deviation from the ideal interface. An ideal interface is a flat interface with a step change from material 1 to material 2 constituting the interface.

Instead of taking ρ as the ratio of the reflection coefficients of p- to s-polarised light, ρ is often expressed as a complex number that describes geometrically the

polarisation of the reflected light:

$$\rho = tan\ \Psi\ e^{i\Delta} \tag{2.21}$$

This expression of ρ is linked to the complex expression of the reflection coefficients of p- to s-polarised light (Equation 2.17) with

$$tan\ \Psi = \frac{|r_p|}{|r_s|} \tag{2.22}$$

and

$$\Delta = (\delta_p^r - \delta_s^r) - (\delta_p^i - \delta_s^i). \tag{2.23}$$

When light is reflected at a real interface, only the real part of ρ vanishes and its imaginary parts remains finite. $|\rho|$ goes through a minimum at the Brewster angle but does not vanish.

2.6.3. Physical interpretations of ellipticity

Drude developed a theory to interpret the ellipticity in terms of interface characteristics [Drude, 1891]. He found that, at the Brewster angle, the coefficient of ellipticity is directly proportional to the quantity η_B, the *ellipsometric parameter* (see Equation (6.2)).

$$\overline{\rho}_B = \frac{\pi}{\lambda} \times \frac{\sqrt{\epsilon_1 + \epsilon_2}}{\epsilon_1 - \epsilon_2} \eta_B \tag{2.24}$$

where λ is the wavelength of light, ϵ_1 and ϵ_2 are the dielectric constants of the two media forming the interface.

η_B depends on the characteristics of the interface, which can be described in terms of thickness, roughness and anisotropy. η_B is thus the sum of these contributing factors:

$$\eta_B = \eta^R + \eta_D^L + \eta_A^L \tag{2.25}$$

where η^R is the roughness contribution, η_D^L is the thickness contribution and η_A^L is

the anisotropy contribution.

The expression of η is simplified by making assumptions about the interface.

Rough interface First, the interface between two fluids can be characterised by its roughness arising from thermally excited capillary waves at the interface. Beaglehole proposed to express the roughness contribution to the ellipsometric parameter as

$$\eta^R = -\frac{3}{2} \times \frac{(\epsilon_1 - \epsilon_2)^2}{\epsilon_1 + \epsilon_2} \times \sum_{q>\pi/\lambda}^{\infty} q|\zeta_q|^2 \tag{2.26}$$

where q is the wavevector of a surface mode and ζ_q its amplitude [Beaglehole, 1980].

Roughness is a sinusoidal deformation at the plane of the interface. The light scattering of a liquid interface can be calculated from the summation of the mean square amplitudes of each sinusoidal wave. A sinusoidal wave is characterised by its amplitude ζ_q and its surface mode of wavevector q. The average roughness over the interface is $(\overline{\zeta^2})^{1/2}$.

The creation of this deformation requires thermal energy (k_BT) to overcome the three restoring forces: gravity, surface tension and mean bending elasticity. Gravity is not important for q-values that contribute to the ellipticity. In fact, low values of q give rise to off-specular scattering which is by definition not captured by reflection ellipsometry. On the other hand, a cut-off value at high q needs to be introduced to avoid the divergence of the summation of Equation (2.26). Physically, the cut-off value q_{max} is a consequence of the curvature energy of the interface, which is introduced in the expression of the mean square amplitude of a wavevector (see Equation (2.27) [Zielinska et al., 1981]).

$$|\zeta_q|^2 = \frac{k_BT}{\Delta\rho g + \gamma q^2 + Kq^4} \tag{2.27}$$

where k_B is Boltzman's constant, T is the absolute temperature, $\Delta\rho$ is the density difference, g is the gravity acceleration, q is the wavevector of a surface mode, γ is the interfacial tension, and K is the rigidity coefficient of the interface. From

Equation (2.27), the wavevector cut-off of surface modes q_{max} becomes

$$q_{max} = \frac{\pi}{2}\sqrt{\frac{\gamma}{K}} \tag{2.28}$$

The contributions to the mean square amplitude of a capillary wave q in thermal equilibrium are

- the energy due to gravity $\Delta\rho g$,

- the capillary energy γq^2, and

- the curvature energy Kq^4.

The roughness contribution to the ellipsometric parameter thus becomes

$$\eta^R = -\frac{3}{8}\frac{k_B T}{\sqrt{\gamma K}}\frac{(\epsilon_1 - \epsilon_2)^2}{\epsilon_1 + \epsilon_2} \tag{2.29}$$

and is always negative.

For interfaces without rigidity, Meunier expressed the roughness contribution to the ellipticity as

$$\overline{\rho}_B^R = -\frac{3\pi}{2\lambda}\frac{\epsilon_1 - \epsilon_2}{\sqrt{\epsilon_1 + \epsilon_2}}\sqrt{\frac{\pi k_B T}{6\gamma}} \text{([Meunier, 1987])}. \tag{2.30}$$

The roughness of a fluid-fluid interface gives a measure of its interfacial tension.

An alternative way to treat the roughness of an interface is to consider a smooth variation of the density profile across a transition thickness between the two bulk fluids. This approach can be seen as allocating a *thickness* to the interface and is treated in the next paragraph. A contrario, the approach resulting in Equation (2.30) considers the fluctuation of a *sharp* interface by thermally excited capillary waves.

Thin interface The interface can be considered as a transition of a finite thickness L between the two bulk media defining the interface. At an ideal interface, the dielectric constant varies sharply from one bulk value to the other, ϵ_1 to ϵ_2. In reality, the density profile varies smoothly across the interface. With this idea at

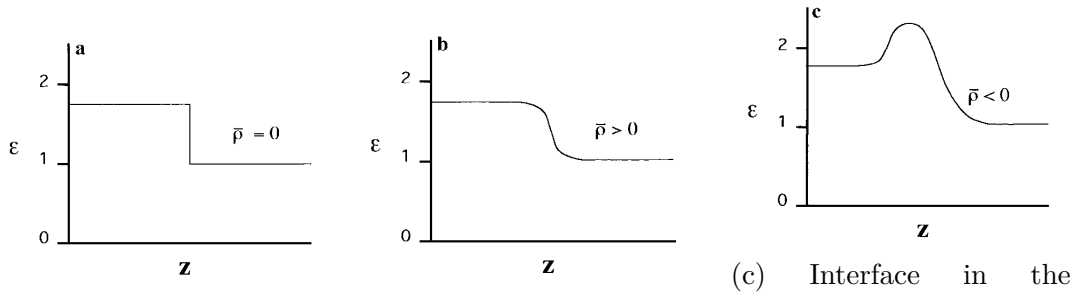

(a) Ideal interface (b) Real interface (c) Interface in the presence of a monolayer

Figure 2.8: Schematic illustration of permittivity profile variation at the water-air interface. Reproduced from [Manning-Benson et al., 1997].

hand, the expression of the thickness contribution to the ellipsometric parameter becomes

$$\eta_D^L = \int_0^L \frac{(\epsilon_1 - \epsilon_z)(\epsilon_2 - \epsilon_z)}{\epsilon_z} dz \tag{2.31}$$

where ϵ_z is the dielectric constant of the interface at the height z on the z-axis normal to the interface.

Three density profiles across an interface are illustrated in Figure 2.8 reproduced from [Manning-Benson et al., 1997]. Figure 2.8 (b) shows the density profile across a physical air-water interface varying smoothly between the dielectric constant of water (ϵ_2=1.78) and that of air (ϵ_1=1). η_D^L is negative and the ellipticity of the interface is positive, given that $\epsilon_1 - \epsilon_2 < 0$. In Figure 2.8 (c), the negative ellipticity arises from a non-monotonic variation in the density profile across the interface due to the presence of a surfactant monolayer.

Azzam and Bashara described the procedure to calculate the thickness of a thin film between two semi-infinite media with reflection ellipsometry [Azzam and Bashara, 1977], based on an ideal three-phase model (as illustrated in Figure 2.9) and the original work of Drude [Drude, 1891].

This three-phase model considers a thin film of lateral dimensions many times its thickness. The Fresnel coefficients of reflection R_p and R_s, arising from this model, are a summation of an infinite geometric series of the partial waves reflection coefficients, leading to the expressions

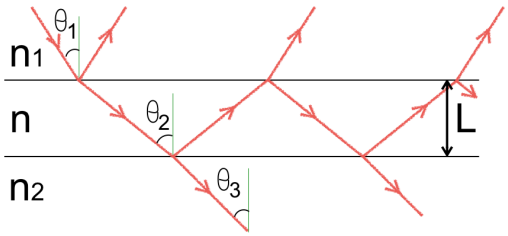

Figure 2.9: Transmission and reflection of light (schematically represented with red lines) within a film of thickness L and refractive index n between media 1 and 2, of refractive indexes n_1 and n_2, respectively. θ_1, θ_2 and θ_3 are the angles of incidence at the interfaces, measured from the normal to the interface.

$$R^p = \frac{r_{1f}^p + r_{f2}^p e^{-i2\beta}}{1 + r_{1f}^p r_{f2}^p e^{-i2\beta}} \tag{2.32a}$$

$$R^s = \frac{r_{1f}^s + r_{f2}^s e^{-i2\beta}}{1 + r_{1f}^s r_{f2}^p e^{-i2\beta}} \tag{2.32b}$$

where r_{1f} and r_{f2} are the reflection coefficients at the medium 1-film interface, and the film-medium 2 interface respectively for the p- or s-polarised light, depending on the superscripts; β is the propagation phase delay, or phase angle expressed in Equation (2.33). This model considers that the partial waves combine coherently.

$$\beta = 2\pi \frac{L}{\lambda} n_1 cos(\theta_2) \tag{2.33}$$

where L is the thickness of the film, λ is the wavelength of light, n_1 is the refractive index of medium 1, and θ_2 is the angle of incidence within the film as illustrated in Figure 2.9. The angles θ_1, θ_2 and θ_3 are related by Snell's law

$$n_1 sin\theta_1 = n sin\theta_2 = n_2 sin\theta_3 \tag{2.34}$$

where n_1, n and n_2 are the refractive indexes of medium 1, the film layer and medium 2, respectively.

The expression of β shows that one value of ellipticity (i.e. R_p/R_s) cannot inform on both the refractive index and the thickness of the film. In this thesis, the refractive index of the film was measured independently with a refractometer when the film was a microemulsion middle phase. In practice, the experimental value of ellipticity is compared to the calculated values for layers of different thickness and the layer is attributed the thickness of the matching calculated ellipticity.

The layer may not be isotropic and a correction term η_A^L may be needed. Langevin et al. showed that the two contributions η_A^L and η_D^L to ellipticity can be of a similar order of magnitude, [Langevin et al., 1992]. For the disordered (liquid) interfaces considered here, η_A^L may be neglected.

Ellipsometry is a tool which gives very little information ($\overline{\rho}$), to characterise a complex interfacial profile. The approach chosen to model the interface depends on the properties under investigation. The accuracy of one model to predict the ellipticity $\overline{\rho}$ compared to another model can be a clue on the interfacial properties. Each approach is based on assumptions about the interface which must be born in mind when interpreting the data. The use of more than one model can enrich the understanding of the interface properties.

2.6.4. Ellipsometry

Principle of operation

In ellipsometry, information about an interface (such as its thickness) is retrieved by analysing the change of polarisation of light upon reflection onto this interface. An ellipsometer is a simple set up consisting of two optical arms mounted on a wheel to vary the angle of incidence. The sample is placed in between the two arms at a suitable height, depending on the angle of incidence. On one arm, a light source is coupled with a polariser. The polarisation of the incident light is known. After reflection onto the sample, the light passes through an analyser on the second arm where the light is detected. Different configurations of ellipsometers exist to identify the polarisation of the reflected beam. Garcia-Caurel et al. described the instrumental implementations of ellipsometers and gave an overview

of the strengths and weaknesses of the designs [Garcia-Caurel et al., 2013]. In this thesis, the oil-water interface was studied with phase-modulated ellipsometry. This ellipsometer design has the advantage of not having any rotating elements, making it a fast-response instrument. In addition, it has a high signal-to-noise ratio.

2.6.5. Phase-modulated ellipsometer

In a phase-modulated ellipsometer, the measured signals are not physical parameters but can be linked to the polarisation state of light by taking a few mathematical steps. Ψ and Δ (Equations (2.21)) can be determined with two detections with different orientation combinations for the polariser and analyser.

In phase-modulated ellipsometry, the incident beam is modulated at a high frequency ω_0 (50 kHz), inducing a time-varying phase shift $\delta(t)$ between the p- and s-polarised light, see Equation (2.35).

$$\delta(t) = \delta_0 sin(\omega_0 t) \tag{2.35}$$

where δ_0, which is the phase shift between the p- and s- components of the incident light in the absence of modulation.

Prior to being modulated, the incident beam is set to have equal p- and s-amplitudes by passing through a polariser, at 45^o to the s- or p-direction. The reflected beam passes through an analyser orientated parallel or perpendicular to the polariser. Under these conditions, the signal at the detector I is

$$I = I_0 |r_s|^2 (1 + (\rho)^2 \pm 2\rho cos(\Delta - \delta(t))) \tag{2.36}$$

where $\pm$ refers to the orientation of the analyser [Beaglehole, 1980]. The signal at the detector I is proportional to the cosine of the retardation $\delta(t)$. An expression of the form $cos(Asin(\omega t))$, such as Equation (2.36), can be expressed with a series of Bessel functions.

The DC signal of the modulated signal is kept constant and a lock-in amplifier is used to detect the modulation frequencies ω_0 and $2\omega_0$. The signals at these two

frequencies are respectively proportional to Equation (2.37) and Equation (2.38):

$$\pm \frac{4tan\Psi sin(\Delta)J_1(\delta_0)}{1+(tan\Psi)^2 \pm 2tan\Psi cos(\Delta)J_0(\delta_0)} \tag{2.37}$$

$$\pm \frac{4tan\Psi cos(\Delta)J_2(\delta_0)}{1+(tan\Psi)^2 \pm 2tan\Psi cos(\Delta)J_0(\delta_0)} \tag{2.38}$$

where J_0, J_1 and J_2 are Bessel functions.

The value of δ_0, which is the phase shift between the p- and s- components of the incident light in the absence of modulation, is adjusted so that the Bessel function $J_0(\delta_0)$ is equal to zero. This manipulation simplifies the expressions (2.37) and (2.38), and the signals become proportional to $\pm|\rho|sin(\Delta)$ (ω_0 frequency signal) and $\pm|\rho|cos(\Delta)$ ($2\omega_0$ frequency signal). As mentioned earlier, $\rho = tan\Psi e^{i\Delta} = |\rho|e^{i\Delta} = |\rho|(cos\Delta + isin\Delta)$ and so the signal of the lock-in amplifiers at ω_0 frequency and $2\omega_0$ frequency become respectively proportional to $\pm Im(\rho)$ and $\pm Re(\rho)$.

The main contribution to the phase shift between the reflected and incident beams is due to the reflection of the beam onto the interface of interest. However, other smaller phase shifts may be induced by transmission through optical components of the set-up [Beaglehole, 1980]. The phase shift contribution from the set-up will remain constant while the contribution from the interface will change with time as adsorption at the interface occurs. Hence, observation of relative changes in phase-modulated ellipsometry will carry exclusively interfacial characteristics. In addition, the contributions coming from the set-up rather than adsorption at the interface could be isolated and removed by measuring the signal at two opposite positions of the analyser (0 and 180^o).

2.6.6. Operating procedure

Instrument and set-up procedure

The ellipsometer used in this thesis was a Picometer Ellipsometer (Beaglehole Instruments, NZ). The light source was a He-Ne laser of wavelength 632.9 nm.

In a first instance, the optical elements on the two arms of the ellipsometer were aligned, choosing the 0^o position as the s-direction (i.e. perpendicular to the plane of incidence). The analyser's 0^o-position was first found by reflecting polarised light onto a glass sample at its Brewster angle (57^o) and finding the analyser's position at which the detected light intensity was minimum. As the sample was illuminated at its Brewster angle, only the s-component of the light was reflected. The analyser's angle at which the detected light intensity was minimal thus corresponded to the p-direction. This angle was then set to be equal to 90^o. The polariser position was then set relative to that of the analyser. The polariser was set at 45^o for the light to have an equal amplitude of the p- and s-polarised waves.

The light detector was a photo-multiplier (PMT). A PMT amplifies the light intensity by creating an avalanche of secondary electrons for every incoming photon. The secondary electrons are produced at the surface of a succession of dynodes that terminates by an anode. The electrons are accelerated by a voltage across the dynodes. When working in automatic-gain mode, the voltage of the PMT was automatically and continuously adjusted for the anode to work at its nominal current ($10\,\mu A$). Alternatively, the cathode voltage could be limited to a *ceiling* value. When the cathode ceiling voltage was lower than the voltage needed to work at nominal current, the current of the anode indicated the amplitude of the DC signal. In this thesis, the PMT was used in automatic-gain mode.

Finally, the lock-in amplifier was used to amplify again the signal and isolate the chosen frequency of the modulated signal. The amplifier had a sensitivity ranging from 1 to 500 mV. In a lock-in amplifier, the amplified signal of frequency ω_S is multiplied by an alternative reference signal of frequency ω_R. The multiplication of the two signals results in a signal of frequency from $\omega_S - \omega_R$ to $\omega_S + \omega_R$. With a low-pass filter, only the signal over this range of frequency is detected. The corner or cut-off frequency f_c, given as the frequency above which the power output has fallen under a certain proportion of the power of the signal in the pass band, can be adjusted by modifying the time constant t_c ($f_c = \frac{1}{t_c}$). In addition to the amplitude information, lock-in amplifier detection is sensitive to the phase of the signal. In

fact the signal resulting from the multiplication of the original and reference signals is:

- positive, if the two signals are in phase ($\phi = 0^o$)

- negative, if the two signal are out of phase ($\phi = 180^o$)

- nil, if the two signals have a phase shift of $\phi = 90^o$

Therefore the lock-in amplifier method of detection is called phase sensitive detection (PSD). For the ellipsometer used in this thesis, t_c could be varied from 0.1 ms to 10 s. The greater the cut-off frequency, the more rapid the measurement; however more noise may be picked-up as the span of frequency is enlarged. One lock-in amplifier was used for each of the two harmonics of interest, 50 and 100 kHz signals.

Finally, the measuring time and signal averaging could be adjusted with the lock-in wait factor and the sampling factor. One measuring stage was defined as follows:

1. the system stayed idle for a period equal to the product of the lock-in wait factor and the time constant t_c,

2. signal was acquired and averaged over a period equal to the product of the sampling factor and the time constant t_c. The measuring stage was repeated at a frequency defined by the time step.

This sequence is then repeated a second time, with the analyser at 180^o from its initial position if the modulation of the analyser was enabled.

2.7. Conclusion

This chapter reviewed the principles of the techniques used in this thesis and the methodologies used for the measurements. Results and discussions are described in the following chapters.

Chapter 3

Continuum scale

3.1. Introduction

The water-flood of a reservoir leaves behind up to 60%-70% of the oil originally in place. The remaining oil is held by capillary pressure which cannot be matched by the pressure exerted by the flood at the oil interface. The capillary pressure is inversely proportional to the pore radius and proportional to the interfacial tension between oil and brine. Coreflood experiments showed that the reduction of the oil-brine interface by three orders of magnitude is key to displace residual oil [Wilkinson, 1984]. The oil-brine interfacial tension, typically 50 $mN.m^{-1}$, is reduced to ultra-low values, 0.01 $mN.m^{-1}$ and lower, by the use of surfactants. Oil-brine systems exhibiting ultra-low interfacial tensions (ULIFT) form microemulsions whose phase behaviours have been the subject of many publications since the pioneer work of Winsor [Winsor, 1948]. Phase behaviour tests on mixtures of crude oil, brine and surfactant are extensively used in petroleum industry to screen the efficiency of various surfactants and cosurfactant combination to reach ULIFT. Such bottles lab tests are useful to estimate interfacial tension [Chun, 1979], and microemulsions properties such as viscosity. Microemulsions can be obtained from surfactants alone [Aveyard et al., 1986]. These surfactants are high-molecular weight molecules with two major drawbacks despite their great efficiency in lowering the interfacial tension to ULIFT:

- they form viscous microemulsion phases, and

- they are poorly soluble in water.

These two shortcomings have severe consequences in surfactant EOR including poor flood mobility and pore blockage [Hirasaki and Zhang, 2004]. Addition of alcohol remediates both problems because alcohol increases surfactants' solubility in the aqueous surfactant flood and breaks ordered phases resulting in low-viscosity microemulsions [Salter, 1977].

Alcohols are amphiphiles and thus coadsorb at the oil-brine interface. Considered as a cosurfactant, alcohol can have a hydrophilic or lipophilic contribution with respect to a given oil-brine system [Bourrel and Chambu, 1983]. Addition of a lipophilic alcohol to a L1 system can trigger a L1-to-L3-to-L2 transition as with increased brine salinity in ionic-surfactant systems [de Bruyn et al., 1989], [Najjar and Stubenrauch, 2009]. In addition, alcohols partition between oil and brine bulk phases in a proportion which depends on the alcohol concentration because of the self-association of alcohol in oil. In the bulk phase, alcohol can play the role of polar specie in the apolar oil and modify its characteristics.

Microemulsions are at least four-component systems and their phase behaviours are transcribed into a tetrahedron. However, quaternary dimensional space is not always practical and it is desirable to reduce the dimensionality of the phase diagram to three. In EOR literature, this is commonly achieved by considering surfactant and alcohol mixture as a pseudo-component. This choice is not such an acceptable assumption because, as mentioned previously, alcohol and surfactant can take different places in a microemulsion. Furthermore, this approach imposes a constant surfactant-to-alcohol ratio and reduces the span of alcohol concentrations investigated.

In a reservoir, one pore volume of flood solution is needed to displace one pore volume of oil. It is thus reasonable to describe the phase behaviour of oleic and aqueous phases mixtures prepared in 1:1 v:v as the "reservoir-scale phase behaviour". In this chapter, the reservoir-scale phase behaviour of SDS-butan-1-ol-brine-dodecane system was investigated at different

surfactant-to-alcohol ratios and brine salinities. The phase behaviour was assessed qualitatively by visual inspection (presence of two or three phases) and in more details using diffusion NMR. Diffusion coefficients were used to calculate the size of the swollen micelles in the water-continuous microemulsion and have an idea of the proportion of oil to water domains in the bicontinuous microemulsion; they also shed light on the location of butan-1-ol in the microemulsion. In order to further characterise the system, the interfacial compositions of L1 and L3 systems were estimated using the pseudo-phase model and refractive indexes (RI) of oil phases. The model of pseudo-phases is based on the assumption that the phase(s) solubilised in the microemulsion phase has (have) the same composition(s) as the corresponding excess phase(s). This chapter describes in detail the phase behaviour of the system used throughout this thesis. Alcohol was not assumed to be a pseudo-component together with the surfactant to generate data useful for the subsequent chapters investigating the oil-water interface under non-equilibrium conditions.

The remainder of this chapter is structured as follows. First, the notations and definitions used in this chapter are clarified. Second, the choice of the system studied is explained and the method to calculate bulk and interfacial compositions is defended. Finally, results are presented and discussed in the light of the literature.

3.2. Notations and definitions

Throughout this thesis, the same notation was used for concentrations and masses: subscript indicated the entity of interest and superscript indicated the phase of interest. For example, C^{oil}_{ButOH} referred to the concentration of *butan-1-ol* in the *oleic phase*. The absence of superscript was equivalent to considering the total mixture. The superscript ^{tot} was added in certain cases to improve clarity.

Butan-1-ol partitions between brine and dodecane in proportion depending on salinity and butan-1-ol content. Partition coefficient p is defined in Equation (3.1) as the ratio by mass concentration of butan-1-ol in oil C^{oil}_{ButOH} to butan-1-ol in brine

C^{aq}_{ButOH},

$$p = \frac{C^{oil}_{ButOH}}{C^{aq}_{ButOH}} = \frac{wt^{oil}_{ButOH}/wt_{oil}}{wt^{aq}_{ButOH}/wt_{aq}}, \tag{3.1}$$

where wt^{oil}_{ButOH} is mass of butan-1-ol in the oleic phase, wt^{aq}_{ButOH} mass of butan-1-ol in the aqueous phase and

$$wt_{oil} = wt^{oil}_{ButOH} + wt_{dodecane} \tag{3.2}$$

$$wt_{aq} = wt^{aq}_{ButOH} + wt_{brine}, \tag{3.3}$$

where wt_{oil} and wt_{aq} are respectively masses of the oil and aqueous phases. The butan-1-ol saturation concentration in brine was noted $C_{ButOH,sat}$.

In this thesis, the notation L1, L2 and L3 was used to denote respectively water-continuous microemulsion with excess oil, oil-continuous microemulsion with excess aqueous phase and bicontinuous microemulsion with excess oil and excess aqueous phase. The surfactant-rich phase was denoted the microemulsion phase; L3 microemulsion phase was also named middle phase. L1, L2 and L3 systems denoted the total mixture, i.e. microemulsion phase + excess phase(s). The term *microemulsions* was used in the Method section to describe the total mixtures.

The mass fraction γ of surfactant and alcohol in a formulation is defined in Equation (3.4),

$$\gamma = \frac{wt_{SDS} + wt_{ButOH}}{wt_{dodecane} + wt_{brine} + wt_{SDS} + wt_{ButOH}} \tag{3.4}$$

where wt_{SDS} is mass of SDS, wt_{ButOH} mass of butan-1-ol, $wt_{dodecane}$ mass of dodecane and wt_{brine} mass of brine. When the microemulsion was prepared with D_2O, the weight of deuterated brine was corrected to the density of H_2O to calculate γ.

The solubilisation factors are defined as ratios by volume of water (or oil) to SDS in the microemulsion phase (see Equations 3.5)

$$S_{wm} = \frac{\text{volume of aqueous phase in microemulsion}}{\text{volume of SDS}} \tag{3.5a}$$

$$S_{om} = \frac{\text{volume of oleic phase in microemulsion}}{\text{volume of SDS}} \tag{3.5b}$$

where S_{wm} and S_{om} denote respectively solubilisation factors of oil and aqueous phases in the microemulsion phase. The density of SDS was postulated to be 1.03 g.cm^{-3}.

The volumes of aqueous and/or oleic phase(s) in the microemulsion phase were estimated by comparing the initial volumes of brine and dodecane to the excess-phases volumes. The contribution of butan-1-ol to the initial volumes of brine and dodecane was taken into consideration using the partition coefficient of butan-1-ol calculated from the RI of the oil phase.

A salinity scan is a set of microemulsions for which the only variable in the brine salinity. Optimal salinity is defined as the salinity at which the oleic and aqueous phases are solubilised in equal proportions in the middle phase.

3.3. Materials and solutions preparation

3.3.1. Choice of the oil-brine-surfactant-alcohol system

Butan-1-ol is an interesting cosurfactant/cosolvent because it is the first of the linear alcohols to show a lipophilic contribution to the phase diagram (see the study of Bourrel and Chambu on the variation of linear-alcohol chain length in hexane-brine-SDS system [Bourrel and Chambu, 1983]). In addition, butan-1-ol has received less attention than longer-chain alcohols in the investigation of interfacial compositions, probably because of the extensive use of the dilution method which imposes the use of alcohols with very poor solubility in water.

Dodecane is a 12-carbon linear alkane. Shorter alkanes are often studied, e.g. hexane-pentanol-SDS-brine [Bourrel and Chambu, 1983], heptane-butanol-SDS-brine [van Nieuwkoop and Snoei, 1985]. However, dodecane is experimentally easier to handle because of its slower evaporation rate. Straight alkanes are used in petroleum industry as replicates of crude oils. A crude oil is a complex mixture of polar and apolar, large and small molecules and quantitative descriptive parameters have been developed to allow for the comparison of

different crude oils. One of these characteristics is the equivalent alkane carbon number (EACN) which is in essence a measure of the polarity of a crude oil [Salager et al., 2013]. Dodecane would thus be used in preliminary tests to screen surfactant mixtures for an EACN = 12 oil, such as the Dulang crude oil (Malaysia) [Mumtaz et al., 2015]. In addition, dodecane offers a large polarity difference with butan-1-ol. Finally, dodecane and sodium dodecyl sulfate have an alkane chain of equal length which is an attractive characteristic for optical measurements.

Surfactant blends used in surfactant EOR often contain one sulfate surfactant. To keep the system simple, sodium dodecyl sulfate (SDS) was chosen as the sole surfactant because it does not form a lamellar phase and is thoroughly studied in the interface and colloid scientific community. In addition interfacial-tension measurements between dodecane and brine at different concentrations of SDS and butan-1-ol are available [Zhou and Dupeyrat, 1990].

3.3.2. Salinity scans

Microemulsions were prepared by weight in test tubes. Dodecane (99% pure, Acros Organics), butan-1-ol (ACS grade, Sigma-Aldrich) and sodium dodecyl sulfate (SDS) (ACS grade > 99%, Sigma-Aldrich) were used without further purification. Brine solutions of 6 and 10% w/v NaCl were prepared with sodium chloride (analytical reagent grade, Fisher) which was used as received. Lower salinity brines were prepared by dilution. Dodecane (3 mL), brine (3 mL), SDS and butan-1-ol were added sequentially. Microemulsions were prepared at $\gamma = 0.17$. The relative proportion of butan-1-ol to SDS varied. Microemulsions were shaken by hand. They were left to equilibrate at room temperature (20 ± 2^{o}C) for at least 48 hours. Phase volumes were inferred from the heights of phase boundaries with a height/volume calibration curve. The precision on the rule was 0.5 mm, corresponding to 0.07 mL.

3.3.3. Phase diagram at fixed salinity

A series of nine samples was prepared by weight at room temperature in 1-mL plastic vials with equivolume of dodecane to 6% w/v NaCl brine and SDS recrystallised

three times in ethanol. Each sample weighted 520 mg. The mass of SDS was varied from 5 to 76 mg corresponding to a weight fraction of 1 to 15 wt%. The volumes of dodecane and brine were varied from 300 to 200 µL. The samples were titrated with butan-1-ol aliquots and phase behaviours were recorded after equilibration. First, the phase boundaries were approximately located with a 20 µL-aliquot titration, corresponding to 3 wt%-butan-1-ol steps. The titration was then repeated with 2-µL aliquots close to the phase-transition volumes, corresponding to 0.3 wt%-butan-1-ol steps. A tenth sample was prepared by weight in an NMR tube pretreated with 0.1 M NaOH solution, with 690 µL dodecane and 690 µL of a 6% w/v NaCl brine solution of 19 mM SDS. The weight fraction of SDS was 0.3 wt%. The sample was titrated with 10 µL aliquots of butan-1-ol, corresponding to 0.7 wt%-butan-1-ol steps. A middle phase down to 2 µL could be visualised in the NMR tube. The samples were titrated up to 15 wt% butan-1-ol and up to 9 wt% butan-1-ol for the sample in the NMR tube.

3.3.4. Solution preparation for diffusion NMR analysis

Microemulsions

Three microemulsions were prepared by weight in test tubes. 3 mL of dodecane (99% pure, Acros Organics, filtered through silica gel and alumina) were added to 3 mL of brine. 6% w/v NaCl brine was prepared by weighting 0.6 g of sodium chloride (analytical reagent grade, Fisher - used as received) in a 10-mL volumetric flask which was filled with D_2O (Goss Scientific, D > 99.9%). 0.6% w/v NaCl brine was prepared by dilution with D_2O. Butan-1-ol (ACS grade, Sigma-Aldrich - used as received) and SDS (ACS grade > 99%, Sigma-Aldrich, recrystallised three times in ethanol) were added to the dodecane-brine mixture in a 2:1 w:w ratio. Mass fraction of surfactant + cosurfactant γ (see Equation (3.4)) was equal to 0.17 for the low salinity microemulsion. The high salinity microemulsions were prepared at $\gamma = 0.17$ and 0.27. Microemulsions were left to settle for at least 48 hours at room temperature (20 ± 2 ^{o}C). 0.7 mL of the microemulsion phases (middle phase of L3 and lower phase of L1) were transferred in NMR tubes with a Pasteur pipette.

Solutions in the NMR tubes were clear single phases.

Other solutions

SDS solutions in D_2O were prepared above and below the critical micellar concentration (cmc) with recrystallised SDS, at 0.6 and 6% w/v NaCl. In absence of salt, the SDS cmc is equal to 8.1 mM. In 6% w/v NaCl, SDS cmc was measured to be equal to 0.13 mM by pendant drop tensiometry. At 0.6% w/v NaCl, it was estimated to be 1.2 mM [Mysels and Princen, 1959]. Two surfactant solutions were prepared at 0.05 and 0.64 mM in 6.0% w/v NaCl brine, and two surfactant solutions were prepared at 0.05 and 8.53 mM SDS in 0.6% w/v NaCl brine.

3.4. Methods

Peak assignments in order to attribute species contributions to the measured apparent coefficients

DOSY ^{1}H NMR was carried out on the lower-phase of an L1 system and the middle phases of two L3 systems. In DOSY NMR, a pulse sequence of magnetic field with increasing gradient strength is applied to the sample. As the gradient amplitude of the pulse becomes more intense, peaks intensities decrease exponentially. Different peaks may decrease at different rates. Diffusion coefficients can be inferred from the decay of the peak intensities with increasing gradient strength. The faster a peak decays, the larger its diffusion coefficient. For each peak, the measured apparent diffusion coefficient D_{app} is a weighted sum of the mobilities of the free analyte, of the analyte within larger entities (analyte in clusters/micelles) and of the mobility of the entity itself, if species exchange between environments on a time rate which is fast compared to the diffusion time in the pulse sequence. In these experience, the pulse sequence lasted 200 ms which is two orders of magnitude longer than typical molecular exchanges.

In addition, signals of more than one molecule may have the same chemical shift. In this case, the decrease of the peak signal with increasing gradient strength is a

combination of exponentials. More than one combination of exponential coefficients and apparent diffusion coefficients can fit the measured shape of the decrease, even in the case of overlapping chemical shifts of only two molecules. Multivariate analysis is used to overcome this issue, but it is a demanding technique because only very stable data can be analysed. More simply in this study, signals that were overlapping signals, and those that were not, were identified to avoid the analysis of composite signal decrease because of overlapping signals. For this purpose, each component of the microemulsion phase was run alone under the same conditions than the microemulsion-phase samples. In Figure 3.1, the spectra of, from top to bottom,

1. dodecane in $CDCl_3$,
2. 6.2 wt% butan-1-ol in 0.6% w/v NaCl brine solution,
3. 8.5 mM SDS in 0.6% w/v NaCl brine solution, and
4. microemulsion phase of low salinity microemulsion

were stacked to identify peaks in the spectrum of the microemulsion phase corresponding to non-overlapping signals.

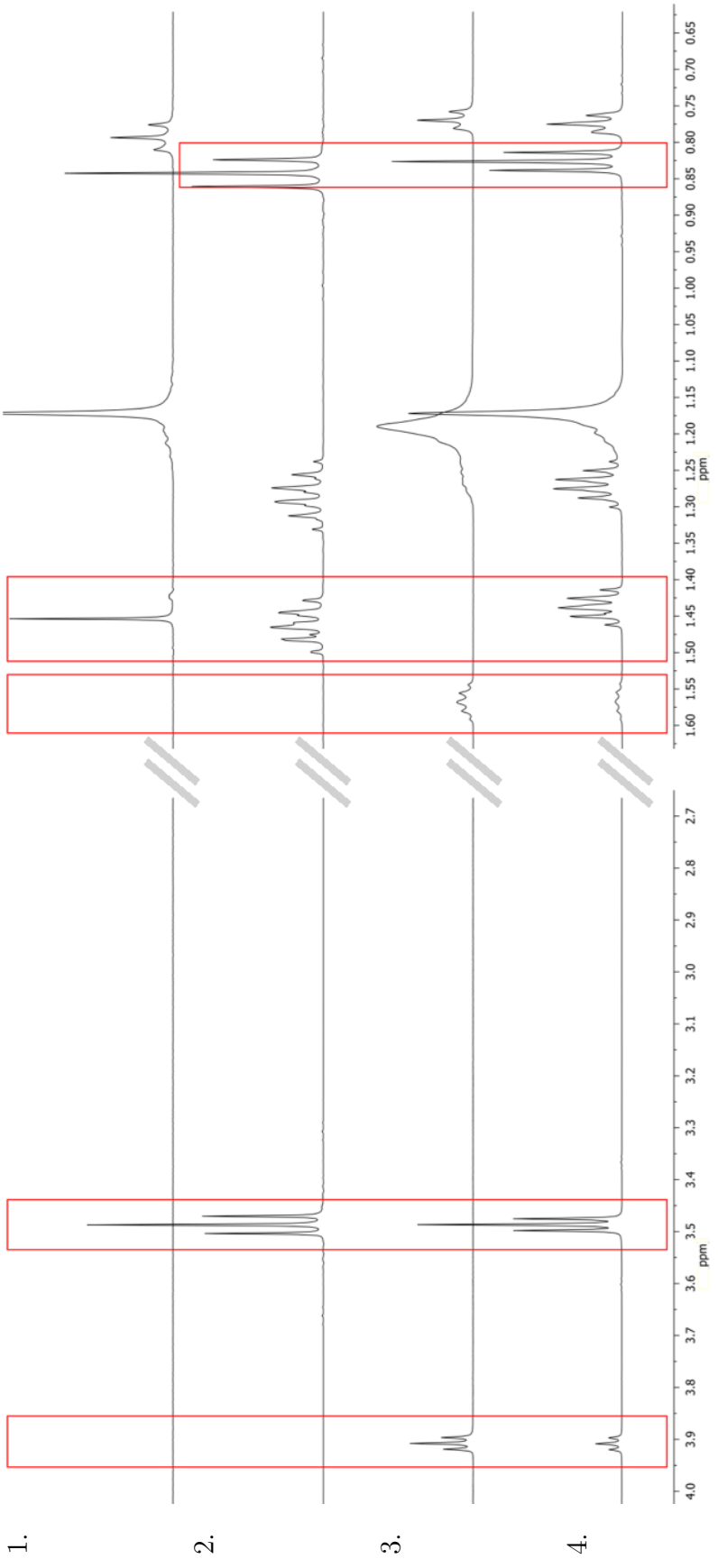

Figure 3.1: Spectra of (1.) dodecane in $CDCl_3$; (2.) 6.2 wt% butan-1-ol in 0.6% w/v NaCl brine solution; (3.) 0.85 M SDS in 0.6% w/v NaCl brine solution, and (4.) microemulsion phase of 0.6% w/v NaCl:dodecane microemulsion, stacked to identify peaks in spectrum 4. corresponding to non-overlapping signals, highlighted with red boxes.

The attribution of the peaks in the microemulsion-phase spectrum of Figure 3.1 are summarised in Table 3.1. The impurity peak in dodecane at 1.45 ppm is likely trace of water [Fulmer et al., 2010].

Table 3.1: Peaks attributions in microemulsion phase. t triplet, m multiplet, s singlet. The structures of the molecules are shown in Figure 3.2.

Shift /ppm	Multiplicity	Dodecane	Butan-1-ol	SDS	Mono-component signal?
3.92	t	–	–	H^a	Yes
3.48	t	–	H^A	H^b	Yes
1.57	m	–	–	H^c	Yes
1.44	m	–	H^B	–	Yes
1.27	m	–	H^C	H^d	No
1.17-1.25	s (with shoulder)	H^{ii}	–	H^d	No (main contribution from dodecane)
0.83	t	–	H^D	–	Yes
0.77	m	H^i	–	H^e	No

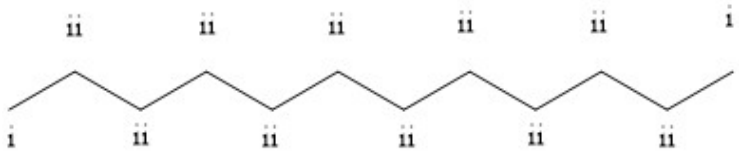

(a)

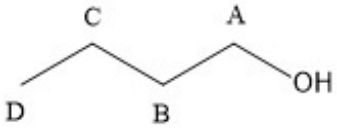

(b)

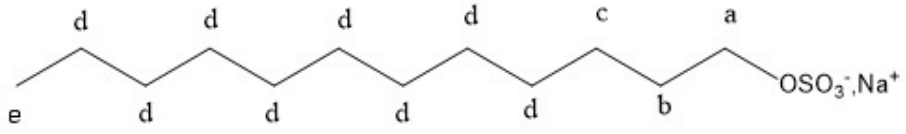

(c)

Figure 3.2: Structures of (a) dodecane, (b) butan-1-ol, and (c) SDS.

3.4.1. Butan-1-ol partition coefficient

Butan-1-ol partitions between brine and oil. Partition coefficients of butan-1-ol were calculated based on refractive index of the oil phase, or ^{1}H NMR in the aqueous or oil phase.

Butan-1-ol concentration in oil determined from the refractive index of the oil phase

Two series of dodecane-butan-1-ol mixtures were prepared by weight by mixing 6.0 g of dodecane with butan-1-ol. The mass of butan-1-ol varied from 14 mg to 1.4 g. One of the two series was wetted by adding aliquots of water to the samples. Samples with butan-1-ol concentrations below and above 9 wt% were wetted with 10 and 100 µL respectively. Considering a butan-1-ol solubility in water of 1.1 M, less than 1.5% of the butan-1-ol of the dodecane-butan-1-ol mixtures were lost to the water aliquots. Refractive indices of the *dry* and *wet* mixtures were measured at 20^{o}C (see Figure 3.3).

Table 3.2: Second order polynomials to relate RI of the oleic phase to its butan-1-ol concentration

$C^{oil}_{ButOH} = a_0 + a_1 \times RI + a_2 \times RI^2$			
	$a_0 \times 10^3$	$a_1 \times 10^3$	$a_2 \times 10^3$
dry calibration	1.141	-1.571	0.540
wet calibration	-0.200	0.319	-0.125

The RI of the two series were undistinguishable below 9 wt% butan-1-ol. Above 9 wt% butan-1-ol, the RI of the wet samples were lower than their dry counterparts. The uptake of water in the oleic phase was estimated using the Lorentz-Lorenz equation shown in Equation (3.6),

$$\frac{n^2_{wet}-1}{n^2_{wet}+2} = \phi_{water}\frac{n^2_{water}-1}{n^2_{water}+2} + \phi_{dry}\frac{n^2_{dry}-1}{n^2_{dry}+2} \tag{3.6}$$

where n_{wet} is the refractive index of the wet dodecane-butanol mixture, n_{water} and n_{dry} are the refractive indexes of water and the dry dodecane-butan-1-ol mixture and

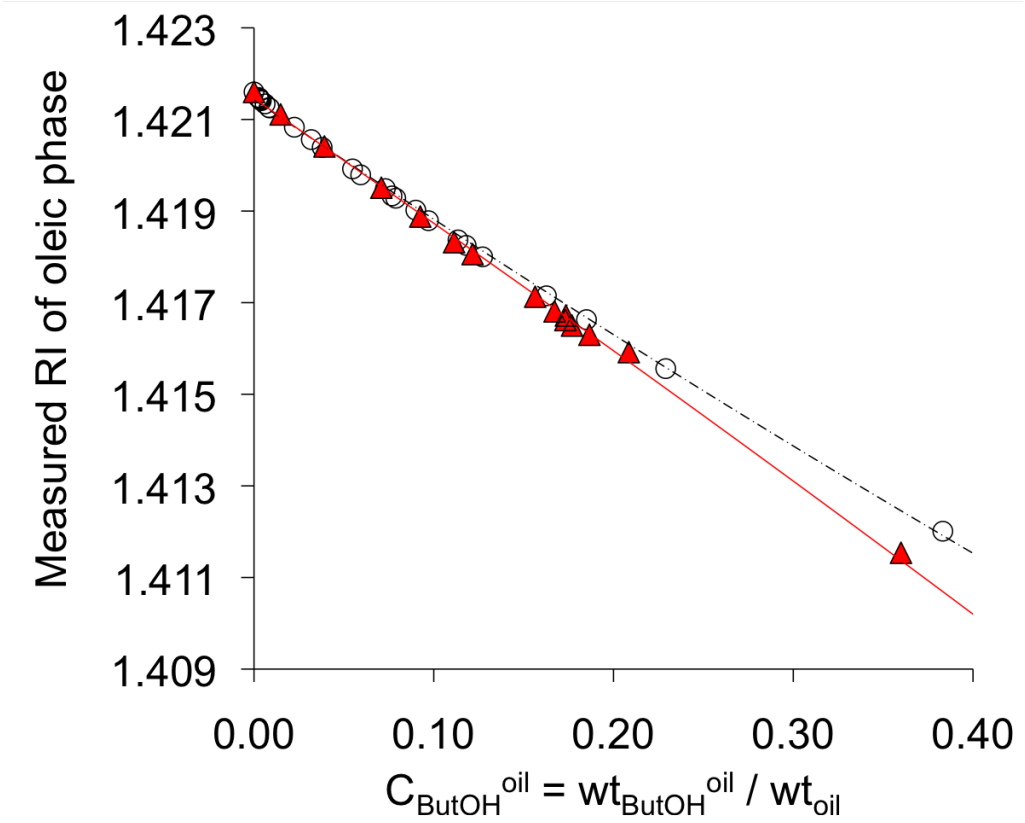

Figure 3.3: RI of *dry* (circles) and *wet* (triangles) dodecane-butan-1-ol mixtures, measured on 500-µL volumes at 20^{o}C. The lines are the second order polynomial fits used to relate RI of the oleic phase to its butan-1-ol concentration, see Table 3.2.

ϕ_{water} and ϕ_{dry} their volume fractions respectively. The dry dodecane-butan-1-ol mixture was considered as a pure component.

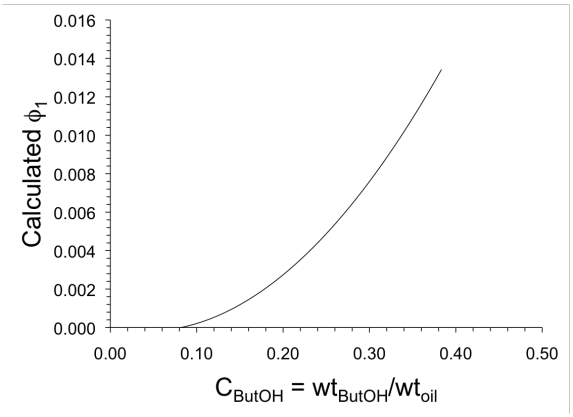

Figure 3.4: Volume fraction of water uptake ϕ_1 in dodecane-butan-1-ol mixtures as a function of butan-1-ol content, calculated using the Lorentz-Lorenz equation.

Oleic phase RI was impacted when more than 0.1% v/v of water was solubilised in the solution (see Figure 3.4). The amount of water driven into the oil phase by butan-1-ol molecules varied non-linearly with the butan-1-ol concentration.

Butan-1-ol concentration in oil determined by ^{1}H NMR

The aforementioned dodecane-butan-1-ol mixtures were analysed with ^{1}H NMR, in chloroform-d_3 at 400 MHz. The hydrogens of dodecane and butan-1-ol are labelled in Figure 3.2. Their chemical shifts were as follows:

- Butan-1-ol: H_D δ 0.93 ppm (t, J = 7.4 Hz), H_C δ 1.41 ppm (m), H_B δ 1.63 ppm (m), H_A δ 3.65 ppm (td, J = 6.5, 5.0 Hz).

- Dodecane: H_i δ 0.88 ppm (t, J = 7.1 Hz), H_{ii} δ 1.27 ppm (m).

The butan-1-ol concentrations in the prepared mixtures were calculated from peak-area ratios of butan-1-ol to dodecane. Figure 3.5 compares the concentrations calculated for different peak-area ratios. Butan-1-ol content was determined most accurately when using the ratio of the butan-1-ol peak area at 3.65 ppm to that of the hydrogen of the methyl group of dodecane at 0.88 ppm. When using the butan-1-ol

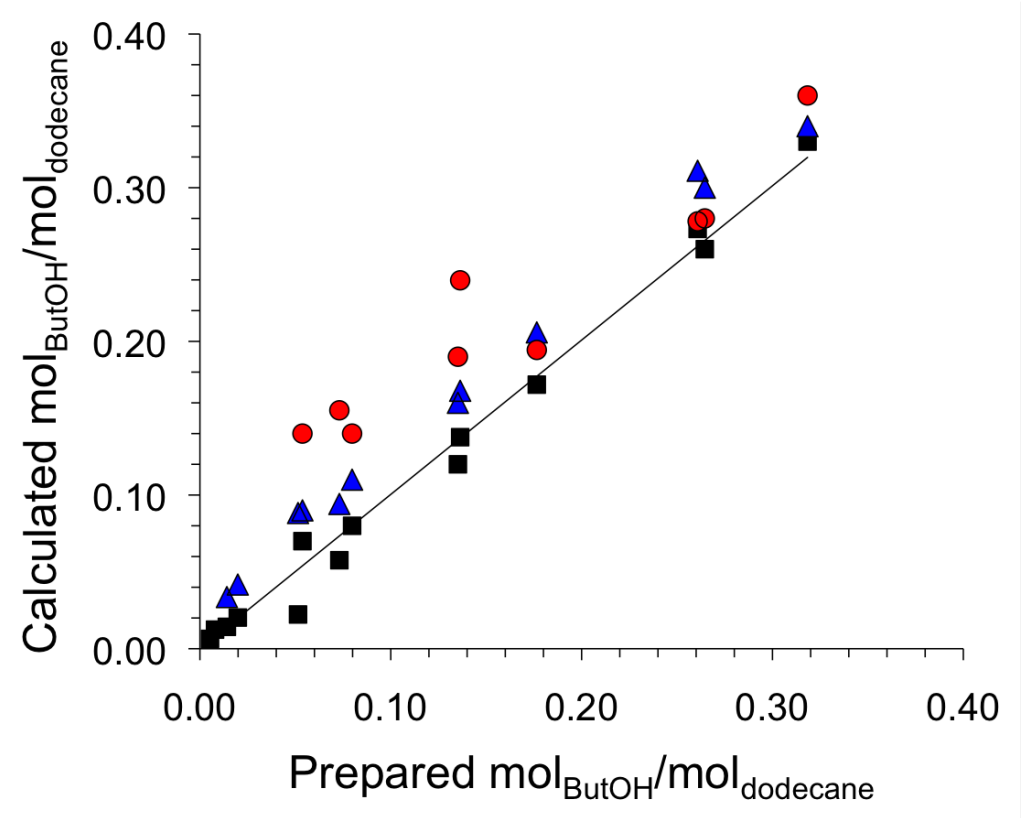

Figure 3.5: Mole ratios of butan-1-ol in dodecane determined by ^{1}H NMR, calculated from the weighted area ratios of the butan-1-ol peaks at 3.65 ppm (black squares), 1.63 ppm (red circles) and 0.93 ppm (blue triangles) to the dodecane triplet at 0.88 pm.

peak area at 1.63 ppm, butan-1-ol concentration was consistently over-estimated. The area ratio of the butan-1-ol peak at 3.65 ppm to the dodecane peak at 0.88 ppm was thus used to calculate butan-1-ol concentrations in oleic phases.

Butan-1-ol concentration in aqueous phase determined by ^{1}H NMR

Butan-1-ol concentrations in aqueous phases were determined by ^{1}H NMR using acetone as an internal standard, which gave a single peak at 2.14 ppm in D_2O. Acetone concentrations were chosen so that the peak areas of butan-1-ol and acetone were within a factor of 5. Results presented in Table 3.3 shows that the butan-1-ol concentration in the aqueous phase was underestimated by 2 to 4%.

Table 3.3: Accuracy of aqueous-butan-1-ol-concentration measurements by ^{1}H NMR with internal standard

Brine salinity /% w/v NaCl	Butan-1-ol concentration /M	
	Prepared	Measured with ^{1}H NMR
10	0.452	0.433
8.5	0.432	0.425
6	0.598	0.581

For the determination of butan-1-ol concentrations in the aqueous phases of equilibrated brine-dodecane mixtures, the aqueous phases were sampled from the bottom of the vials not to contaminate the samples with oil phase. This precautionary approach prevented a loss of acetone towards the aliquot of oil in the NMR tube and an underestimation of the partition coefficient.

A second method was developed to avoid the use of internal standard. In this procedure, spectra of 6% w/v NaCl brine solutions of butan-1-ol were recorded before and after equilibration with dodecane which was added directly into the NMR tubes. NMR tubes were pre-treated with a solution of 1 M NaOH to increase the hydrophilicity of the tube wall. 700 µL of the brine solution of butan-1-ol were poured in an NMR tube with 50 µL D_2O. The absolute integral of each resonance peak of butan-1-ol ($A_{aq,init}$) was recorded. Then, 750 µL dodecane were poured into the NMR tube. The tube was turned upside down about 15 times. The absolute

integral of each butan-1-ol resonance peak was recorded after extraction ($A_{aq,extract}$), keeping the dodecane in the NMR tube for the NMR scan. The oil phase in the NMR tube stood outside of the magnetic field of the instrument. Thus even with the dodecane present in the NMR tube, only butan-1-ol in the aqueous phase (the lower phase) was resonating.

After equilibrium, the butan-1-ol concentration in the aqueous phase C^{aq}_{ButOH} was proportional to $A_{aq,extract}$, while the butan-1-ol concentration in the oil phase C^{oil}_{ButOH} was proportional to $A_{aq,init} - A_{aq,extract}$.

Calculated partition coefficient

Mixtures of brine (3 mL) and dodecane (3 mL) were prepared by weight with butan-1-ol content varying from 0.1 to 17 wt% of total mass. Solutions were shaken by hand and let to rest overnight.

Partition coefficient below 6 wt% butan-1-ol Butan-1-ol concentrations in the equilibrated oil phases were calculated based on refractive index of the oil phases and ^{1}H NMR. Aqueous-butan-1-ol concentrations were measured by ^{1}H NMR with and without internal standard (see Section 3.4.1. for methods). Partition coefficient was defined as the concentration ratio of butan-1-ol in the oil and aqueous phases. The butan-1-ol concentration in one phase was calculated from the measurements aforementioned and the butan-1-ol concentration in the other phase was calculated by mass balance. Figure 3.6 shows that the different techniques used to calculate the partition coefficients were in general agreement.

Partition coefficient above 6 wt% butan-1-ol Measure of RI was the most straight-forward measurement. Since methods gave similar results for the calculation of partition coefficient below 6 wt% butan-1-ol (see Figure 3.6), partition coefficient above 6 wt% butan-1-ol was calculated from RI of oil phases only. Oleic-butan-1-ol concentrations of brine-dodecane mixtures were calculated from RI of oil phases, using the *wet* calibration (see Table 3.2), and aqueous-butan-1-ol concentrations were calculated from mass balance. The *dry* calibration resulted in non-physical

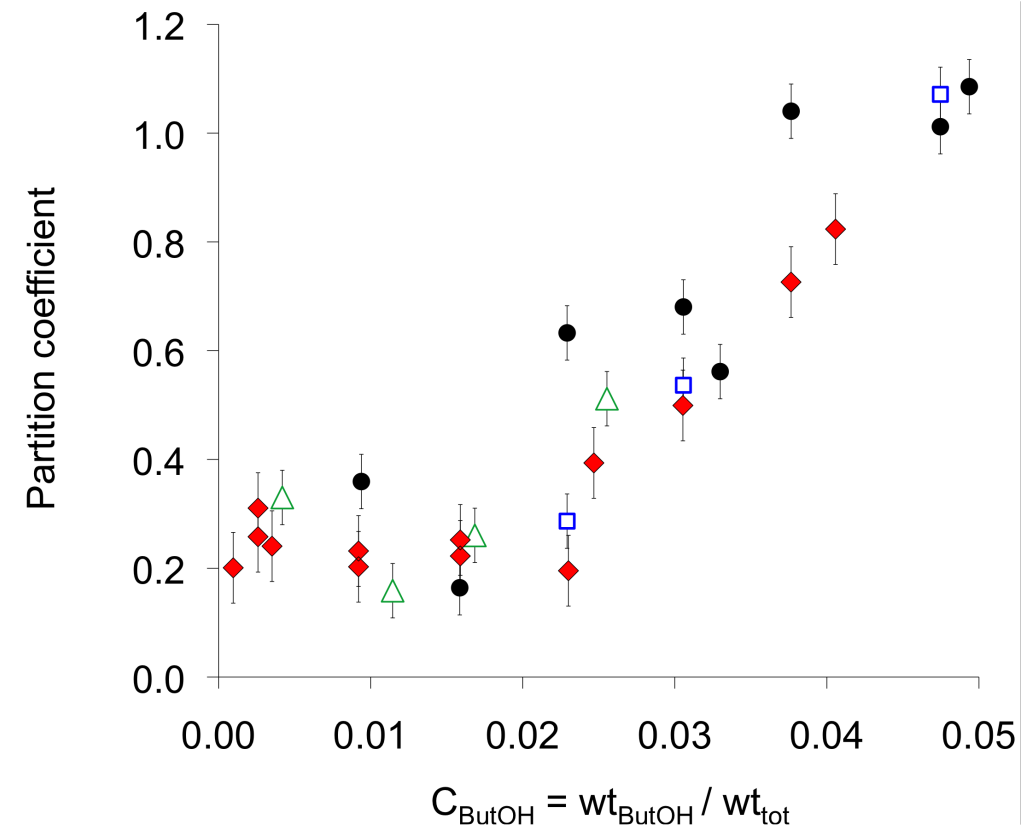

Figure 3.6: Comparison of partition coefficient of butan-1-ol between 6% w/v NaCl and dodecane calculated from:
- oleic-butan-1-ol concentration based on ^{1}H NMR (filled circles), RI (red diamonds), and
- aqueous-butan-1-ol concentration based on ^{1}H NMR with (open squares) and without (green triangles) internal standard.

(negative) calculated aqueous concentrations for mixtures with 15 wt% butan-1-ol overall and more. Figure 3.7 shows the calculated aqueous phase concentrations, based on aqueous phase densities below 6 wt% butan-1-ol, and calculated from RI of oil phases above 6 wt% butan-1-ol. The aqueous-phase density was related to its butan-1-ol content by

$$\rho = \sum_i \rho_i x_i, \tag{3.7}$$

where ρ is the density of an ideal mixture composed of i components of densities ρ_i and mass fractions x_i. Density of brine was taken from the density table of sodium chloride at 20°C provided by Mettler Toledo. Density of butan-1-ol was 0.8098 g.cm^{-3}. One can note that for simplicity, the excess volume of mixing was assumed to be zero. Herráez et al. showed the butan-1-ol/water mixtures has a negative excess molar volume which reaches an extremum for 40% butan-1-ol mixture in water, reaching -0.65 mL.mol^{-1} [Herráez, 2006]. The excess volume of mixing is thus non-negligible. However, this underestimate did not have a lot of impact as the compositions at the interface of microemulsions were not calculated from density measurements.

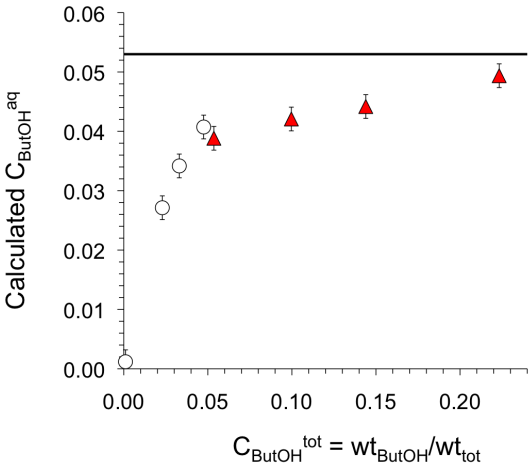

Figure 3.7: Aqueous-butan-1-ol concentrations in 5% w/v NaCl-dodecane mixtures, calculated from aqueous phase densities (circles) using Equation 3.7 and from mass balance and RI of oil phases (triangles). Black line is the butan-1-ol solubility limit in 5% w/v NaCl.

3.4.2. Determination of bulk and interfacial compositions of microemulsions

Method justification

Interfacial composition can be inferred from interfacial tension measurements using the Gibbs equation ([Verhoeckx et al., 1987], [Zhou and Dupeyrat, 1990], [Kegel et al., 1993]), the dilution method ([Verhoeckx et al., 1987], [Moulik et al., 2000], [Bidyut and Debdurlav, 2007]) or other techniques such as Raman spectroscopy ([Shih and Williams, 1986]). The Raman method is based on the observation that certain chemical bonds display a shift in vibrational frequency as the solvent environment changes. Shih et al. investigated dilute aqueous solutions of surfactant and benzyl alcohol [Shih and Williams, 1986]. The quantitative interpretation of Raman spectra for a system containing oil and of bicontinuous structure would be far more complicated, and is beyond the scope of this thesis. The dilution method, or Schulman's titration [Bowcott and Schulman, 1955], is appropriate for L2 microemulsions. With this method, the compositions of the continuous phase and the interface are calculated from the dilution path of the microemulsion. The microemulsion is titrated sequentially with aliquots of oil and of alcohol resulting in the dilution of the microemulsion with a solution of oil and alcohol having the composition of the continuous phase; such dilution is however impossible for bicontinuous microemulsions [Cazabat et al., 1982]. In addition, the titration method makes the assumption that the alcohol concentration is nil in the aqueous phase and therefore that the alcohol in the reverse micelles is essentially in the interfacial film. While this assumption is prudent for pentanol and higher alcohols, it is not satisfactory for butan-1-ol which has a non-negligible solubility in water (1.1 M). Finally, the use of the Gibbs equation implies the knowledge of alcohol activity coefficients, which cannot be assumed to be one because of the self-association of alcohol in oil. Finally, the experimental studies reporting on interfacial compositions deduced from interfacial tension measurements were made at SDS concentration up to just above the cmc ([Verhoeckx et al., 1987],

[Zhou and Dupeyrat, 1990], [Kegel et al., 1993]) to avoid the formation of a middle-phase. An ultimate indirect method to know the interfacial composition consists of using the model of pseudo-phases which is based on the assumption that the phase(s) solubilised in the microemulsion phase has (have) the same composition(s) as the corresponding excess phase(s). The interfacial alcohol concentration is calculated from the concentration of alcohol in the excess phase(s) and mass balance on the alcohol. The use of this method was reported for L1 systems [Zhou and Rhue, 2000] and was used in this thesis on L1 and L3 systems.

In these studies, concentrations of alcohol in bulk phases were measured by gas chromatography (GC). GC measurements take typically 15 minutes per sample and can become tedious when considering the need for blanks, sample spikes and calibration standards [Zhou and Rhue, 2000]. In this thesis, alcohol in the oil phase was calculated from refractive index (RI) which is a faster and more straight-forward measurement.

Method

Excess phase compositions and interfacial compositions of microemulsion phases of L1 and L3 systems were determined in terms of butan-1-ol from RI of the oleic phase. The butan-1-ol concentrations in L1 or L3 systems were determined as follows:

1. Butan-1-ol concentration in the oleic phase was determined from the RI of the phase.

2. Butan-1-ol concentration in the aqueous phase was calculated from partition coefficient and butan-1-ol concentration in the oleic phase.

3. Butan-1-ol at the interface in the microemulsion phase was calculated from mass conservation on butan-1-ol (see Equation (3.8))

$$wt_{ButOH}^{interface} = wt_{ButOH}^{tot} - (wt_{ButOH}^{oil} + wt_{ButOH}^{aq}) \tag{3.8}$$

where $wt_{ButOH}^{interface}$ is mass of butan-1-ol at the interface, wt_{ButOH}^{tot} total mass of

butan-1-ol in the formulation, wt^{oil}_{ButOH} mass of butan-1-ol in the oleic phase and wt^{aq}_{ButOH} mass of butan-1-ol in the aqueous phase.

This equation neglects the amount of butan-1-ol and SDS present as mixed micelles in the aqueous phase. In the aqueous phase, SDS is present at its critical micellar concentration (cmc) which was measured by pendant drop tensiometer to be 0.13 mM in 6% w/v NaCl brine. If the excess aqueous phase is 4 mL, then 0.5 µL SDS is present in the excess aqueous phase. This corresponds to less than 0.2% of total SDS and can thus be neglected. Butan-1-ol is at least twice the weight of SDS in the prepared mixtures and it is thus reasonable to neglect the portion of butan-1-ol present in mixed micelles.

In addition, this method did not work for L2 phase behaviour because the microemulsion phase is in the oleic phase. In this case, the oleic phase RI could not relate to the butan-1-ol content in the phase because a portion of the aqueous phase is solubilised in reverse swollen micelles.

In this chapter, two kinds of butan-1-ol to SDS (ButOH:SDS) ratios were defined:

- *a mixture ratio* which is obtained by dividing the total amount of butan-1-ol by the total amount of SDS present in the mixture,
- *a ratio specific to the interface.*

The interfacial butan-1-ol to SDS ratio may differ from the mixture ratio. This difference accounts for the proportion of butan-1-ol that was not at the interface but in the bulk phases.

3.5. Results

3.5.1. Partition coefficient of butan-1-ol

The partition coefficient of butan-1-ol between brine and dodecane depended on the total amount of butan-1-ol in the system and the salinity of the brine solution. The partition coefficient was measured below 5 wt% butan-1-ol for 6% w/v NaCl

- dodecane mixtures (see Figure 3.8 (a)). Two regions can be distinguished: below 1.8 wt% butan-1-ol the partition coefficient was constant, 0.24 ± 0.02; above 1.8 wt% butan-1-ol the partition coefficient increased linearly with the butan-1-ol concentration. One could suggest that above 1.8 wt% butan-1-ol, the concentration in the 6% w/v NaCl reached a value above which the entropy penalty due to the rearrangement of water molecules around the carbon chain of butan-1-ol reaches a threshold value whereby no more butan-1-ol may be solubilised. On the other hand, butan-1-ol molecules may form cluster or self-associate in the dodecane phase [Biais et al., 1981], accounting for the increasing proportion of butan-1-ol solubilised in the oleic phase.

Partition coefficients of butan-1-ol between brine and dodecane mixtures containing more than 5 wt% butan-1-ol overall were measured at different ionic strength (see Figure 3.8 (b) and see Table 3.4 for correspondence between mass and molar concentrations of NaCl brine solutions). In addition, saturation concentrations of butan-1-ol in brines of increasing ionic strength were measured by ^{1}H NMR (Table 3.5). For the butan-1-ol range investigated, partition coefficient varied linearly with the butan-1-ol concentration and was correlated to the brine salinity of the aqueous phase (see Figure 3.9). This result can be explained in terms of the Hofmeister series. The early ions of the series (NH_4^+, K^+, Na^+) decrease the solubility of non-polar molecules by increasing the hydrophobic interactions between the non-polar molecules; this phenomenon is entropy-driven [Zangi et al., 2007]. Here, Na^+ salts out butan-1-ol. Kegel et al. observed the same trend for the partition of pentanol between cyclohexane and brine [Kegel et al., 1993]. The partition coefficient of butan-1-ol between 2.5% w/v NaCl and dodecane was estimated to be 2.4 ± 0.2 with 14 wt% butan-1-ol; for the same system [Zhou and Dupeyrat, 1990] measured a partition coefficient of 2.

It is worth noting that when C^{oil}_{ButOH} tends to one, the partition coefficient tends to one over the butan-1-ol-saturation concentration in brine, i.e. circa 19 for 5% w/v NaCl brine.

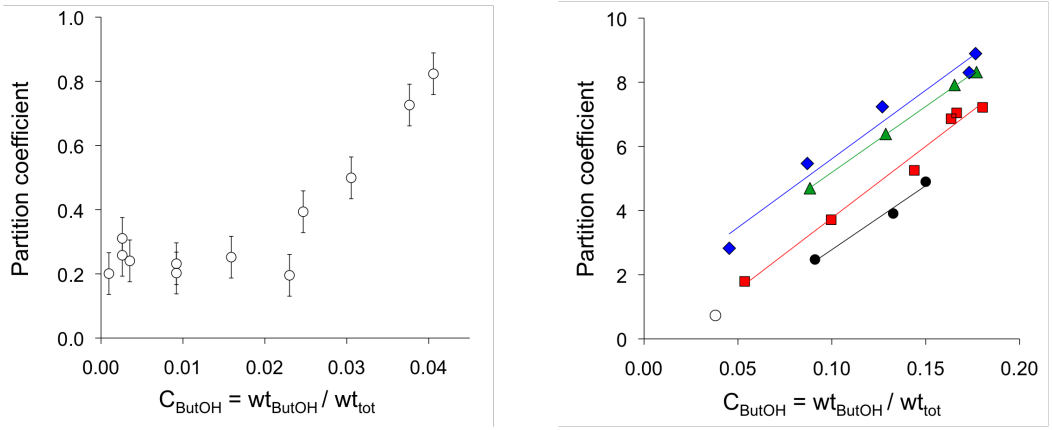

(a) 6% w/v NaCl brine - dodecane (b) Varying w/v NaCl brine - dodecane

Figure 3.8: Partition coefficient of butan-1-ol between brine and dodecane. 1.6% (filled circles), 5.2% (squares), 6.0% (empty circles), 8.0% (triangles), and 10.0% (diamonds) w/v NaCl brine solutions. Lines are a guide to the eye. Partition coefficients were calculated from RI of the oil phase.

Table 3.4: Correspondence between mass and molar concentrations of NaCl brine solutions.

NaCl concentration	
% w/v	mol.L^{-1}
1.6	0.28
5.2	0.92
6.0	1.07
8.0	1.45
10.0	1.83

Table 3.5: Butan-1-ol-saturation concentrations C_{sat} in brines of increasing salinity

Brine salinity /wt% NaCl	$C_{sat} = wt^{aq}_{ButOH}/wt_{aq}$
1.6	0.074 ± 0.004
5.2	0.053 ± 0.003
8.0	0.040 ± 0.002
10.0	0.036 ± 0.002

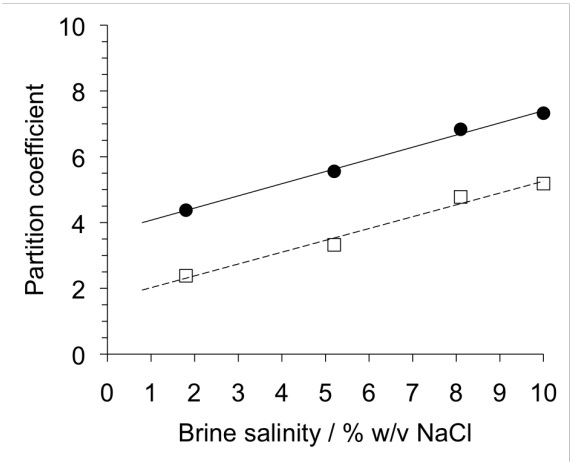

Figure 3.9: Partition coefficient of butan-1-ol between brines of different salinities and dodecane; solutions contained 9 (squares) and 14 wt% (circles) butan-1-ol overall. Lines are a guide for the eye. Partition coefficients calculated from RI of the oil phase.

3.5.2. Microemulsion phase analysis by diffusion NMR

SDS apparent diffusion coefficient in brine

The cmc of SDS was measured by pendant drop tensiometry to be 1.2 mM and 0.13 mM in 0.6% and 6.0% w/v NaCl brine, respectively. Apparent diffusion coefficients of SDS in 0.6 and 6.0% w/v NaCl brine solutions were measured above and below cmc (see Table 3.7). Correspondence between mass and molar concentrations of NaCl can be found in Table 3.6. The apparent diffusion coefficients of SDS in brine below the cmc were very similar in low and high salinity brines. The slight difference could be attributed to the difference in viscosity.

Molecular exchanges in solution are fast compared to the time scale of the signal detection. Hence, a single average signal is probed over all environments: above the cmc, the measured apparent diffusion coefficient is a weighted average of the SDS molecules mobilities in different states.

The apparent diffusion coefficient of SDS above the cmc in 0.6% w/v NaCl brine was a bit faster than the diffusion coefficient of a spherical micelle (1.4×10^{-10} and 0.92×10^{-10} $m^2.s^{-1}$ [Stigter et al., 1955], respectively). This difference could be attributed to the contribution of the mobility of free SDS to the apparent diffusion coefficient in the former case.

Table 3.6: Correspondence between mass and molar concentrations of NaCl

/% w/v	/mol.L^{-1}
6.0	1.07
0.6	0.10

Table 3.7: Apparent diffusion coefficient of SDS **above** and below cmc in brine solutions of 0.6 and 6% w/v NaCl

Salinity /% w/v NaCl	Prepared SDS conc. /mM	$D_{app} \times 10^{-10}$ /m^2.s^{-1} SDS	HDO
6.0	0.05	4.5 ± 0.1	17.777 ± 0.006
6.0	**0.64**	**2.87 ± 0.03**	**18.16 ± 0.02**
0.6	0.05	4.8 ± 0.1	18.834 ± 0.005
0.6	**8.53**	**1.405 ± 0.002**	**19.4 ± 0.2**

SDS diffused apparently faster in 6% w/v NaCl brine solution than in 0.6% w/v NaCl brine solution; the measured apparent diffusion coefficients were respectively $D_{app} = 2.9 \times 10^{-10}$ m^2.s^{-1} and 1.4×10^{-10} m^2.s^{-1}. The greater mobility of SDS in higher salinity brine solution was interpreted as an indication that spherical micelles became rod-like upon supplementary addition of salt. In the case of elongated micelles, although the micelle diffuses less rapidly than a spherical micelle [Mazer et al., 1976], the absolute position of a SDS molecule in the micelle can move because the molecule can diffuse as far as the rod length and thus SDS in micelle contribute to the apparent diffusion coefficient. The self-diffusion of a SDS molecule in a rod-like micelle ($D_{SDS\ in\ micelle}$) may be smaller than that of free SDS in water because the viscosity of the micellar environment is larger than that of water. However, $D_{SDS\ in\ micelle}$ is faster than the self-diffusion of the micelle, and will thus increase the apparent diffusion coefficient of SDS.

Calculated diffusion coefficients of butan-1-ol

The diffusion coefficients D of butan-1-ol in dodecane and brine solutions were calculated from the Stokes-Einstein equation, Equation (3.9) (see Table 3.8). The radius of butan-1-ol (2.9 Å) was taken as half the length of the molecule obtained

from Avogadro Software.

$$D = \frac{k_B T}{6\pi\mu r} \tag{3.9}$$

where k_B is the Boltzmann constant, T the absolute temperature, μ the solvent viscosity and r the radius of the particle.

Table 3.8: Diffusion coefficients D of butan-1-ol calculated at 25^{o}C from the Stokes-Einstein equation, see Equation (3.9).

Solvent	Viscosity /mPa.s	Radius /Å	$D \times 10^{-10}$ /m^2.s^{-1}
Dodecane	1.38	2.9	5.4
0.6% w/v NaCl	1.00	2.9	7.4
6% w/v NaCl	1.08	2.9	6.9

Apparent diffusion coefficients in microemulsion phases

The apparent diffusion coefficients from the spectra of the microemulsion phases shown in Figures 3.10, 3.11 and 3.12 are gathered in Table 3.9. The apparent diffusion coefficient of water decreased sequentially from the microemulsion phase of the L1 system prepared at $\gamma = 0.17$ to the middle phase of the L3 system prepared at $\gamma = 0.17$ to the middle phase of the L3 system prepared at $\gamma = 0.27$. Figure 3.13 shows that the apparent diffusion coefficients of HDO and dodecane were correlated to the volume fraction of aqueous/oil phase in the microemulsion phase.

In all three microemulsion phases, there were three diffusion bands. They are represented with horizontal rectangles in Figures 3.10, 3.11 and 3.12.

Table 3.9: Apparent diffusion coefficients in microemulsion phases. Microemulsions were prepared from 1:1 v:v mixtures of dodecane and brine and a 1:1 w:w ratio of butan-1-ol to SDS

Salinity /% w/v NaCl	γ	Phase behav.	$D_{app} \times 10^{-10}$ /m^2.s^{-1} SDS	HDO	Butan-1-ol	Dodecane
0.6	0.17	L1	0.4 ± 0.2	12.2	2.8 ± 0.1	0.6 ± 0.1
6.0	0.17	L3	1.1 ± 0.2	7.6	3.1 ± 0.1	2.6 ± 0.2
6.0	0.27	L3	1.1 ± 0.2	4.5	3.1 ± 0.1	3.9 ± 0.1

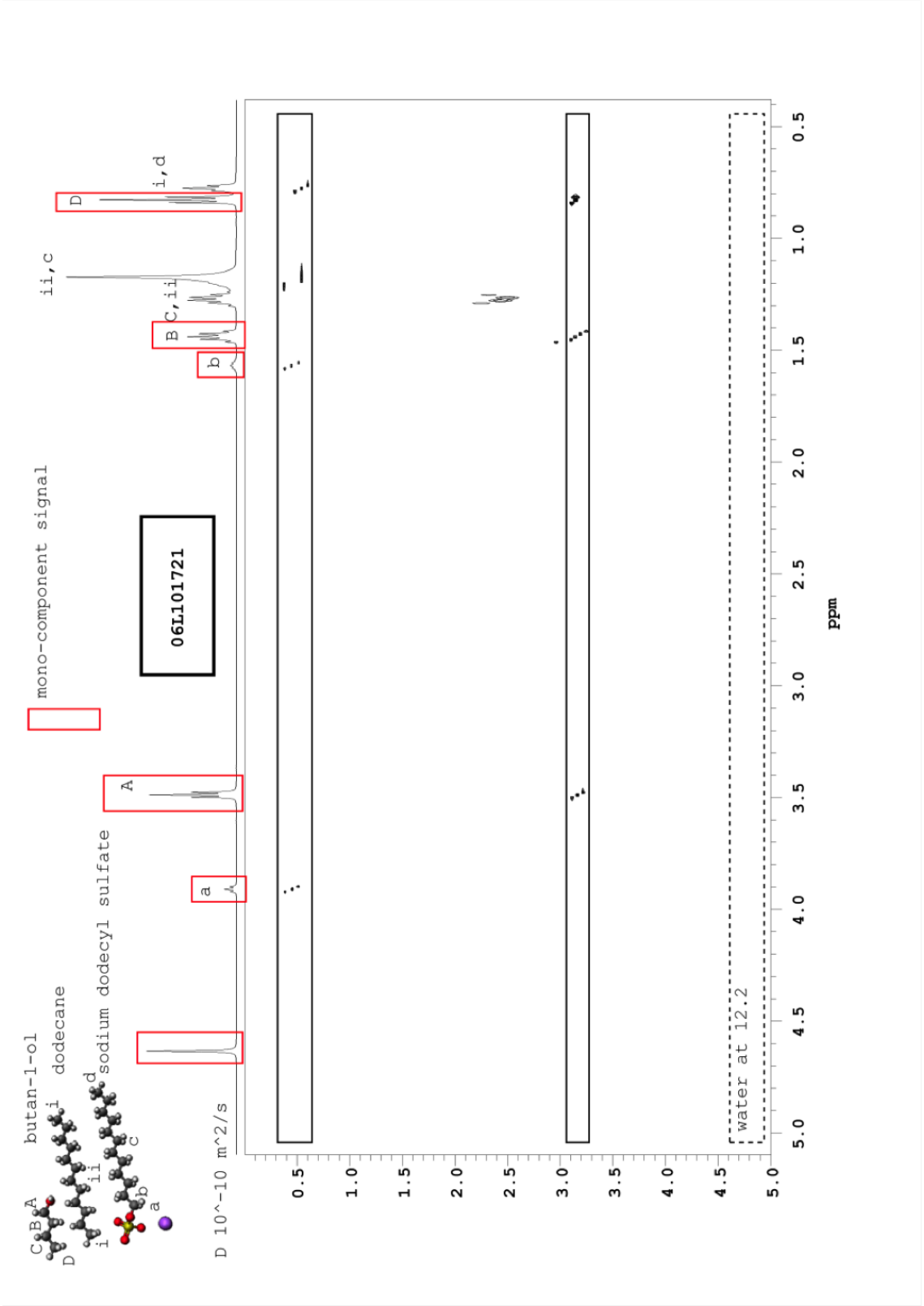

Figure 3.10: Spectrum of the microemulsion phase of the L1 system prepared with a 1:1 v:v mixture of dodecane to 0.6% w/v NaCl and a 2:1 w:w ratio of butan-1-ol to SDS added at $\gamma = 0.17$.

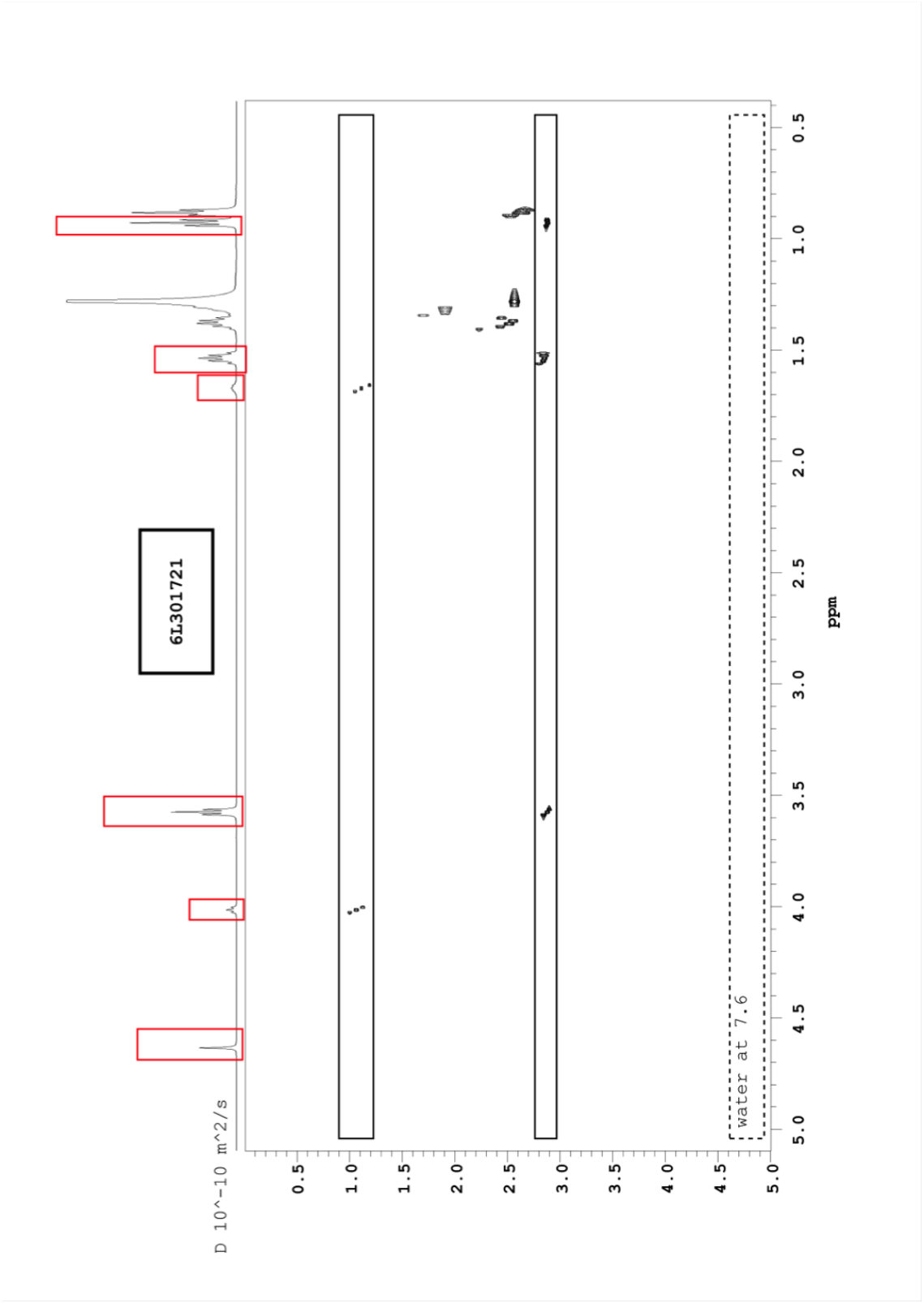

Figure 3.11: Spectrum of the microemulsion phase of the L3 system prepared with a 1:1 v:v mixture of dodecane to 6% w/v NaCl and a 2:1 w:w ratio of butan-1-ol to SDS added at $\gamma = 0.17$.

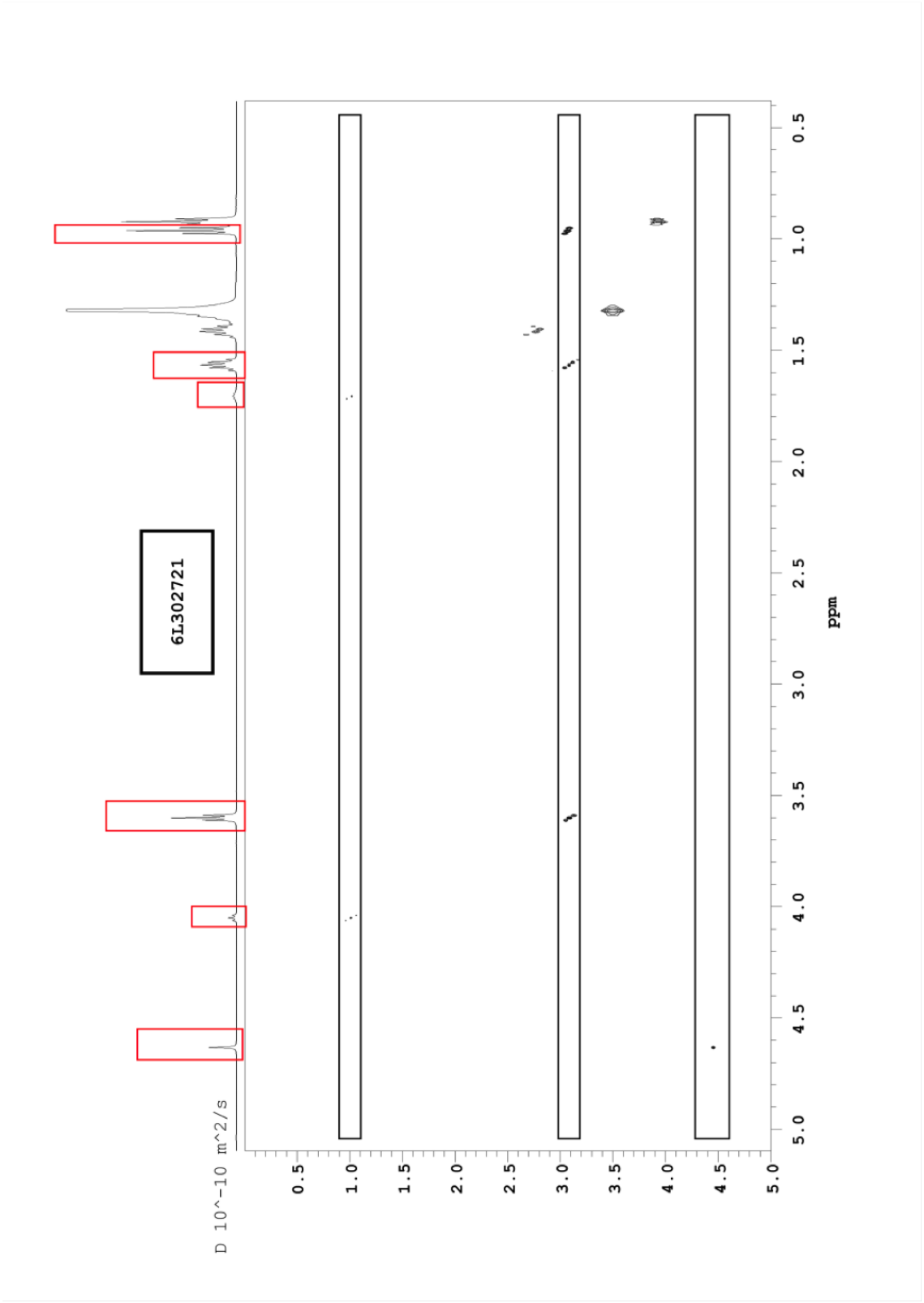

Figure 3.12: Spectrum of the microemulsion phase of the L3 system prepared with a 1:1 v:v mixture of dodecane to 6% w/v NaCl and a 2:1 w:w ratio of butan-1-ol to SDS added at $\gamma = 0.27$.

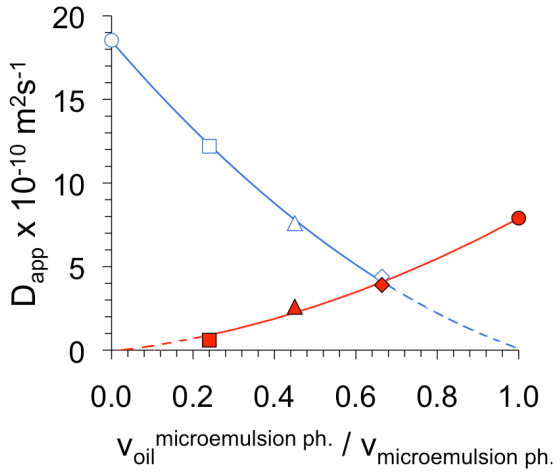

Figure 3.13: Apparent diffusion coefficient of HDO D_{app}^{HDO} (empty symbols) and dodecane D_{app}^{dd} (filled symbols) measured in the microemulsion phases of the L1 micromemulsion prepared at $\gamma = 0.17$ (square) and of the L3 microemulsions prepared at $\gamma = 0.17$ and 0.27 (triangle and diamond, respectively) as a function of the volume proportion of oil in the microemulsion phase. D_{app}^{HDO} at the origin is a mean of the values measured for HDO in 0.6 and 6% w/v NaCl above the cmc. D_{app}^{dd} at oil-volume fraction equal to one is the measured apparent diffusion coefficient of dodecane in dodecane. The lines are a guide for the eye.

Microemulsion phase of the L1 system prepared at $\gamma = 0.17$ The slowest diffusion domain was defined by the surfactant molecules, at circa 0.5×10^{-10} m^2.s^{-1}. This value was typical of swollen micelles which are bigger than spherical micelles and diffuse thus less rapidly. In the microemulsion phase of the L1 system, dodecane was contained within these micelles (same diffusion band). Butan-1-ol defined the second diffusion domain at circa 3×10^{-10} m^2.s^{-1}. Butan-1-ol in the microemulsion phases was slower than free butan-1-ol in brine (see Table 3.8) but was not as slow as the SDS diffusion band. At the butan-1-ol concentrations used in the formulations, butan-1-ol partitioned in favour of the oil phase. The clusters of butan-1-ol formed in the oil and low value of $D_{ButOH\ in\ micelle}$ contributed to the reduction of its apparent diffusion coefficient. The apparent diffusion coefficient of butan-1-ol did not vary across the microemulsion phases studied, which was an unexpected result. The third diffusion domain was that of the continuous phase at 12.4×10^{-10} m^2.s^{-1} mainly constituted of brine. Water was slightly slower than free water as it evolved in an environment containing swollen micelles.

Middle phases of the L3 systems prepared at $\gamma = 0.17$ and 0.27 SDS was two times faster in the middle phases of the L3 systems than in the microemulsion phase of the L1 system. This apparent enhanced mobility can be explained if SDS molecules diffused along a more opened/flatter interface than swollen micelles. In the middle phases of the L3 systems, dodecane was not part of the slowest SDS diffusion band and could thus be considered as a continuous phase. The measured apparent diffusion coefficients of dodecane in the middle phases were smaller than the one of free dodecane in dodecane, measured to be 7.9×10^{-10} $m^2.s^{-1}$, because it evolved in an environment containing water domains. The third and fastest diffusion band was defined by water. The water mobility was reduced further when γ was increased from 0.17 to 0.27 because proportion of oil domains increased (see Figure 3.13). The two middle phases can still be considered water-continuous phases because water was not part of the slowest SDS diffusion band.

Discussion

The L3 microemulsion phases studied were seen as bicontinuous phases. There was a clear difference in the diffusion of dodecane between the L1 and L3 microemulsion phases. Dodecane was contained in swollen micelles in the L1 microemulsion phase and free to diffuse in the L3 microemulsion phases. In the L3 microemulsion phases, water mobility was reduced as it may encounter obstacles in its diffusion path. SDS in the L1 microemulsion phase diffused at 0.4×10^{-10} $m^2.s^{-1}$, corresponding to a micelle radius of 5.4 nm characteristic of swollen micelles. Sodium docecyl sulfate micelles in presence of butan-1-ol were measured to have a radius of 1.6 nm, in absence of salt [Varela et al., 1995]. SDS diffused twice as fast in the L3 microemulsion phases but was however never as fast as observed for SDS alone in 6% w/v NaCl brine, when SDS molecules were likely to form rod-like micelles. It is not obvious why SDS micelles would diffuse faster in rod-like micelles. Butan-1-ol apparent diffusion coefficient was slower than that of free butan-1-ol in brine. Guering et al. made the same observation for their SDS-butan-1-ol-toluene-brine system [Guering and Lindman, 1985]. In addition, the apparent diffusion coefficient

of butan-1-ol did not vary across the microemulsion phase studied.

Finally, middle phases were clear solution indicating that the length scale of order in the phases was much smaller than light. Diffraction techniques could shade some light on the organisation of the microemulsion phases, but this was beyond the scope of this study.

3.5.3. Bulk and interfacial compositions

Varying salinity

Salinity scans based on mixtures of 3 mL of dodecane and 3 mL of brine solution, were prepared at $\gamma = 0.17$ with a butan-1-ol-to-SDS mass ratio of 2:1, 3:1 and 8:1. On the right hand side of Figure 3.14, the optimal salinity is the abscissa at which the solubilisation factor of oil in the microemulsion phase S_{om} (in red squares) equals the solubilisation factor of the aqueous phase in the microemulsion phase $S_w m$ (in blue circles). The optimal salinity decreased from 7.5 to 3.5% w/v NaCl as more butan-1-ol was added to the mixture, inferring that the alcohol had a lipophilic contribution to the phase diagram [Bourrel and Chambu, 1983]. A second set of salinity scans was made at a lower surfactant-cosurfactant mass fraction, $\gamma = 0.06$. For formulations made at $\gamma = 0.17$, one salinity scan consisted of five microemulsions, with brine at 1, 3, 6, 8 and 10% w/v NaCl. Salinities at which transitions between L1 and L3 phase behaviour were observed are reported in Table 3.10. Both optimal salinities and solubilisation factor at the optimal salinity were correlated to butan-1-ol content in the formulations, see Figure 3.15. Optimum salinities and solubilisation factors of the formulations made at $\gamma = 0.06$ could not be calculated and included in Figure 3.15 because for each salinity scan at $\gamma = 0.06$ there was at most one solubility factor of aqueous phase in the microemulsion phase for the brine-salinity range investigated.

Interfacial compositions of the microemulsions prepared for the salinity scans at $\gamma = 0.17$ presented in Figure 3.14 were calculated from RI values of the oil phases and are shown in Figure 3.16. Butan-1-ol concentrations ranged from 3.8 to 15.1 wt% of the total weight of the formulation. First, interfacial composition alone

1:1 v:v dodecane:brine microemulsions, 2:1 w:w Butan-1-ol:SDS

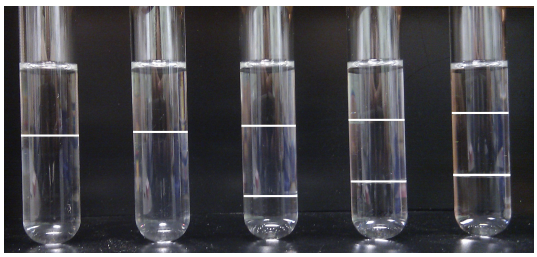

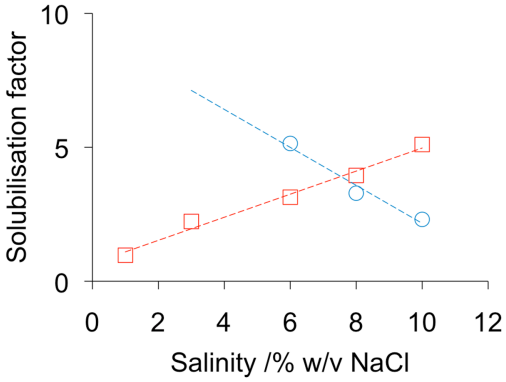

1:1 v:v dodecane:brine microemulsions, 3:1 w:w Butan-1-ol:SDS

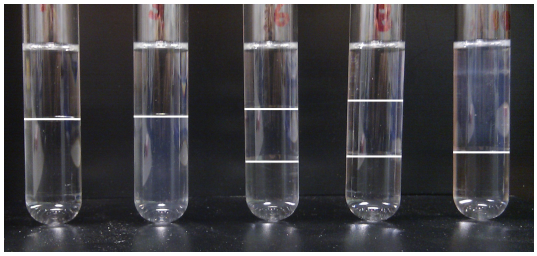

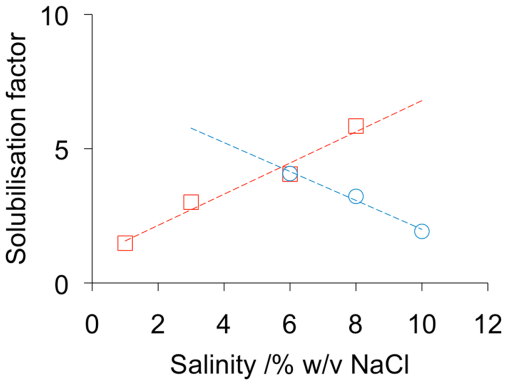

1:1 v:v dodecane:brine microemulsions, 8:1 w:w Butan-1-ol:SDS

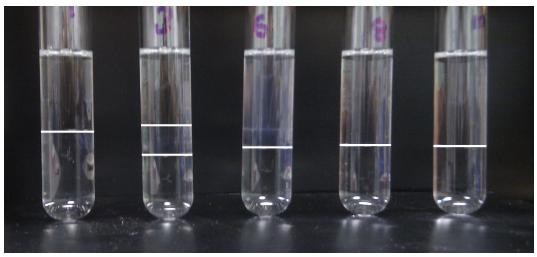

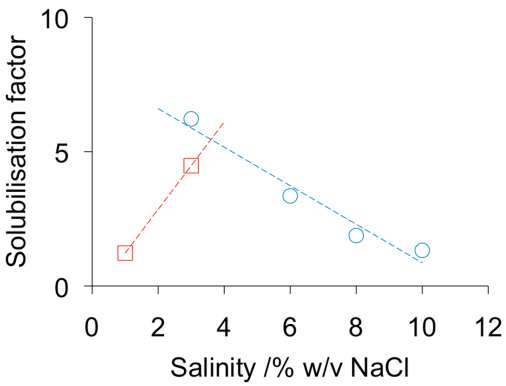

Figure 3.14: Salinity scans and corresponding solubilisation factors of 1:1 v:v dodecane:brine microemulsions prepared at $\gamma = 0.17$. Phase boundaries in salinity scans are highlighted with white lines. Brine salinity in test tubes from left to right was 1, 3, 6, 8 and 10 % w/v NaCl. Solubilisation factor of oil in the microemulsion phase S_{om} in red squares, solubilisation factor of the aqueous phase in the microemulsion phase S_{wm} in blue circles.

Table 3.10: Salinity at which L1-to-L3 phase transition occurred

γ	wt_{ButOH}/wt_{tot}	% w/v NaCl for transition between L1 to L3 systems
		ButOH:SDS 2:1 w:w
0.06	0.039	$> 10\%$
0.17	0.108	between 3 and 6%
		ButOH:SDS 3:1 w:w
0.06	0.045	between 8 and 10%
0.17	0.124	between 3 and 6%
		ButOH:SDS 8:1 w:w
0.06	0.053	between 6 and 8%
0.17	0.148	between 1 and 3%

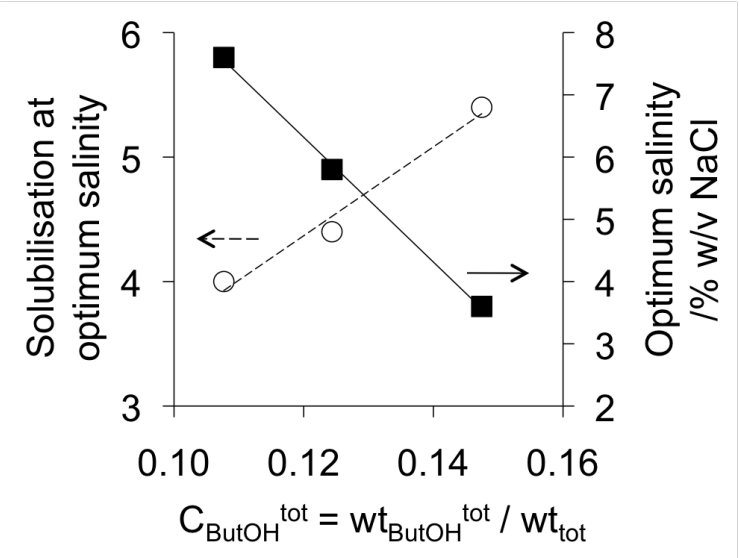

Figure 3.15: Optimal parameters (optimal salinity - empty symbols, solubilisation factors at optimal salinity - filled symbols) as a function of total butan-1-ol content in the formulation. Lines are guides for the eye.

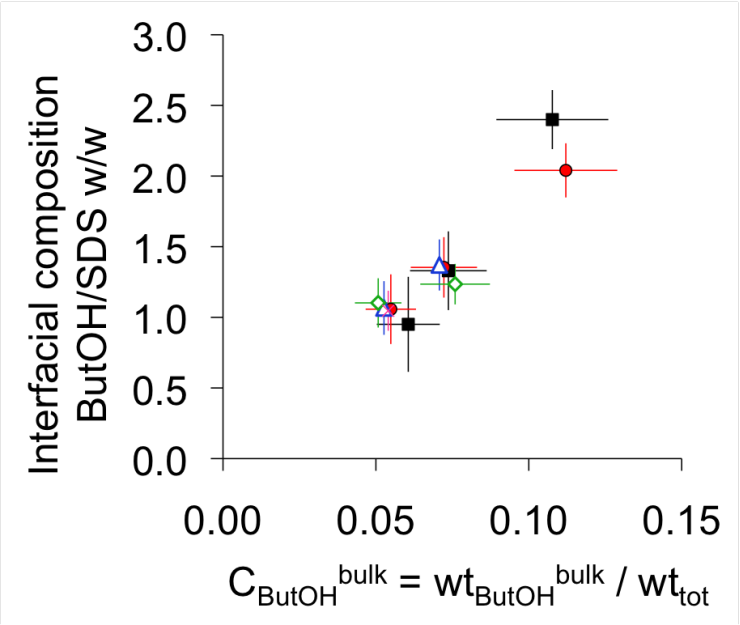

Figure 3.16: Calculated interfacial compositions from oil-phase RI values of microemulsions prepared at γ = 0.17, at 1 (black), 3 (red), 6 (blue), 8 (green) and 10% (magenta) w/v NaCl. L1 systems (filled symbols) and L3 systems (empty symbols). Bulk butan-1-ol concentrations were calculated by subtracting the butan-1-ol at the interface from the butan-1-ol in the formulation.

did not dictate the phase behaviour: certain L1 and L3 microemulsions (in filled and empty symbols respectively in Figure 3.16) had the same interfacial compositions. Secondly, the more butan-1-ol in bulk, the more butan-1-ol at the interface in the microemulsion phase. For the salinity and butan-1-ol-to-SDS range investigated, the butan-1-ol at the interface represented a third of the butan-1-ol in bulk. Finally, at a given butan-1-ol content, the interfacial composition did not correlate to the ionic strength in brine.

Fixed salinity

Microemulsions were prepared from 3 mL dodecane and 3 mL 6% w/v NaCl brine solution, with 2:1, 4:1 and 5:1 w:w butan-1-ol to SDS added at mass fractions γ between 0.06 and 0.22. Butan-1-ol concentrations ranged from 3.9 to 16.0 wt% of the total weight of the formulation. Figure 3.17 illustrates that the more butan-1-ol in the formulation the more soluble the oil phase in the microemulsion phase. In addition, microemulsions with a partition coefficient of bulk butan-1-ol below

2.1 ± 0.2 had a L1 behaviour and those with a partition coefficient above 2.1 ± 0.2 had a L3 behaviour, see Figure 3.18.

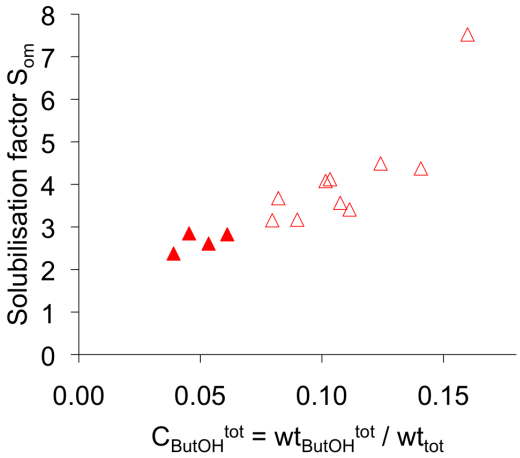

Figure 3.17: Oil-solubility factors of microemulsions as a function of the total butan-1-ol concentration. Microemulsions were prepared from 1:1 v:v mixtures of dodecane to 6% w/v NaCl brine, and mixtures of butan-1-ol to SDS added in different mass ratios and at mass fractions γ between 0.06 and 0.22. Filled symbols for L1 systems and empty symbols for L3 systems.

The interfacial compositions of microemulsion phases were calculated from RI values of oil phases and are presented in Figure 3.19 (a). There is no data for formulations prepared at $\gamma = 0.06$ because RI values of oil phases were not measured. Interfacial composition was correlated to the amount of butan-1-ol in the system, and followed the same trend as the one observed in Figure 3.16, see superposed data in Figure 3.19 (b). Figure 3.20 shows a linear enrichment of the interface in butan-1-ol with the butan-1-ol concentration in oil. As more butan-1-ol was added into the system, the aqueous phase concentration in butan-1-ol asymptotically increased towards the butan-1-ol saturation concentration in brine. The transition between L1 and L3 phase behaviours occurred for a butan-1-ol concentration in the aqueous phase between 2.8 and 3.3 wt% in brine and for a butan-1-ol concentration in the oil phase between 4.9 and 7.5 wt% in oil. The butan-1-ol-to-SDS ratio used in the formulations always exceeded the ratio at the interface.

A partial phase diagram was obtained for equivolume solutions of dodecane to 6% w/v NaCl brine mixed with SDS and butan-1-ol in different proportions. The

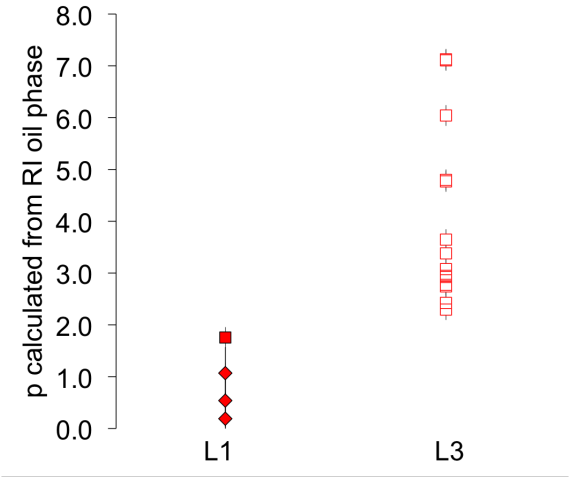

Figure 3.18: Partition coefficient of butan-1-ol measured from RI measurements of oil phase (squares) and estimated for three data points (diamonds) leading to a larger error ± 0.5. Microemulsions were prepared from 1:1 v:v mixtures of dodecane to 6% w/v NaCl brine, and mixtures of butan-1-ol to SDS added in different mass ratios and at mass fractions γ between 0.06 and 0.22. Filled symbols for L1 systems and empty symbols for L3 systems.

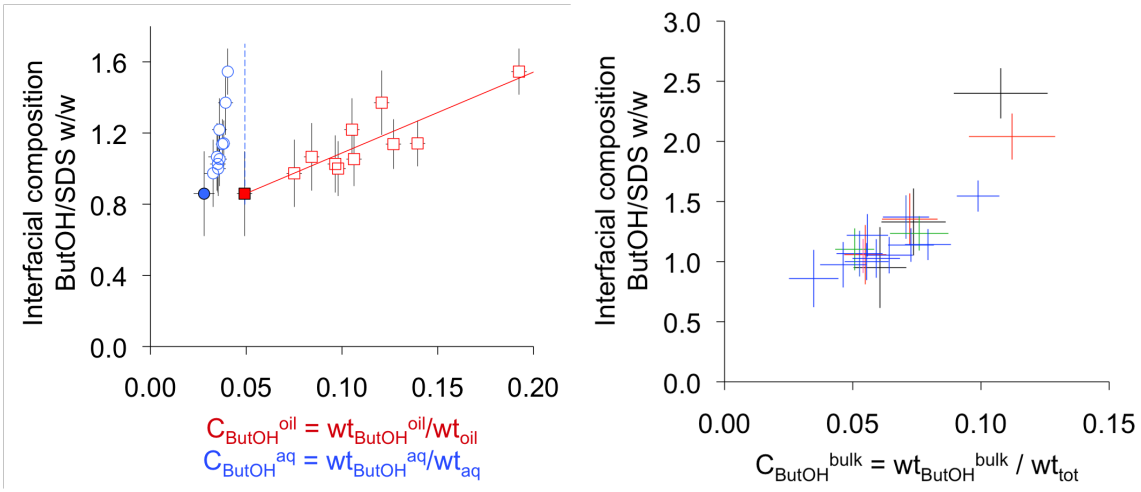

(a) (b)

Figure 3.19: (a) Calculated interfacial compositions from oil-phase RI values of microemulsions prepared at 6% w/v NaCl. L1 systems (filled symbols) and L3 systems (empty symbols). The line is a guide for the eye. (b) Calculated interfacial compositions from oil-phase RI values of all microemulsions (Data of Figures 3.16 and 3.19 (a)). For clarity only error bars are shown. 1 (black), 3 (red), 6 (blue), 8 (green) and 10% (magenta) w/v NaCl.

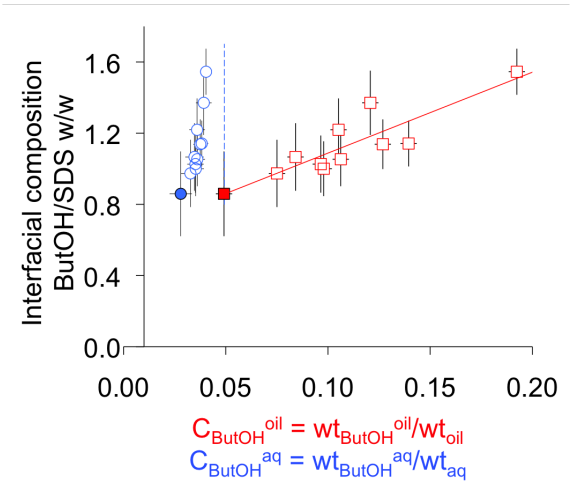

Figure 3.20: Calculated interfacial compositions versus calculated bulk concentrations of butan-1-ol in the oil phase (squares) and in the brine (circles) of microemulsions prepared at 6% w/v NaCl, calculation from oil-phase RI values. L1 systems (filled symbols) and L3 systems (empty symbols). The plain line is a guide to the eye. The dashed line is the butan-1-ol saturation concentration in 6% w/v NaCl brine.

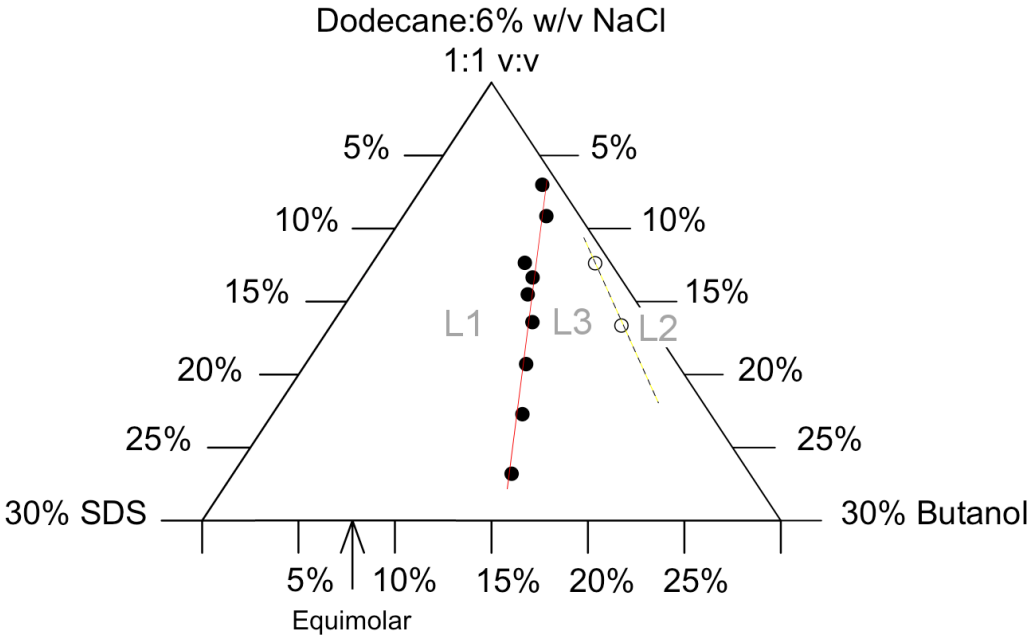

Figure 3.21: Oil- and aqueous-phase-rich corner of the pseudo-ternary phase diagram of dodecane, 6% w/v NaCl, butan-1-ol and SDS. Compositions are on a weight-fraction basis.

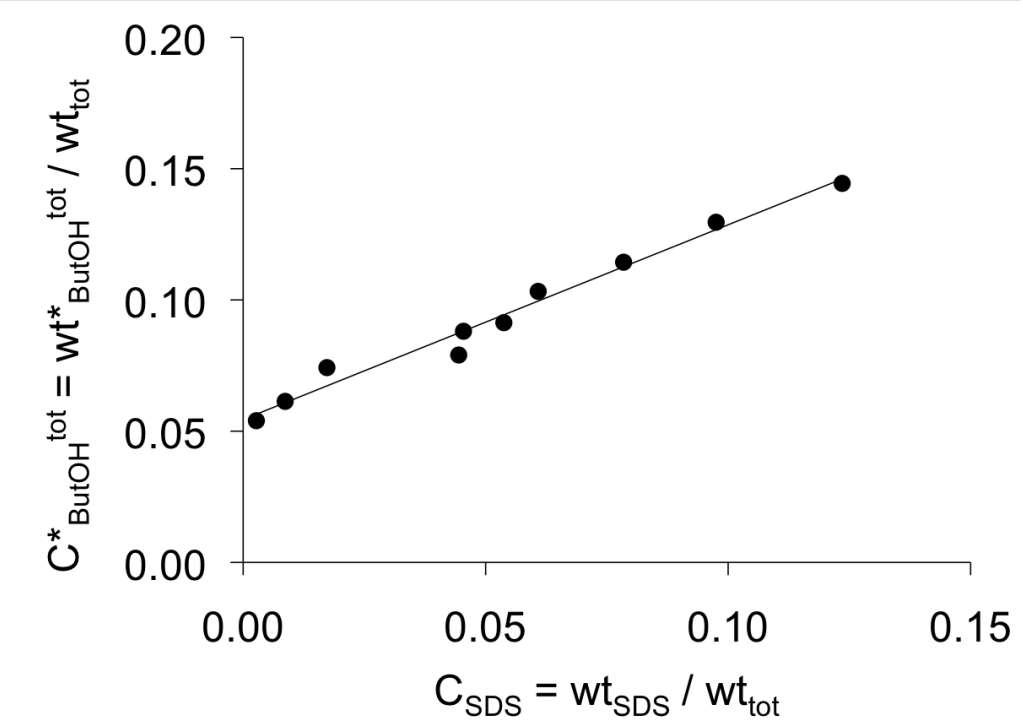

Figure 3.22: Butan-1-ol concentrations C^{*tot}_{ButOH} in microemulsions along the L1-to-L3 phase boundary of Figure 3.21, as a function of SDS. Formulations below the line were L1 systems. Formulations above the line were L3 systems.

dodecane-brine rich corner of the pseudo-phase-ternary phase diagram is represented in Figure 3.21. Figure 3.22 exploits the compositions of the data points along the L1-to-L3 phase boundary of the pseudo-ternary phase diagram shown in Figure 3.21. The phase boundary was obtained by titrating microemulsions, prepared from 1:1 v:v mixtures of dodecane to 6% w/v NaCl of different SDS content, with aliquots of butan-1-ol. The data points defining this phase boundary represented the compositions of the three-phase microemulsions obtained after addition of the least amounts of butan-1-ol required to obtain L3s. First, Figure 3.22 shows a linear increase of the minimal mass of butan-1-ol to obtain an L3 behaviour with the mass of SDS. The slope corresponds to a 0.74 ± 0.02 w:w ratio of butan-1-ol to SDS. The calculated interfacial composition at the transition between L1 and L3 phase behaviour presented in Figure 3.19 (a) was between 0.8 ± 0.2 and 1.0 ± 0.2 w:w ButOH:SDS. Secondly, one observes that the linear regression of Figure 3.22 does not pass through the origin, C^{*tot}_{ButOH} for SDS = 0 was 0.054 ± 0.002. At the minimum SDS concentration to form a L3 system, i.e. at the cmc, most of the butan-1-ol is in the bulk and $C^{*tot}_{ButOH\ \mathrm{bulk}}$ = 0.054 ± 0.002. This bulk butan-1-ol concentration corresponds to a partition coefficient of 2.3 ± 0.2. From the microemulsion formulations at 6% w/v NaCl, the partition coefficient for the L1-to-L3 transition was estimated to be 2.1 ± 0.2.

3.6. Discussion and Conclusion

Water-continuous and bicontinuous structures of microemulsions were assessed by diffusion ^{1}H NMR. The phase behaviour showed that butan-1-ol had a lipophilic effect on the system consisting of dodecane, brine and SDS. The addition of butan-1-ol lowered the optimal salinity of the system. The optimal salinity was 6 % w/v NaCl when butan-1-ol represented 12.3 wt% of the formulation. The addition of butan-1-ol at constant salinity triggered a L1-to-L3 transition. The phase transition occurred for a partition coefficient of butan-1-ol of 2.3 ± 0.2 for 6% w/v NaCl formulations. When the minimum amount of butan-1-ol was added

to form a L3 system, the interface of the microemulsion phase was composed of a 0.8 ± 0.2 w:w ratio of butan-1-ol to SDS. As butan-1-ol was added in excess of this minimal quantity, butan-1-ol continued to partition between the aqueous phase, the interface and the oil phase. At the interface, butan-1-ol strongly coadsorbed with SDS and the butan-1-ol coverage increased with butan-1-ol in bulk. Zhou et al. reported this strong competition on L1 systems prepared with dodecane, butan-1-ol, SDS and 2.5 % w/v NaCl, [Zhou and Dupeyrat, 1990]. At 1 M butan-1-ol in brine, equivalent to 6.8 wt% in brine, they measured Γ_{ButOH} / Γ_{SDS} = 4.9, equivalent to 1.3 in mass ratio. Their measured interfacial composition was compared to the interfacial composition calculated from bulk butan-1-ol concentration, based on the method and measurements presented in this chapter. The measurement of Zhou and Dupeyrat was undertaken at the cmc of SDS. Butan-1-ol at the interface with SDS was neglected compared to the total amount of butan-1-ol and the interfacial tension was calculated for a bulk concentration of butan-1-ol of 6.8 wt%. From Figure 3.16 one obtains a calculated interfacial composition of 1.3 ± 0.2 w:w ButOH:SDS which agrees with the measurement of Zhou and Dupeyrat, [Zhou and Dupeyrat, 1990]. The measurement of interfacial compositions in L1 and L3 microemulsion phases based on refractive index of oil phase and the pseudo-phase model is a method which generated results in agreement with measurements of surface coverages but with the advantage of the need for fewer and quicker measurements.

Solubilisation of oil in the microemulsion phase increased with the butan-1-ol content in the formulation. Both interface and bulk phases became richer in butan-1-ol at increasing overall butan-1-ol content, and the enhanced solubilisation of oil could be due to the composition change of either or both interface and bulk phases. At increasing alcohol concentrations, the polarity of the oil phase is altered because the solubilised butan-1-ol plays the role of a polar specie in the apolar oil [Salager et al., 2013]. Polar fractions of oils fractionate preferentially near the interface. Buijse et al. showed in their dissipative particle dynamics (DPD) simulation that the polar fraction of the oil (propane in a 60:40 w:w oil mixture of octadecane to propane) segregated preferentially near the

interface: the propane/octadecane ratio was significantly higher at the interface, [Buijse et al., 2012]. The surfactant was a C_{15}-internal olefin. This preferential interfacial segregation was observed experimentally for a higher molecular-weight polar oil: ethyl oleate in hexadecane [Graciaa et al., 1993b]; the surfactant was a octylphenyl ethoxylate. One can thus speculate that the preferential segregation of butan-1-ol near the interface promotes a smoother polarity transition between hydrophilic brine and lipophilic oil and thickens the interfacial layer. This blurring of the brine-oil interface is efficient in increasing the solubilisation capacity of microemulsions [Graciaa et al., 1993a].

Self-association of alcohol in the oil is important to promote ULIFT. This conclusion, in agreement with the work of Zhou and Dupeyrat [Zhou and Dupeyrat, 1990] and Biais et al. [Biais et al., 1981], emphasises the need to *not* consider surfactant and alcohol mixtures as a pseudo-component. This chapter showed that a minimum amount of butan-1-ol at the interface was needed to promote the L1-to-L3 transition together with a minimum partition coefficient. If the butanol-to-SDS ratio used in the pseudo-phase diagram is equal to or smaller than the interface ratio (which was never the case in this chapter) there may never be enough butan-1-ol available for the bulk phase to trigger a L1-to-L3 transition.

Chapter 4

Fracture scale

4.1. Introduction

Water flood typically recovers only 30-40% of initial oil reservoir capacity. In the areas of the reservoir swept by water flood, residual trapped oil is likely to be disconnected and form individual blobs or ganglia. In surfactant EOR, a flood of surfactant and cosurfactant solution is then injected into the reservoir to lower the interfacial tension. If the interfacial tension is low enough, viscous forces overcome capillary forces to push the blobs of oil through pore throats and displace the residual oil towards the production well. Additionally, if ultra-low interfacial tension is reached, the surfactant flood solubilises the blobs of oil and the residual oil may be displaced as a microemulsion.

The pore structure of a rock results from the original deposition and compaction of sediments which is later altered by geological phenomena including diagenesis, redeposition, and stresses. A rock reservoir is therefore a heterogeneous material which exhibits varying forms of porosity: connected porosity, unconnected voids, and fractures. Connected and unconnected porosities are on the grain/micrometric scale. Fractures, common in carbonate reservoirs, exist at different scales, from millimetric fissures to kilometer-size structures.

In this study, the early stage of diffusive surfactant transport in a millimetric fracture was explored to investigate alternative scenarios which may occur prior

to the displacement of oil ganglia by viscous forces (i.e. no external flow) or solubilisation (i.e. away from the relevant part of the phase diagram). A fresh drop of oil was put in contact with a brine solution of surfactant and cosurfactant, in a confined space with no external flow. The surface of the container was hydrophilic and the oil drop did not wet its surface. In the aqueous phase, the anionic surfactant concentration was above the critical micellar concentration while the amount of cosurfactant in the system was limited to its saturation concentration. In addition, the cosurfactant was soluble in oil. To the best of our knowledge, no studies has been reported on this type of geometry and surfactant system. The limited and finite amount of cosurfactant available prevented build-up of cosurfactant in the oil phase to the concentration necessary for the formation of an ultra-low-interfacial-tension (ULIFT) system. The buoyant oil drop did not wet the surface of the channel and was separated from it by a film of aqueous phase, which is referred to as *the wetting film*. An interfacial gradient along the oil-brine interface (less than 1% of the initial IFT) led to aqueous-phase transport along the wetting film above the oil drop leading to build-up of an aqueous droplet inside the oil drop, which eventually fell through, giving the appearance of a dripping aqueous drop through the oil drop. For this reason, the aqueous phase accumulating *within* the oil drop is referred to as *a drip* in the rest of this chapter. This process of accumulation and expulsion cycled tens of times before reaching equilibrium. The maximum volume of a drip is named the burst volume.

The reminder of this chapter is structured as follows. After materials and methods are described, a qualitative account of the observations made on one oil drop introduces the descriptive terms used in this chapter. Flow of the aqueous phase in the bulk and the wetting film is quantitatively analysed using particle tracking. The effect of oil drop volume is investigated as well as the effect of the initial butan-1-ol concentration in the aqueous phase and the alkane chain-length of the oil phase.

4.2. Materials and Methods

4.2.1. Preparation of solutions

Brine solutions of surfactant and cosurfactant were prepared by weight as follows. A brine solution of surfactant (50 mL) was prepared from a stock solution of 6 % w/v NaCl and recrystallised sodium dodecyl sulfate (SDS) (72 mg). The brine solution of surfactant was warmed up above the Krafft temperature. 6 mL were poured into a vial and let to cool before butan-1-ol was added (between 5 and 200 mg). The solutions were sonicated for five minutes and let to rest for at least one hour.

1300 µL of the 6% w/v NaCl brine solution of 5 mM SDS and butan-1-ol were poured in a quartz cell with a 5-mm wide window and a 10-mm pathlength, purchased from Hellma Analytics. The cell was cleaned beforehand using a piranha solution (3:1 v:v mixture of H_2SO_4 to H_2O_2). Oil (filtered through silica gel and alumina) was added atop of the aqueous phase (about 200 µL) to fill the quartz cell. The cell was sealed with a PTFE cap which had a run-through hole, working as a leak valve. The shape of the cell cavity, forming a V close to the cap (see Figure 4.1), was used to keep the channel free of oil when the quartz cell was placed horizontally in front of the camera. The oil drop was generated by manually tilting the cell to release an aliquot of oil into the channel. The experiments were run at room temperature (20.5 ± 1.0 ^{o}C). To track flow in the bulk of the aqueous phase, brine solutions of surfactant and cosurfactant were prepared with 0.03 wt% polystyrene beads, of diameter 3.11 ± 0.21 µm (Bangs Laboratories, Inc.). These beads were charge-stabilised; their stability in brine were thus limited and they eventually aggregated before sedimenting. However, measurements were recorded on fresh solutions and image analysis showed that the aggregation or sedimentation of the particles did not occur on the time scale of the measurements. To track flow within the wetting film, brine solutions of surfactant and cosurfactant were prepared with 0.007 wt% of sterically stablised polystyrene (PS) beads, of diameter 977 nm and PdI = 0.77. These PEGMA-PS (poly(ethylene glycol) methacrylate-PS) beads were made at Leeds University.

Figure 4.1: Schematic representation of the quartz cuvette with an oil drop in the aqueous phase. Not to scale.

4.2.2. Images collection

Side-view images

The quartz cell was placed onto a tilt stage (Thorlabs) which was coupled to a manual XYZ moving stage (Edmund Optics). The images, obtained through the optical set-up of the FTA-200 First Ten Ångstrom tensiometer and collected with high resolution WAT-902B camera (Watec), contained 480 × 640 pixels on a grey scale. Images were captured with a frequency of 0.5 to 60 frames per second, depending if the images were used for particle tracking or not. In absence of particles in the aqueous phase, the camera was set up to capture the entire volume of the oil drop and the typical spatial resolution was 10 µm.pixel^{-1}.

Alternatively images were recorded for particle tracking using the Highspeed CamRecord CR450x3 Optronics camera on a second optical set-up. The source of illumination was a collimated LED (λ = 407 nm, Thorlabs). The camera was aligned with a LaVision telescopic lens. Images obtained with the Optronics camera contained 600 × 800 pixels on a grey scale and were collected at a frequency of 15 to 125 frames per second. The typical resolution of images capture for particle tracking was 2 µm.pixel^{-1}.

Top-view images

A custom-made glass container of 1 × 1 × 4 cm^3 was used for top-view imaging. A 2.5 × 2.5 cm^2 cover slip was slid onto the open face of the container which was filled with the aqueous phase containing 0.007% of 977 nm PS particles. A 18-gauge U-shaped needle mounted onto a 500-µL gas-tight syringe was immersed in the aqueous phase from the top of the container, through the liquid surface not covered

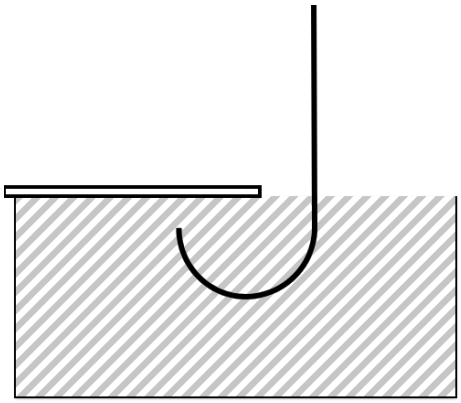

Figure 4.2: Schematic representation of the set-up used for top-view images. The hatched area represents water. Not to scale.

by the cover slip (see schematic set-up in Figure 4.2). The needle tip was raised close to the cover slip for it to support the drop as the oil was drawn out of the needle, and prevent an early break-off of the oil drop at the needle tip. The container was placed on a tilt stage (Thorlabs). The position of the container was controlled with a motorised XYZ stage (Zaber Technologies T-LS13). The travelling range of the motorised Zaber stage was 13 mm, with a microstep size of 0.1 µm. The repeatability of the stage positions was better than 2 µm. The container was illuminated by a collimated LED light (450 nm, Thorlabs). The transmitted light was collected by a ×50 Nikon objective (NA 0.6). Images were recorded with the Highspeed Cam-Record CR450x3 Optronics camera at 250 frames per second. The grey-scale images contained 400 × 330 pixels, with a typical resolution of 0.25 µm.pixel^{-1}. The depth resolution is given by

$$\lambda/\mathrm{NA}^2, \tag{4.1}$$

where λ is the wavelength of illumination and NA the numerical aperture of the objective. The ×50 Nikon objective thus offered a depth resolution of 1.3 µm.

This objective was used to measure the thickness of the wetting film by vertically scanning through it. In addition, the velocity profile in the wetting film was determined by measuring particle velocities at different depths within the wetting film of one oil drop immersed into a brine solution of surfactant and cosurfactant. Recordings lasted 15 seconds. Particles were tracked far from the center of the oil

drop to minimise the deformation of the wetting film during the recordings. The zero position, i.e. at the cover slip, was recorded before each tracking measurement within the wetting film to determine the depth of measurement.

4.2.3. Images analysis without particle tracking

The collected images were analysed with Matlab. The edge of an oil drop was detected using a threshold on the grey scale. For each frame, the number of pixels inside the drop edge was counted to analyse volume variation with time. The volume was calculated by counting the number of pixels inside the edge assuming a radial symmetry around the central vertical axis. Considering that the position of the edge of a drop was detected within one pixel of accuracy, the error on the volume measured by image analysis was 1%. The volume of cosurfactant solubilised into the oil was negligible compared to the oil drop volume. For the largest butan-1-ol concentration used in this study, butan-1-ol in oil at equilibrium represented 3 % of the oil drop volume, i.e. of the order of the error on the drop-volume measurement. The oil-drop volume was thus considered constant with time. The edge of the oil drop detected during image analysis was used to calculate a total volume which was effectively the oil-drop volume plus the volume of the growing drip. Drip volumes were thus calculated by subtracting the oil-drop volume from the total volume. The rates of volume variation of deformed oil drops defined the growth rates at which drips developed, expressed in $\mu L.min^{-1}$. They were determined by linear regression (see Figure 4.3).

The rupture of the oil film sustaining a drip inside an oil drop was an easily identifiable event: the volume variation changed abruptly at regular intervals when the oil film sustaining the drip ruptured (see Figure 4.3). The times at which this event occurred were either automatically retrieved from the fluctuations of the derivative of the drop volume as a function of time or they were manually determined. Figure 4.4 shows, for two different oil drops, the times at which the oil film ruptured as a function of the number of occurrences of oil-film rupture, named *bursting number*. The *dripping periodicity* was defined as the slope of the

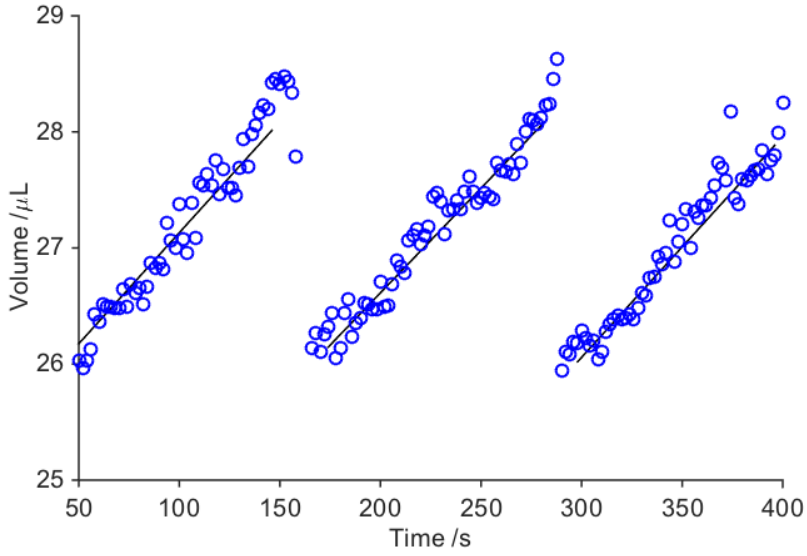

Figure 4.3: Example of linear regression, black lines, of the volume variation (blue circles) to calculate the growth rate of drips in an oil drop.

times of the first nine oil-film ruptures as function of their bursting numbers. The consideration of three additional occurrences of oil-film rupture to calculate the dripping periodicity did not modify the result by more than 3%. An oil drop was thus described with its *dripping periodicity* in seconds, which expressed how often a drip was expelled from the oil drop.

4.2.4. Particle tracking

Images were analysed with Matlab. The core of the tracking code was taken from The Matlab Particle Tracking Code Repository of Daniel Blair and Eric Dufresne from the department of Physics of Georgetown University, USA. The particle velocities were calculated from the changes of particle positions between two frames. With this code, each particle was assigned an identity number and two velocity components v_x and v_y. A particle kept its identity number as long as it reappeared within a chosen pixel range of its previous position. Only particles that were within the focal plane (xy plane) of the camera were tracked. However particles travelled in and out of the focal plane, in the z-direction; a particle was thus given a lapse of time (typically three frames) to get a chance to reappear in the focal plane and

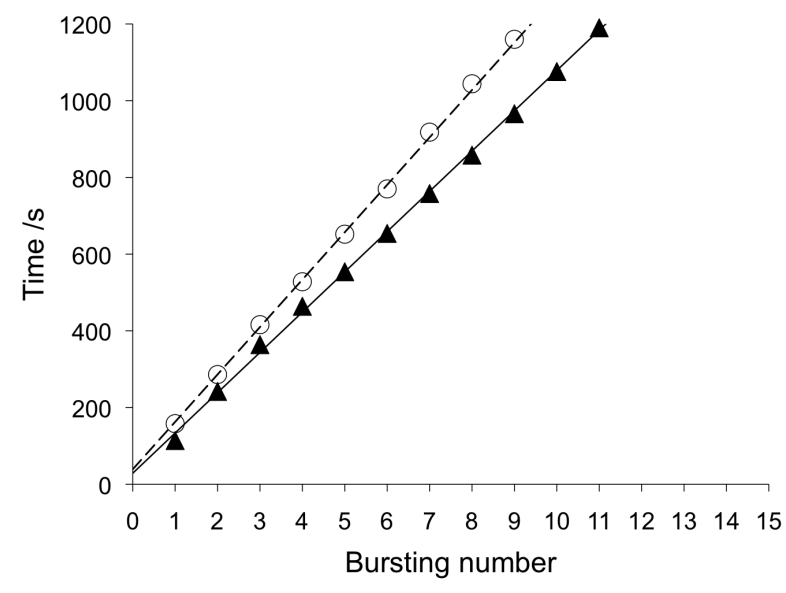

Figure 4.4: The times at which drips were released into the bulk were recorded for two different oil drops (circles and triangles). The dripping periodicities, given by the slopes, were different for the two oil drops (124 s and 105 s, respectively).

be reassigned its original identity number. The v_x and v_y components of the mean velocity vector were finally converted into local tangential and normal components v_t and v_n relative to the edge of the oil drop in the case of side-view tracking.

Particle tracking in the bulk of the aqueous phase Particle velocities were averaged in space and time. First, the bulk of the aqueous phase was divided in discrete spaces, or bins as follows. First, the edge of the oil drop was divided in sections of length dS (see Figure 4.5 (a)). At the extremities of each section, normals to the edge were determined and imaginary tubes of diameter $D = dS$ and centred on the normal to the edge were drawn. The radius of the tubes was incremented by a distance $\delta D(R) = tan\theta \times R$, where θ is the angle between two consecutive normals and R the normal distance from the edge. The tangent to each section was determined and each imaginary cone was sliced in portions of width D. A mesh of size $D \times (D + \delta D)$ was thus successfully constructed to cover the bulk of the aqueous phase. Secondly, the population of each bin was merged with the population of consecutive frames to increase the bin populations over which the

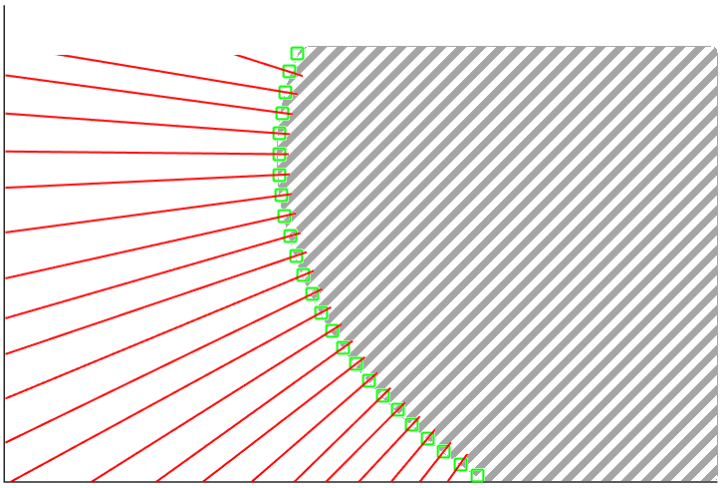

(a) First step of mesh construction: the space is discretised in tubes centred around normals to the surface (red lines).

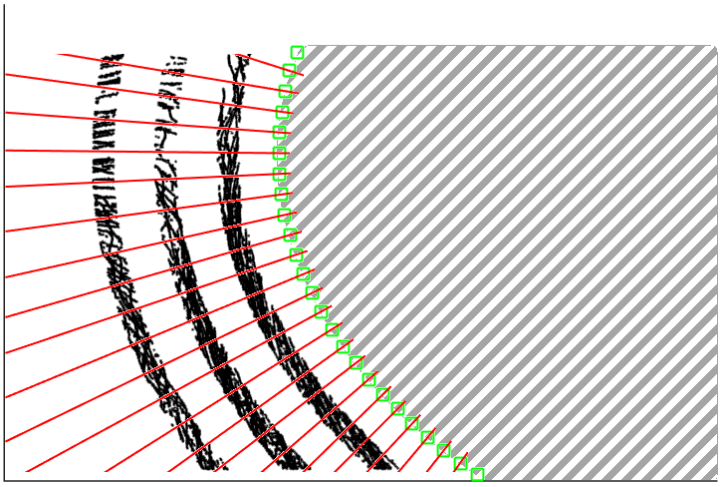

(b) Second step: the space is discretised in shells. Here the particles falling in three different shells were plotted.

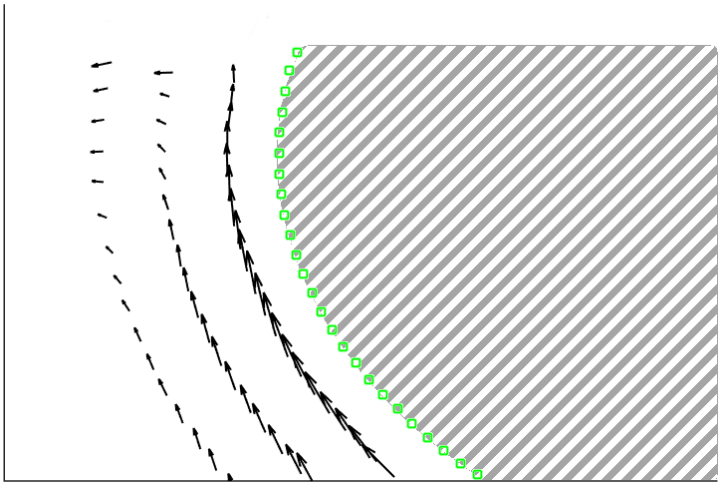

(c) Third step: velocities are averaged over the bins to create a velocity map.

Figure 4.5: Construction of a velocity map. Oil drop is hatched.

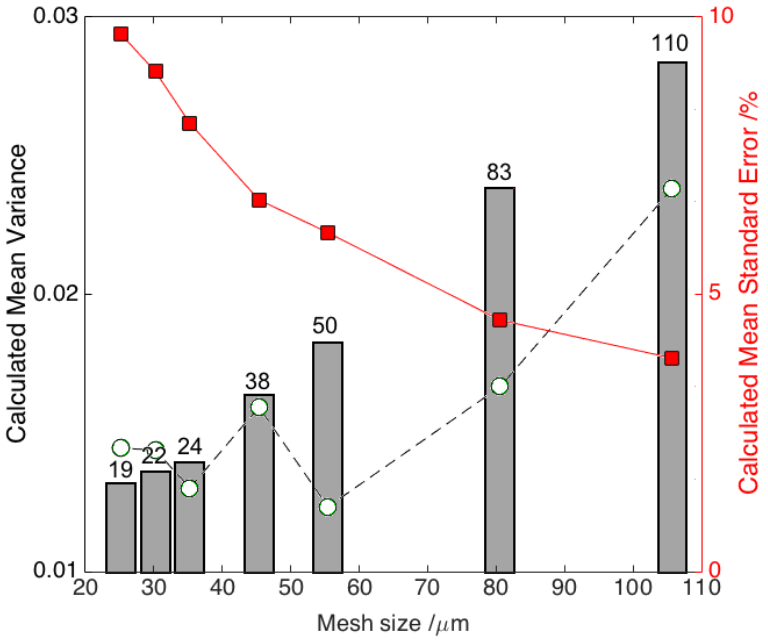

Figure 4.6: Calculated mean variance (circles, left axis) and calculated mean standard deviation (squares, right axis) in tangential velocity as a function of mesh size. The lines are a guide for the eye. Measured mean bin population represented with bars and labels.

mean velocity vectors were calculated. Averaging over a long time increased the bin populations but decreased the time resolution on the variation of the velocity vectors. Particle movements were averaged over a period of 0.8 second. Figure 4.15 in Results Section 4.3.2. shows that this choice of time span gave a good time resolution to follow variation of flow directions and intensities, and, on the other hand, it enabled enough particles to be tracked to obtain a standard error on averaged velocities below 10% (see further).

Statistical analysis was carried on the tangential velocities of a sample of tracked particles to rationalise the choice of a mesh size. The sample of particles was centred around one of the normals to the edge of the oil drop. For each mesh size D, a cone of diameter $D+\delta D$ and length 350 µm was sliced in portions of width D, thus defining a number of bins of size $D \times (D + \delta D)$. Variance, standard error and population were calculated for each bin. The average values obtained for each mesh size are reported in Figure 4.6. Variance was defined as

$$\frac{\sum_i (X_i - mean)^2}{n}, \tag{4.2}$$

and the relative standard error was defined as

$$\sqrt{\frac{\sum_i (X_i - mean)^2}{n-1}} \times \frac{mean}{\sqrt{n}} \tag{4.3}$$

where X_i is the tangential velocity of the ith particle and n is the bin population, i.e. the number of particles tracked in the bin.

The bin population increased as the mesh size became coarser, decreasing by definition the standard error. However, Figure 4.6 shows that the variability in tangential velocity, measured with the variance, doubled with the mesh size, from a mesh size of 55 µm. Therefore, the mesh size offering the smallest standard deviation with a minimised variance on tangential velocity was chosen to analyse particle tracking in the bulk, i.e 55 µm mesh size corresponding to a standard error on the tangential velocity of 6%.

Particle tracking in the wetting film Similarly, the particle velocities were averaged in space and time. With the ×50 objective, particle velocities were averaged over the entire field of view, equal to 0.008 mm^2. Within this small field of view, particles trajectories were parallel (see Figure 4.7) and particle velocities were measured along their line of travel. In addition, analysis showed that particle velocities did not vary for the duration of the recordings which lasted 15 seconds; the particles velocities were thus averaged over the entire duration of the recordings. The depth resolution of the objective was equal to 1.3 µm, i.e. of the order of magnitude of the particle diameters used for tracking (977 nm).

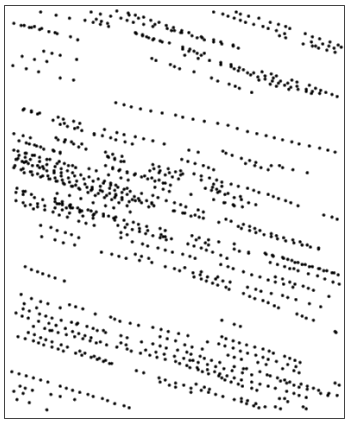

Figure 4.7: Trajectories of particles in the wetting film tracked during 15 seconds using the ×50 objective. Image measures 100 × 80 µm.

Particle tracking in the wetting film was undertaken to find out the velocity profile of the aqueous phase above the oil drop by measuring the velocity of the flow at different depths in the wetting film. It was thus important to differentiate particles that were in focus from particles that were not in order to record only velocities from a unique plane. A criterion on the sharpness of particle edge was developed to this effect. Gradients of grey, calculated radially from the identified particle centres to the aqueous phase, of idle particles settled onto the cover slip and brought to focus defined a threshold. Moving particles were considered focused if their gradient of greys were equal to this threshold, plus or minus 15%.

Images were analysed in Matlab. First, coordinates of particles centres were identified by using a threshold on the grey scale. Then, each particle was attributed

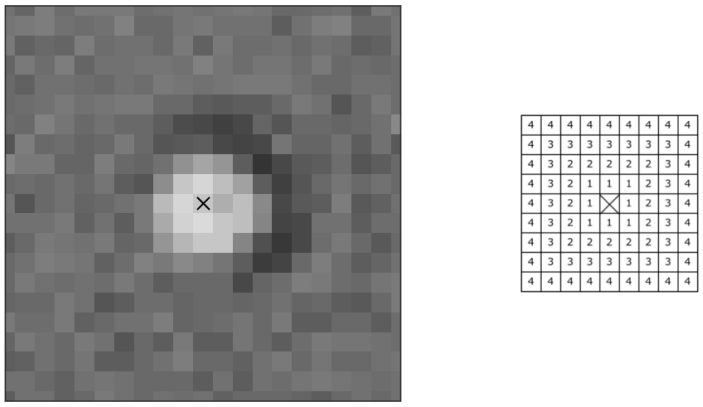

(a) (b)

Figure 4.8: The gradient of greys of a particle was defined as the variation of the average grey levels of the first three shells of pixels (b) centred around the particle centre coordinates, tagged here with a cross. (a) Typical image of a focused particle, $0.25\,\mu m.pixel^{-1}$.

a gradient of greys by calculating the average grey values for the first three shells of pixels centred around the particle centre as represented in Figure 4.8 (b). Finally, particles with gradient of greys above the threshold were tracked. Figure 4.9 (b) shows an example of a focused particle detected among out-of-focus particles using this method. The resulting population distribution of velocities measured at one depth within the wetting film was Gaussian, see Figure 4.10.

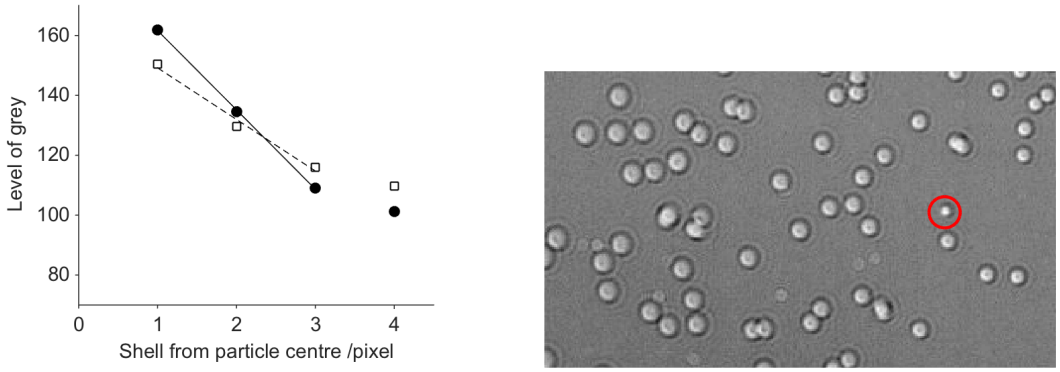

(a) (b)

Figure 4.9: The difference in the gradient of greys of particles (a) allows the distinction between out-of-focus particles (squares in (a)) and focused particles (circles in (a)). Figure (b) ($74 \times 43\,\mu m$) highlights a focused particle distinguished from out-of-focus particles using this method.

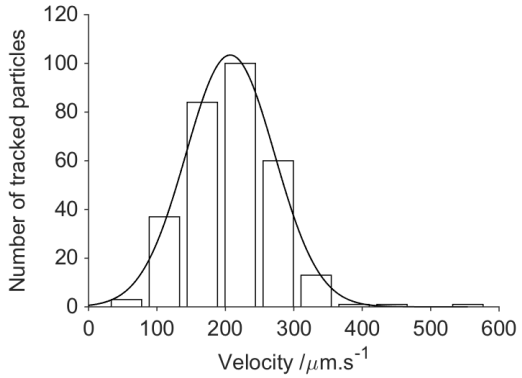

Figure 4.10: The population distribution (bar) of velocities measured during one recording in the wetting film above a dodecane drop was a Gaussian distribution (line).

4.2.5. Tangential velocity and interfacial gradient

The variation of the tangential velocity with respect to the normal distance from the edge ($\frac{\partial v_t}{\partial_n}$) is related to the interfacial tension gradient along the edge as shown in Equation (4.5) expressing the boundary condition for tangential stress.

$$\mu \frac{\partial v_t}{\partial_n} = -\nabla_t \gamma \tag{4.4}$$

where μ is the viscosity of the phase, v_t the velocity tangent to the edge, γ the interfacial tension and n the normal to the interface.

4.2.6. Interfacial tension

0.360 g recrystallised SDS were solubilised with circa 200 mL of Milli-Q water in a 250-mL volumetric flask; the solution was sonicated until surfactant solubilisation. Then, 15 g NaCl were added to the solution. The solution was sonicated in a warm water bath (45^{o}C) until the mixture was a transparent solution. When the salt and SDS were solubilised, the volumetric flask was topped up to 250 mL with water. 15 mL (15.6 g) of the lukewarm 6% w/v NaCl brine solution of 5 mM SDS were transferred in a glass vial where butan-1-ol was added to the solution. The butan-1-ol concentration varied from 0.02 wt% to 4.04 wt% (3.7 mg to 691 mg).

10 mL of the brine solutions of SDS and butan-1-ol were each mixed with 1 mL of dodecane. Samples were shaken by hand and let to rest for at least 3 hours, or until the solutions were clear, at room temperature 20.5 ± 0.5^{o}C. At 20.5 ± 0.5^{o}C, SDS salted out of the brine solutions of 5 mM SDS and butan-1-ol when the butan-1-ol concentration was below 0.55 wt%. When the brine solutions of 5 mM SDS and butan-1-ol below 0.55 wt% were mixed in 10:1 v:v ratio with dodecane, SDS salted out of the equilibrated aqueous phase and at the oil-water interface part of the liquid was forming opaque beads wrapped with a thin film. Sonication and further mixing did not improve the solubilisation. Interfacial tension measurements were carried out on the solutions prepared with more than 0.55 wt% butan-1-ol, at 21.0 ± 0.2^{o}C with the SITE100 spinning drop tensiometer from Krüss. Prior to each measurement, the capillary which had a capacity of circa 0.5 mL was washed sequentially with 3 mL of Milli-Q water, 3 mL of 0.1 M NaOH solution, 5 mL of Milli-Q water and 2 mL of the equilibrated aqueous phase. The drop of oleic phase was introduced with a needle with the capillary rotating at 500 rpm. The system was let to thermally equilibrate for at least 10 minutes before taking measurements. The capillary was rotated typically at 2600 rpm or until the oil drop became a cylindre. The diameter of the drop was typically 1 mm, and the image resolution was 460 pixels per millimiter. The reported interfacial tensions were the average of the measurements made on at least two drops, with at least three measurements per drop. The typical standard error was 3%.

4.3. Results

4.3.1. Conditions for drips to develop within an oil drop

Two prerequisites were identified for drips to develop within a non-wetting oil drop immersed in a brine solution of surfactant and cosurfactant. First, the oil drop must exceed a critical size. Very small oil drops (circa $\leq 2\,\mu L$) remained idle when submerged in a brine solution of surfactant and cosurfactant. No drip developed. For relatively small oil drops (between 3 and 7 µL), no drip was observable. However,

unlike the smallest oil drops, these oil drops did not keep a fixed position within the cuvette: oil drops within this volume range were propelled at regular interval (minutes) over a distance about equal to their diameter, at a speed of circa 7 $mm.s^{-1}$. The displacements occurred in any direction and, after their propulsions, the oil drops came slowly back to their original positions suggesting that the propulsions were not due to a tilt in the levelling of the cuvette.

Water accumulated inside larger oil drops only, from 8-9 µL. For oil drops just exceeding this critical volume above which water droplets formed inside the oil drop, the volume of the accumulated water only reached 3% of the oil volumes. The water droplets inside oil drops thus never deformed the lower interface of the oil drops, as illustrated in Figure 4.11 (a). Such accumulations of water were thus expelled along wetting films.

The accumulation of water inside oil drops was more substantial in larger oil drops, from 12 µL. Drip volumes became such that the lower interfaces of oil drops were deformed and drips were eventually retained only by a stretched film of oil (see Figure 4.11 (b)). Releases of drips into the bulk of aqueous phases thus occurred "through" the oil drops as their film ruptured, i.e. dripping occurred.

The dependence of the out-flow processes of drips was not a consequence of the height of the oil drops, which were independent of oil-drop volumes in this volume range (see Section 4.3.3. on oil-drop volume variation). On the other hand, the volume from which a drip could deform the lower interface of an oil drop depended on the interfacial tension. The values given in this section are typical for an interfacial tension of 0.9 $mN.m^{-1}$.

Secondly, drips developed in large enough oil drops only if the brine solution of surfactant contained butan-1-ol: non-wetting oil drops submerged in a solution of SDS above the critical micellar concentration (in the absence of butan-1-ol) did not develop drips. In addition, drips did not develop in non-wetting drops of oil pre-equilibrated with the brine solution of cosurfactant. It is worth stressing the fact that to attain the solubility limit of butan-1-ol in the aqueous phase, brine solutions were saturated with butan-1-ol in absence of SDS, see Appendix for notes

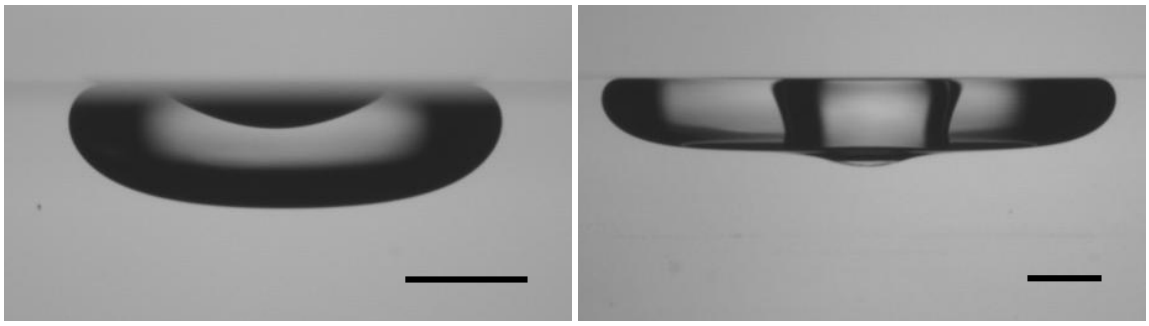

(a) 10-µL oil drop (b) 33-µL oil drop

Figure 4.11: Two dodecane drops in 6 w/v % NaCl brine solution of 5 mM SDS and 1.3 wt% butan-1-ol, just before the end of a cycle. Scale bars measure 1 mm.

on the saturation of brine solutions of SDS with butan-1-ol.

The upper limit to drop size was not investigated because of the limited width of the channel in the quartz cuvette.

The rest of the study focuses on oil drops larger than 13 µL, i.e. on oil drops within which aqueous phase accumulated to such volume that the aqueous droplets within oil drops deformed the lower interface of the oil drops and dripping occurred.

4.3.2. In-flow and out-flow processes before reaching equilibrium

It took several hours for an oil drop to reach equilibrium with the aqueous phase and for drips to cease. In-flow process, i.e. building-up of a drip of aqueous phase within an oil drop and out-flow process whereby the drip was expelled from the oil drop, marked, at regular intervals, the duration preceding equilibrium, at which point no convective flows were observed. These processes are described for oil drops larger than 13 µL in the following sections. The out-flow process is defined as the release of one drip from an oil drop, i.e. along the wetting film or through the deformed oil drop. All the drips of one oil drop were released by the same out-flow process. This statement is true with the exception of drips in large oil drops when the system was close to reaching equilibrium; in that case, the volume of the drips decreased abruptly and their out-flow process changed from through-the-oil-drop to along-the-wetting-film. Figure 4.12 shows the typical variation of drip volumes

developing in one oil drop. In the last stage to equilibrium, drips contents were not fully excluded from the oil drops and the drip volumes oscillated from and to a residual volume with an amplitude decreasing with time.

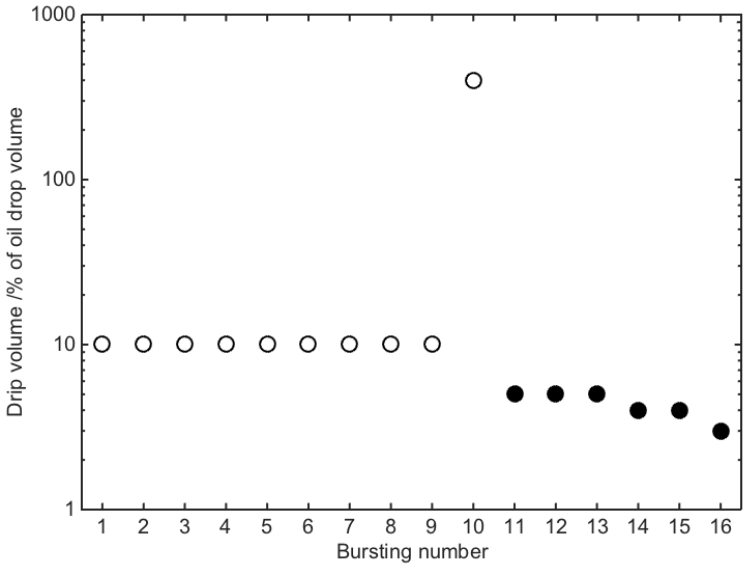

Figure 4.12: Typical drip volumes at burst inside one dodecane drop in a 6% w/v NaCl brine solution of 5 mM SDS and 2 wt% butan-1-ol. Empty symbols for through-the-drop out-flow process, filled symbols for along-the-wetting-film out-flow process.

In-flow process

Drips developed inside an oil drop because of the radial transport of aqueous phase above the oil drop along the wetting film (see Figure 4.13), and its accumulation at the centre of the oil drop. As the aqueous phase volume increased inside the oil drop, the diameter of the oil drop increased to accommodate the drip which eventually deformed its lower interface (see Figure 4.14).

Polystyrene beads were placed in the aqueous phase as flow trackers and filmed from the side. Velocity and flow direction of the aqueous phase in the bulk varied over periods shorter than the lifespan of a drip. The flow variations of the aqueous phase in the bulk did not affect the transport of aqueous phase within the wetting film which sustained a constant volume increase of drips (see Figure 4.16).

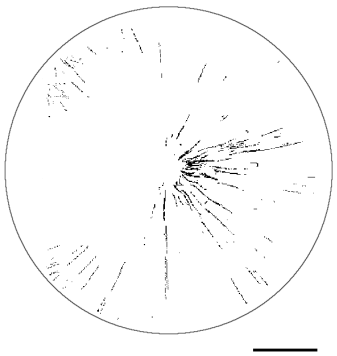

Figure 4.13: Traces of particles tracked in the wetting film of an oil drop from top view. The scale bar measures 1 mm.

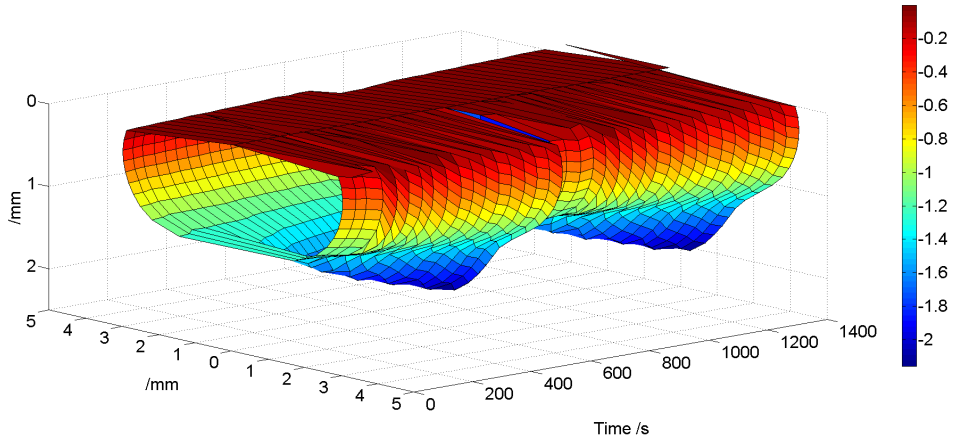

Figure 4.14: Determination of the surface of an oil drop during two consecutive cycles.

Figure 4.15: Nine successive velocity maps (1.3×0.9 mm ^{2}) in the aqueous phase (6% w/v NaCl brine solution of 5.0 mM SDS and 2.0 wt% butan-1-ol) surrounding a dodecane drop (hatched area). Each velocity map resulted from particle tracking over 0.8 second within the time frame indicated below each panel. The amplitude of the arrows relates to the velocity. Arrows were scaled to the largest velocity recorded in this data set $387 \pm 5\,\mu\text{m.s}^{-1}$. Scale bar measures 200 µm.

The velocity maps in Figure 4.15 show a typical succession of flow variations in the bulk of the aqueous phase:

1. The flow in the bulk is nearly at a halt. Near the cuvette wall, the flow is directed away from the oil drop edge;
2. The flow reverses and is directed downwards towards the apex;
3. The flow hits the interface at a normal angle and divides in two flows tangential to the oil drop edge: downwards to the apex and upwards to the oil drop top;
4. The upwards flow eventually dominates;
5. The flow subdivides again in two tangential flows of opposite directions;
6. The upwards flow develops.

The above sequence (1-6) occurred a few numbers of time within the life span of a single drip. More precise estimates of the number of repeats of the flow sequence per drip were not available because the length a tracking movie was shorter than the life span of a single drip due to the limited camera memory.

The dripping periodicity of the oil drop analysed in Figure 4.16 was about 100 seconds. Figure 4.16 shows first that the growth of one drip was constant, i.e the volume as a function of time can be fitted to a linear regression. A faster volume increase was sometimes observed during the few seconds before the oil film ruptured. Secondly, consecutive drips grew at the same rate, i.e. the linear regressions on successive drips have the same slopes. This constancy suggests that a proportion of the bulk flow near the top corner of the oil drop always entered the wetting film. At the outer and upper part of the oil drop, the aqueous flow divided into two streams:

- away from the oil drop, in the bulk.

- toward the oil drop, entering the wetting film.

A drip grew at a constant rate but was eventually released into the bulk when the interfacial tension could no longer support the weight of the heavier water phase. Aqueous phase was constantly entering the wetting film.

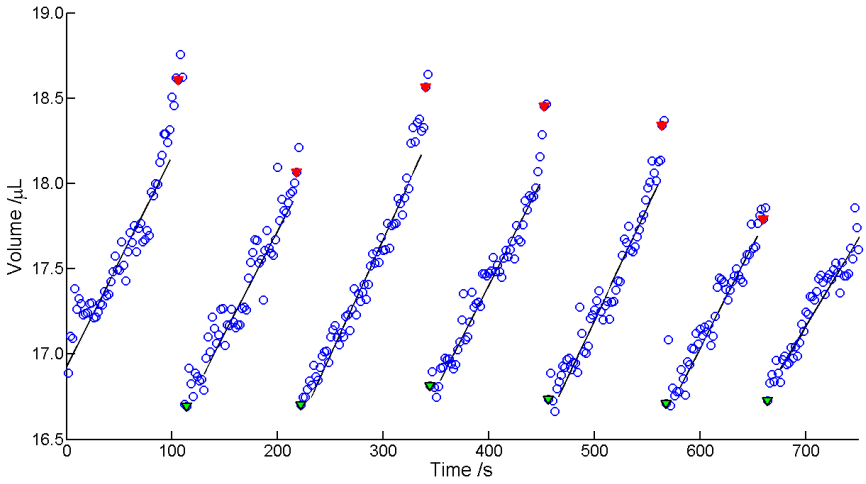

Figure 4.16: Volume variation of a deformed dodecane during seven consecutive cycles (blue circles) and linear regressions (black lines). The green and red filled symbols highlight the volumes at the beginning and end of each cycle respectively. The aqueous phase was a 6% w/v NaCl brine solution of 5 mM SDS and 1.3 wt% butan-1-ol.

Velocity gradient Figure 4.17 highlights the existence of a velocity gradient when moving away from the edge of the oil drop into the bulk of the aqueous phase. This experiment was done with a dodecane drop immersed in a 6% w/v NaCl brine solution of 5 mM SDS and 1.3 wt% butan-1-ol. Velocities diminished more rapidly into the bulk when considering starting points on the oil drop edge nearer to the top, leading to sharper velocity gradients nearer the oil drop top.

Figure 4.17 can be compared to Figure 4.18, where no velocity gradient was recorded as the flow hit perpendicular to the interface. In this case, velocity components tangential to the oil drop were calculated to be equal to $40\,\mu m.s^{-1}$ while one would have expected them to be near zero as the flow hit the drop at a normal angle. This overestimate was due the following experimental limitation. Particles were tracked at a 125 frames per second and the spatial resolution was $3.2\,\mu m.pixel^{-1}$. A calculated velocity of $40\,\mu m.s^{-1}$ thus corresponded to the displacement of a particle by one pixel every ten frames. Particles moving slower were considered idle and were not tracked, resulting in the overestimation of the velocity. However this limitation did not affect the measurements of velocities larger

than 50 µm.s^{-1} and thus the determination of the velocity gradient at the surface.

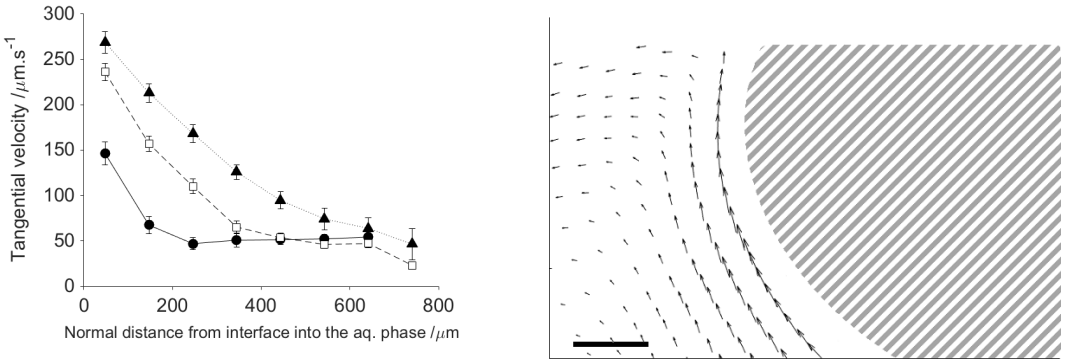

(a) (b)

Figure 4.17: (a) Velocity component tangent to the oil drop edge as a function of normal distance from the oil edge into the aqueous phase, at three positions on the oil drop edge: 300 (circles), 800 (squares) and 1300 µm (triangles) from the oil drop top corner of the oil-drop projection in (b). Lines are a guide for the eye. Data calculated from velocity map Figure 4.15 panel 5 (b). Scale bar measures 200 µm.

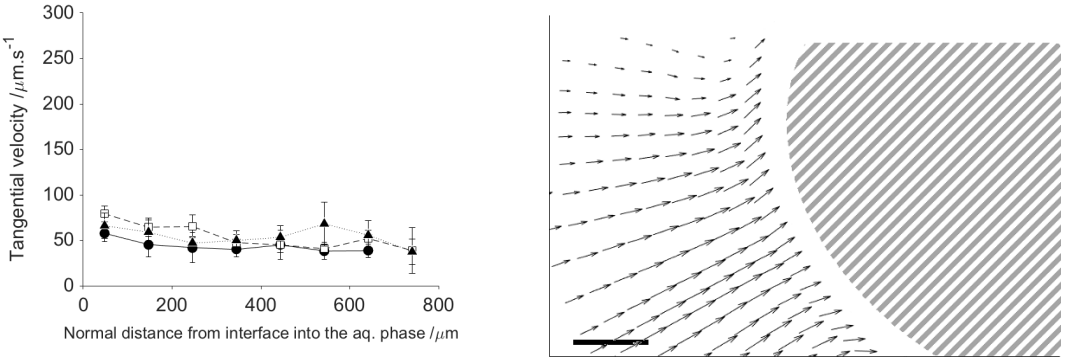

(a) (b)

Figure 4.18: (a) Velocity component tangent to the oil drop edge as a function of normal distance from the oil edge into the aqueous phase, at three positions on the oil drop edge: 300 (circles), 800 (squares) and 1300 µm (triangles) from the oil drop top corner of the oil-drop projection in (b). Lines are a guide for the eye. Data calculated from velocity map Figure 4.15 panel 8 (b). Scale bar measures 200 µm.

The velocity gradient in the normal direction is proportional to the interfacial gradient in the tangent direction as expressed in Equation 4.5

$$\mu \frac{\partial v_t}{\partial_n} = -\nabla_t \gamma \tag{4.5}$$

where μ is the viscosity of the phase, v_t the velocity tangent to the edge, γ the interfacial tension and n the normal to the interface. The three velocity gradients $\frac{\partial v_t}{\partial_n}$ determined from Figure 4.17 (a) were equal to -0.80, -0.64 and -0.48 mN.m^{-2} respectively for the positions on the oil drop edge at 300, 800 and 1300 µm from the oil drop top corner of the oil-drop projection of Figure 4.17 (b), with the viscosity of the aqueous phase equal to 1 mPa.s. The interfacial gradient $\nabla_t \gamma$ was used to estimate the difference in interfacial tension between the apex of the drop and the edge of the drop. The radius of the drop was 4.5 mm (half the length of the oil drop edge projected in side view). The interfacial tension differential was estimated to be circa 3 µN.m^{-1}. The equilibrated interfacial tension of dodecane and the aqueous phase was equal to 0.85 mN.m^{-1}. The interfacial tension differential represented circa 0.3% of the equilibrated interfacial tension. This estimate highlights how very small differences in interfacial tension can drive complex hydrodynamic behaviour.

Wetting film The thickness of the wetting film was determined by measuring the distance between the cover slip and the position from which no particle were detected. The cover slip position was established by bringing into focus the few particles that adhered to it. When scanning down from the cover slip, the absence of particles indicated that the objective was probing the oil phase rather than the aqueous phase. The wetting film was measured to be 6-µm thick for a 4-mm diameter dodecane drop in a 6% w/v NaCl brine solution of 5 mM SDS and 1.3 wt% butan-1-ol.

Figure 4.19 shows the population distributions of velocities measured at four different depths within the wetting film above a dodecane drop immersed into a 6% w/v NaCl brine solution of 5 mM SDS and 1.3 wt% butan-1-ol. At least a hundred particles were tracked during one recording. Fewer particles were tracked closer to the zero position (i.e. nearer the cover slip). A particle was tracked during 0.2 second on average. One could expect a Couette flow in the wetting film, with a no-slip boundary condition at the cover slip. Data shown in Figure 4.20 were consistent with this expectation. The velocities recorded in the wetting film were very similar to those recorded in the bulk of the aqueous phase and ranged from 0

to 300 µm.s^{-1}.

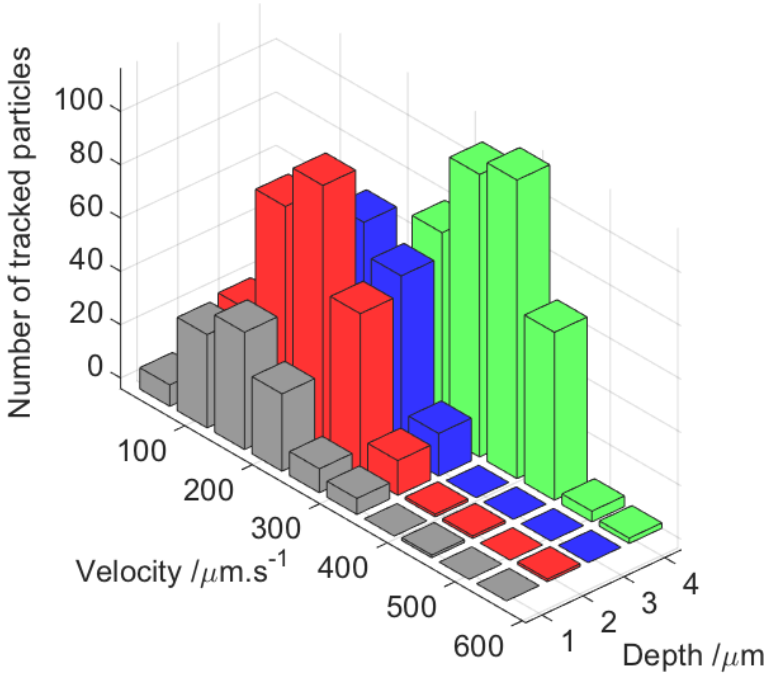

Figure 4.19: Comparison of population distributions of velocities of particles tracked within the thickness of the wetting film above a dodecane drop of 4 mm diameter.

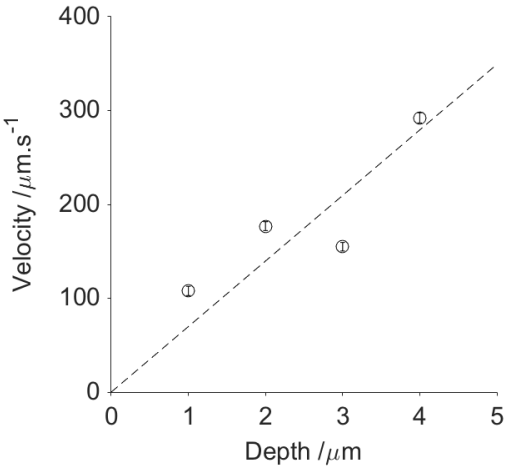

Figure 4.20: Measured velocities at different depths within the wetting film above a dodecane drop. Depth zero is the top wall of the cell.

The measured thickness and velocity profile were consistent with the measured flow rates. The dripping periodicity is the ratio of the burst volume to the volumetric flow rate. The volumetric flow rate in the 6-µm thick wetting film of a 4-mm diameter (r) oil drop is $2 \times \pi \times r \times thickness \times v \ = 2 \times \pi \times 0.006 \times 0.2 \ = 0.015$ mm^3.s^{-1},

with v the velocity within the wetting film (200 µm.s^{-1}). Considering a burst volume of 1.5 µL, the calculated dripping periodicity is 1.5/0.015 = 100 seconds, which is consistent with the experimental dripping periodicity.

Out-flow process

For large enough oil drops, drips eventually deformed the lower interface of drops and fell through when they could be no longer be supported. The rupture of the film of oil holding a drip was captured with high speed camera (Fastcam APXRS Photron) at 5000 frames per second, see Figure 4.21. The film of oil, stretched from the weight of the drip, burst within a millisecond. As soon as ruptured, the oil film retracted within ten milliseconds. An aliquot of oil was lost during the film retraction and formed a satellite spherical droplet. The kinetic energy from the recoil of the oil drop propagated and stretched the drop to the shape of an elongated doughnut. As the oil drop recovered, the aqueous phase was expelled. It took circa another 140 milliseconds for the hole to seal. The aqueous phase pinned to the bottom of the oil droplet detached creating a fluctuation at the interface, which took tens of milliseconds to recover and after which the oil drop recovered its initial shape. Subsequently, flow along the wetting film from the bulk continued and another drip built inside the oil drop, which eventually broke through the oil drop etc.

The velocity of retraction of a film v where viscous effects are negligible was expressed by Taylor and Culick by balancing momentum and surface tension forces:

$$v = \sqrt{\frac{2\gamma}{\rho \times d}} \tag{4.6}$$

where γ is the interfacial tension, ρ the film density and d its thickness.

The velocity of retraction of the oil film was measured to be equal to 0.1 m.s^{-1}. The oil film thickness was estimated to be equal to 14 µm, by evaluating the volume of the rim as the oil film burst. The measured velocity was smaller than its estimation using the Culick-Taylor expression (Equation (4.6)) which predicted a velocity of retraction of 0.35 m.s^{-1}. This overestimation is expected as the expression does not

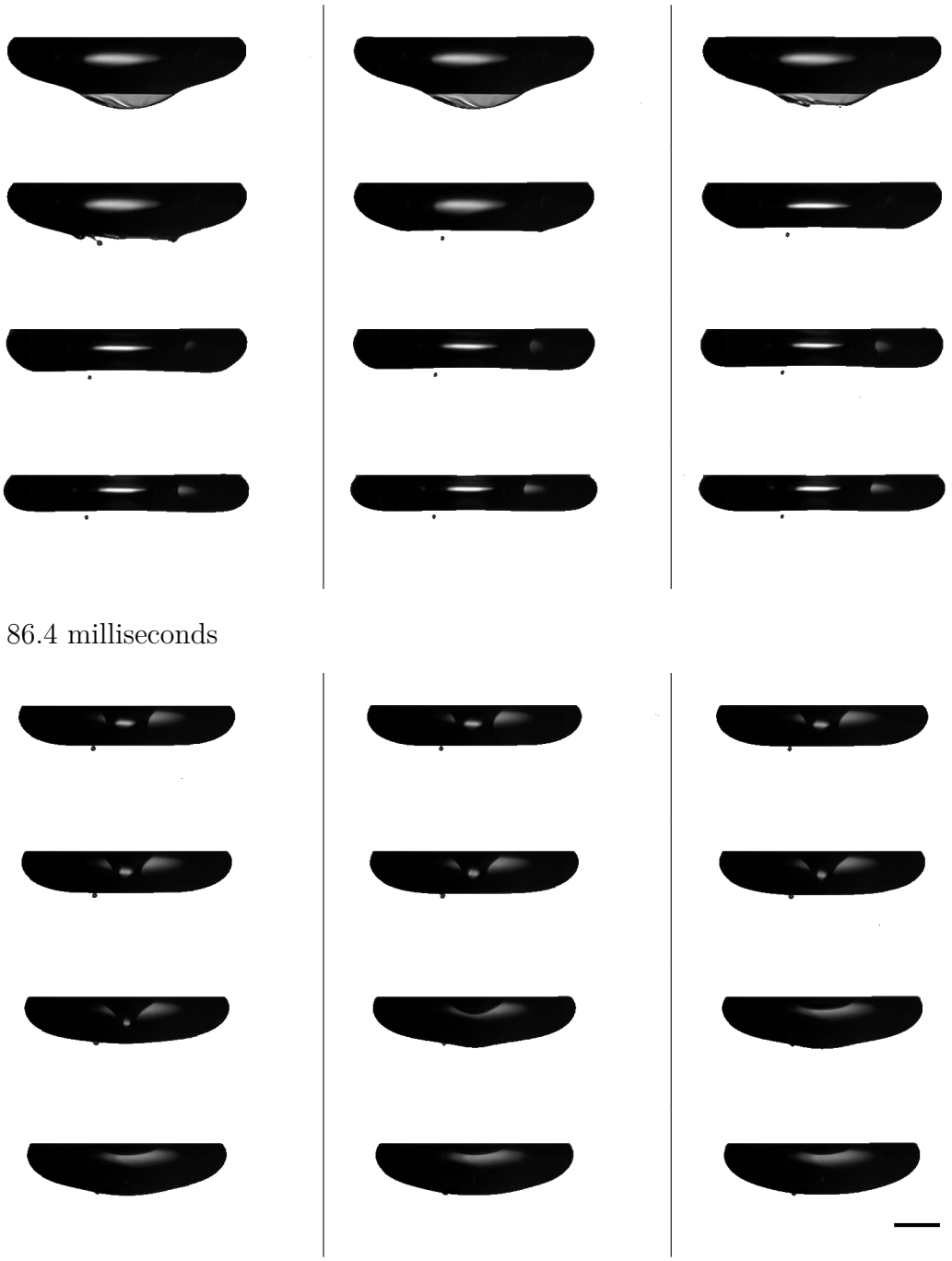

Figure 4.21: Snapshots (read direction horizontally left to right) of the rupture of the oil film retaining a drip in a 25-μL oil drop. 5.4 milliseconds between each frame. The scale bar measures 1 mm.

account for viscous drag.

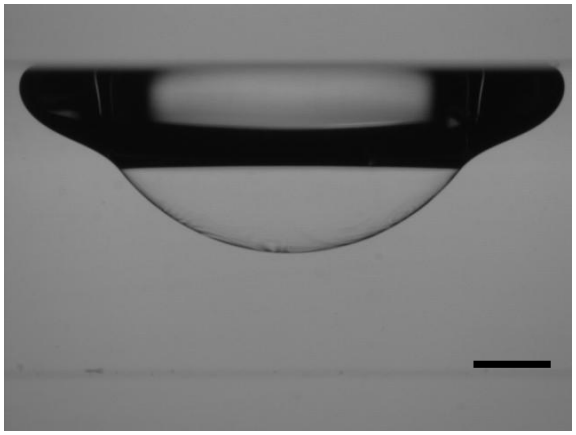

Figure 4.22: A super drip developing in a 29-µL oil drop. The drip reached 400% of the oil volume. The scale bar measures 1 mm.

For large oil drops, the development of a "super drip" (a drip reaching a volume largely exceeding that of the oil drop, as shown in Figure 4.22) marked the transition to a period of time preceding equilibrium where drip volumes were much smaller (circa 5% of the oil-drop volume) and their out-flow process was no longer through the oil drop but along the wetting film. The volumes of drips preceding a "super drip" were constant. The rate of growth of a "super drip" was approximately equal to that of the preceding drips. The transition from regular drips to a "super drip" and the transition from "super drip" to the smaller drips occurred abruptly, typically after one or two "super drips", see Figure 4.12. The right-hand column of Figure 4.23 shows that certain oil drops having reached equilibrium still contained an idle residual drip. These residual drips were not systematically observed.

Equilibrium

The shape of an oil drop having reached equilibrium in the aqueous phase differed from its initial shape, as highlighted in Figure 4.23. The shape of a buoyant oil drop depended on

- interfacial tension,

- buoyancy, i.e. the density difference between oil and aqueous phase,

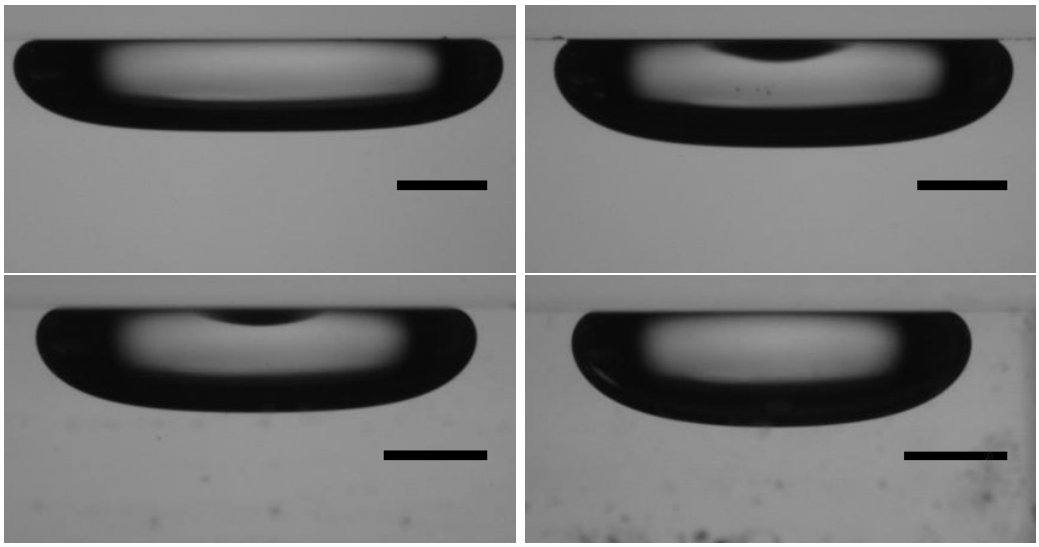

Figure 4.23: Two dodecane drops (14 and 11 µL, respectively), freshly drawn (left-hand column) and after ten hours (right-hand column). The aqueous phase was a 6% w/v NaCl brine solution of 5 mM SDS and 2.1 and 2.5 wt% butan-1-ol, respectively. The scale bars measure 1 mm.

- oil-drop volume.

The oil-drop volume did not increase by more than 3% with the solubilisation of butan-1-ol and was thus considered constant. On the other hand, the interfacial tension is expected to decrease with time as surfactant and cosurfactant diffuse to the interface and cosurfactant partition into the oil drop (see Figure 4.25). Lower interfacial tensions are associated with flatter drops, however Figure 4.23 shows that oil drops at equilibrium were thicker. Buoyancy of oil drops decreased too with time because butan-1-ol, which has a density intermediate to that of the brine solution and dodecane, partitioned between the two phases (densities of 6% w/v NaCl brine solution, butan-1-ol and dodecane are equal to 1.0413, 0.8098 and 0.7487 g/L at 20^oC respectively).

The shape of oil drops resulted from the competing effects of interfacial tension and buoyancy, which both depended on butan-1-ol content. The more butan-1-ol, the larger the butan-1-ol partition towards the oil and consequently the less buoyant the equilibrated oil drop. On the other hand, the higher the butan-1-ol content the lower the interfacial tension. Flat drops are associated with low interfacial tension or large buoyancy.

4.3.3. Oil-drop volume variation

As noted in the previous section, the shape of an oil drop depends on its volume. However, there is a critical volume from which the height of the drop becomes independent of its volume, i.e. drops of increasing volume gain in diameter but not in height. This critical volume decreases with interfacial tension. Figure 4.24 shows that this critical volume is smaller than 10 µL for an interfacial tension of about 1 $mN.m^{-1}$. Oil drops studied in this chapter were larger than their critical volume.

Dripping period, growth rates of drips and burst volumes of drips were measured for dodecane drops, ranging from 13 to 24 µL, in 6% w/v NaCl brine solution of 1.3 wt% butan-1-ol and 5 mM SDS. Within this volume range, the dripping periodicity was independent of the oil drop volume and was equal to 100 ± 6 seconds. Similarly, the growth rate of drips did not significantly vary with the oil drop volume and was 1.0 ± 0.2 $\mu L.min^{-1}$ and the burst volume of drips, i.e. the maximum volume of a drip, reached 1.5 ± 0.3 µL on average. During the period preceding the development of a super drip, the growth rate of consecutive drips in one oil drop varied by 2 to 10%, typically by 6%. Similarly, the burst volumes of consecutive drips in one oil drop varied by 2 to 15%, typically by 10%.

4.3.4. Interfacial tension variation

Interfacial tensions between oil drops and the aqueous phases were changed by varying the length of the alkane chain of oil drops or by keeping the alkane chain length constant and varying the amount of butan-1-ol in the brine solutions of surfactant.

Butan-1-ol variation

Interfacial tension between dodecane and aqueous phase decreased from 0.8 to 0.3 $mN.m^{-1}$ when increasing the butan-1-ol concentration in the 6% w/v NaCl brine solution of 5 mM SDS from nil to 5.0 wt%, see Figure 4.25. In addition, a greater proportion of butan-1-ol partitioned towards the dodecane drop the more butan-1-ol in the brine solution of surfactant and cosurfactant. The partition coefficient p

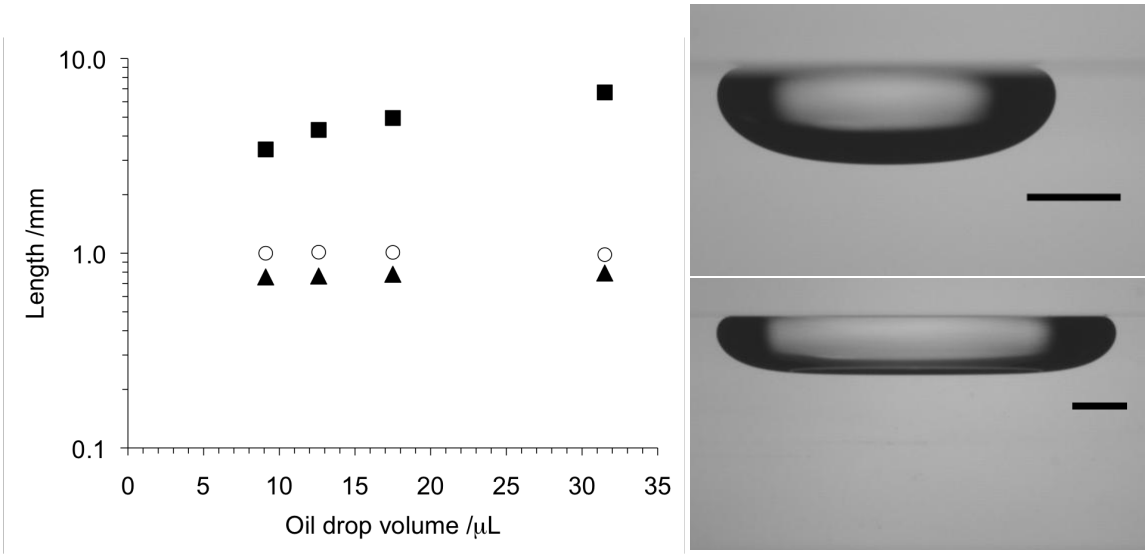

(a)

(b)

Figure 4.24: (a) Equatorial diameters (square), heights (circles) and heights from equator (triangles) of dodecane drops of different volumes in 6% w/v NaCl brine solution of 5 mM SDS and 1.3 wt% butan-1-ol. (b) Snapshots of the 9.1- and 31.5-μL dodecane drops, respectively top and bottom images. The scale bars measure 1 mm.

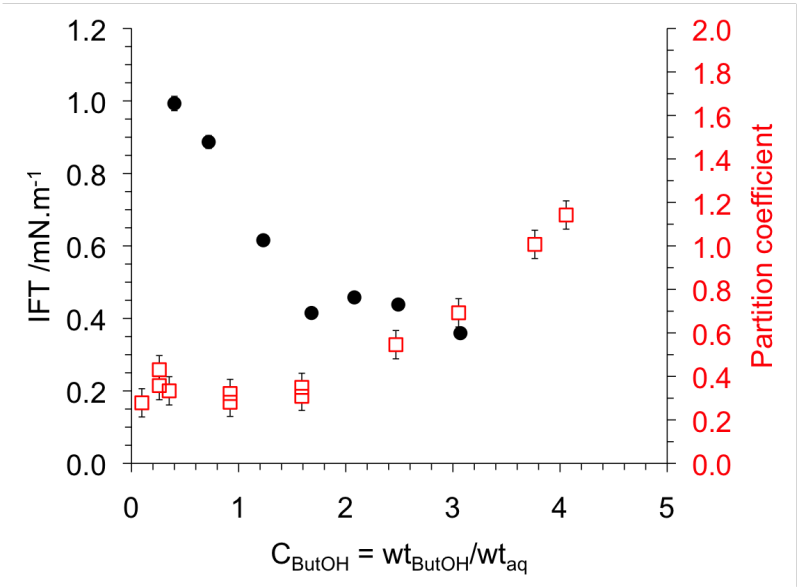

Figure 4.25: Measured interfacial tensions (black circles) and partition coefficients (red squares) of oil drops of dodecane in 6% w/v NaCl brine solutions of 5 mM SDS and varying butan-1-ol concentrations. IFT measured at 20.5 ± 0.5°C with spinning drop tensiometer. No interfacial tension was measured at butan-1-ol concentration smaller than 0.55 wt% because SDS salted out.

presented in Figure 4.25 was defined as the concentration ratio of butan-1-ol in the oil and in the aqueous phase

$$p = \frac{C^{oil}_{ButOH}}{C^{aq}_{ButOH}}, \tag{4.7}$$

where the butan-1-ol concentrations, C^{oil}_{ButOH} and C^{aq}_{ButOH}, are mass ratios of butan-1-ol in the respective phases, see Chapter Continuous scale.

Dripping periodicity, growth rates of drips and burst volumes of drips were measured for 24- to 37-µL dodecane drops in 6% w/v NaCl brine solutions of 5 mM SDS and butan-1-ol. Cosurfactant concentrations varied between 1% and the solubility limit of butan-1-ol in 6% w/v NaCl brine, i.e. 5.4 wt%.

Drips developed in dodecane drops which were immersed in aqueous phase containing less than 3.9 wt% butan-1-ol. Drips reached the largest volumes for aqueous phases containing 2.2 to 2.8 wt% butan-1-ol, see Figure 4.26. In addition within this butan-1-ol-concentration range, the variation of the burst volumes of consecutive drips in an oil drop largely exceeded the typical 10% volume variation observed in oil drops immersed in aqueous phases of lower butan-1-ol concentrations, see Section 4.3.3. on oil-drop volume variation. Consequently, the duration between consecutive oil-film ruptures in these systems was not constant and dripping periodicities were not used to characterise these systems. This lack of constancy in burst volumes is highlighted in Figure 4.27 which compares the volume variation of two deformed dodecane drops in 6% w/v NaCl brine solutions of 5 mM SDS and 1.0 and 2.7 wt% butan-1-ol.

Drips in Figure 4.27 (a) grew repeatedly at constant rate. Below 2 wt% butan-1-ol in the aqueous phase, drips developed within dodecane drops at a constant rate equal to 1 to 2 µL.min^{-1}, see Figure 4.28. Between 2 and 3 wt% butan-1-ol in the aqueous phase, two growth rates existed per drip. The growth rate of a drip initially equal to circa 1.5 µL.min^{-1}, increased sharply to 3.0 ± 0.2 µL.min^{-1} and remained constant until the rupture of the oil film sustaining the drip. The existence of two slopes within each cycle of the volume variation of the deformed dodecane drop with time are noticeable in Figure 4.27 (b) but not (a). At 3.2 wt% butan-1-ol, drips developing in the oil drop also had two growth rates but they were

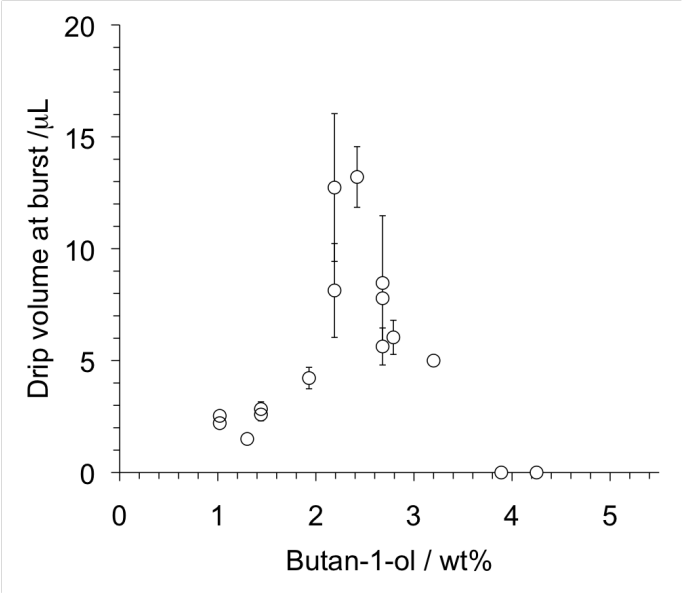

Figure 4.26: Mean burst volumes of consecutive drips developing in dodecane drops immersed in 6% w/v NaCl brine solutions of 5 mM SDS and varying butan-1-ol content.

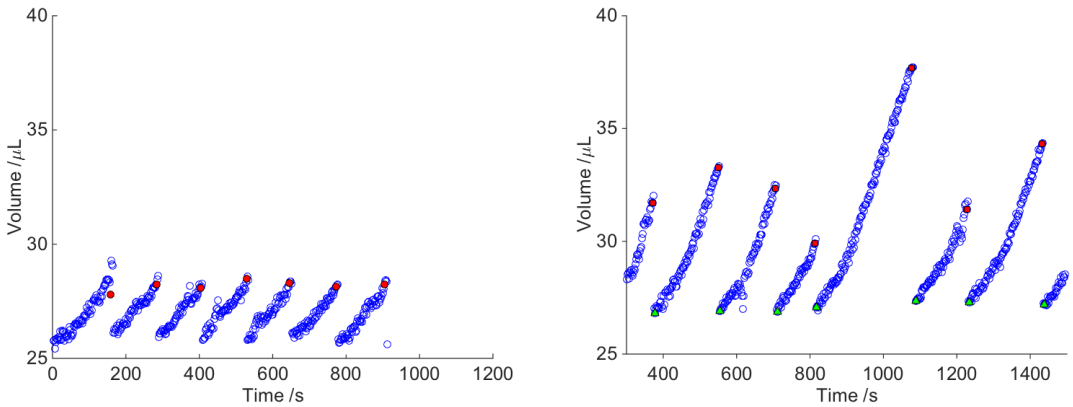

(a) (b)

Figure 4.27: Volumes of two deformed oil drops immersed in a 6% w/v NaCl brine solution of 5 mM SDS and (a) 1.0 wt% butan-1-ol, (b) 2.7 wt% butan-1-ol, as a function of time. Red squares highlight the total volume reached before oil-film rupture.

slower, at 0.8 and 1.3 µL.min^{-1}. One note that the butan-1-ol concentration range where maximum drip grow rate is observed correspond to maximum in slope of IFT versus butan-1-ol concentration, see Figure 4.25.

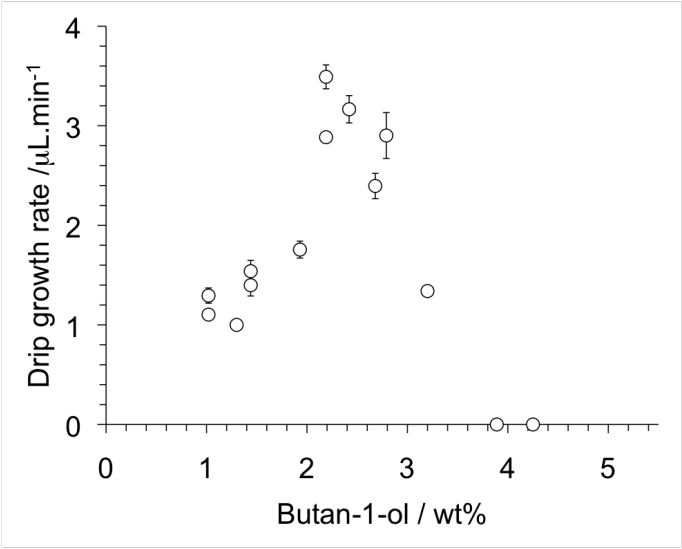

Figure 4.28: Mean growth rate of consecutive drips developing in dodecane drops immersed in 6% w/v NaCl brine solutions of 5 mM SDS and varying butan-1-ol content.

Above 4 wt% butan-1-ol in the aqueous phase, dodecane drops did not develop drips. From this butan-1-ol content, partition coefficient of butan-1-ol is larger than one, i.e. towards the oil, see Figure 4.25. At equilibrium, the butan-1-ol concentration in the dodecane drop is thus larger than 4 wt%.

Oil variation

Interfacial tension between oil drops and 6% w/v NaCl solutions of 5 mM SDS and 1.3 wt% butan-1-ol (see Figure 4.29, left axis) was equal to 0.55 ± 0.03 mN.m^{-1} for hexane, heptane and octane but increased with the alkane chain length for alkane with eight carbons or more. The viscosities increased continuously with the alkane chain length (see Figure 4.29, right axis).

Dripping periodicities, growth rates of drips and burst volumes of drips were measured for hexane, nonane, decane, undecane, dodecane, and pentadecane drops

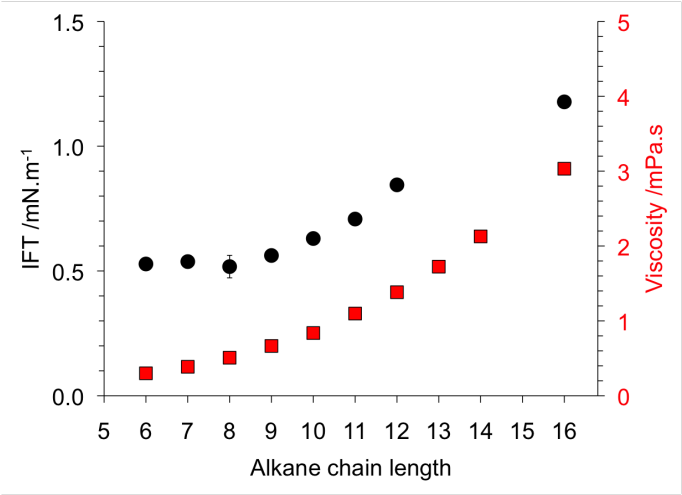

Figure 4.29: Measured interfacial tensions (black circles) and viscosities (red squares) of alkane drops in 6% w/v NaCl brine solutions of 5 mM SDS and 1.3 wt% butan-1-ol. IFT measured at 20^{o}C with spinning drop tensiometer. Viscosities at 25^{o}C from Physical Chemistry Handbook 86th Edition.

in 6% w/v NaCl brine solutions of 5 mM SDS and 1.3 wt% butan-1-ol. The oil-drop volumes ranged from 11 to 23 µL.

The growth rate of drips did not depend on the alkane chain length for oils between nonane and dodecane and was equal on average to 1.1 ± 0.1 µL.min^{-1}, see Figure 4.30. Drips in pentadecane developed slower at 0.3 µL.min^{-1}; drips in hexane developed at 0.05 µL.min^{-1}.

Drips developing in oil drops immersed in the brine solutions of surfactant and 1.3 wt% butan-1-ol reached a maximum of 2.5 µL (see Figure 4.31) i.e. a volume five times smaller than the largest drips observed in the butan-1-ol variation series. All the drips of oil drops studied in the alkane series were released into the bulk by rupture of the oil film. This was the case too for the 0.5-µL drips in hexane; such a small volume deformed the lower interface of the oil drop because the oil drop height was 0.7 mm. The burst volumes of consecutive drips in these oil drops were equal within 10% and there was no increase of variability as observed in the butan-1-ol series. The dripping periodicities of oil drops were thus calculated as the gradient of the times at which the oil film ruptured as a function of the number of occurrences of oil-film rupture. The burst volumes of drips could not alone be linked

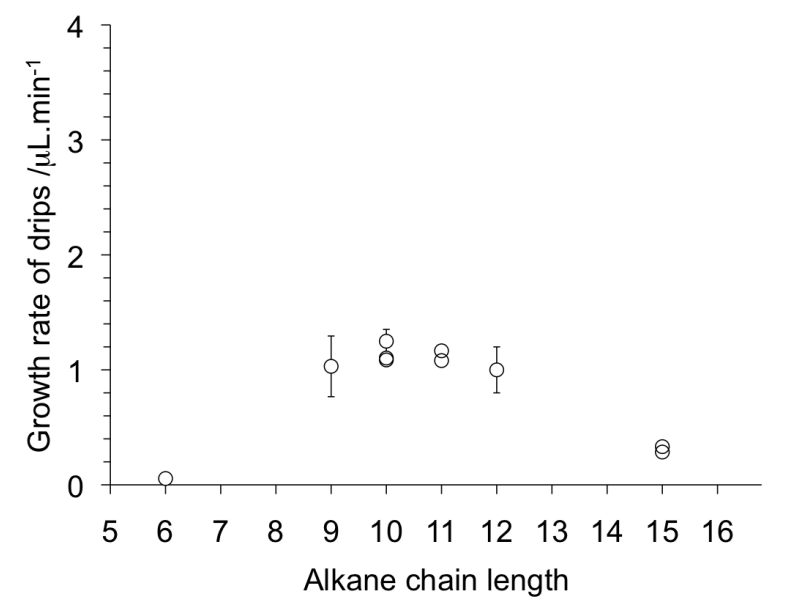

Figure 4.30: Mean growth rate of consecutive drips developing in alkane drops immersed in 6% w/v NaCl brine solutions of 5 mM SDS and 1.3 wt% butan-1-ol.

to the interfacial tension or the viscosity of the oil. On the other hand, Figure 4.32 shows that dripping periodicities in the alkane-variation series, with the exception of hexane, were proportional to the equilibrium interfacial tension, and the viscosity of the oil drop. The dripping periodicity for hexane was equal to 310 seconds and did not fit this trend.

Partition coefficients of butan-1-ol between alkanes and 6% w/v NaCl brine solution of 5 mM SDS and 1.3 wt% butan-1-ol were equal to 0.5 over the entire range of alkane-chain length investigated (hexane to pentadecane).

4.4. Discussion

Cosurfactant was central to understanding the phenomenon of the *dripping drops*.

First, butan-1-ol initially in the aqueous phase diffused to the oil to reach an equilibrium composition, described by the partition coefficient of butan-1-ol. Considering the diffusion coefficient of butan-1-ol in 6% w/v NaCl brine solution to be 6.9×10^{-10} $m^2.s^{-1}$, a butan-1-ol molecule took a characteristic time of 0.05 second

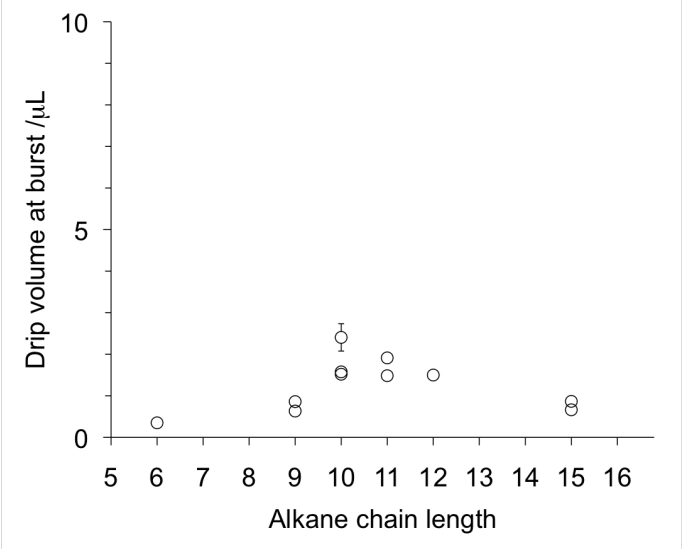

Figure 4.31: Mean burst volumes of consecutive drips developing in alkane drops immersed in 6% w/v NaCl brine solutions of 5 mM SDS and 1.3 wt% butan-1-ol.

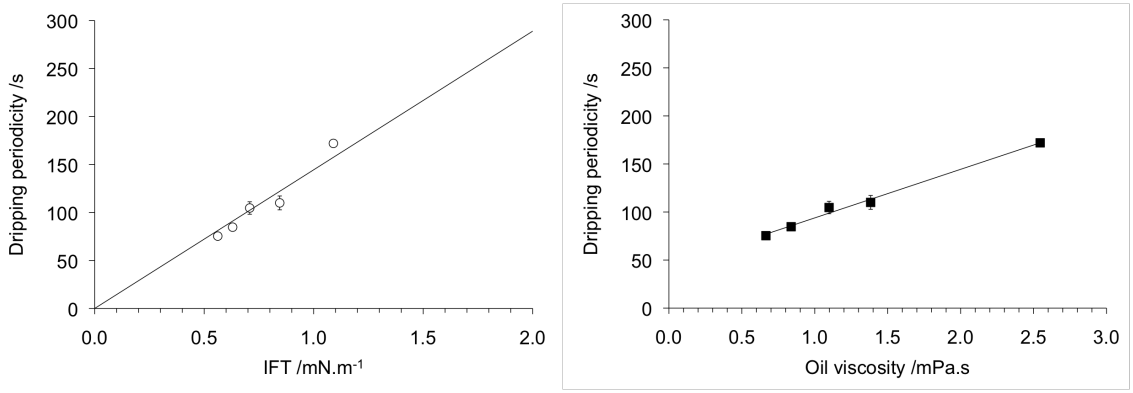

(a) (b)

Figure 4.32: Dripping periodicity in oil drops of nonane to pentadecane immersed in 6% w/v NaCl brine solutions of 5 mM SDS and 1.3 wt% butan-1-ol as a function of interfacial tension (a) and alkane viscosity (b). Lines are a guide for the eye.

to diffuse across the 6-µm thick wetting film above an oil drop. On the other hand, the characteristic diffusion time for a butan-1-ol molecule to reach the center of the wetting film from the bulk of the aqueous phase was of the order of the hour. The upper part of the oil drop had thus limited access to butan-1-ol and Marangoni flows, arising from varying butan-1-ol concentration in the wetting film, transported aqueous phase to the centre of the oil drop, forming a *drip*. The Marangoni stress was estimated to be about 0.6 $mN.m^{-2}$.

Secondly, the partition coefficient of butan-1-ol had an effect on the development of drips. Drips growth rates in n-alkane from dodecane to nonane drops immersed in brine solutions of surfactant and 1.3 wt% butan-1-ol were $1.1 \pm 0.1\,\mu L.min^{-1}$ while the interfacial tensions of these systems varied from 0.8 to 0.6 $mN.m^{-1}$. The increase of drips growth rate in the butan-1-ol-variation series could thus not be attributed to the corresponding interfacial tension reduction. The partition coefficient of butan-1-ol between brine solution of 1.3 wt% butan-1-ol and these alkanes was 0.5, regardless of the alkane chain length, i.e. the butan-1-ol concentration in the aqueous phase at equilibrium was twice the butan-1-ol concentration in the oil phase. On the other hand, the partition coefficient of butan-1-ol between 6% w/v NaCl brine and dodecane increased linearly with butan-1-ol concentration from 1.8 wt% butan-1-ol. In addition, the largest burst volumes were observed for butan-1-ol concentrations with the largest $d\gamma/dC_{ButOH}$. The increase of drip growth rates and larger variability of drip burst volumes in dodecane drops observed above 2 wt% butan-1-ol in the aqueous phase seemed to stem from the increasing partition coefficient or interfacial tension variation rather than the interfacial tension alone. For a given system, the partition coefficient increased the burst volume of drips and the growth rate of drips (see Table 4.1).

The butan-1-ol-variation study on dodecane drops showed that drips did not develop in oil drops immersed in brine solutions of surfactant and cosurfactant containing more than 4 wt% butan-1-ol. From 4 wt% butan-1-ol, the partition coefficient was larger than one. Interfacial tension measurements with a spinning drop tensiometer highlighted that a middle phase formed between a dodecane drop

C12 in 6% w/v NaCl brine solution of 5 mM SDS and butan-1-ol			
ButOH /wt%	p	Burst vol. /μL	Growth rate /μL.min^{-1}
1.3	0.30	2	1.0
2.4	0.52	13	3.2

Table 4.1: Burst volumes and growth rates of drips inside alkane drops immersed in 6% w/v NaCl brine solutions of 5 mM SDS and butan-1-ol. p butan-1-ol partition coefficient.

and a brine solution of SDS and 4.3 wt% butan-1-ol (see Figure 4.33). The presence of a middle phase above the oil drop could be the cause of the absence of drip above 4 wt% butan-1-ol in the aqueous phase, although a middle phase was not directly observed above the oil drop.

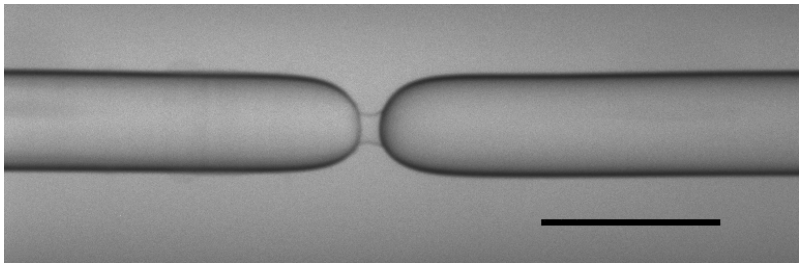

Figure 4.33: Middle phase formed between two spinning dodecane drops immersed in a 6% w/v NaCl brine solution of 0.05 mM SDS and 4.3 wt% butan-1-ol. The scale bar measures 1 mm.

Finally, butan-1-ol seemed to play a role in the visco-elastic properties of the oil films sustaining drips. In the time preceding equilibrium, transport of aqueous phase inside an oil drop was constant and continuous; rupture of the oil film acted as a perturbation but did not interrupt the flow of aqueous phase. Oil film ruptured when the volume of aqueous phase inside the oil drop reached a critical volume which could no longer be sustained; dripping period was a measure of how quickly this critical volume was reached. In the alkane-variation series, undertaken at 1.3 wt% butan-1-ol, the dripping periodicity could be correlated with the interfacial tension of the system and the viscosity of the oil. In the butan-1-ol-variation series however, dripping periodicity was not an appropriate way to characterise systems as a large variability in burst volumes of consecutive drips was observed for larger butan-1-ol

content. The study of the elasticity of such an oil film at different butan-1-ol content could shed some light on these observations.

The perpetuation of the development of aqueous drips inside the oil drop for hours remained a puzzling aspect of the phenomenon. The interfacial tension gradient along the oil-brine interface originated from the depletion of butan-1-ol at the top of the oil phase. In the aqueous wetting film above the oil drop, a molecule of butan-1-ol diffused across the width of the channel (6 µm) in a characteritic time of 0.05 second, considering a diffusion coefficient of butan-1-ol in a 6% w/v NaCl brine solution of 6.9×10^{-1} m^2s^{-1}. On the other hand, the characteristic diffusion time of a butan-1-ol molecule to reach the centre of the wetting film from the bulk of the aqueous phase was of the order of the hour, $((1 \times 10^{-3})^2/(4 \times 6.9 \times 10^{-1}) = 54$ min). The wetting film was thus depleted in butan-1-ol because butan-1-ol partitioned into the oil before the wetting film could be replenished in butan-1-ol by diffusion from the bulk of the aqueous phase. The phenomenon however, continued for hours before ceasing, i.e. several folds the time needed for the butan-1-ol in the bulk of the aqueous phase (infinite reservoir of butan-1-ol) to reach the centre of the oil drop by diffusion. In the comparison of the diffusion time for butan-1-ol to reach the centre of the oil drop to the duration of the phenomenon, the diffusion coefficient of butan-1-ol in dodecane was taken to be equal to that in the aqueous phase. This estimation may be underestimating the coefficient of diffusion because butan-1-ol can form clusters in the oil phase, which would slow down the butan-1-ol concentration equilibration. A second hypothesis to explain the duration of the phenomenon is the following. The aqueous drips which develop inside the oil drop may be depleted in butan-1-ol compared to the bulk of the aqueous phase because the aqueous butan-1-ol partitioned into the oil drop before the aqueous phase fed into the aqueous drips. When the content of an aqueous drip was released into the bulk of the aqueous phase by the rupture of the oil film retaining the drip, the oil phase was then surrounded by a brine solution of surfactant depleted in butan-1-ol. The butan-1-ol in the oil phase thus diffused back into the bulk of the aqueous phase to satisfy its partition coefficient, delaying eventually the time when

the oil phase would reach its equilibrium concentration. With this scenario, the interfacial-tension gradient thus reversed. Experimentally, the inversion of the flow direction was observed by particle tracking in the aqueous phase. Furthermore, a subtle difference in grey scale was observed between the bulk of the aqueous phase and the aqueous phase of the drip when the rupture of the oil film retaining the aqueous drip was captured on fast camera. The difference of grey could be attributed to a difference in refractive index between the bulk aqueous phase and the aqueous phase of the drip because of the butan-1-ol depletion of the latter.

4.5. Conclusion

This chapter aimed to simulate the early stage of diffusive transport to a non-wetting oil drop. The observations highlighted the importance of the system geometry because of which a region of the oil was depleted of cosurfactant. An interfacial gradient of less than 1% of the equilibrated interfacial tension led to substantial fluid motion, with flows typically at $300\,\mu m.s^{-1}$. The solubility of short chain alcohols in oil is an important topic in surfactant EOR. Ultra-low interfacial tensions are targeted to enable displacement of oil blobs through pore throats by viscous forces. However, the solubility of short-chain alcohols in oil slows down build-up to cosurfactant concentrations necessary to reach ULIFT-system formation. The results in this chapter demonstrated that Marangoni stresses occur at the oil-brine interface as soon as a region of the oil is depleted in cosurfactant. In this chapter, gravity pulled down, and eventually through the drop (dripping), the aqueous phase accumulating in an oil drop as a result of the Marangoni stresses. However, one can imagine that at a smaller scale, where gravity becomes negligible, these flows would act as a force on an oil blob. These flows may displace an oil drop over a few millimetres along a fracture but the pressure exerted by the flows on the drop would be too small to displace the drop through a constriction. More generally, this work highlighted how very small differences in interfacial tension drive complex hydrodynamic behaviour.

Chapter 5

Pore scale

5.1. Introduction

The ability of a surfactant mixture to displace oil from a pore network is commonly assessed using coreflood experiments. A cylindrical sample of reservoir rock (a core plug) is cleaned and imbibed with crude oil before a flood solution is pumped through the core. The outlet effluent is monitored with time and the mean water saturation (1-volume fraction of oil) can be determined as a function of the pumped volume of flood solution. The first major limitation of this method is that it does not give direct information on the mechanisms by which oil is mobilised. The second limitation is that the water saturation is averaged over the entire volume of the core by volume balance of oil originally in place to oil recovered and is thus not assessed locally. The nature of the effluent - presence/absence of surfactant, clear/cloudy solution, may not reflect *local* phenomena and does not inform on the evolution of the oil-water interface.

Local water saturation in a core plug can be monitored during a flood by NMR imaging techniques (e.g. [Mitchell et al., 2012]). The typical spatial resolution of this technique is 1 mm [Mitchell et al., 2013], which limits the scope for the asssessment of pore-scale mechanisms during oil displacement. MicroCT is another non-optical method used in the study of fluids in core plugs which offers better spatial resolution, typically tens of micrometers. Oil displacement was successfully

monitored during flooding with fast microCT [Youssef et al., 2014], a method only recently demonstrated [Mokso et al., 2011]. Fast microCT generates rapidly very large amount of raw data which can create storage issues [Youssef et al., 2014]. In addition, this technique requires the use of specific facilities for access to synchrotron-based X-rays. Finally, with both techniques, the distinction between continous oil phase and microemulsion phase is challenging. With NMR imaging technique, most of the NMR signal comes from the oil and a microemulsion phase would look like a "shadow" in oil saturation [Howe et al., 2015]. Similarly in microCT, as the distinction between phases is based upon magnetic susceptibility contrast, a microemulsion phase containing oil and brine would be seen as a less saturated oil region.

Microfluidics offer a highly tailorable means to visualise the oil-water interface [Lifton, 2016]. The distinction between oil, brine and microemulsion phase is straightforward as the contact lines between phases can be visualised with this optical method; the use a colouring agent in one of the phases makes this distinction easier [Howe et al., 2015]. This technology allows the fabrication of specific dual channels designed to study the local effects of floods during enhanced oil recovery, e.g. the pulling-effect of polymer flood [Afsharpoor et al., 2014], the formation of microemulsion [Unsal et al., 2016], or the fabrication of pore networks, designed to be representative of rocks porous structures, e.g. [He et al., 2014], [Howe et al., 2015]. The advantage of using a microfluidic device to monitor the displacement of oil by a flood, is that the image resolution allows to visualise local phenomena at the pore scale, anywhere in the pore network and at any time during the flood. The set-up is also very simple namely a homogeneous light source illuminating the microfluidic device and a camera. The visualisation of a surfactant flood is a powerful tool to assess the efficiency of a flood, and the mechanisms by which oil is recovered.

In this chapter, brine solutions of surfactant and cosurfactant were flooded into micromodels constitutive of a grid of channels with widths varying from 80 to 250 µm and a constant depth of 100 µm. The approach of Howe and his co-authors

[Howe et al., 2015], whereby the oleic phase was dyed with an organic colourant to be distinguished from the aqueous phase for image analysis, was followed. Both hydrophobic micromodels initially saturated with oil and hydrophilic micromodels were flooded.

The investigation presented in this chapter highlights the evolution of the oil-water interface in a sequence of pores under steady-state flow, when the surfactant and cosurfactant are present in the aqueous phase. It presents two unanticipated oil displacement types: the complete oil desaturation of a hydrophobic micromodel without the solubilisation of the oil bank into a third phase and the displacement of oil in the direction opposite to the flood direction in hydrophilic micromodels.

The remainder of this chapter is structured as follows. After the description of the methods and materials, including micromodels, the results of the micromodel floods are presented, first on hydrophobic micromodels, secondly on hydrophilic micromodels. Finally the results are discussed in light of the reservoir-scale phase behaviour.

5.2. Materials

Sodium dodecyl sulfate (SDS) (ACS grade > 99%, Sigma-Aldrich) was recrystallised three times in ethanol. Dodecane (99% pure, Acros Organics) was purified on silica gel and alumina. Butan-1-ol (ACS grade, Sigma-Aldrich), sodium chloride (analytical reagent grade, Fisher), oil Red EGN (Sigma-Aldrich) - structure shown in Figure 5.1, and SPAN-80 (Sigma-Aldrich) were used without further purification.

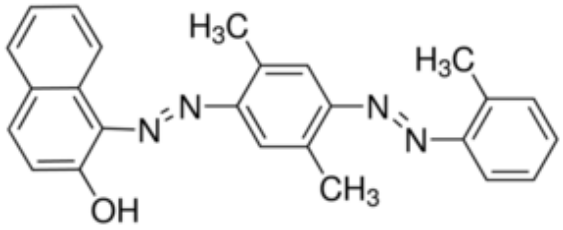

Figure 5.1: Oil Red EGN structure

(a)

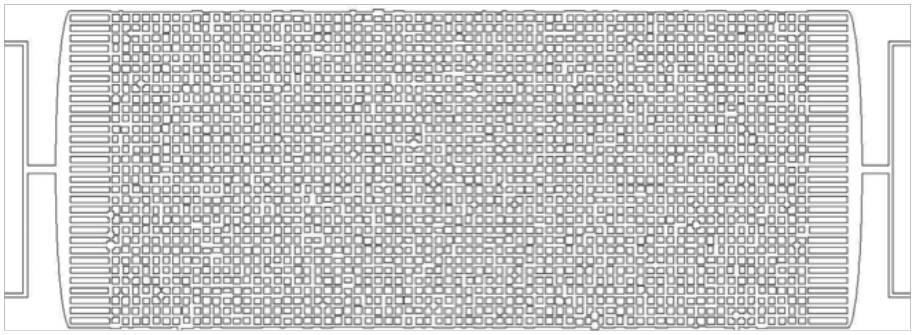

(b)

Figure 5.2: (a) Photo of a micromodel and (b) the design layout of the micromodel channels reproduced from [Howe et al., 2015].

Micromodels were supplied by Epigem Ltd, see Figure 5.2. They consisted of channels of epoxy-based negative photoresist SU-8 embedded in PMMA. The model channels had a uniform depth of 100 µm and width of 80 to 250 µm. The liquid reached the grid of channels after an inlet comb, composed of 32 channels of 200-µm width, positioned on a 480-µm pitch. The same structure was present at the outlet. The total volume of the grid of channels (or pore volume, PV) was 25 µL. Some micromodels had microfluidic filters at the inlets and outlets (out of the field of view of Figure 5.2 (b)). In addition, some micromodels had two pressure-monitoring channels vertical to the flow direction and connected to the edge of the micromodel. Pressure transducers were not connected to the micromodel and not used during the flooding experiments.

5.3. Methods

5.3.1. Solutions preparations

Oleic solutions

100 mg of oil Red EGN was added to 100 mL of dodecane pre-filtered on silica gel and alumina. The stock solution was left overnight on a roller mixer before being filtered using 3-µL pore-size nitrocelluose filter paper. The impact of oil Red EGN on the phase diagram was assessed by comparing two salinity scans, prepared with and without dye. For this purpose, five microemulsions were prepared at room temperature (20 ± 1^{o}C) in 20-mL graduated glass tubes by mixing 3 mL of dyed dodecane, 3 mL of brine, 0.70 g butan-1-ol and 0.35 g SDS. Brine solutions of 1, 3, 6 and 8% w/v NaCl were prepared by dilution of a 10% w/v NaCl stock solution. The weight ratio of butan-1-ol to SDS was kept constant at 2; the masses of surfactant and alcohol represented 17 wt% of the formulation. Solutions were shaken by hand and phase boundaries were recorded after separation. Solubilisation factors, defined as ratio by volume of water (or oil) to SDS in the microemulsion phase were calculated from the phase volumes. Preparation of the salinity scan without dye is reported in Chapter 3 Continuum scale. The dye did not alter the optimal salinity of the system, defined as the salinity for which oil and aqueous phase are solubilised in equal proportion in the microemulsion phase, nor did it alter the solubilisation factors, see Figure 5.3. It was concluded that oil Red EGN was not surface active, as observed by Howe and his co-authors [Howe et al., 2015].

Butan-1-ol-enriched dodecane solutions were prepared by weight for a total volume of circa 5 mL. Solutions used in micromodels were filtered on 47-mm-diameter nitrocelluose filter papers with 3-µm pore size, provided by Millipore.

Aqueous solutions

Flood solutions were prepared using two methods.

In the first method, 0.395 g recrystallised SDS were solubilised with circa 7 mL of

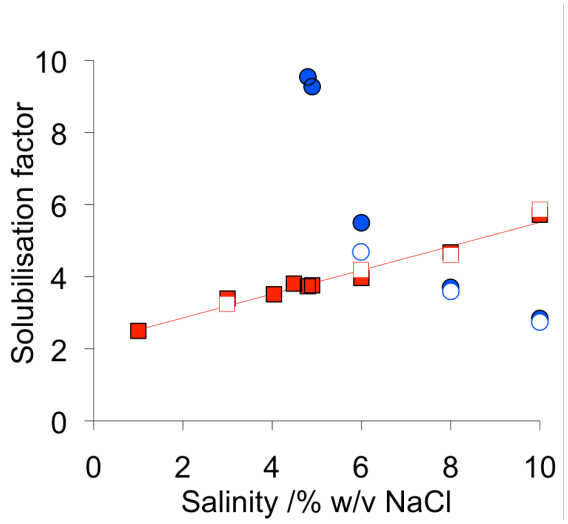

Figure 5.3: Comparison of solubilisation factors of oil (squares) and aqueous phase (circles) in the microemulsion phase in absence (filled symbols) and presence (empty symbols) of oil Red EGN. 1:1 v:v dodecane:brine microemulsions. The masses of surfactant and alcohol represented 17 wt% of the formulation, with a butan-1-ol-to-SDS mass ratio of 2. The red line is a linear regression.

Milli-Q water in a 10-mL volumetric flask; the solution was sonicated until surfactant solubilisation. Then, 0.6 g NaCl was added to the solution. The solution was sonicated in a warm water bath (45^{o}C) until the mixture was a transparent viscous solution. When the salt and SDS were solubilised, the volumetric flask was topped up to 10 mL with water. The 10 mL of the 6% w/v NaCl brine solution of 137 mM SDS were transferred in a glass vial where 900 µL (0.73 g) butan-1-ol were added to the solution. This procedure led to a one-phase 6% w/v NaCl brine solution of 137 mM SDS and 6.3 wt% butan-1-ol which was used as a surfactant-flood solution. A one-phase 6% w/v NaCl brine solution of 0.5 mM SDS and 5.3 wt% butan-1-ol was prepared following the same procedure.

The second method consisted in adding butan-1-ol to a 10-mL 6% w/v NaCl brine solution of SDS (167 mM SDS or 24 mM SDS) until the solution formed a two-phase mixture; the denser phase was used as the surfactant-flood solution. A short study detailed in Appendix showed that upon phase-separation, a non-negligible amount of surfactant and brine partitioned into the lighter, butan-1-ol-rich phase. The concentrations of SDS and alcohol in the flood solutions prepared with this method

were not measured after their preparation but could be estimated based on the results derived from the study presented in Appendix and tests solutions assessing the solubility limit of butan-1-ol in brine solutions of SDS. The concentrations of SDS and butan-1-ol in the flood solutions were estimated to be 71 ± 4 mM SDS and 5.7 ± 0.3 wt% butan-1-ol, and 10 ± 1 mM SDS and 5.4 ± 0.1 wt% butan-1-ol for the flood solutions prepared from the saturation of brine solutions of 167 mM SDS and 24 mM SDS respectively, with butan-1-ol.

5.3.2. Micromodel floods

Solutions were transported into the micromodel through fluorinated ethylene propylene tubing with 250-µm internal diameter, sourced from The Dolomite Centre Ltd. The glass syringes (500, 250, 100 and 50 µL) containing the solutions were driven by two Mitos Syringe Pumps (xs-Duo) from The Dolomite Centre Ltd.

Hydrophobic model Without pre-treatment, micromodels were hydrophobic. First, hydrophobic micromodels were sequentially flushed with 500 µL of IPA at 100 $\mu L.min^{-1}$, 250 µL of dodecane + 0.02 wt% SPAN-80, and 250 µL of dyed dodecane, both at 30 $\mu L.min^{-1}$. Initial oil saturations in hydrophobic models were consistently equal to 1, i.e. all the pores were filled with dodecane, see Figure 5.4. Last, oil-saturated micromodels were flooded with a brine solution of surfactant and alcohol at 0.4 or 0.1 $\mu L.min^{-1}$.

Hydrophilic model Micromodels were rendered hydrophilic using the wet-chemical method described in [Walther et al., 2010]. First, hydrophilic micromodels were sequentially flushed with 500 µL of IPA, 250 µL of 6% w/v NaCl brine, both at 100 $\mu L.min^{-1}$, and 250 µL of dyed dodecane at 30 $\mu L.min^{-1}$. Initial oil saturation in the micromodel, i.e. before the surfactant flood, depended on the wettability of the model, see Figure 5.4, but never exceeded 0.72 in the hydrophilic micromodels. This value was independent of the flow rate used to fill the micromodel, for the range of flows obtainable with the pump. Last, oil-saturated micromodels were flooded with a brine solution of surfactant and alcohol at 0.4 or 0.1 $\mu L.min^{-1}$.

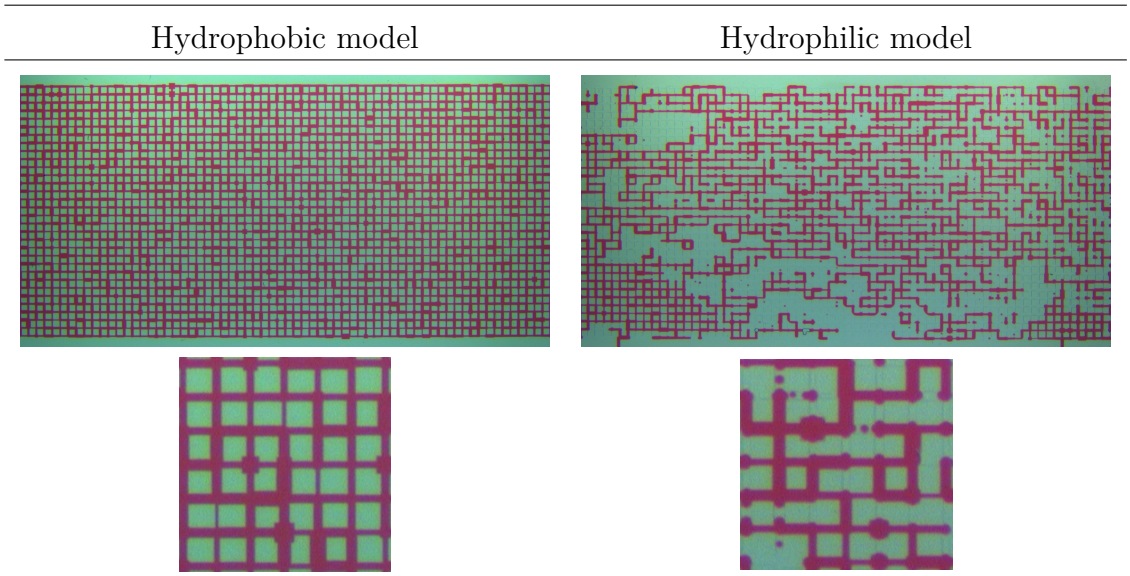

Figure 5.4: Full and zoomed-in images of two micromodels before surfactant flood. The initial oil saturation in a hydrophobic micromodel (left) was one, while it only reached up to 0.72 in the case of the hydrophilic micromodel (right). The two zoomed-in regions were taken towards the centre of the micromodels.

Note on successively passing solutions through tubings supplying micromodels Portions of the tubing supplying a micromodel contained sequentially IPA and the surfactant-flood solution. Milli-Q water was flushed through the tubing, but not into the micromodel, to displace IPA when the surfactant flood was the next solution to be passed through the tubing. This procedure prevented the surfactant-flood solution from contacting directly the IPA and hence NaCl from precipitating. Dodecane in the tubing was displaced by the surfactant solution, initially transported through the tubing at $10\,\mu L.min^{-1}$ and then at $2\,\mu L.min^{-1}$. Once the surfactant solution had displaced all the oil through the peripheral channel feeding into the micromodel, the set-up was ready for the surfactant-flood experiment.

5.3.3. Image capture and analysis

Image capture Micromodels were illuminated in transmission by a Dolan-Jenner QVABL fibre-optic back-light spanning the entire area of a micromodel to ensure homogeneous illumination. Images were captured using an AVT F-505C (Pike)

firewire camera together with a Navitar lens stack. The image acquisition was controlled by a LabVIEW programme. The resulting colour images contained 2452 × 1254 pixels. Images were captured in time-lapse mode, every 2.5 to 30 seconds. Subsequent image analysis was carried out with Matlab.

Image analysis Captured images were converted from RGB to HSV space. Saturation was fixed to one, and a threshold on the hue allowed the differentiation between pink pixels containing dyed dodecane and clear pixels containing surfactant solution. Local water-saturations in micromodels were calculated as follows. First, on a filled hydrophobic model, i.e. model before a flood, a threshold on hue isolated the channels from the background. All "channel-pixels", i.e. corresponding to full saturation, were summed over the width of the micromodel and along a 10-pixel span in the direction of flow. Secondly, the same procedure was undertaken for each image obtained during the flood, such as in Figures 5.5 (a), summing only channel-pixels containing surfactant solution over the width of the micromodel and along a 10-pixel span in the direction of flow. Finally, the pixel-trace obtained at a particular time was divided by the pixel-trace obtained for the filled model to obtain local water-saturations, ranging from zero to one, as a function of space, see Figures 5.5 (b). Finally, this line-vector of local water-saturations was converted into colours, see Figures 5.5 (c), from deep-red for fully oil-saturated to deep-blue for fully water-saturated local regions. The same pixel-trace generated from the oil-filled model was used for all subsequent images of one flood. Last, these colour lines obtained for each micromodel captured at regular intervals during the flood were vertically stacked to build a saturation scan to visualise local water-saturations as a function of space (horizontal axis) and time (vertical axis).

5.3.4. Capillary number

The capillary number of a flood gives a measure of the competition between viscous and capillary forces. For each flood, the capillary number Ca was calculated using

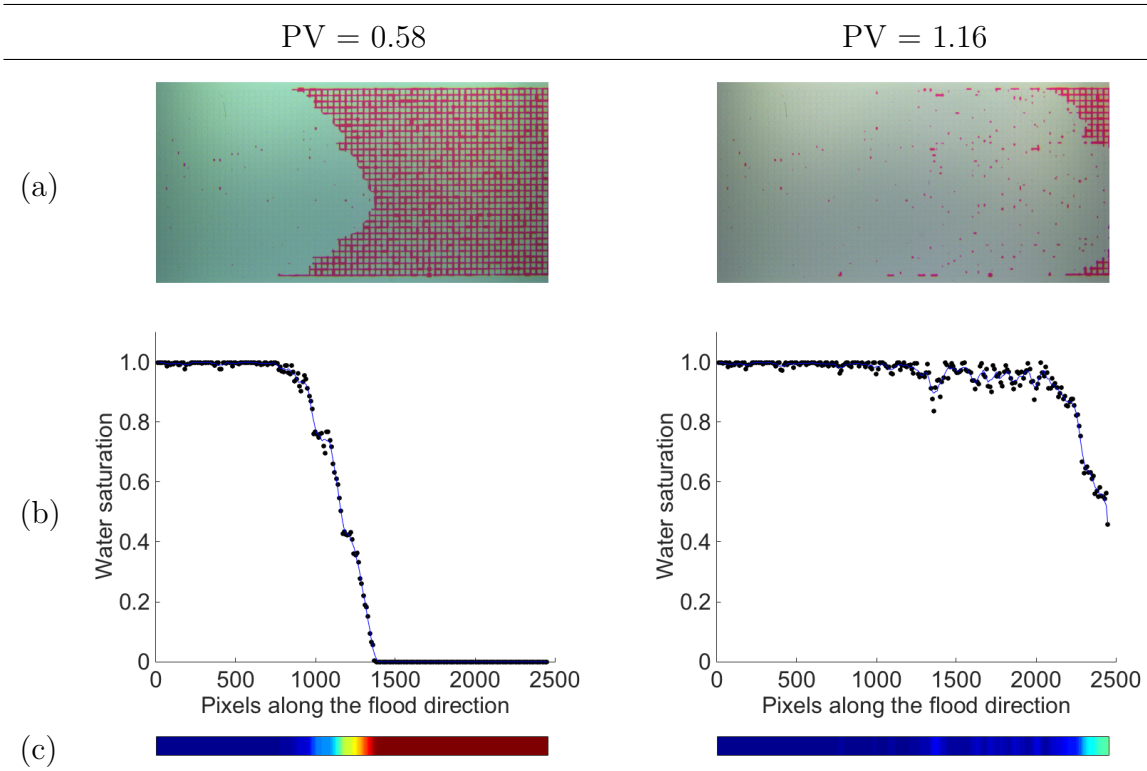

Figure 5.5: Image analysis during (PV = 0.59) and towards the end (PV = 1.16) of the flood. (a) Images of micromodel captured during the flood. Surfactant solution was flowing from left to right. (b) Corresponding local water-saturations averaged over the width of the micromodel and along a 10-pixel span in the direction of flow. The black dots are the raw data and the blue lines the corresponding smoothed functions. (c) Local water-saturations were translated into colours where deep-blue corresponds to complete local water-saturation and dark-red to complete local oil-saturation.

the equation

$$Ca = \frac{\mu \times v}{\gamma} \tag{5.1}$$

where μ and v are respectively the viscosity and velocity of the flood solution, and γ the interfacial tension between the flood and the oil initially in the micromodel. The viscosity μ of the surfactant flood was estimated to be that of water, i.e. 1 mPa.s. Its velocity v was calculated assuming a constant cross-section of 100 µm × 100 µm. Finally the interfacial tension γ was measured at 23 ± 1^{o}C with a SITE100 Krüss spinning drop tensiometer, unless stated otherwise, between the oleic and aqueous phases used in the micromodel which were pre-equilibrated in equal volume parts in a vial before the measurements.

5.4. Results

5.4.1. Hydrophobic models

A hydrophobic micromodel initially filled with dodecane was flooded with a 6% w/v NaCl brine solution at 0.4 µL.min^{-1}. The interfacial tension between dodecane and brine was measured by pendant drop tensiometer to be 50 mN.m^{-1} at 20 ^{o}C; the capillary number was calculated to be 1.3×10^{-5}. A second hydrophobic micromodel initially filled with dodecane was flooded with a 6% w/v NaCl brine solution of 0.5 mM SDS and 5.3 wt% butan-1-ol, at 0.1 µL.min^{-1}. The interfacial tension was measured with spinning drop tensiometer between the two phases equilibrated in 1:1 v:v to be 0.34 ± 0.03 mN.m^{-1}; the capillary number of the flood was calculated to be 4.9×10^{-4}. The two experiments are compared in Figure 5.6.

Oil blobs left behind the flood front of the surfactant-and-alcohol solution were smaller than those behind the front of the brine flood. The front of the surfactant-and-alcohol flood was consequently smoother, see Figures 5.6 (a) and (b). The front of the brine flood, behind which larger patches of oil remained, progressed initially more rapidly than the surfactant-and-alcohol front because of volume conservation. The development of lines with well-defined vertical edges in the salinity

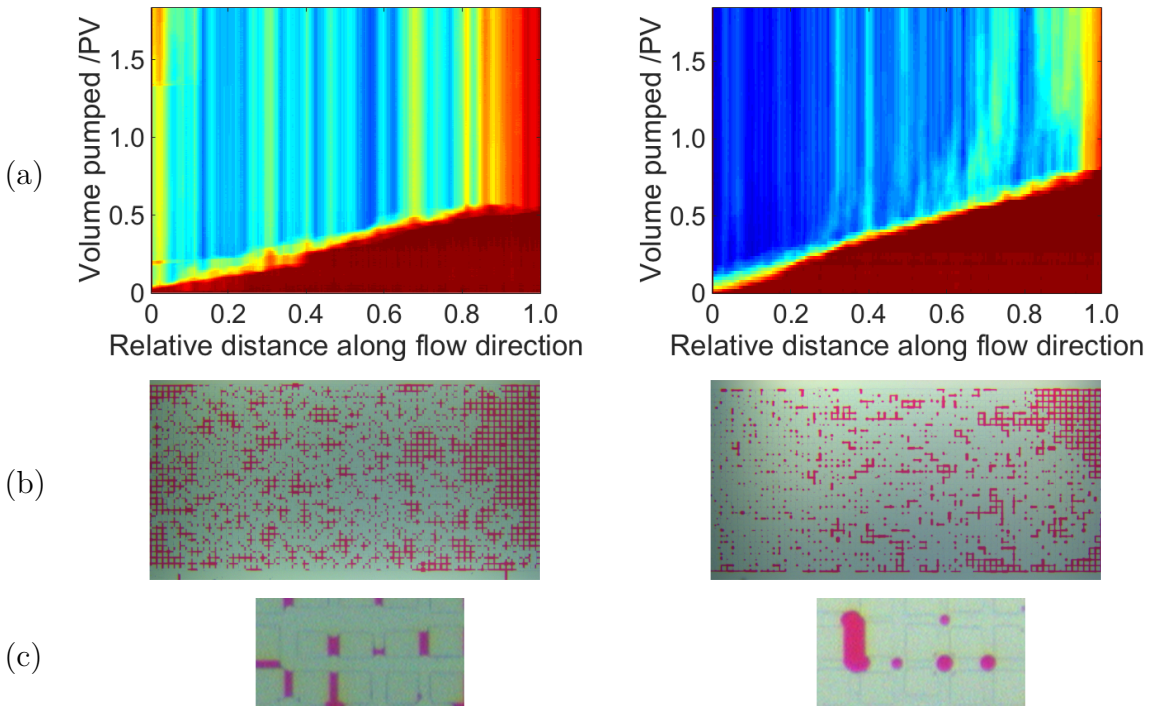

Figure 5.6: (a) Two saturation scans of two hydrophobic models initially fully saturated with dodecane and flooded with a 6% w/v NaCl brine solution free of surfactant and alcohol at 0.4 µL.min^{-1} (left), and with a 6% w/v NaCl brine solution of 0.5 mM SDS and 5.3 wt% butan-1-ol at 0.1 µL.min^{-1} (right). (b) Full images and (c) zoomed areas of the micromodels at the end of the floods (at 1.8 PV). Flood direction from left to right.

scan of the brine flood indicates that there was no displacement of oil blobs behind the flood front. This observation was less marked in the surfactant-and-alcohol flood. Just over half of the oil originally in place (56%) was recovered from the micromodel with the brine flood. On the other hand, the brine solution of 0.5 mM SDS and 5.3 wt% butan-1-ol recovered more than two-thirds (72%) of the oil originally in place. Additional volume of flood pumped into the micromodel after the flood front reached the outlet did not improve the oil recovery further. Finally, the brine flood did not modify the wettability of the micromodel, contrary to the brine solution of 0.5 mM SDS and 5.3 wt% butan-1-ol as highlighted in Figures 5.6 (c). The wettability modification from hydrophobic to hydrophilic did not occur instantaneously. Two coexistent wettabilities were observed when 0.9 PV of flood had been pumped into the micromodel (see Figure 5.7).

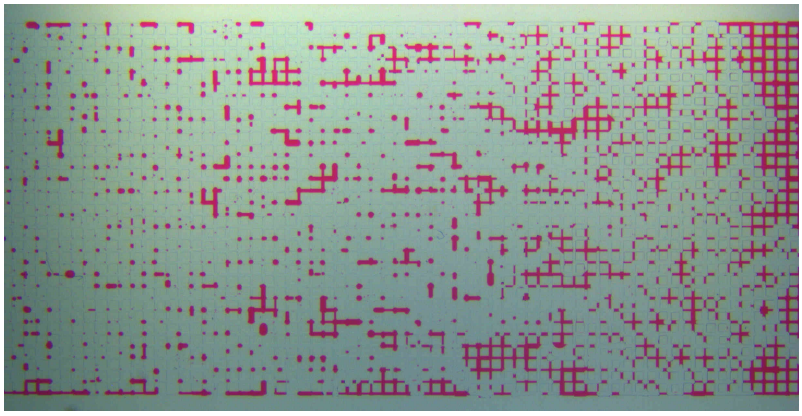

Figure 5.7: Hydrophobic micromodel flooded after 0.9 PV of 6% w/v NaCl brine solution of 0.5 mM SDS and 5.3 wt% butan-1-ol. Flow direction from left to right.

With a flow direction from left to right,

1. the left-hand side half of the micromodel, which was in contact with the surfactant-and-alcohol flood for longer, was hydrophilic: left behind oil formed circular drops and menisci of oil did not wet the micromodel channels;

2. the right-hand side half of the micromodel, more recently in contact with the surfactant-and-alcohol flood, was still hydrophobic: the narrower channels were still filled with oil and the contact angle of oil with the channel walls was

smaller than 70^o.

After 1.7 PV of flood pumped into the micromodel, the entire micromodel was hydrophilic (see Figure 5.6 (b) right).

The walls of the micromodel were SU-8, an epoxy-based polymer, treated with SPAN-80 (sorbitan oleate) to render the micromodel walls more hydrophobic. The sorbitan part of SPAN-80 adsorbs to the polar groups in SU-8, leaving the oleic ester of SPAN-80 to interact with the oil. When SDS is present, it can form a bilayer with the oleic ester of the adsorbed SPAN-80, and the polar heads of SDS render the walls hydrophilic. SDS adsorption on the walls of the micromodel was estimated considering a maximum adsorption on water-solid interface of 3.2×10^{-10} mol.cm^{-2} [Tajima et al., 1970], to be 2.6 nanomoles. A 25-µL solution of 0.5 mM SDS filling the micromodel could thus be nearly entirely depleted of its surfactant through adsorption on the walls. In the right-hand side half of the micromodel in Figure 5.7, the flood was depleted in surfactant: the displacement of oil and maintenance of original micromodel wettability were comparable to that of the brine flood. As more surfactant-flood solution was pumped into the micromodel, the surfactant remained in solution and altered the contact angle of the oil-water interface with the walls.

Finally, one notes in Figure 5.6 (c) that in the case of the hydrophobic micromodel flooded with brine, i.e. with no change of wettability, the larger channels were first imbibed with the flood solution and the narrower channels were left filled oil. Conversely, when the wettability became hydrophilic with the flood solution of brine with surfactant and alcohol, the narrower channels were imbibed with the flood solution and the larger channels were left filled with oil.

Another hydrophobic micromodel initially saturated with dodecane was flooded with a more concentrated surfactant and alcohol flood, a 6% w/v NaCl brine solution of 137 mM SDS and 6.3 wt% butan-1-ol at 0.1 µL.min^{-1}. The interfacial tension measured with spinning drop tensiometer between the two phases equilibrated in equivolume was 0.28 ± 0.03 mN.m^{-1}. The capillary number of this flood was calculated to be 5.9×10^{-4}. The more concentrated surfactant-and-alcohol flood displaced the oil differently from the 6% w/v NaCl brine solution of 0.5 mM

SDS and 5.3 wt% butan-1-ol. First, the contact line between the oil and the more concentrated surfactant-and-alcohol flood instantaneously became flat, with no distinctive wetting preference (see Figure 5.8).

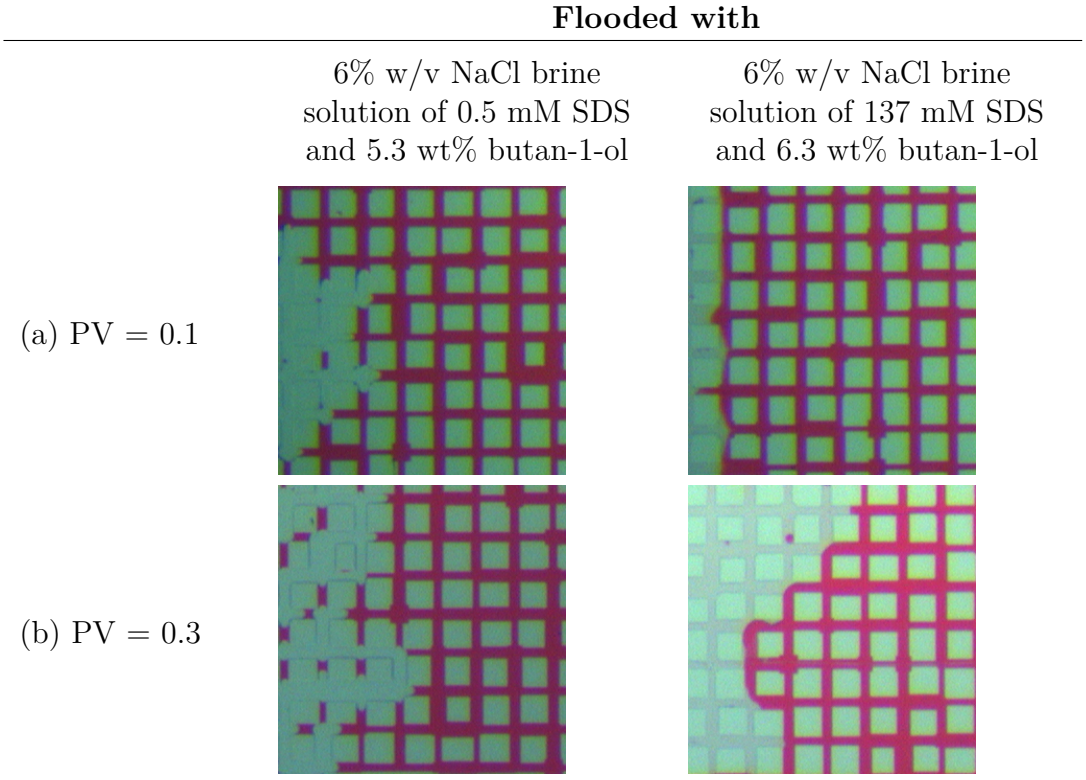

Figure 5.8: Zoomed areas at the flood fronts of two hydrophobic micromodels initially filled with dodecane at (a) PV = 0.1 and (b) PV = 0.3.

Secondly, the more concentrated surfactant-and-alcohol flood did not leave oil blobs behind the flood front. Finally, entire regions of the micromodel were by-passed by the more concentrated surfactant-and-alcohol flood (see second column of Figure 5.9). Consequently, the oil recovery obtained with the more concentrated surfactant-and-alcohol flood was very similar to the oil recovery obtained with the less concentrated surfactant-and-alcohol flood, despite a more efficient local oil displacement with the former. Oil recovery was 74% and 72% for the 6% w/v NaCl brine solutions of 137 mM SDS and 6.3 wt% butan-1-ol, and of 0.5 mM SDS and 5.3 wt% butan-1-ol, respectively.

Finally, a second hydrophobic micromodel was flooded with the more concentrated surfactant-and-alcohol flood, i.e. the 6% w/v NaCl brine solution

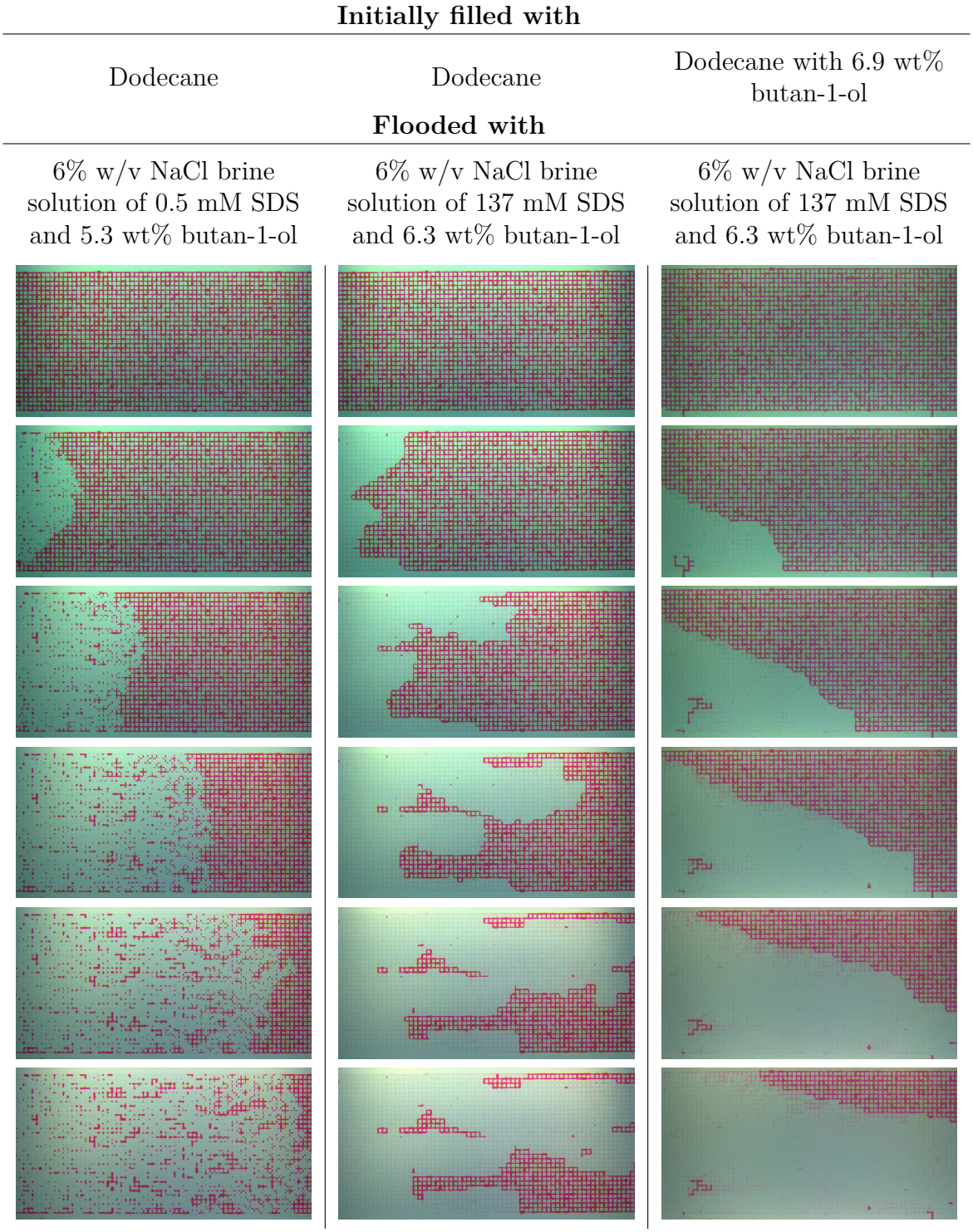

Figure 5.9: Sequential micromodel surfactant-flood images of three hydrophobic micromodels taken at regular volume intervals of injected surfactant-flood (0.17 PV). Flood direction from left to right, at 0.1 µL.min^{-1}. The ganglion of oil in the first third of the model of the third column was trapped in one of the pressure taps and released upon carrying out the flood.

of 137 mM SDS and 6.3 wt% butan-1-ol, at 0.1 µL.min^{-1}. For this experiment, the micromodel was initially filled with dodecane enriched in butan-1-ol (6.9 wt%) (see third column of Figure 5.9). The oleic and aqueous phases used with this micromodel formed a three-phase microemulsion when mixed in equal volume parts in a test tube. The interfacial tension used for the calculation of the capillary number was measured with spinning drop tensiometer between the middle phase and the excess aqueous phase, and was 0.006 ± 0.001 mN.m^{-1}. The capillary number was calculated to be 2.6×10^{-2}.

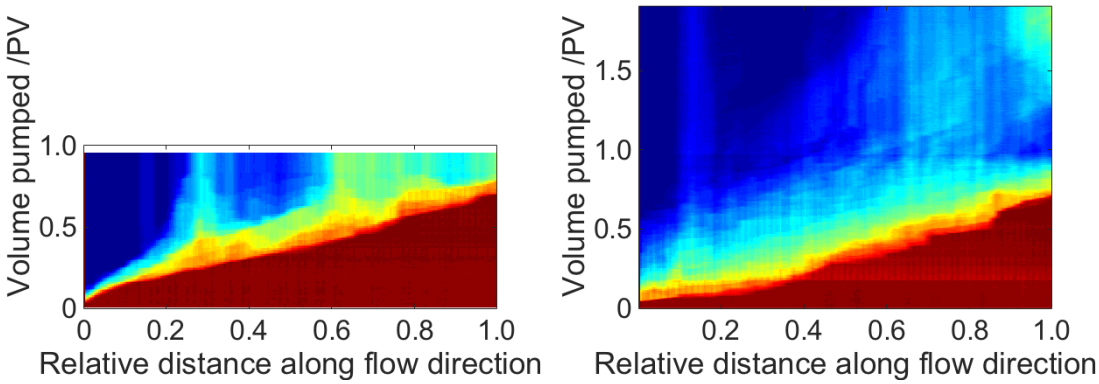

Figure 5.10: Saturation scans derived from the floods of two hydrophobic micromodels with 6% w/v NaCl brine solutions of 137 mM SDS and 6.3 wt% butan-1-ol, showed in the second and third columns of Figure 5.9. (a) Micromodel initially filled with dodecane, (b) micromodel initially filled with dodecane enriched with butan-1-ol (6.9 wt%).

The saturation scans obtained from the two floods carried out with the 6% w/v NaCl brine solution of 137 mM SDS and 6.3 wt% butan-1-ol are compared in Figure 5.10. The micromodel initially filled with dodecane was flooded with a total volume of 1.0 PV only; on the other hand a total of 1.8 PV was pumped into the micromodel initially filled with dodecane enriched in butan-1-ol (6.9 wt%). At 1.0 PV, the oil recovery was 74% for the micromodel initially filled with dodecane and for the micromodel initially filled with dodecane enriched in butan-1-ol was 85%. In the latter flood, a further 2% of oil was recovered with an additional 0.8 PV of flood. Figure 5.10 shows that after a slower start, the front velocity in the micromodel initially filled with dodecane was constant during the time of the flood.

In the micromodel initially filled with dodecane enriched in butan-1-ol, the front velocity decreased after 0.1 PV of flood was pumped into the micromodel. This time corresponds to the first appearance of a lighter-pink phase (see Figure 5.12). After the flood front reached the end of the micromodel, the oil bank at the top right-hand corner of the micromodel continued to be displaced, and solubilised in the lighter-pink phase which grew in volume as the flood progressed. The lighter-pink areas were associated with a third phase because of the uniformity of its colour across the entire micromodel and the existence of contact lines between both the colourless flood solution and the pink oil phase, and the lighter-pink areas (see Figure 5.11). There was a zero contact angle between the dodecane enriched in butan-1-ol and the lighter-pink phase, which wetted the micromodel channels. The saturation scan derived from this flooding complements what was observed in the images of the micromodel during the flood:

1. the flood front progressed smoothly, leaving no oil trapped behind;
2. a saturation shadow followed the flood front;
3. the water saturation continued to progress after the flood front reached the end of the micromodel.

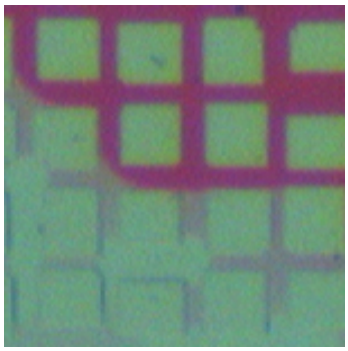

Figure 5.11: Zoomed-in image of the micromodel during the flood where three phases coexisted.

In the results presented so far, the largest recovery obtained reached 87% at 1.2 PV; the flood solution was a concentrated brine solution of SDS and butan-1-ol,

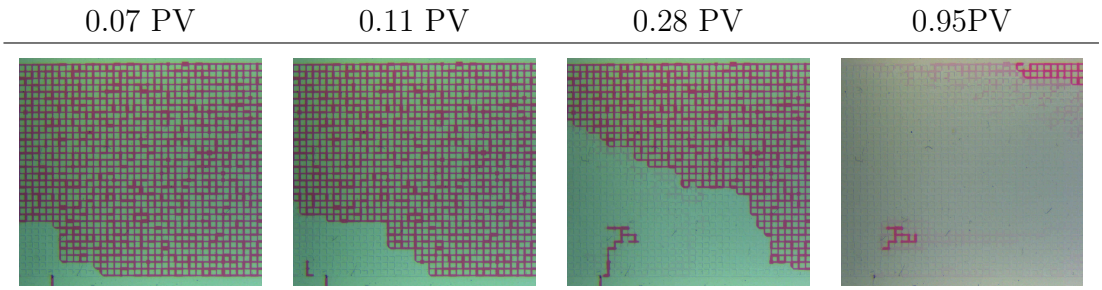

Figure 5.12: Four images of the first half of the micromodel initially filled with dodecane enriched in butan-1-ol (6.9 wt%) and flooded with a 6% w/v NaCl brine solutions of 137 mM SDS and 6.3 wt% butan-1-ol, taken at four times during the flood, at 0.07 PV, 0.11 PV, 0.28 PV and 0.95 PV. Flow direction left to right. The ganglion of oil in the first half of the images was trapped in one of the pressure taps and released during the flood.

137 mM SDS and 6.3 wt% butan-1-ol, displacing a dodecane solution enriched in butan-1-ol (6.9 wt%). This was the only flood where the development of large area of third-phase was observed. Larger oil recoveries were obtained from the floodings of two hydrophobic micromodels with a 6% w/v NaCl brine solution of 71 ± 4 mM SDS and 5.7 ± 0.3 wt% butan-1-ol, which was the denser aqueous-rich phase of a 6% w/v NaCl brine solution of 167 mM SDS that became biphasic upon addition of excess butan-1-ol. The micromodels were initially filled with dodecane and the fluids were pumped at 0.1 and 0.4 µL.min^{-1}. The interfacial tension between the flood solution and the oil was measured with the spinning drop tensiometer to be 0.280 ± 0.005 mN.m^{-1}. The capillary numbers were calculated to be 5.9×10^{-4} and 2.4×10^{-3}, for the floods at 0.1 and 0.4 µL.min^{-1} respectively. The saturation scans derived from the floods are shown in Figure 5.13; images of the floods in Figure 5.14.

A complete oil desaturation was obtained in the first third of the two micromodels. At 0.1 µL.min^{-1}, a large area of oil was by-passed. The entire area of the micromodel was swept by the flood when increasing the velocity of the flood to 0.4 µL.min^{-1}. However, sporadic non-wetting oil spots were left behind the front flood in the second half of the micromodel which were not remobilised. With this surfactant flood, 82.5% and 94% of the oil was recovered after 1 PV of flood solution was pumped into the micromodels, for the floods at 0.1 and 0.4 µL.min^{-1} respectively. In both cases, no large area of light-pink third phase developed, as

observed during the flood of the micromodel initially filled with dodecane enriched in butan-1-ol.

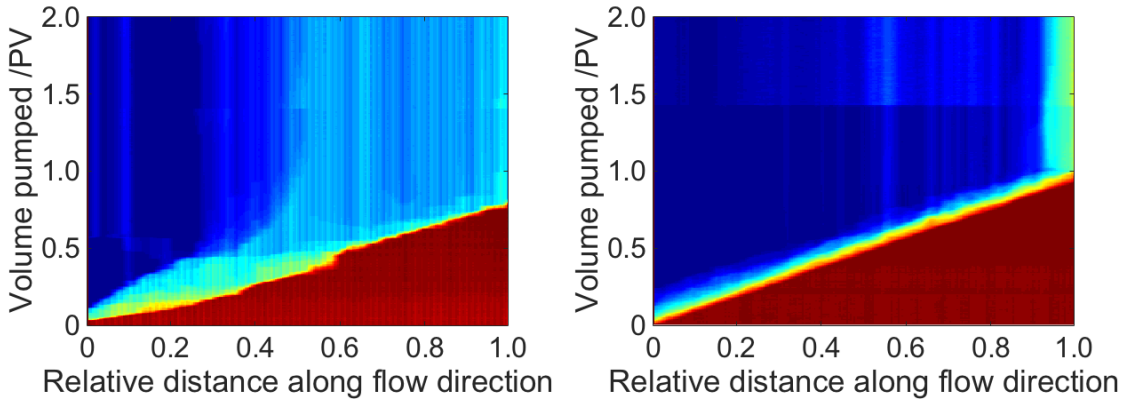

(a) (b)

Figure 5.13: Saturation scans derived from the flood showed in Figure 5.14 at (a) $0.1\,\mu L.min^{-1}$ (a) and (b) $0.4\,\mu L.min^{-1}$

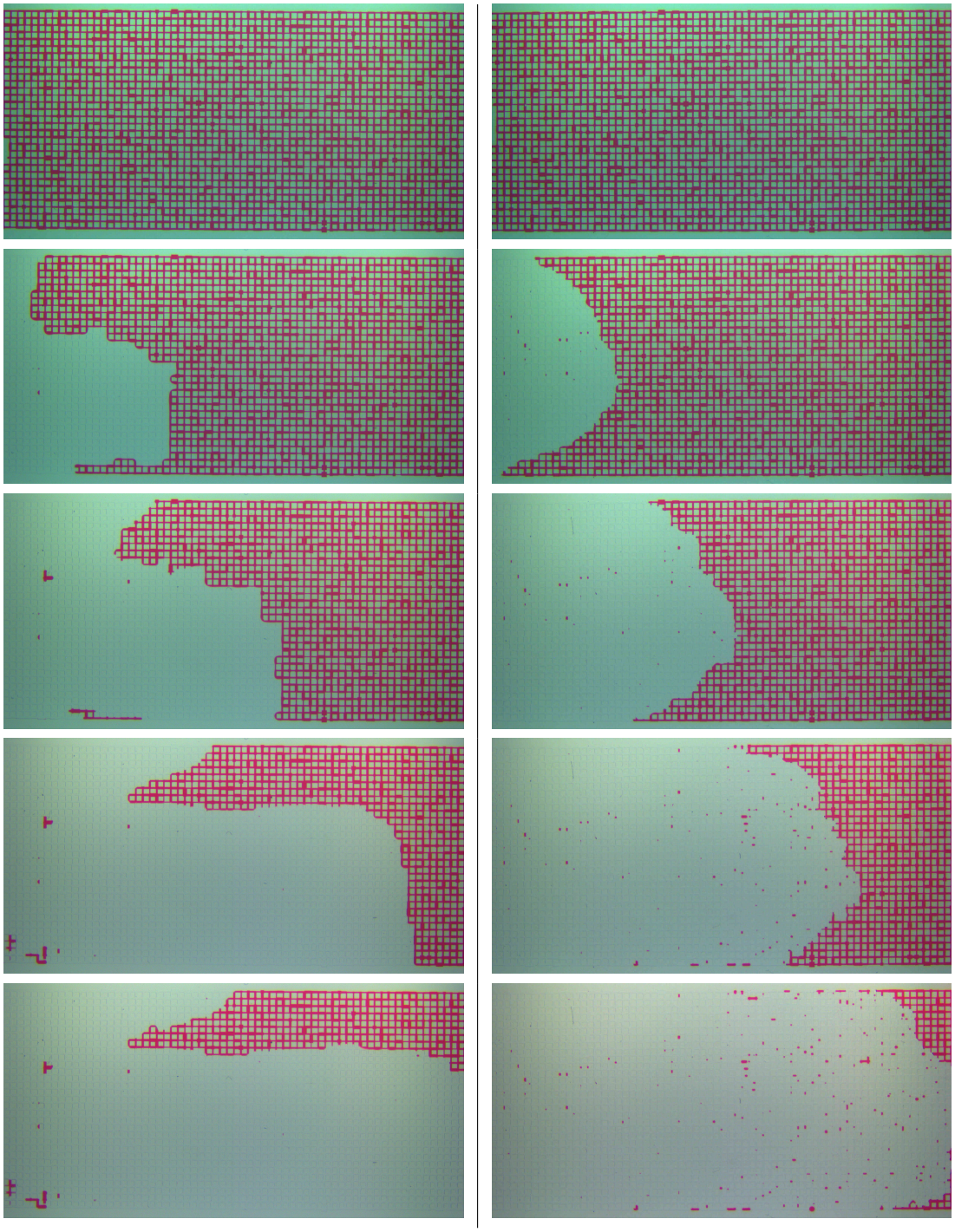

Figure 5.14: Sequential micromodel surfactant-flood images of hydrophobic micromodel taken at regular volume intervals of injected surfactant-flood (0.24 PV). The micromodel was initially saturated with dodecane. The surfactant-flood solution was a 6% w/v NaCl brine solution of 71 ± 4 mM SDS and 5.7 ± 0.3 wt% butan-1-ol. Flow direction from left to right, (left) flood at 0.1 µL.min^{-1}, (right) flood at 0.4 µL.min^{-1}.

5.4.2. Hydrophilic models

In this section, floods are described for hydrophilic micromodels prepared from two different starting conditions. The difference was in the aqueous system used prior to the dodecane fill. The first to be discussed was a pre-fill with 6% w/v NaCl and the second was a pre-fill with deionised water. A hydrophilic micromodel with a background salinity of 6% w/v NaCl was initially filled with dodecane; initial oil saturation was 69% (see Figure 5.15 (a)). The micromodel was flooded, at $0.4\,\mu L.min^{-1}$, with a 6% w/v NaCl brine solution of 10 ± 1 mM SDS and 5.4 ± 0.1 wt% butan-1-ol, which was the denser aqueous-rich phase of a 6% w/v NaCl brine solution of 24 mM SDS that became biphasic upon addition of excess butan-1-ol. Oil was displaced in an unexpected fashion through the micromodel as shown in Figure 5.16. There was no front spanning across the width of the micromodel. Instead, early in the flood, oil ganglia of the second half of the micromodel, i.e. far from the flood front, were displaced. Moreover, oil ganglia were displaced in direction *opposed* to the flood direction. The saturation scan derived from this flood looks thus different from the ones obtained for flooding of hydrophobic micromodels (see Figure 5.17). The formation of middle phase was observed locally twice at the beginning of the flood (see Figure 5.18). Eventually only 45% of the oil originally in place was recovered.

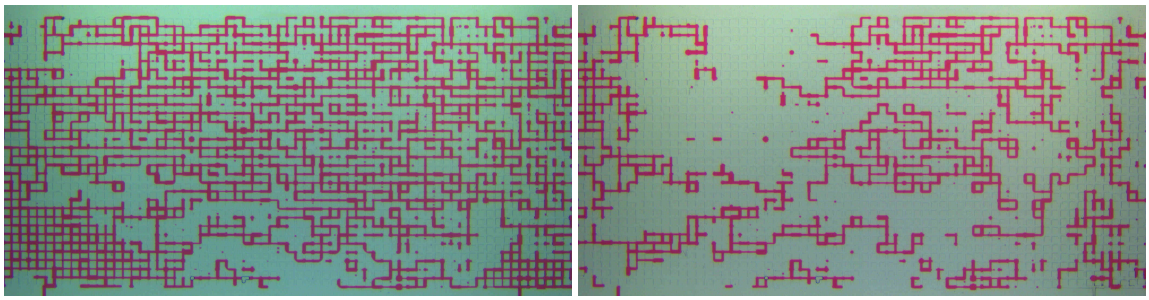

(a) (b)

Figure 5.15: Images of a hydrophilic micromodel initially filled with dodecane with a background salinity of 6% w/v NaCl (a) before the flood and (b) at the end of the surfactant-and-alcohol flood (1.3 PV). Flood direction from left to right.

A second hydrophilic micromodel filled with dodecane was flooded with the same aqueous flood solution at the same flow rate, $0.4\,\mu L.min^{-1}$. This time however, the

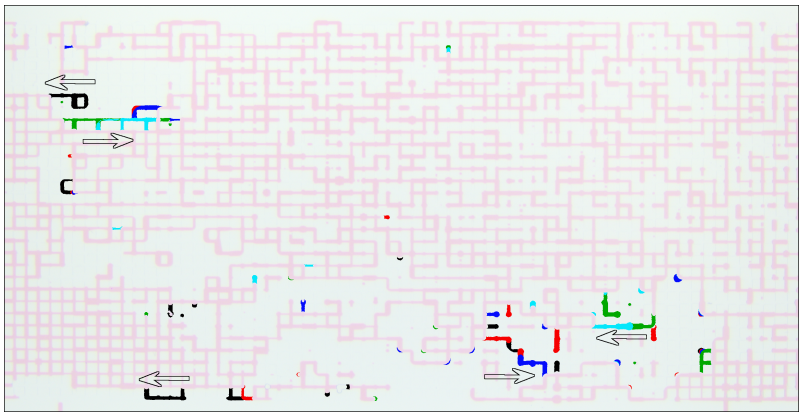

(a)

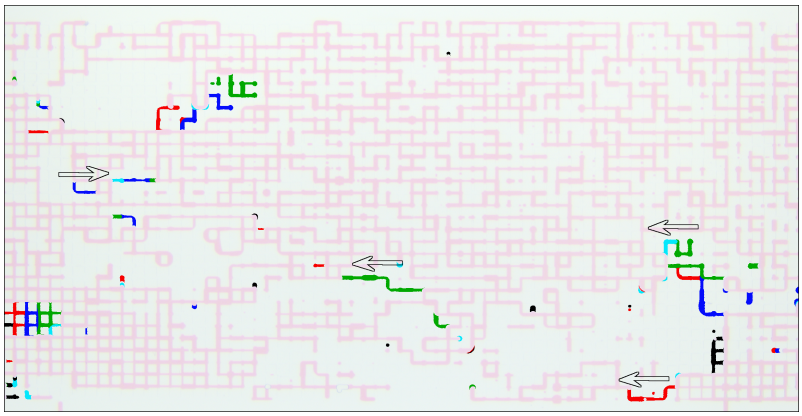

(b)

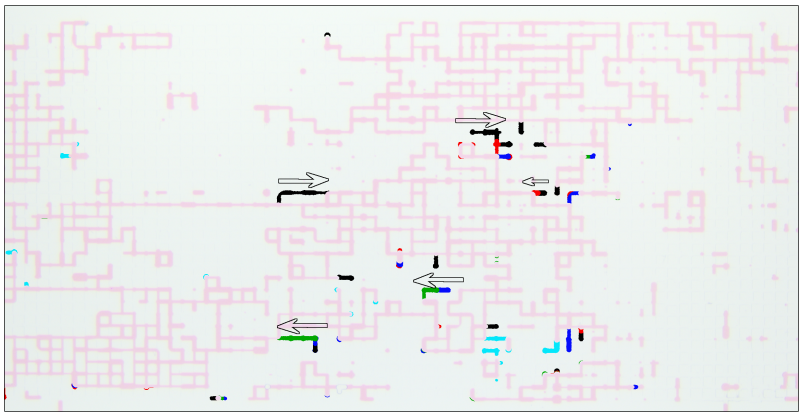

(c)

Figure 5.16: Sequential images of the hydrophilic micromodel with 6% w/v NaCl background salinity, flooded with 6% w/v NaCl brine solution of 10 ± 1 mM SDS and 5.4 ± 0.1 wt% butan-1-ol at 0.4 µL.min^{-1}. Images taken at (a) 0.01 PV, (b) 0.03 PV, and (c) 0.24 PV, over periods of 60 seconds. Flow direction from left to right. Immobile oil during this period has a faint colour; bright colours highlight the channels where oil was displaced. The arrows point to the direction of displacement. A colour-code breaks up the 60-second period into five time-intervals: red (0 to 12 s), black (12 to 24 s), blue (24 to 36 s), green (36 to 48 s) and cyan (48 to 60 s).

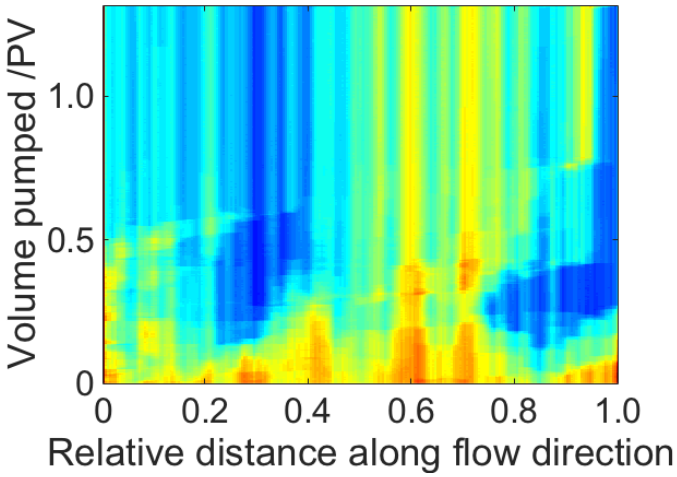

Figure 5.17: Saturation scan derived from the flood of the hydrophilic micromodel. Micromodel initially filled with dodecane with 6% w/v NaCl background salinity.

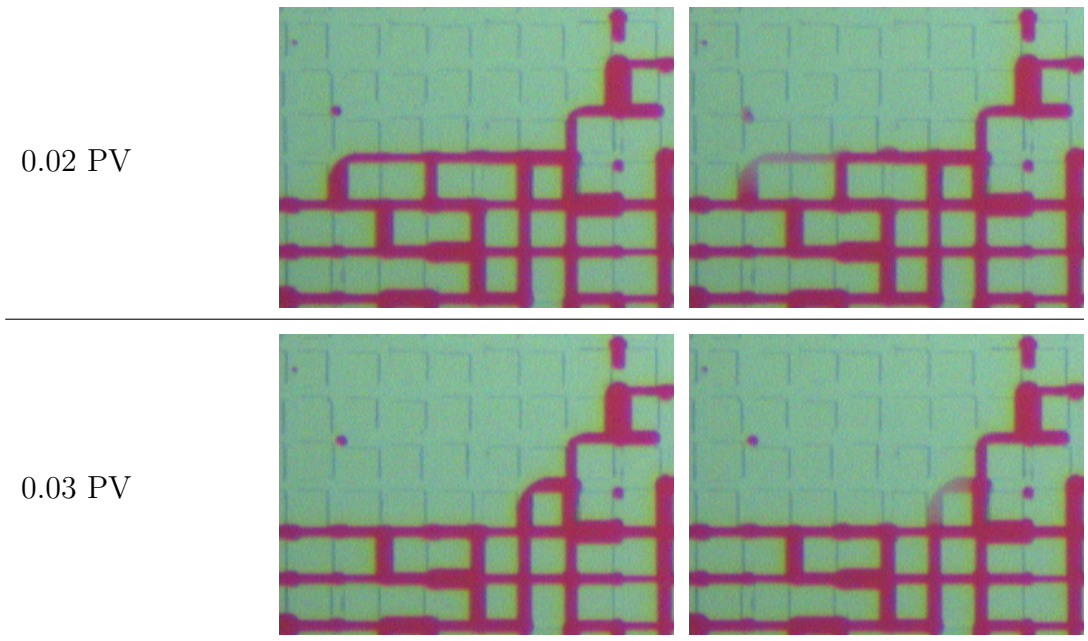

Figure 5.18: Two sets of successive images in the first quarter of the micromodel (time difference between two successive images was 2.5 s) taken during the flood, at 0.02 PV, and 0.03 PV.

micromodel had no background salinity, i.e. it had been pre-filled with Milli-Q water before dodecane was pushed through the model. The initial oil saturation was higher (72%), resulting in an initially more connected oil network than in the previous (6% w/v NaCl pre-filled) hydrophilic micromodel, see Figure 5.19 (a). Oil movement against the flow direction was observed locally once at 0.45 PV, i.e. when approaching the final oil recovery. Initially, and during most of the flood duration, oil was connected to the exit: a continuous path of oil existed through the horizontal channels; in addition, images of the micromodel during this flood were recorded less frequently (every 30 seconds compared to every 2.5 seconds in the flood of the hydrophilic micromodel with 6% w/v NaCl background salinity). Both factors hindered the tracking of the directions of local oil-displacements. A flow front was more distinguishable than during the flood of the hydrophilic micromodel with 6% w/v NaCl background salinity, see Figure 5.20. Eventually, 68% of the oil originally in place was recovered.

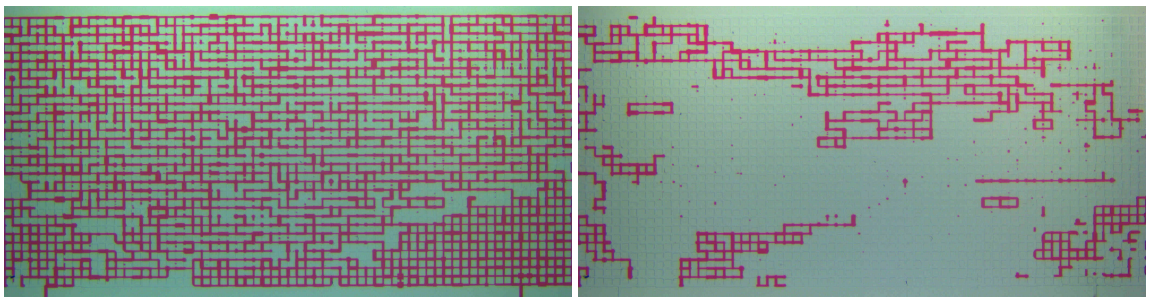

(a) (b)

Figure 5.19: Images of a hydrophilic micromodel initially filled with dodecane with no background salinity (a) before the flood and (b) at the end of the surfactant-and-alcohol flood (1.3 PV). Flood direction from left to right.

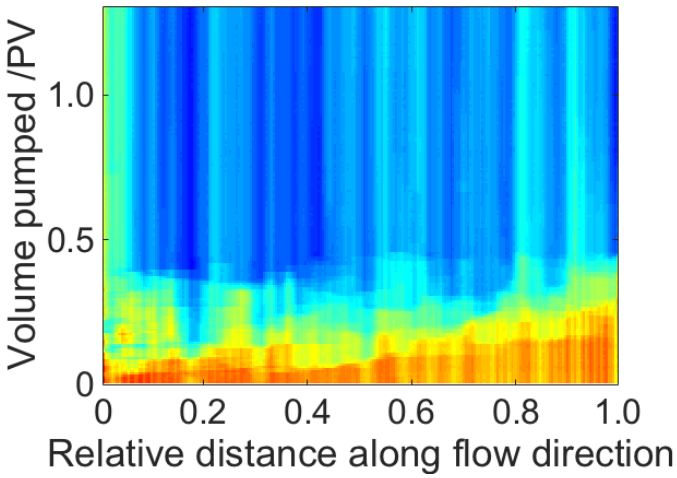

Figure 5.20: Saturation scan derived from the flood of the hydrophilic micromodel. Micromodel initially filled with dodecane with 6% w/v NaCl background salinity.

5.5. Discussion

5.5.1. Pink phase

Observed pink phase

During flooding of the hydrophobic micromodel, initially containing dodecane enriched in butan-1-ol (6.9 wt%), with a 6% w/v NaCl brine solution of 137 mM SDS and 6.3 wt% butan-1-ol, the oil was initially displaced without the presence of a middle phase at the pore scale and the oil was completely desaturated in the bottom left-hand corner of the micromodel (see Figure 5.21).

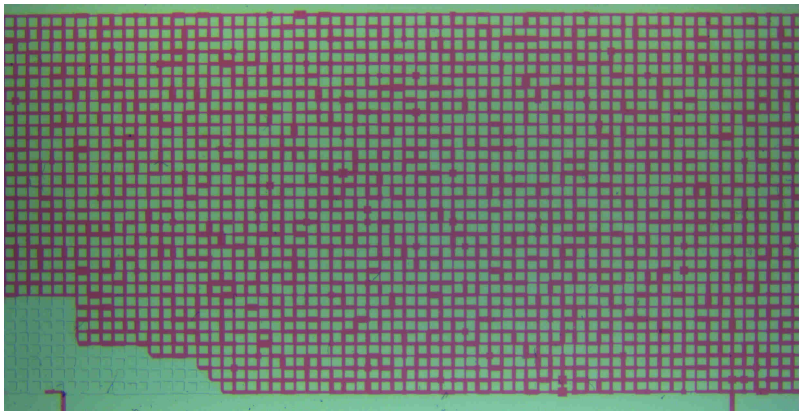

Figure 5.21: Desaturation of oil in the micromodel at 0.04 PV. Flood direction from left to right at 0.1 µL.min^{-1}.

After 0.04 PV, the lighter pink phase appeared for the first time at the edge of the field of view of the micromodel, near the oil that had not been mobilised, i.e. not at the moving front. During the rest of the flood, the most advanced position of the oil front continued to progress without the presence of a middle phase at the interface with a complete desaturation of the pores; further back, areas of light pink phase developed at or near the oil-flood interface (see Figure 5.22).

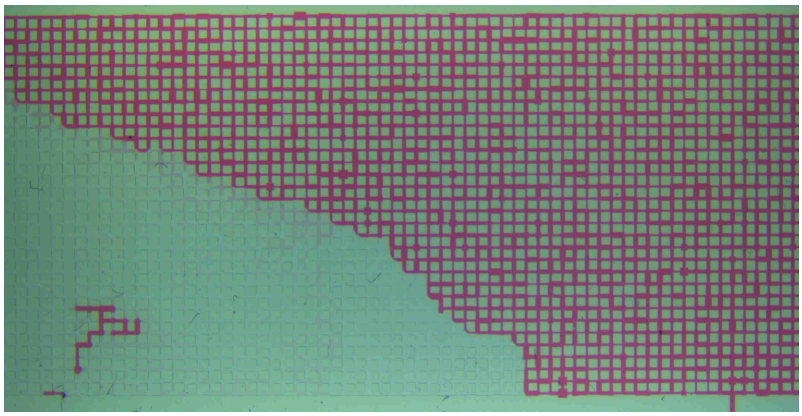

Figure 5.22: Desaturation of oil in the micromodel at 0.34 PV. Flood direction from left to right at 0.1 µL.min^{-1}.

The contact angles between the three phases could be assessed by taking a closer look at the micromodel during the flood, see Figure 5.23. When the oil-pink phase interface was pinned at the corners of a channel intersection, the interface had no curvature. However, Figure 5.23 shows that the pink phase wetted the walls of channels imbibed with the dodecane enriched in butan-1-ol (6.9 wt%) constituting the oil phase, and wetted the channels imbibed with the flood solution. Finally, Figure 5.23 highlights that the pink phase existed at, and away from, the oil interface.

No pink phase was observed during the floods of the hydrophobic micromodels initially containing dodecane, with 6% w/v NaCl brine solutions of

- 0.5 mM SDS and 5.3 wt% butan-1-ol,

- 71 ± 4 mM SDS and 5.7 ± 0.3 wt% butan-1-ol, and

- 137 mM SDS and 6.3 wt% butan-1-ol.

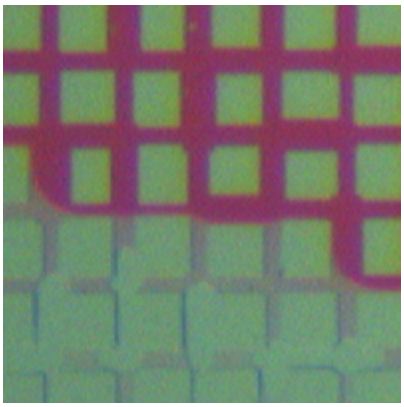

Figure 5.23: Zoomed area of the hydrophobic micromodel where the pink phase coexists with the oil phase and the flood solution, at 0.42 PV.

During flooding of the hydrophilic micromodel with 6% w/v NaCl background salinity and initially containing dodecane, with a 6% w/v NaCl brine solution of 10 ±0.1 mM SDS and 5.4 ± 0.1 wt% butan-1-ol, the pink phase was observed locally twice at the beginning of the flood. The pink phase developed at the corner of an intersection schematically represented in Figure 5.24. In the hydrophilic micromodel, the pink phase did not wet the walls imbibed with flood solution. In the images of the micromodels where the pink phase was observed, the contact angle between the oil phase and the pink phase could not be clearly assessed because the interface was either pinned at the corners of an intersection or the interface was blurred.

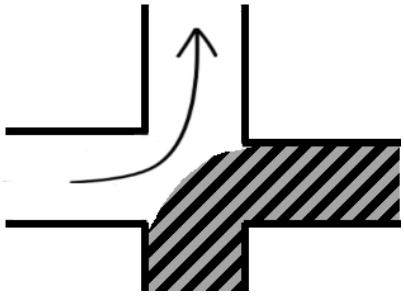

Figure 5.24: Schematic representation of the location of the observation of the development of the pink phase during the flood of the hydrophilic micromodel. The hatch area is the oil phase which became a light pink phase before being displaced. The arrow represents the supposed flow path of the flood solution.

Finally, no pink phase was observed during the flood of the hydrophilic micromodel with no background salinity.

Phase behaviour

To dislodge one pore volume of oil, at least one pore volume of surfactant solution must be pumped (volume conservation). It is thus reasonable to mix one volume of oil and one volume of surfactant solution to assess the phase diagram resulting from the flood. This procedure is a common practice in the oil industry to screen and select surfactants for flood formulations. The phase behaviours observed in two hydrophobic micromodels during the floods with the 6% w/v NaCl brine solution of 137 mM SDS and 6.3 wt% butan-1-ol were reproduced in test tubes, see Figure 5.25. No third phase developed when the micromodel was initially saturated with dodecane, but a third phase developed in the second micromodel when the flood solution was displacing dodecane enriched in butan-1-ol at 6.9 wt%. Similarly in the test tubes, the phase behaviour was that of an L1 system when the oil was pure dodecane, and that of an L3 system when the dodecane was enriched in butan-1-ol at 6.9 wt%.

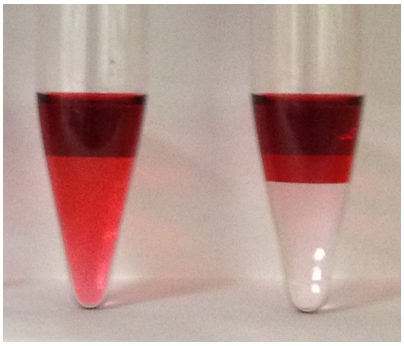

Figure 5.25: Microemulsions prepared with 6% w/v NaCl brine solution of 137 mM SDS and 6.3 wt% butan-1-ol and equal volume part of dodecane (left-hand side test tube) and dodecane enriched in butan-1-ol at 6.9 wt% (right-hand side test tube).

In the same way, the phase behaviour observed during the flooding of the hydrophobic micromodel with a 6% w/v NaCl brine solution of 74 $\pm$ 4 mM SDS and 5.7 $\pm$ 0.3 wt% butan-1-ol was reproduced in a test tube (see Figure 5.26). No middle phase was observed at the pore scale during the flood and the 1:1 v:v mixture of the flood solution to pure dodecane in a test tube presented an L1 behaviour.

During the flood of a micromodel, the oil phase may be in contact with the flood solution within the length of a pore. In this case, only the SDS and butan-1-ol of

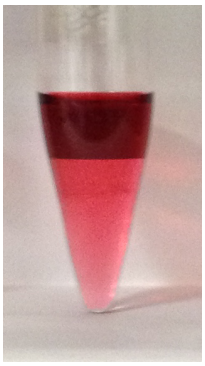

Figure 5.26: Microemulsion prepared with a 1:1 v:v mixture of 71 ± 4 mM SDS and 5.7 ± 0.3 wt% butan-1-ol to dodecane.

the water phase that are within a diffusion length of the oil-water interface are put to contribution to form a middle phase with the volume of the oil phase that is also within a diffusion length of the interface. In this case, the equivolume mixture of the oil phase and the flood solution prepared in test tube is representative of the phase behaviour that may develop at the oil-water interface during the flood.

As observed during the floods presented in the chapter, it is common for the oil-water interface to be at the intersection of two channels. Figure 5.24 represents such case. In this instance, the aqueous butan-1-ol within a diffusion length of the interface is constantly renewed by the flow of fresh flood solution circulating by the oil. The phase behaviour that may develop at the interface is thus better represented by mixing the oil with an excess of aqueous phase, rather than with a 1:1 v:v mixture. To illustrate the point that the phase behaviour at the oil-water interface may depend on the local geometry, mixtures of brine solutions of SDS and butan-1-ol and dodecane were prepared in NMR tubes with 10:1 v:v mixtures of aqueous phase to dodecane. The use of NMR tubes allowed the visualisation of middle phase volume as low as 2 µL (see Chapter Continuum scale). The aqueous solutions prepared were 6% w/v NaCl brine solutions of

- 5 mM SDS and 3.5 wt% butan-1-ol,

- 10 mM SDS and 4.0 wt% butan-1-ol,

- 71 mM SDS and 6.0 wt% butan-1-ol, and

- 137 mM SDS and 6.3 wt% butan-1-ol.

The formulations were also prepared with equivolume of aqueous phase to dodecane for comparison (see example in Figure 5.27). The results were gathered in Figure 5.28 (black points), where the data points obtained from the pseudo-ternary phase diagram in Chapter Continuum scale are also presented (green-circles points).

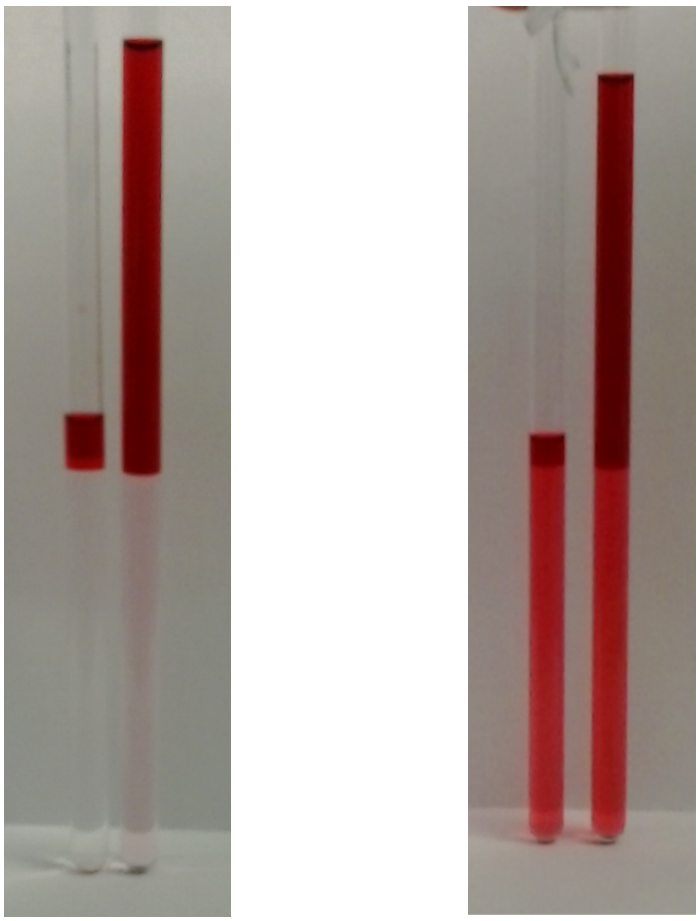

(a) (b)

Figure 5.27: Microemulsions prepared with 6% w/v NaCl brine solution of (a) 10 mM SDS and 4.0 wt% butan-1-ol, (b) 137 mM SDS and 6.3 wt% butan-1-ol, mixed with dodecane in 10:1 v:v (left tubes in (a) and (b)) and 1:1 v:v (right tubes in (a) and (b)) ratio of aqueous phase to dodecane.

The formulations prepared with brine solutions of high SDS concentrations (137 mM SDS and 6.3 wt% butan-1-ol, and 71 mM SDS and 6.0 wt% butan-1-ol) showed an L1 behaviour for both 10:1 and 1:1 v:v ratios of flood solution to dodecane. On the other hand, the formulations prepared with brine solutions less concentrated

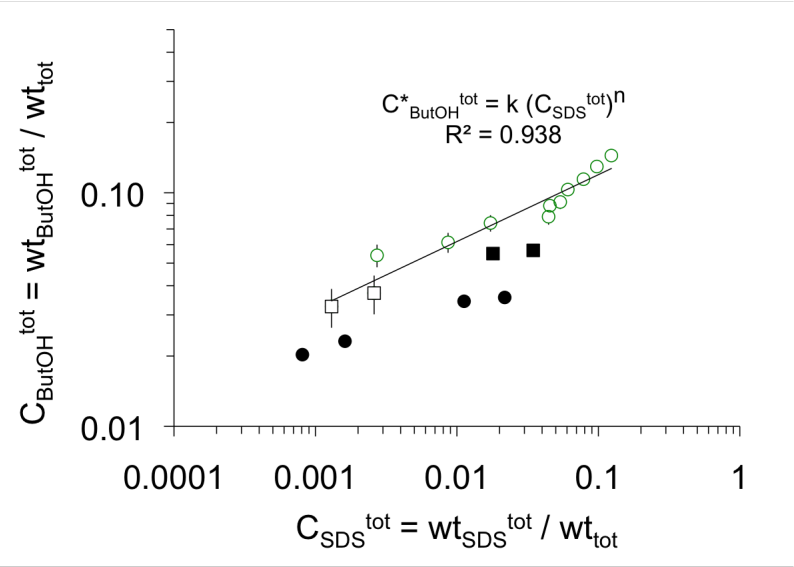

Figure 5.28: Phase behaviours of microemulsions prepared from 1:1 v:v (circles) and 10:1 v:v (squares) mixtures of 6% w/v NaCl brine solutions of SDS and butan-1-ol to dodecane. L1 microemulsions shown with filled symbols, L3 microemulsions shown with empty symbols. Green empty circles are data points obtained from the pseudo-ternary phase diagram in Chapter Continuum. The line is the power law of the minimal butan-1-ol concentration $C^{*\,tot}_{ButOH}$ needed to obtain an L3 behaviour as a function of SDS concentration C^{tot}_{SDS}, with $k = 0.25 \pm 0.02$ and $n = 0.31 \pm 0.04$.

in SDS (10 mM SDS and 4.0 wt% butan-1-ol and 5 mM SDS and 3.5 wt% butan-1-ol) showed an L3 behaviour when prepared from 10:1 v:v mixtures of aqueous solutions to dodecane, and L1 with 1:1 v:v mixtures. These phase behaviours correlates with the observation of the local development of a middle phase during the flooding of the hydrophilic micromodel with a 6% w/v NaCl brine solution of 10 ±0.1 mM SDS and 5.4 ± 0.1 wt% butan-1-ol and the absence of such observation during the flooding of the hydrophobic micromodels filled with butan-1-ol with brine solutions of high SDS concentrations.

However, given the power-law relationship between the SDS concentration in the formulation and the minimum butan-1-ol concentration to give an L3 behaviour, one would have expected to observe locally the formation of a middle phase during the flooding of the micromodel with the brine solution of 0.5 mM SDS and 5.3 wt% butan-1-ol, which was not the case. During this flood, the amount of SDS adsorbed on the walls was non-negligible compared to the low SDS content of the

flood. Considering a maximum adsorption on water-solid interface of 3.2 mol.cm^{-2} [Tajima et al., 1970], 70% of the SDS in the flood solution could be adsorbed onto the walls. At the moving flood front, it is possible that the concentration of SDS was thus below the cmc (0.13 mM SDS in 6% w/v NaCl brine) rendering the formation of a middle phase impossible. More generally, flooding is a dynamic process, and at low concentrations of components, concentrations may deviate significantly from equilibrium because of local depletion. Local interfacial tension and phase behaviour may thus not be the same as observed in equilibrium studies.

Middle phase and oil desaturation in hydrophobic micromodels

The results of the floodings of the hydrophobic micromodels were grouped in a desaturation curve in Figure 5.29 where the residual oil saturations are plotted as a function of the capillary numbers. The percentage of oil recovered from hydrophobic micromodels initially saturated in oil phase increased with increasing capillary number.

The largest oil recovery was obtained with the flood of the hydrophobic micromodel initially filled with dodecane, with a 6% w/v NaCl brine solution of 71 ± 4 mM SDS and 5.7 ± 0.3 wt% butan-1-ol at 0.4 µL.min^{-1}. The residual oil was 6% at 1 PV. During this experiment, the oil was displaced without the observation of a middle phase at the pore scale and the oil did not wet the walls of the micromodels, see Figure 5.30. These observations suggest that a complete oil desaturation of the micromodel was obtained without the solubilisation of the oil phase in a middle phase. With the same surfactant flood, a large area of oil at the top right-hand corner of the micromodel was by-passed when the flood solution was pumped at 0.1 µL.min^{-1}, resulting in a lower oil recovery of 82.5% at 1 PV.

The largest capillary number was calculated for the flood of the hydrophobic micromodel initially filled with dodecane enriched in butan-1-ol (6.9 wt%) with a 6% w/v NaCl brine solution of 137 mM SDS and 6.3 wt% butan-1-ol. The flood did not progress at the same speed across the width of the micromodel: the flood progressed faster in the bottom half of the micromodel. At the most

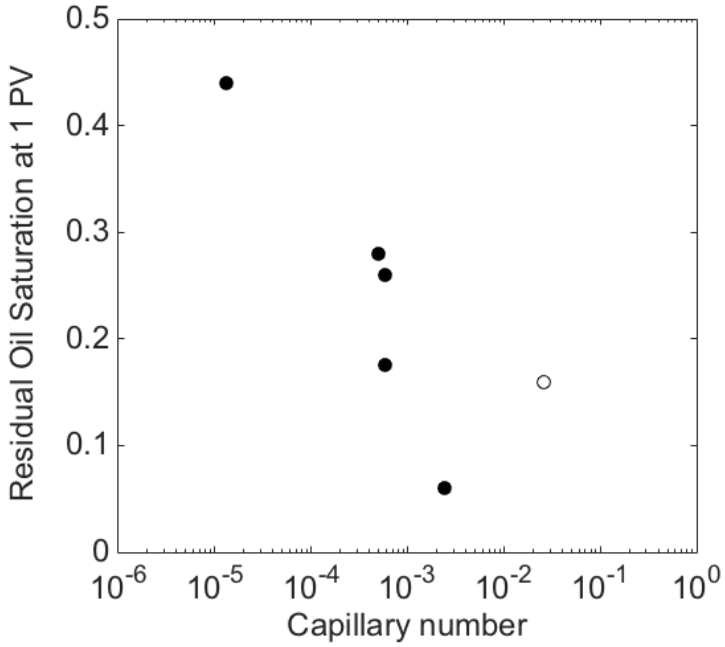

Figure 5.29: Residual oil saturations (1-water saturations) obtained for the floods of hydrophobic micromodels at 1 PV as a function of their capillary numbers. Filled symbols: the 1:1 v:v mixtures of oil phase to flood solution showed a L1 behaviour, with no middle phase. Empty symbol: the 1:1 v:v mixture showed a L3 behaviour; interfacial tension measured between the oil phase and the middle phase.

(a) (b)

Figure 5.30: Dodecane displaced without the observation of middle phase at the pore scale during flood with a 6% w/v NaCl brine solution of 71 ± 4 mM SDS and 5.7 ± 0.3 wt% butan-1-ol, examples at (a) 0.29 PV and (b) 0.40 PV.

advanced position of the oil front, the micromodel was desaturated in oil without the observation at the pore scale of a middle phase at the oil interface. In this case, the oil phase did not wet the walls of the micromodel, see Figure 5.31. On the other hand, the observed middle phase, at the rearmost flood front, did wet the walls of the micromodel, see Figure 5.23. Thus, one cannot attribute the complete oil desaturation of the micromodel at the foremost position of the oil flood to the presence of a middle phase of very small volume which was be observable under the experimental conditions, because the observed contact angles were not consistent with this hypothesis. The displacement of the oil located at the top-half of the micromodel contrasts with that of the flood previously mentioned where an entire area at the top-half of the micromodel was by-passed. In the latter flood, the by-passed area was not mobilised. In the micromodel filled with dodecane enriched in butan-1-ol, the oil recovery at 1 PV was similar to that of the flood with the by-passed area, i.e. 84%. However, in the micromodel filled with dodecane enriched in butan-1-ol, the oil would be eventually recovered through the solubilisation of the oil in the pink phase. With a constant recovery rate, the micromodel would have been completely desaturated (i.e. no oil left in the micromodel) after 1.3 PV of flood solution pumped into the micromodel.

(a) (b)

Figure 5.31: Dodecane displaced without the observation of middle phase at the pore scale during flood with a 6% w/v NaCl brine solution of 137 mM SDS and 6.3 wt% butan-1-ol, examples at (a) 0.12 PV and (b) 0.15 PV.

To conclude, the pore scale study with the hydrophobic micromodels highlighted that similar oil recovery was obtained with flood solutions less concentrated in surfactant. The accessibility of butan-1-ol to partition to the oil phase was reduced in the flood solutions more concentrated in SDS because butan-1-ol coadsorbed in

SDS micelles and was solubilised in them. This result pointed out that the cost of a surfactant flood could be reduced by decreasing the amount of surfactant while maintaining the flood performance. Finally, the solubilisation of oil in a middle phase was shown not to be an essential condition to displace an oil bank through a pore network without leaving oil blobs behind (i.e. complete oil desaturation).

5.5.2. Oil migration against the flood

The movements of oil opposed to the flow direction during the flooding of the hydrophilic micromodel with 6% w/v NaCl salinity background were unexpected and demand some explanation.

The displacement of oil occurs because of a pressure gradient. Let us consider first the simple case of a hydrophobic pore presented in Figure 5.32. Oil is displaced from a location when the difference between the local pressures in the non-wetting (aqueous) and wetting (oleic) phases, $p_{aq,i} - p_{oil,i}$, is smaller than a local threshold pressure, given by the expression of the local capillary pressure

$$p_{c,i} = \frac{2\gamma_i \ cos\theta}{r} \tag{5.2}$$

where γ_i is the local interfacial tension, θ is the contact angle measured through the wetting (oleic) phase and r the radius of the locus i.

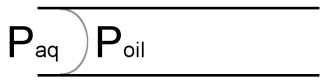

Figure 5.32: Schematic representation of a pore where oil is the wetting phase.

During the flooding of a micromodel, displacement of oil stems from a combination of the viscous and capillary effects during the surfactant flood. First, we take into consideration only the viscous effect of the flood for the simple case presented in Figure 5.32. With an aqueous phase injected into the micromodel on the left, displacement occurs from left to right when the pressure p_{aq} exceeds a threshold pressure $p_{aq} > p_{oil} + \frac{2\gamma \ cos\theta}{a}$.

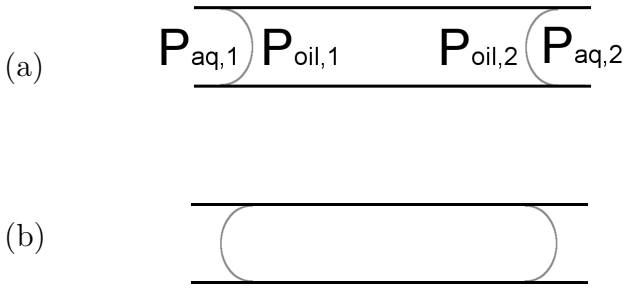

Figure 5.33: Schematic representations of an oil ganglion in a pore, where (a) oil is the wetting phase, (b) the aqueous phase is the wetting phase.

As the flood progresses, the continuous oil bank may disconnect into oil ganglia, schematically represented in Figure 5.33 for two wettablity cases, where (a) the pore is hydrophobic, (b) the pore is hydrophilic. Let us now consider a potential consequence of the capillary effects of the flood: the reduction of interfacial tension due to the presence of surfactant. Surfactant is present in the aqueous phase, which is injected on the left hand-side of these schematic representations. The local interfacial tension γ_1 is thus smaller than γ_2, hence, the local capillary pressure

$$p_{c,1} < p_{c,2}. \tag{5.3}$$

In the case (a) of Figure 5.33, the oil is the wetting phase and the local capillary pressure at the locus i is thus expressed as

$$p_{aq,i} - p_{oil,i}. \tag{5.4}$$

Considering a pore opened at both ends,

$$p_{aq,1} = p_{aq,2}, \tag{5.5}$$

leading to

$$p_{oil,1} > p_{oil,2}, \tag{5.6}$$

resulting in a displacement from left to right.

On the other hand in the case (b), where the oil phase is not wetting the pore wall, the capillary pressure is

$$p_{oil,\ i} - p_{aq,\ i}, \tag{5.7}$$

resulting in

$$p_{oil,\ 1} < p_{oil,\ 2}, \tag{5.8}$$

and a displacement from right to left, i.e. against the net direction of flow. These results were observed experimentally, [Piroird et al., 2011].

In the case of the flooding of a hydrophilic micromodel, a right-to-left displacement of an oil ganglion, i.e. in the direction opposed to that of the injected flood solution, could occur if the pressure gradient stemming from the interfacial-tension asymmetry of the oil ganglion's interfaces was larger than the pressure gradient resulting from the injected flood solution. The flood solution was driven into the micromodel at a constant injection rate. The pressure gradient can be calculated from a macroscopic law, such as Poiseuille's law

$$Q = \frac{\Delta p\ \pi\ r^4}{8\ L\ \mu}, \tag{5.9}$$

relating the flow Q to the pressure gradient Δp applied on a liquid of viscosity μ across a tube of length L and of radius r.

The pressure gradient can be estimated with Equation 5.9. For a tube of diameter 100 µm, with a flow rate of 0.1 µL.min^{-1}, the pressure gradient over a length of 1 mm is 4.3 $\times$ 10^6 Pa. The flow a pore may be significantly lower, lowering the pressure gradient.

It should be noted, that in the case where micromodels are fully saturated with oil, the imbalance of surfactant concentration and hence interfacial tension across a ganglion is very unlikely to occur, and such counter-flood oil displacement correspondingly unlikely to be observed.

5.6. Conclusion

This chapter highlighted the evolution of the oil-water interface in a network of pores during the displacement of oil by an aqueous surfactant flood using micromodels. The formulations of the floods were chosen to investigate a range of SDS concentrations. The alteration of the wettability of a hydrophobic micromodel to water-wet was observed during the flood of a hydrophobic micromodel with a brine solution of 0.5 mM SDS and 5.3 wt% butan-1-ol. This low-concentration flood (SDS was less than 5 times the cmc) recovered nearly as much oil as a highly concentrated flood of surfactant (more than 1000 times the cmc) and 6.3 wt% butan-1-ol. The development of a third-phase at the scale of the micromodel was only observed when the oil phase was enriched in butan-1-ol. Furthermore, the largest oil recovery at 1 PV (94%) was obtained without the solubilisation of the oil bank in a third phase. This results highlighted that the solubilisation of oil in a middle phase is not an essential condition to displace an oil bank through a pore network without leaving oil blobs behind (i.e. complete oil desaturation). Furthermore, this result highlighted the importance of the local phase behaviour, i.e. at the pore scale, with respect to the phase behaviours observed in test tubes during preliminary tests. Finally the use of the micromodels enabled visualisation of unexpected local flow during the flooding of hydrophilic micromodels, namely oil displacement against the flow direction.

The micromodels used in this chapter were initially fully saturated with oil; the experiments were thus representative of surfactant floods sweeping rock regions completely by-passed by water floods, which commonly precede enhanced oil recovery. The micromodels did not have dead-end pores. It would be interesting to repeat the floodings of the hydrophilic micromodels with dead-end pores and link the observations to the investigation of Chapter Fracture scale on the non-uniform adsorption of surfactant and alcohol at the interface of non-wetting oil drops.

Chapter 6

Molecular scale

6.1. Introduction

Surfactant EOR relies principally on the decrease of the interfacial tension between crude oil and the flood solution to diminish the capillary pressure of pore throats where oil ganglia are held in place after water-flooding. A decrease of the interfacial tension by a 1000 fold, down to 0.01 $mN.m^{-1}$ or less, is conventionally seen as necessary to dislodge the trapped oil with the viscous forces applied by the moving flood, typically at a velocity of a pore per second. The formation of microemulsion or middle phase between the oil and the flood underwrites ultra-low interfacial tension. Understanding the formation of these phases in-situ and their evolution with time is important because they affect the flood, and eventually the recovery of oil, by locally diminishing, sometimes substantially, the interfacial tension, modifying contact angles, and potentially locally increasing the viscosity.

The formation of middle phase can be observed visually during the floodings of networks of pores in microfluidic devices (see Chapter Pore Scale, [Howe et al., 2015]), or in a T-junction ([Unsal et al., 2016]); however, these methods offer a limited amount of information. First, the presence of a middle phase was only localised when its volume was substantial (a few microliters). Furthermore, these methods did not inform on the local concentration of surfactant and cosurfactant. Finally, in the case of the network of pores, because the

oil-water interface was mobile, the phenomena observed were influenced by local geometries. By using a simpler geometry, a flat oil-water interface, the formation of microemulsion can be studied independently of geometric constraints. The adsorption of surfactant at the oil-water interface can be followed dynamically by ellipsometry. Surfactant adsorption modifies the dielectric profile of the oil-water interface and hence changes the reflection properties as encompassed by the ellipticity. Furthermore, the evolution of the thickness between the oil and water can be related to the change of the ellipticity by using a three-layer model [Azzam and Bashara, 1977].

This chapter presents the development of a methodology to study the formation of microemulsion at the oil-water interface by ellipsometry. For this purpose, the flow cell developed by Curwen et al., originally designed for the study of adsorption at the liquid-solid interface [Curwen et al., 2007], was adapted to liquid-liquid interface. First, the flow cell was tested for surfactant adsorption without cosurfactant. Solutions which formed a middle phase in the micromodel in Chapter Pore Scale were then used in the flow cell.

The exploration related in the chapter highlights the challenges of probing the oil-water interface with a laser while forming a middle phase. First, pinning of the interface was challenging because a microemulsion has inherently a high solubilisation power. Secondly, the flow rates accessible in the flow cell were limited in order to maintain a stable interface. Finally, these factors coupled with the complexity of the set-up made the generation of data challenging. Nonetheless, this chapter is a proof-of-concept study establishing ellipsometry as a suitable and informative tool to study the formation and evolution of microemulsion at the oil-water interface.

The remainder of this chapter is structured as follows. The design of the flow cell is reported before describing the methods of surface modification and typical procedure in the flow cell. After numerical simulation of concentration profiles in the flow cell, results are presented of adsorption at the oil-water interface in absence and presence of cosurfactant. Finally, alterations to the cell design are suggested to

tackle the challenges encountered.

6.2. Materials

Sodium dodecyl sulfate (SDS) (ACS grade > 99%, Sigma-Aldrich) was recrystallised three times in ethanol. Dodecane (99% pure, Acros Organics) was purified on silica gel and alumina. Butan-1-ol (ACS grade, Sigma-Aldrich) and sodium chloride (analytical reagent grade, Fisher) were used without further purification. Hydrogen peroxide (35 wt% solution in water, Acros Organics) and sulfuric acid (ACS reagent, 95-98%, Sigma-Aldrich) were used as received for piranha solution. Hexamethyldisilazane (98%, Alfa Aesar) was used as received for surface modification of the stainless steel. Hexane (> 95%, Sigma-Aldrich) and propan-2-ol (ACS reagent grade, Fisher) were used without further purification.

The flow cell was made of stainless steel and was manufactured by the mechanical workshop of Durham University. The neutral density (ND) filter, sourced from Thorlabs (1/2" diameter and 1.5 mm thick), had an optical density of 6 and was anti-reflection coated. The Dove prism, sourced from Thorlabs, was made of uncoated N-BK7, lateral windows measured 15 × 15 mm and the prism was 63.4-mm long. The lateral windows formed an angle of 45^o with the base of the prism. The top window of the Dove prism was polished using a Logitech LP50 flat plate polisher. The gaskets placed in the surfactant inlet and bottom plate recess were a silicone elastomer, 0.5-mm thick (sourced from Goodfellow Cambridge Ltd.). Connectors were in Teflon and supplied from Omnifit.

6.3. Design of the flow cell

The ellipsometry measurements at the oil-water interface were made in a flow cell which was adapted from the flow cell developed by Curwen et al. [Curwen et al., 2007]. The cell, which was originally designed to study adsorption kinetics at the solid-liquid interface, had two main features.

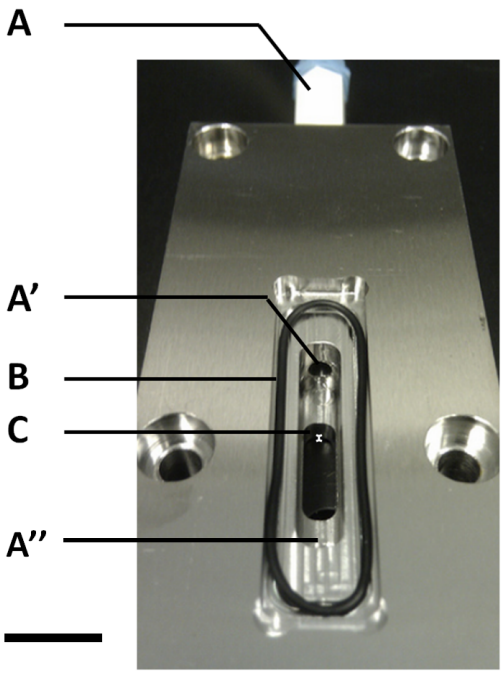

Figure 6.1: The top plate of the flow cell consists of a recess where the oil is introduced by the syringe inlet (A) through a channel (A'). A" points to the oil outlet. B is the O-ring that ensures the seal with the prism and C points to the 0.5-mm height of the aqueous channel, highlighted by a white cross. The top plate is drilled through on a length of 1.5 cm where the oil and water phases meet. The scale bar (1 cm) represents the horizontal scale at the centre of the image.

1. The design of the cell offered controlled hydrodynamic conditions, i.e. the surfactant was delivered to the interface of interest under controlled mass-transfer conditions.

2. The surfactant diffused through a shallow recess of water (0.5-mm deep) to allow measurements under diffusive conditions on a reasonable time-scale (of the order of hundreds of seconds). Under the flow conditions of the experiments of Curwen et al., surfactant reached about half-way of the channel, before diffusing to the interface in absence of flow [Curwen et al., 2007]. Under these conditions, the time for SDS to reach the probed interface would be $(0.25 \times\ 10^{-3})^2/4D = 17$ seconds with the micelle self-diffusion coefficient of SDS $D = 9.2 \times\ 10^{-10}$ m^2.s^{-1} [Stigter et al., 1955]).

The flow cell designed for this chapter was composed of four rectangular blocks of stainless steel assembled with screws. The top plate (Figure 6.1) hosted a recess of circa 5 cm^3. Two boreholes of 0.3-cm diameter connected the oil recess to the oil inlet and outlet. A groove was carved at the top of the oil recess into which an O-ring was placed. A Dove prism, pressed onto the O-ring, sealed the flow cell (see Figure 6.2). The recess was drilled through, over a rectangular surface of 1.5×0.7 cm,

where the oil and water phases met. At the shorter side of the aperture, the drill angle was altered to 45^o to sharpen the anchoring point of the oil-water interface and favour its pinning (see Figure 6.3).

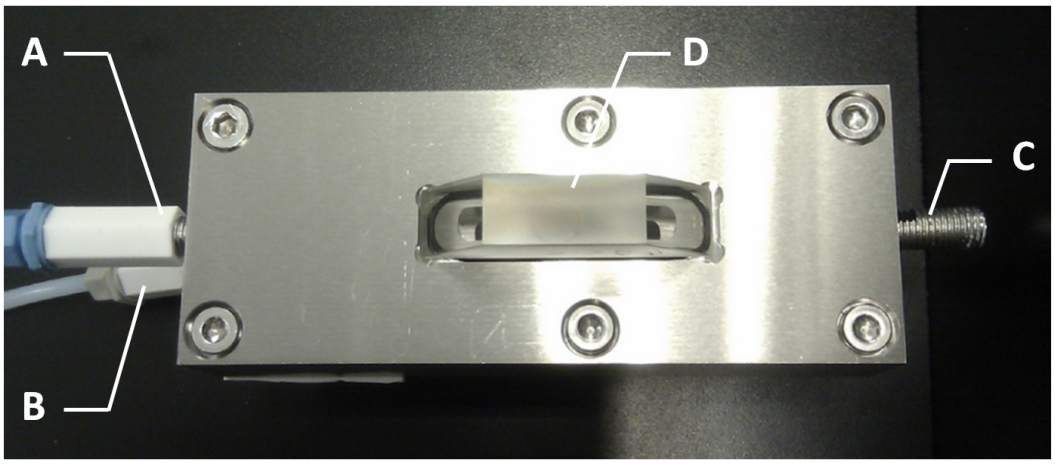

Figure 6.2: To seal the cell, the Dove prism (D) was clamped to the cell (clamps not shown in this picture). A and B point respectively to the inlets of the oil and surfactant solutions, C to the outlet.

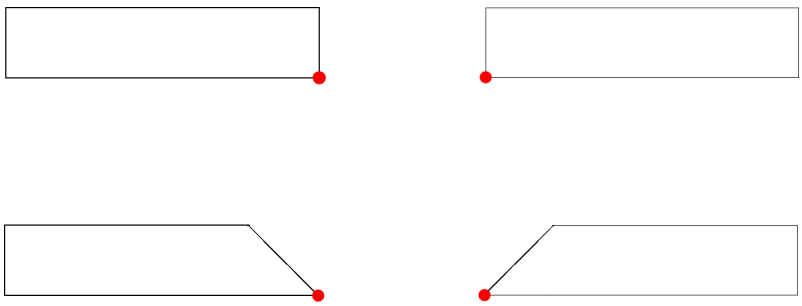

Figure 6.3: Not-to-scale schematic cross-section of the top plate. The pinning of the oil-water interface at the points highlighted with red dots is favoured by tapering the oil recess (bottom schema).

The bottom plate was composed of two blocks of stainless steel (see Figure 6.4). One side of the shorter block was indented over a length of 1 cm by 0.2 mm. The indentation created a 0.2-mm wide slit when the shorter block was attached to the second block constituting the bottom plate. A shallow recess (0.5-mm deep) ran across the bottom plate over a surface of 10×1.5 cm. At the two extremities of the recess, two small alcoves connected the 0.5-mm deep recess to the water inlet and outlet. Finally, an additional cavity was carved at the center of the shallow recess

to host the ND filter so that its surface aligned with the surface of the plate. A 0.5-mm thick gasket was placed around the shallow recess to provide a water-tight seal between the bottom and top plates.

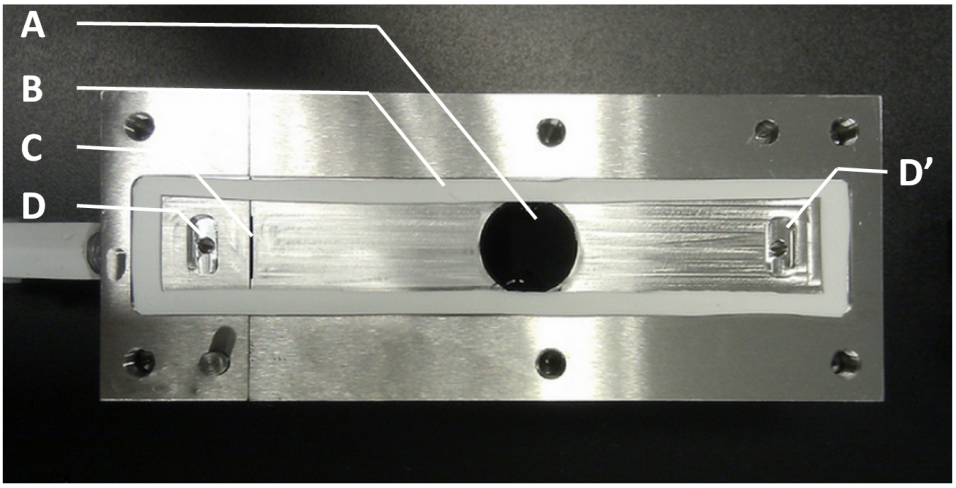

Figure 6.4: In the middle of the bottom plate of the flow cell a shallow well was drilled to place an ND filter (A) of high optical density in order to avoid scattering from the laser on the stainless steel; B points to the 0.5-mm thick gasket which ensures the seal between the bottom and top plates and defines the height of the channel; C points to the 0.2-mm wide slit for the surfactant solution inlet; and D and D' point to the two recesses for inlet of water and outlet, respectively.

The fourth block of the flow cell was attached below the bottom plate to connect the 0.2-mm slit to the surfactant inlet. A gasket ensured a water-tight seal between the surfactant-inlet plate and the bottom plate and guided the surfactant solution through the bore leading to the slit (see Figure 6.5).

Figure 6.6 shows a schematic representation of the assembled cell.

6.4. Methods

6.4.1. Ellipsometer

Measurements were made on a Picometer Ellipsometer (Beaglehole Instruments, NZ). The light source was a He-Ne laser of wavelength 632.9 nm. The instrument was a phase-modulated ellipsometer with a 50-kHz modulation frequency.

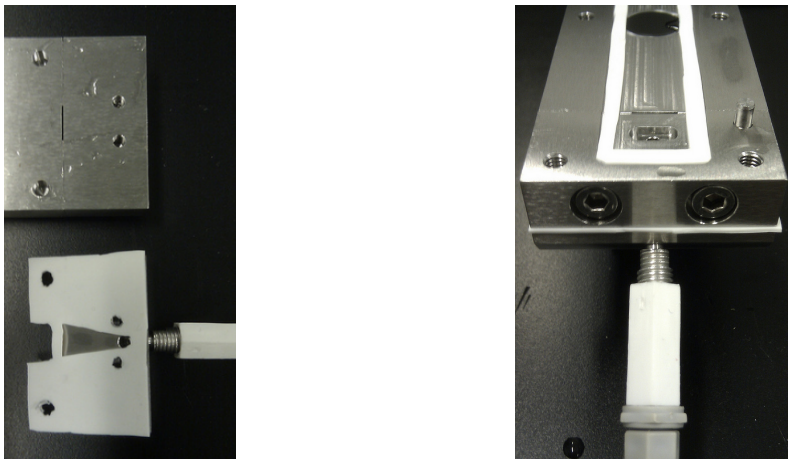

(a) (b)

Figure 6.5: (a) Bottom plate face down (top block) and surfactant-inlet plate with Teflon gasket (bottom block). (b) Surfactant plate assembled to the bottom plate.

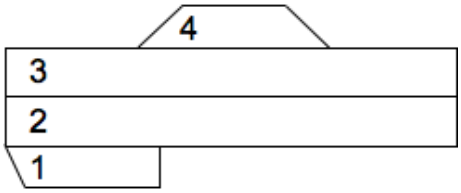

Figure 6.6: Not-to-scale schematic representation of the assembled flow cell: 1) Surfactant-inlet plate, 2) Bottom plate, 3) Top plate, and 4) Dove prism.

The measured parameters were the two harmonics of the phase-modulated ellipsometer collected at 50 and 100 kHz, noted respectively y and x. In the phase-modulated ellipsometer of Beaglehole used in this chapter, the two measured parameters are related to the real and imaginary parts of the ellipticity $\mathrm{Re}(\rho)$ and $\mathrm{Im}(\rho)$ (see Chapter Methods). The ellipticity ρ reflects the change in polarisation of light upon reflection at an interface. It is sensitive to changes at the interface which modify the dielectric profile of the oil-water interface, such as surfactant adsorption or increasing thickness interface. Near the Brewster angle (see definition in Chapter Methods), the signal variation upon interface modification is larger in $\mathrm{Im}(\rho)$, which is the variable presented in this chapter. At the Brewster angle, $\mathrm{Re}(\rho)$ is nil and $\mathrm{Im}(\rho)$ is equal to the coefficient of ellipticity $\overline{\rho}$. The coefficient of ellipticity is linked to the interfacial tension by an equation developed by Meunier [Meunier, 1987] (see Equation (6.1) in Chapter Methods). In addition, the thickness of the interface can be inferred from the ellipticity ρ by using the three-layer model developed by Azzam et al. [Azzam and Bashara, 1977].

In the static cell, measurements were made at the Brewster angle of the oil-water interface.

In the flow cell, the laser beam was incident on the window of the prism at 3^o from the normal of the window surface, unless stated otherwise, corresponding to an angle of incidence of 46^o from the normal at the oil-water interface. In this calculation, angles of refraction were obtained from Snell's law and the refractive indexes of air, the prism and dodecane were equal to 1.0000, 1.5148 and 1.42160, respectively. The sensitivity was set to 500 mV. The time constant was 0.1 s, the lock-in factor and the sampling factor were respectively set to 1 and 6. Finally the step was of 2 seconds. With these settings, during the first 0.1 second of each measurement, the system was idle, then readout occurred continuously during 0.6 second at the end of which signal was averaged.

6.4.2. Static cell

For static measurements, a concentric stainless steel cell (diameter of 3 cm) was used. The cell was mounted by a Teflon gasket (see Figure 6.7) to which the oil-water interface pinned. 3.5 mL of the aqueous phase was placed in the cell with a Pasteur pipette. Then 3.5 mL of the oleic phase was gently poured on top of the aqueous phase with a Pasteur pipette. Finally, a Dove prism, not represented in Figure 6.7, was placed within the indentations of the Teflon gasket made for this effect, to sit in contact with the oil. The cell was placed into a closed brass vessel which was thermostated at 20.0±0.2°C.

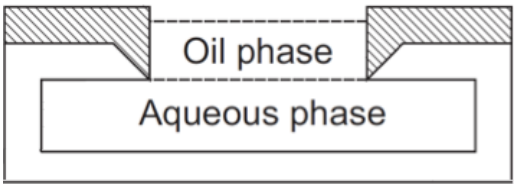

Figure 6.7: Not-to-scale schematic representation of the static cell. The hatched area represents the Teflon gasket. Adapted from [Day and Bain, 2007].

To align the cell, the surface supporting the cell was levelled by means of a tilt stage and vertical laser. Once the cell was placed on the levelled surface, the prism was levelled by adjusting the screws which tightened the Teflon gasket onto the stainless steel cell. Finally, the angle of the cell, with reference to the plane of incidence, was adjusted so that the reflection of the incident light onto the prism window was vertically aligned with the illumination arm pinhole.

6.4.3. Surface modification

Preliminary study

A preliminary study of surface modification was undertaken on 1-cm^2 pieces of stainless steel to find the appropriate surface modification of the flow cell which would facilitate the pinning of the oil-water interface. Hexamethyldisilazane was used for surface modification by direct contact.

A 1-cm^2 stainless steel piece was sonicated in a 1:1 v:v mixture of hexane to

propan-2-ol for 15 minutes. After the piece of metal was activated by a plasma of air for 10 minutes, it was dipped in a beaker filled with the silane for one hour. When using the plasma chamber, the plasma forward power was between 40 and 50 W and the reflected power never exceeded 5 W. The piece of metal was then sonicated for 15 minutes in toluene and dried with inert gas N_2. The piece was finally rinsed consecutively with acetone and water before being dried with inert gas. Contact angles were measured with First Ten Ångstroms F-100 tensiometer, in air and in the aqueous and oleic phases prepared by equilibrating butan-1-ol-saturated 6% w/v NaCl brine with equivolume of dodecane. The pieces of metal were rinsed with water and acetone, and dried with inert gas between contact-angle measurements.

Surface modification of the flow cell

The oil cavity of the top plate was sealed with a microscope slide attached to the base of the top plate. About 5 mL of hexamethyldisilazane was poured in the oil cavity. A small proportion of the solution ran by capillarity between the base of the top plate and the microscope slide. After one hour of contact, hexamethyldisilazane was removed and the top plate was rinsed with acetone and blown dry with inert gas. The bare stainless steel surface of the base of the top plate was recovered by plasma etching. Before placing the top plate in the plasma chamber, Teflon tape was pushed into the oil cavity to prevent etching of the modified surface of the oil cavity. The top plate was then placed in the plasma chamber with its base facing up. The plasma was turned on for 5 seconds to recover the hydrophilicity of the base of the top plate.

6.4.4. Flow cell

Preparation of the flow cell

Figure 6.8 shows the schematic set-up of the flow cell with the syringes connections. A Dove prism was pressed onto the top plate with 2 L-shaped Teflon pieces screwed to the top plate. The oil cavity sat within the top plate, while the water channel

ran between the top and bottom plate. The surfactant solution was introduced from the lower plate.

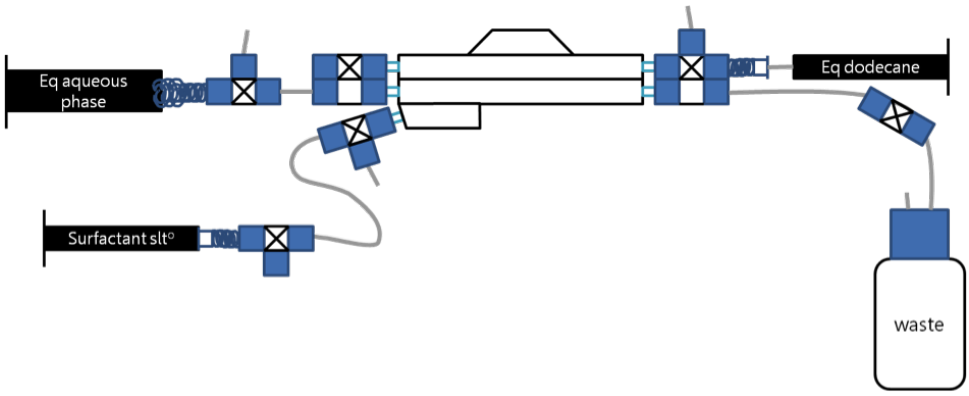

Figure 6.8: Not-to-scale schematic representation of the flow cell set-up.

The stainless steel pieces were dismantled and sonicated in a 1:1 v:v mixture of hexane to propan-2-ol for 15 minutes. Once taken out of the solution, inert gas was blown over the pieces to remove a large part of the solvent. The pieces were then placed in a plasma chamber. The chamber was evacuated for a couple of minutes before switching the plasma on. Stainless steel pieces were plasma-cleaned for 15 minutes. The surface was considered clean when Milli-Q water was completely wetting the surface (contact angle less than 5^o). This two-step cleaning process was repeated a second time if needed.

The Dove prism and ND filter (placed at the bottom of the water channel) were rinsed sequentially in chloroform, acetone and Milli-Q water. Finally, they were placed in a warm piranha solution (3:1 v:v mixture of H_2SO_4 to H_2O_2) for 30 minutes and rinsed 20 times with Milli-Q water. Syringes, tubings, connectors and O-rings were cleaned in a dilute solution of circa 1-2% Decon by sonication for 20 minutes. They were rinsed thoroughly with Milli-Q water. Tubings and connectors hosting the oil phase were first degreased with a 1:1 v:v mixture of hexane to propan-2-ol.

Assembling and filling of the cell The cell was assembled in stages. First the two pieces of the bottom plate were screwed together. The connectors and tubings were then connected to the plates. The surfactant-inlet plate was fixed to the bottom plate. The ND filter was placed in its recess and the Teflon gasket positioned around

the 0.5 mm-deep recess.

When the solutions used did not contain butan-1-ol, the bottom plate was wetted with a few drops of Milli-Q water to prevent trapped air in the 0.5 mm-deep recess. The top plate was screwed and sealed onto the bottom plate. Milli-Q water was gently pushed through the channel until a convex meniscus formed at the sharpened aperture of the base of the top plate. Inlet and outlet water connectors were then turned to their off positions. Oil was gently pushed through to fill the cavity of the top plate. The Dove prism was sealed onto the O-ring by two L-shaped Teflon pieces secured by four screws. The outlet of the oil tubing was opened to push through more oil and displace any air in the outlet borehole of the top plate. Once the oil connectors were turned off, the water connectors were opened to gently push water and displace air in the second half of the channel and in the outlet borehole of the bottom plate. Finally, water was pushed through the surfactant-inlet plate by turning off the water connectors, to displace air. The curvature of the oil-water interface was adjusted by gently pushing through an aliquot of oil and keeping the oil and surfactant inlets closed and the water connector open. Three-way connectors were placed after each syringe to facilitate the removal of air bubbles from the solutions before feeding them into the flow cell.

When the solutions contained butan-1-ol, the cell was first entirely filled with the oleic phase. Once the cell was sealed, the aqueous phase was pushed in the aqueous channel to displace the oleic phase (see relative wettabilities in Results section).

Alignment of the flow cell

First, the horizontality of the stage onto which the flow cell was placed was adjusted and verified with a spirit level. Once the flow cell was placed on top of the stage, the reflection of a vertical laser was used to assess the horizontality of the Dove prism. The level was adjusted using the four screws which were holding the two Teflon pieces securing the prism. The reflection of the incident light onto the prism window was aligned vertically with the illumination arm pinhole to align of the cell with the plane of incidence. The alignment of the flow cell was verified and adjusted

if necessary before each measurement.

Solution delivery into the flow cell

Syringe pumps (Harvard Apparatus Model 11plus and Razel Scientific Instruments Model A99) were used to control the fluid flow into the flow cell. The surfactant-free aqueous phase and surfactant solution were contained in a 50-mL and 25-mL gas-tight syringes (SGE Analytical Science), respectively. The oil was delivered by a 5-mL gas-tight syringe (SGE Analytical Science). Syringes were connected to the flow cell with PTFE tubing of 2-mm internal diameter.

Typical procedure

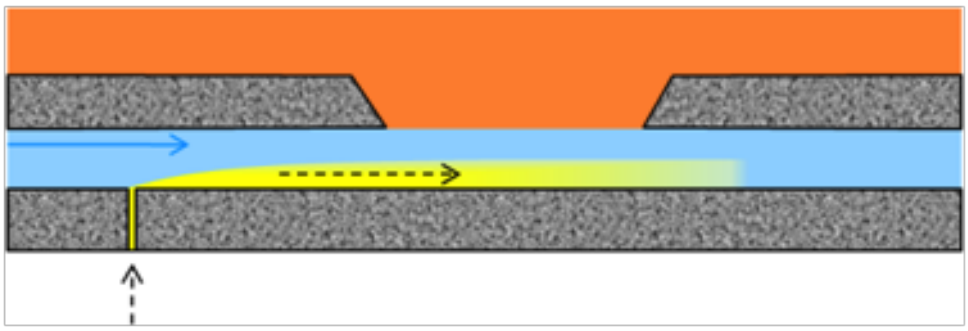

Figure 6.9: Not-to-scale schematic representation of flows in the 0.5-mm deep channel below the oil cavity. There is no flow in the oil, represented in orange. The water is represented in blue and the water flow with the blue arrow. The surfactant solution is represented in yellow and its flow with the dashed black arrows.

The oil phase (in orange in Figure 6.9) stayed immobile in the oil cavity. First, the water was delivered through the cell at 15 $mL.h^{-1}$, corresponding to an average linear velocity of 840 $\mu m.s^{-1}$ (blue arrow). While the water flow was still on, the surfactant solution (100 or 68 mM SDS, in yellow in Figure 6.9) was supplied for a few tens of seconds at 1 or 5 $mL.h^{-1}$ (black dashed arrows). The two syringe pumps were turned off at the same time. To desorb the surfactant from the oil-water interface, water was flushed through the cell at 15 $mL.h^{-1}$.

In the Results section, solid lines were used to show the time at which flow was turned on, dashed lines for turning off flows. Colour code was used to indicate which

solutions were pumped into the cell: green for surfactant solution, blue for water, black if both surfactant and water were turned on and/or off at the same time (see Figure 6.10).

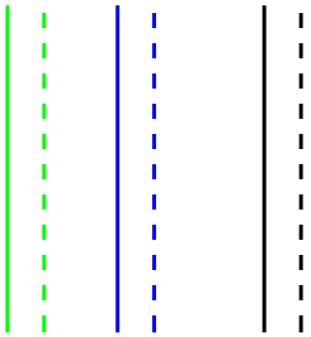

Figure 6.10: Solid (dashed) lines are used to point the time at which flow was turned on (off). Green lines relate to surfactant-solution flow, blue lines to water flow and black lines were used when surfactant and water flows were turned on and/or off at the same time.

6.4.5. Solution preparation

Solutions for equilibrium ellipticity measurements

A 1-L 6% w/v NaCl brine solution was saturated with butan-1-ol and equilibrated with 100 mL dodecane, previously filtered on silica gel and alumina. The resulting equilibrated phases contained respectively 4.3 wt% butan-1-ol in the aqueous phase and 8.1 wt% in the oleic phase. 0.288 g of recrystallised SDS was added to the equilibrated aqueous phase in a 100-mL volumetric flask to form a 100 mM SDS brine solution of 4.3 wt% butan-1-ol. A number of 4.3 wt% butan-1-ol brine solutions of SDS with concentration varying up to 3.7 mM SDS were prepared by dilution. The brine solutions of SDS and 4.3 wt% butan-1-ol (5 mL) were added to 5 mL of the equilibrated oleic phase in centrifuge tubes. The solutions were vigorously shaken by hand before being centrifuged for 10 minutes at 3000 rpm at 20^{o}C.

The upper and lower phases in the centrifuge tubes were then transferred in the static concentric cell.

Solutions for dynamic ellipticity measurements

0.490 g of recrystallised SDS was added to Milli-Q water in a 25-mL volumetric flask to form a 68 mM SDS solution. Dodecane was filtered on silica gel and alumina.

0.395 g recrystallised SDS were solubilised with circa 7 mL of Milli-Q water in a 10-mL volumetric flask; the solution was sonicated until surfactant solubilisation. Then, 0.6 g NaCl was added to the solution. The solution was sonicated in a warm water bath (45^{o}C) until the mixture was a transparent viscous solution. When the salt and SDS were solubilised, the volumetric flask was topped up to 10 mL with water. The 10 mL of the 6% w/v NaCl brine solution of 137 mM SDS were transferred in a glass vial where 900 µL (0.73 g) butan-1-ol were added to the solution. This procedure led to a 6% w/v NaCl brine solution of 137 mM SDS and 6.3 wt% butan-1-ol.

A 6.9 wt% butan-1-ol solution of dodecane was prepared by weight by mixing 20 g of dodecane filtered on silica gel and alumina and 1.48 g of butan-1-ol.

6.4.6. Simulation

Simulation of flow and concentration profiles in the flow cell were undertaken with Comsol Multiphysics software, CFD module. Figure 6.11 illustrates the mesh size used.

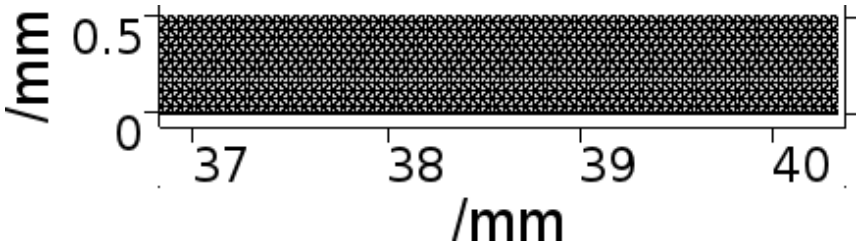

Figure 6.11: Mesh in the flow cell used for flow calculations.

6.5. Results

6.5.1. Equilibrated solutions

The measurement of the ellipticity between pre-equilibrated solutions of dodecane and brine containing butan-1-ol was performed at the Brewster angle (i.e. for Re(ρ)=0) in the concentric stainless steel cell, thermostated at 20.0 $\pm$ 0.2^{o}C. The solutions of 8.1 wt% butan-1-ol in dodecane and 6% w/v NaCl brine solutions of 4.3 wt% butan-1-ol and SDS were pre-equilibrated in centrifuge tubes and sampled with Pasteur pipettes into the measuring cell. Middle-phase microemulsions that would have formed in the tubes would thus not be present in the cell, and the ellipticity would be measured between the excess aqueous and oil phases.

The data shown in Figure 6.12 suggests that above 1.5 mM SDS initially in the aqueous phase, the sampled aqueous and oleic phases were the same or very similar, leading to comparable coefficients of ellipticity (i.e. imaginary part of the ellipticity). One can think that at these concentrations a middle phase formed in the centrifuge tubes and that the ellipticity was measured between the excess phases. On the other hand, below 1.5 mM SDS, the ellipticity varied significantly with the initial SDS concentration in the aqueous phase, suggesting that the sampled bulk phases and/or the interface differed between preparations. It is worth noting that the slope decreased significantly from 1.5 mM SDS, corresponding to a surfactant concentration circa 10 times the cmc of SDS in 6% w/v NaCl brine, without cosurfactant.

The coefficient of ellipticity, $\overline{\rho}$, of two solutions were calculated using the equation of Meunier (Equation (6.1)) describing interfaces without rigidity with the coupled-modes theory [Meunier, 1987]. The refractive indices, $\sqrt{\epsilon}$, of the sampled aqueous and oleic phases were measured or calculated and the interfacial tensions between the two phases were measured or interpolated values.

$$\overline{\rho}^R = -\frac{3\pi}{2\lambda}\frac{\epsilon_1 - \epsilon_2}{\sqrt{\epsilon_1 + \epsilon_2}}\sqrt{\frac{\pi k_B T}{6\gamma}}. \tag{6.1}$$

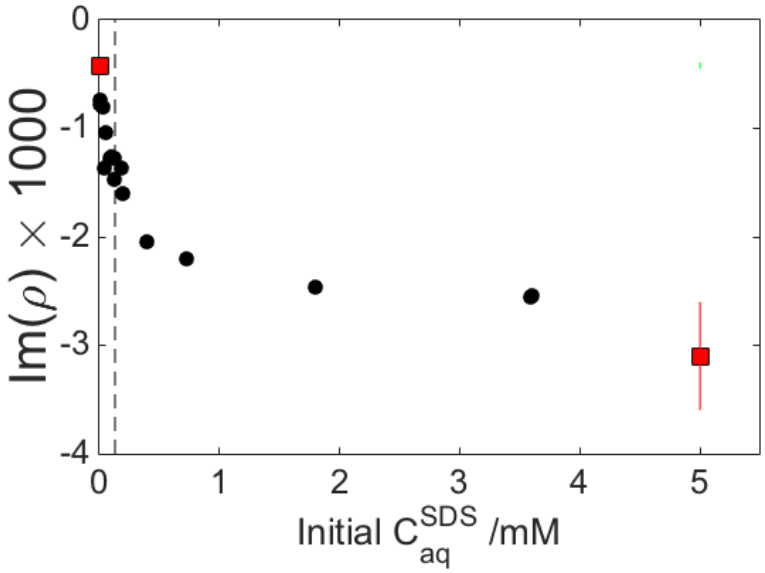

Figure 6.12: Measured (black circles) and calculated (red squares) the imaginary part of the ellipticity between pre-equilibrated solutions of 8.1 wt% butan-1-ol in dodecane and 6% w/v NaCl brine solutions of 4.3 wt% butan-1-ol and SDS. The vertical line drawn at 0.13 mM SDS, i.e. the cmc of SDS in 6% w/v NaCl brine. Measurements were made at the Brewster angle, i.e. for Re(ρ)=0.

where λ is the wavelength of light, ϵ_1 and ϵ_2 are the dielectric constants of the oleic and aqueous phases respectively, k_B is the constant of Boltzmann, T is the absolute temperature, and γ is the interfacial tension between the two liquids.

The solutions used for the IFT measurements contained 4.6 wt% butan-1-ol of the total formulation. With no surfactant, the butan-1-ol content of the equilibrated aqueous and oleic phases were calculated from the predicted oil:brine partition coefficient which was 1.9 ± 0.1. The refractive indices of the bulk phases were subsequently calculated from the Lorentz-Lorenz relation to be 1.3435 and 1.4199 for the aqueous and oleic phases, respectively. The interfacial tension between the two solutions in absence of surfactant was extrapolated from pendant-drop measurements made on dodecane drops in 6% w/v NaCl brine solutions of butan-1-ol up to 5 wt%. The interpolated value was 7.3 ± 1.1 mN.m^{-1}. Using these three values in Equation 6.1, the calculated ellipticity with no SDS was (-0.42 ± 0.03) × 10^{-3}. The second ellipticity datum was calculated for the system prepared with 5 mM SDS as follows. The refractive indexes of the excess phases of an L3 system

prepared with a 6% w/v NaCl brine solution of 4.3 wt% butan-1-ol and SDS and a dodecane solution at 8.1 wt% butan-1-ol, mixed in 10:1 v:v, were measured at 20^{o}C to be 1.3476 and 1.4194 for the excess aqueous and oleic phases, respectively. The interfacial tension between the excess phases of a L3 system prepared with a 6% w/v NaCl brine solution of 4.3 wt% butan-1-ol and 5 mM SDS SDS and a dodecane solution at 8.1 wt% butan-1-ol, mixed in 10:1 v:v, was interpolated from the spinning-drop measurements presented in Chapter Fracture Scale made on drops of dodecane in 6% w/v NaCl brine solutions of 5 mM SDS and butan-1-ol concentrations of up to 4.0 wt%. The interfacial tension was linearly interpolated to be 0.13 ± 0.04 mN.m^{-1}. Using these values in Equation 6.1, the calculated ellipticity value was -3.1 $\pm$ -0.5$\times 10^{-3}$.

At the Brewster angle, the coefficient of ellipticity (i.e. the imaginary part of the ellipticity) is inversely proportional to the square root of the interfacial tension, thus a larger error in the calculated coefficients of ellipticity was found for the lower interfacial tension, i.e. for the larger SDS concentration. In absolute value, the coefficient of ellipticity was underestimated for the system prepared with no SDS and overestimated for the system prepared with 5 mM SDS.

Equation (6.3) only considered the roughness contribution to the coefficient of ellipticity. However, the thickness of the film may contribute too to the coefficient of ellipticity (see Equation (6.2)).

$$\overline{\rho} = \frac{\pi}{\lambda} \times \frac{\sqrt{\epsilon_1 + \epsilon_2}}{\epsilon_1 - \epsilon_2}(\eta^R + \eta_D^L) \tag{6.2}$$

where λ is the wavelength of light, ϵ_1 and ϵ_2 are the dielectric constants of the two media forming the interface, η^R is the roughness contribution, and η_D^L is the thickness contribution.

The contribution of the thickness to the ellipticity is expressed by

$$\eta_D^L = \int_0^L \frac{(\epsilon_1 - \epsilon_z)(\epsilon_2 - \epsilon_z)}{\epsilon_z} dz \tag{6.3}$$

where ϵ_z is the dielectric constant of the interface at the height z on the z-axis normal

to the interface. The sign of η_D^L thus depends on the sign of $(\epsilon_1 - \epsilon_z)(\epsilon_2 - \epsilon_z)$. The carbon chains of butan-1-ol and SDS can be considered to have the same refractive indexes as dodecane, and will thus not contribute to the thickness of the interface. On the other hand, the refractive index of the sulfate head is larger than both that of the oleic and aqueous phases (refractive index used for sulfate head was 1.461 [Song et al., 2013]). The contribution of the sulfate heads of SDS to the thickness of the interface is thus positive. The calculated value of the ellipticity for the system prepared with 5 mM SDS may thus be too negative because it did not take into consideration the positive contribution of the adsorbed monolayer of SDS present at the interface. However, the contribution of the sulfate head groups is small (of the order of 0.5×10^{-3}) and the calculated datum at 5 mM SDS shows that the dominant contribution to the ellipticity for the dodecane, brine, butan-1-ol and SDS (above cmc) system arose from the roughness of the interface.

6.5.2. Simulations

Figure 6.13 shows the calculated concentration profile of SDS after the velocity field was solved with Comsol, 50 and 100 seconds after the flows of water and surfactant solution were stopped. The flow of water and of the 68-mM SDS solution was turned on at the same time for 180 seconds, at 15 mL.h^{-1} and 1 mL.h^{-1} respectively, corresponding to an average velocity in the channel of $896\,\mu\text{m.s}^{-1}$.
After the flows were stopped, the dodecane-water interface was free of surfactant. Below the probed region, the concentration of surfactant in the aqueous channel dropped below the cmc because of the large flow ratio between water and surfactant solution which in effect diluted down the surfactant solution.

6.5.3. Contact angles on modified stainless steel

Table 6.1 describes the contact angles obtained on non-modified and modified stainless steel which were measured with a view to selecting suitable surfaces to pin the interface in the flow cell. Hexasilizane in contact with stainless steel modified effectively its surface: contact angle of water in air was increased to 94 ± 3^o compared

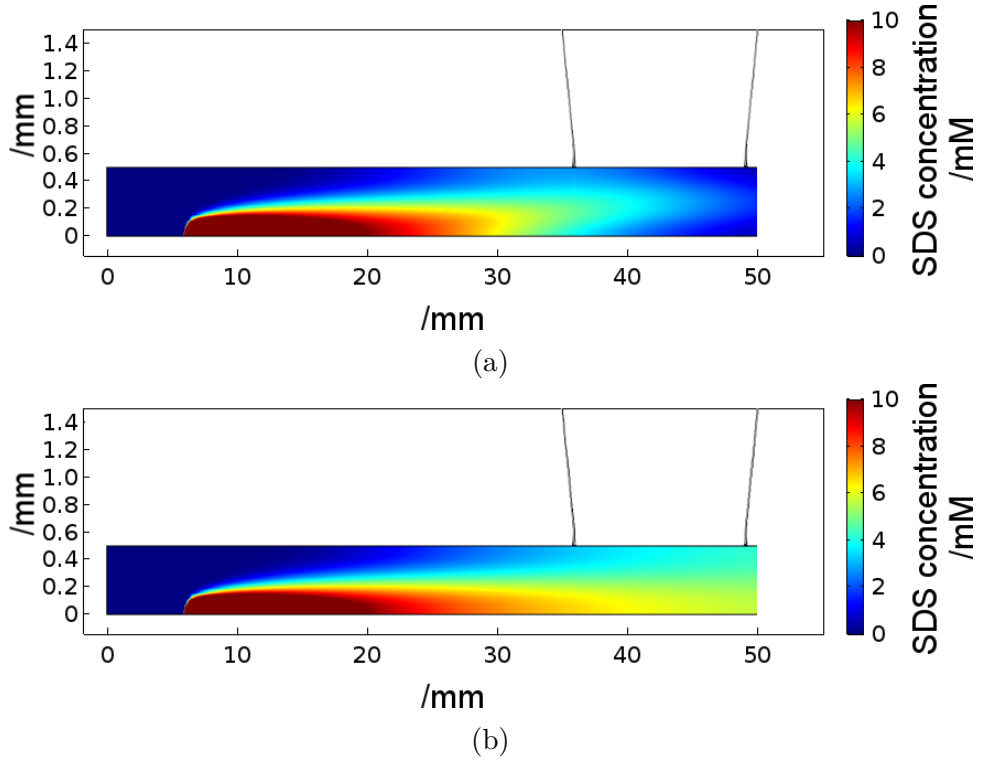

(a)

(b)

Figure 6.13: Concentration profile in the aqueous channel, (a) 50 seconds, (b) 100 seconds after a 68-mM SDS solution was injected at 1 mL.h^{-1} through the slit together with water, pumped through the main aqueous inlet at 15 mL.h^{-1}, during 180 seconds. The vertical axis was zoomed 10 times more than the horizontal axis. Axes are given in millimeters. The colour key gives the surfactant concentration in mM. The colour key was limited to 10 mM to improve the distinction between surfactant concentrations below the cmc.

to a contact angle of less 5^o on non-modified stainless steel. Futhermore, the relative wettabilities of the aqueous phase on the modified stainless steel and of the oleic phase on the non-modified stainless steel were 107 ± 6^o. By modifying only the surface of the oil cavity, these values meant that the aqueous phase and oleic phase were prone not to wet the surfaces of the oil cavity (modified) and of the base of the top plate (non-modified) respectively, promoting the pinning of the interface at the frontier between the two domains.

Table 6.1: Contact angles, in degrees, measured on non-modified and modified stainless steel.

	No treatment	Hexasilizane
Water in air	<5	94 ± 3
Butan-1-ol in air	not measured	68 ± 3
Oleic drop in aq. phase*	107 ± 6	99 ± 3
Aq. drop in oleic phase*	16 ± 3	107 ± 3

* The aqueous and oleic phases were prepared from a 6% w/v NaCl brine solution saturated with butan-1-ol and equilibrated in 1:1 v:v ratio with dodecane.

However, considering the relative wettabilities of the aqueous and oleic phases was not enough to ensure the pinning of the interface. The order with which the solutions were initially pushed into the cell was as important. In fact, the interface between the aqueous and oleic phases containing butan-1-ol did not pin when the cell was initially filled with the aqueous phase before being topped up with the oil phase. Considering the advancing contact angle of the aqueous phase on the stainless steel, butan-1-ol acted as a surfactant at the air-stainless steel interface: butan-1-ol pre-wetted the modified stainless steel interface (contact angle of butan-1-ol on the modified surface was 68 ± 3^o). When the flow cell was filled in this order, the relative wettability of the aqueous phase on the modified surface of the oil cavity was different from the one measured in Table 6.1 because the former surface had been pre-wetted with butan-1-ol.

In order to avoid the creeping of the aqueous phase on the surface of the oil cavity and of the oleic phase on the base of the top plate, the flow cell was initially filled entirely with the oleic phase. The aqueous phase was then pushed in the aqueous

channel to displace the oleic phase. The relative wettability of the aqueous phase on the non-modified stainless steel was 16 ± 3^o, which allowed a complete displacement of the oleic phase by the aqueous phase. The interface between the aqueous and oleic phases was pinned when following this procedure.

6.5.4. Dynamic measurements

Pure dodecane and water interface

In the flow cell, the displacement of water entrained by a volume-control pump in the aqueous channel did not affect the stability of the coefficient of ellipticity reading, i.e. the imaginary part of the ellipiticity ($\mathrm{Im}(\rho)$), for the flow rates used during the experiments (see Figure 6.14). At larger flow-rates such as the ones used by Curwen et al., typically 100 $\mathrm{mL.h^{-1}}$ [Curwen et al., 2007], the interface fluctuated giving a non-uniform ellipticity reading. The standard error was not affected by the water flow and remained small, less than 2% of the signal.

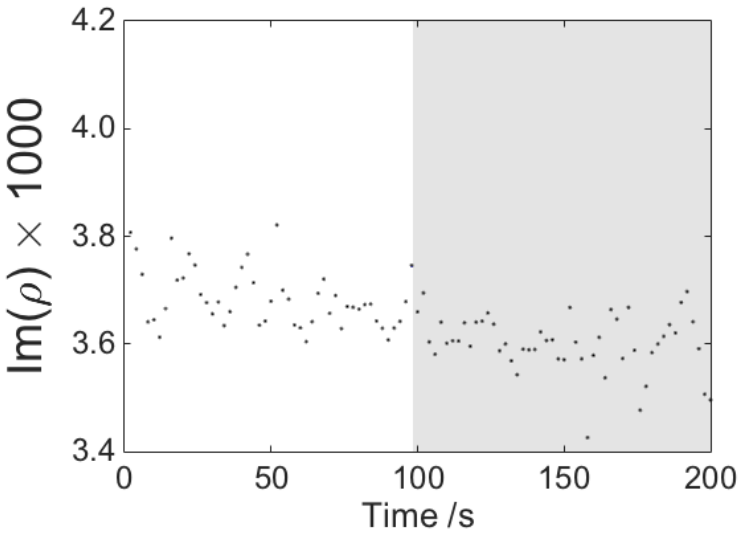

Figure 6.14: Variation in the imaginary part of the ellipticity, $\mathrm{Im}(\rho)$, at the dodecane-water interface measured with time in the flow cell, while water was pushed through the channel at 15.0 $\mathrm{mL.h^{-1}}$ (corresponding to an average linear velocity of $840\,\mu\mathrm{m.s^{-1}}$) during the first 100 seconds; and with no flow in the cell for the last 100 seconds; the grey area highlights the time span where there was no flow. The laser angle of incidence was 47^o from the normal.

Dynamic measurements at the oil-water interface without butan-1-ol

In a first instance, the adsorption of sodium dodecyl sulfate was monitored at the water-dodecane interface. The absence of butan-1-ol simplified the experiment. The water-dodecane interface pinned at the sharp contour of the oil recess. Furthermore in absence of butan-1-ol, the surface treatment of the flow cell prevented effectively the creeping of the aqueous and oleic phases outside of the 0.5-mm channel and the oil recess, respectively. Finally, the liquid-liquid interface was easily flattened by adjusting the level of oil.

Three experiments are presented in this section:

1. A solution of 100 mM SDS was continuously pushed through the 0.5-mm deep aqueous channel from the 0.2-mm wide slit, at 15 $mL.h^{-1}$ (corresponding to an average linear velocity of 840 $\mu m.s^{-1}$), displacing the water initially in place, see Figure 6.15.

2. A solution of 68 mM SDS was pushed through the channel *together* with water. The surfactant solution (through the 0.2-mm wide slit) and water (through the water inlet) were pushed into the channel at 5 and 15 $mL.h^{-1}$, respectively, corresponding to an average linear velocity in the cell of 1120 $\mu m.s^{-1}$, see Figure 6.16.

3. A solution of 68 mM SDS was injected with water at 1 and 15 $mL.h^{-1}$, respectively, corresponding to an average linear velocity in the cell of 896 $\mu m.s^{-1}$.

The three experiments are compared in Figure 6.17.

The interpretation of the measured variation in the imaginary part of the ellipiticity was not straight-forward. First, the observed variation was in the opposite direction than the one observed in the static cell (see Figure 6.12). The dynamic measurements were thus inconsistent with the static measurements. Secondly, without butan-1-ol in the system, the interfacial tension was of a few $mN.m^{-1}$ and the roughness contribution to the imaginary part of the ellipticity was thus small. Furthermore, the measurements in the static cell showed that there was

little contribution of the sulfate heads to the imaginary part of the ellipticity at the oil-water interface. The variation in the imaginary part of the ellipticity showed in Figures 6.15, 6.16, and 6.17, $\Delta(\mathrm{Im}(\rho))$ up to 8×10^{-3}, could thus neither be attributed to the increase of the oil-water interface roughness, nor to the adsorption of SDS at the oil-water interface. Adsorption at the glass (ND filter)-water interface was also ruled out because glass is negatively charged.

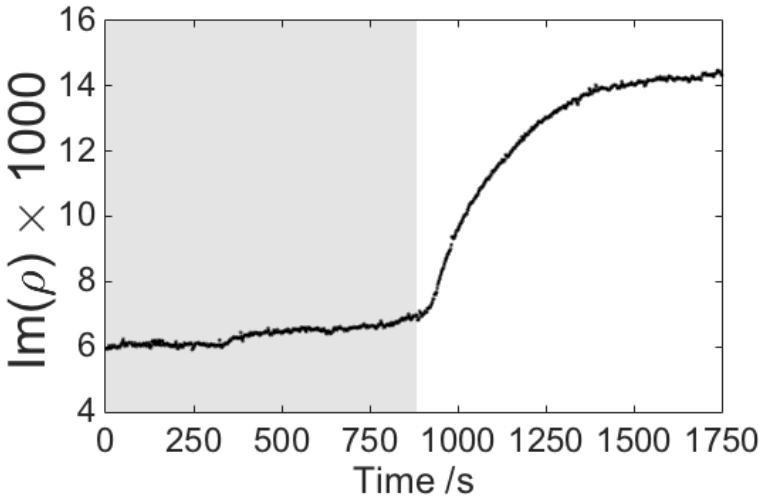

Figure 6.15: Variation in the imaginary part of the ellipiticity, $\mathrm{Im}(\rho)$, at the dodecane-water interface as a solution of 100 mM SDS was continuously injected through the 0.5-mm deep channel at 15 $\mathrm{mL.h^{-1}}$ replacing the water initially in place. The grey area highlights the time span where there was no flow in the cell. The surfactant solution was injected from time t=880 seconds. The laser of incidence was 46^o from the normal.

Interference between the ND filter-water and water-oil interfaces could explain the observed variation in the ellipsometry signal. The interference could be modulated by the refractive index of the aqueous solution as surfactant was pumped into the cell. The two interfaces must be parallel to interfere coherently. The fact that the laser reflections from the ND filter-water and water-oil interfaces were superposed on the reflection arm, about 30 centimetres away from the interface, was a good indication that the two interfaces were parallel. In addition, no interference fringes were observed on the laser reflection spot, strengthening the hypothesis that the two interfaces interfered coherently.

Refractive indices of SDS solutions vary linearly with SDS concentrations at

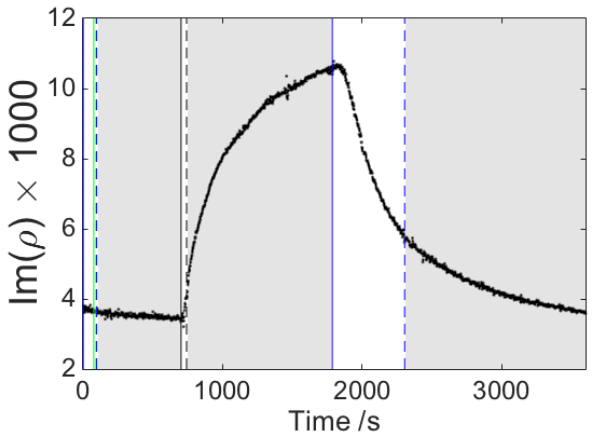

(a)

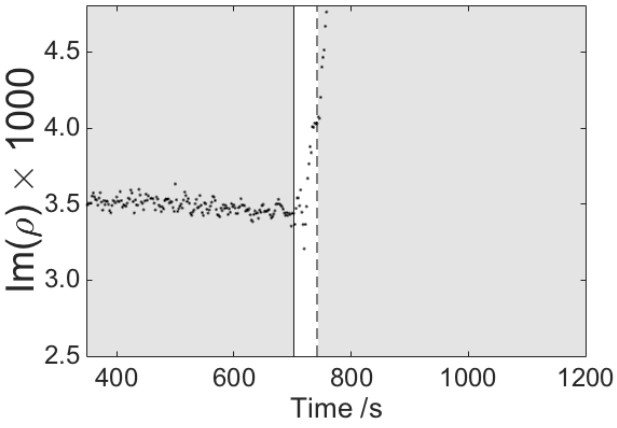

(b)

Figure 6.16: Variation in the imaginary part of the ellipticity, Im(ρ), at the dodecane-water interface. The grey areas highlight the time spans when there was no flow in the cell.
(a) At t=0, water was flowing through the channel at 15 mL.h^{-1}. At t=76 seconds, a 68-mM SDS solution was pushed through the aqueous channel for 16 seconds, at 5 mL.h^{-1} (corresponding to an average linear velocity in the cell of 1120 µm.s^{-1}). At t=92 seconds and 98 seconds, the surfactant and water flows were turned off, respectively. At t=702 seconds, both flows were turned on again, at the same time, for 40 seconds. Finally, at t=1786 seconds, water was injected through the channel at 15 mL.h^{-1} for 518 seconds.
(b) Zoomed area centred around the last injection of water+surfactant solution. The laser angle of incidence was 47^o from the normal.

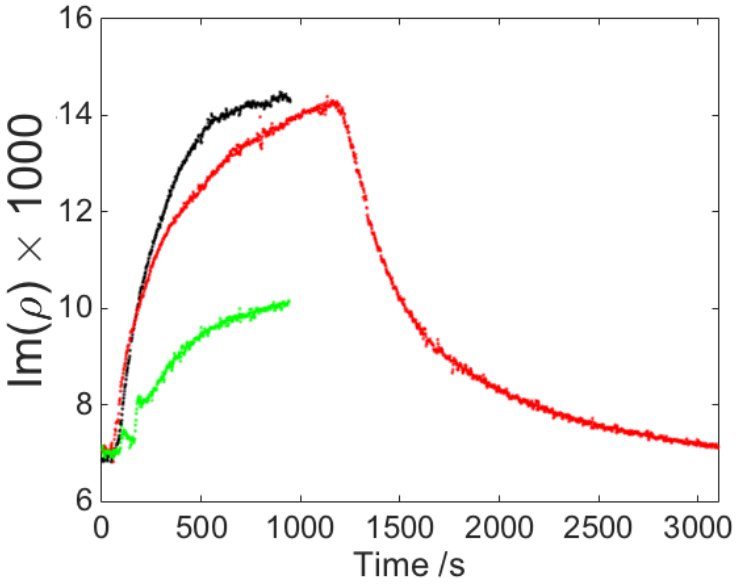

Figure 6.17: Variation in the imaginary part of the ellipticity, Im(ρ), at the dodecane-water interface for three experiments; data were levelled to the same baseline.
Black line: 100 mM SDS was continuously pushed at 15 mL.h^{-1} (data from Figure 6.15).
Red line: 68 mM SDS was injected with water at 5 and 15 mL.h^{-1}, respectively, flows stopped at t=30 seconds (data from Figure 6.16).
Green line: 68 mM SDS was injected with water at 1 and 15 mL.h^{-1}, respectively, flows stopped at t=30 seconds.

different rates below and above the cmc [Tan et al., 2010]. The different flow-rate ratios between surfactant solution and water effectively diluted the surfactant solutions (see Figure 6.13) resulting in different refractive indices in the channel and hypothetically interference modulation reflected in the ellipsometric signal, as read in the imaginary part of the ellipticity, see Figure 6.17. The design of the cell brought too many incertainties to interpret the variation of the ellipsometric signal. The reflection from the liquid-liquid interface should thus be separated from that of the ND filter-water interface.

Dynamic measurements at the oil-water interface with butan-1-ol

To complete the study and to compare the results of the equilibrated solutions of dodecane, brine, butan-1-ol and SDS, to dynamic measurements, the flow cell was initially filled with butan-1-ol-saturated 6% w/v NaCl brine solution in the aqueous channel and dodecane enriched in butan-1-ol at 6.9 wt% in the oil cavity; the surfactant solution was a 6% w/v NaCl brine solution of 137 mM SDS and 6.4 wt% butan-1-ol. The ellipticity of the liquid-liquid interface was recorded as the aqueous and surfactant solutions were pushed in the aqueous channel, through the water inlet and the 0.2-mm wide slit respectively, at 0.5 $mL.h^{-1}$ corresponding to a velocity in the aqueous channel of 56 $\mu m.s^{-1}$.

Figure 6.18 gives an example of the data obtained. In this figure, both the real part and the imaginary part of the ellipticity ($Re(\rho)$ and $Im(\rho)$) are plotted. The signal variation occurred in $Re(\rho)$ rather than $Im(\rho)$, contrary to the variations observed in the experiments previously presented. $Im(\rho)$ was stable around 3×10^{-3}. In addition, the measured variation was an order of magnitude larger than in the static measurements. Static measurements were made at the Brewster angle of the oil-water interface. Here, the incident light was a few degrees above for the Brewster angle for both the ND filter-water and water-oil interfaces. In this experiment, the reflections from the ND filter and the liquid-liquid interface could be resolved and the former was blocked out close to the cell. This separation indicated that the interface was not pinned at the sharp contour of the oil recess but rested higher

up in the recess. The observed signal variation was thus not expected to be due to interferences between the ND filter-water and water-oil interfaces. At the end of the experiment, the reflection spot of the liquid-liquid interface was still a sharp point, while the reflection from the ND filter was more diffuse, suggesting that the surface of the ND filter was impaired.

Signal change was observed about 10 minutes after the flows were turned on in the cell. This delay was the time expected for the surfactant to be displaced from its point source to the probing area ($3.6(\text{cm})\times0.05(\text{cm})\times1(\text{cm})\times3600(\text{s})/1(\text{cm}^3)$ = 643 seconds). The signal became noisier closer to the signal step and it stabilised after an additional 10 minutes. The initial value of $\text{Re}(\rho)$ was recovered when the aqueous phase (free of surfactant) was flushed in the aqueous channel.

The step in $\text{Re}(\rho)$ were not interpreted in terms of thickness because it was not clearly understood why the values were so different from the previous experimental values and why the change was of opposite sign to that in Figure 6.12. On the other hand, the shape of reflection point and its movement accredited the hypothesis that it was indeed the liquid-liquid interface which was probed.

6.6. Discussion and conclusion

6.6.1. Experimental results

Measurements in a static cell showed that the sulfate heads at the oil-water interface contributed only slightly to the measured ellipticity. At low interfacial tension, the main contribution to the ellipticity arose from the roughness of the interface.

In the flow cell, the adsorption of SDS was first monitored at the interface between dodecane and water through a series of flow experiments. In absence of salt and cosurfactant, there was no formation of middle phase. The dynamic measurements were inconsistent with the observations made in the static cell. The variation in ellipsometric signal observed in the flow cell was interpreted in the light of the hypothesis of an interference between the ND filter-water and the water-oil interfaces.

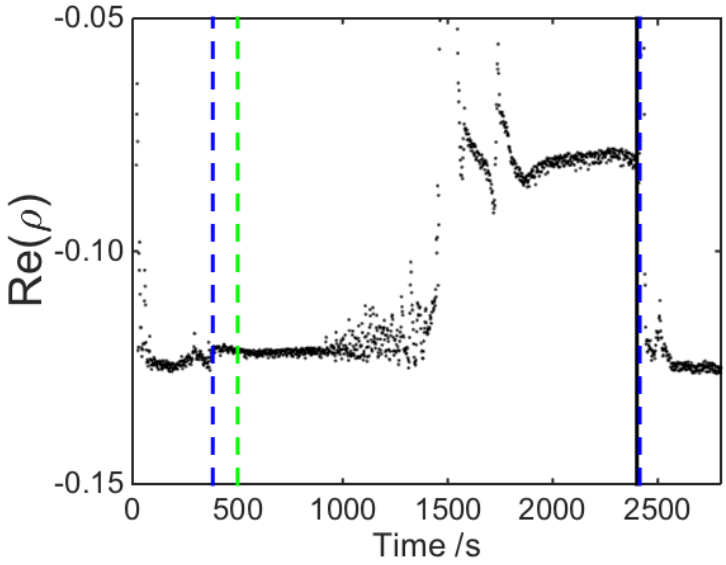

(a)

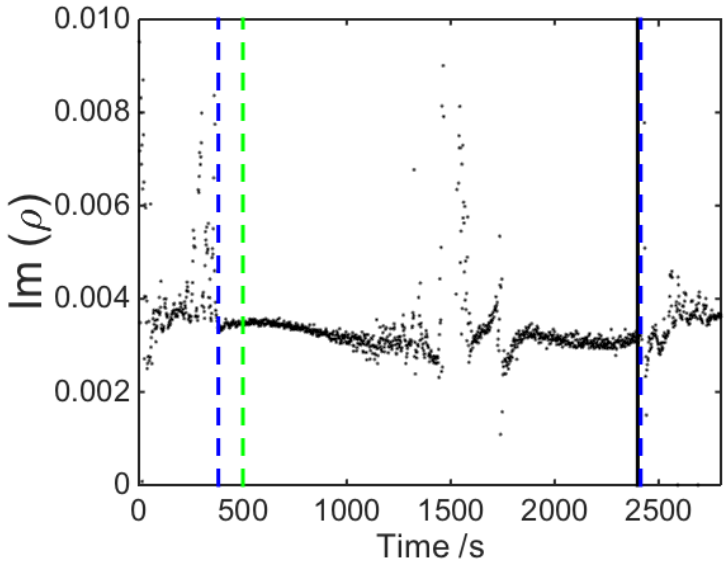

(b)

Figure 6.18: Variation in (a) the real part of the ellipticity, Re(ρ), and (b) the imaginary part of the ellipticity, Im(ρ), at the liquid-liquid interface as the aqueous and surfactant solutions were both pushed in the aqueous channel at 0.5 mL.h^{-1}. Aqueous solution: butan-1-ol-saturated 6% w/v NaCl brine solution. Surfactant solution: 6% w/v brine solution of 137 mM SDS and 6.4 wt% butan-1-ol. Oleic solution: dodecane enriched in butan-1-ol at 6.9 wt% in the oil cavity.
At t=382 and 500 seconds, the aqueous and surfactant-solution flows were turned on, respectively. At t=2400 seconds, both flows were turned off together. Finally, at t=2414 seconds, the aqueous flow was pushed at 5.5 mL.h^{-1}. The laser angle of incidence was 48.4^o from the normal.

The second experimental section with the flow cell investigated the variation of ellipticity at the liquid-liquid interface under the flow of a brine solution of SDS and butan-1-ol. Both bulk phases contained butan-1-ol and the formation of a middle phase between the oleic and aqueous phases was anticipated. In this case, the reflection from the ND filter-water interface was separated from that of the water-oil interface and the signal variation was thus not expected to result from interference. However, the measured data remained puzzling.

In conclusion, the adsorption of surfactant at the oil-water interface, in absence of the formation of a middle phase, could not be analysed successfully because the design of the flow cell brought too many incertainties. Consequently, when salt and cosurfactant were added into the system studied, the results remained puzzling because the simpler system was not characterised by a meaningful ellipsometric signal. The separation of the ND filter-water and the water-oil interfaces would simplify the interpretation of the results, by avoiding interference between the two interfaces.

In addition, the continuous flow experiments became more challenging as the liquid-liquid interface was less rigid (i.e. in presence of butan-1-ol). The monitoring of the thickness of the interface with time, as a middle phase forms, would be easier to achieve in absence of convective flow. The diffusion-dominated experiments need initially larger velocities in the channel in order to bring the surfactant near the interface investigated while preventing the adsorption at the liquid-liquid interface with the superimposed water flow. With the current geometry of the flow cell, these larger flows were not accessible without disturbing the liquid-liquid interface. This restriction could be overcome by amending the design of the cell as suggested in the next section.

6.6.2. Ellipsometry at a liquid-liquid interface

The method of Curwen et al. [Curwen et al., 2007], which inspired the design of the flow cell and the experiments, did not translate easily to the system studied in this thesis for a number of reasons. First, in the case of Curwen's experiments, the

dominant reflection was the reflection of interest. Here, the dominant reflection was from the ND filter/oil interface while the interface of interest was the oil/water interface. Secondly, Curwen et al. investigated the adsorption of surfactant onto a hydrophobic solid surface, resulting in larger adsorption and ellipsometric contribution than that from the adsorption at a liquid-liquid interface. Finally, Curwen et al. studied a solid-liquid interface which is intrinsically more rigid than a liquid-liquid interface. They maintained a flow ratio of 1 or 4% between the surfactant solution and the water; typically, water was pushed in the aqueous channel of the flow cell at 135 $mL.h^{-1}$. This flow ratio confined the surfactant to the first-half of the channel, away from the surface under investigation. Here, such high flow-rates disturbed the liquid-liquid interface, especially when the system studied contained butan-1-ol, in which case the laser reflection was going in and out of the 3-mm pinhole as solutions were being pushed through the cell. On the other hand, maintaining the water flow at 15 $mL.h^{-1}$ and reducing the surfactant flow to 0.15 $mL.h^{-1}$ was discounted because the delivery of surfactant became unreliable at such a low flow rate. In Curwen's study, the high flow ratio isolated the contributions of refractive index variation and adsorption to the ellipsometry signal.

6.6.3. Technique challenges and suggested solutions

One obstacle identified during the use of the flow cell was the stability of the liquid-liquid interface. High flow rates in the aqueous channel directed by volume pumps disturbed the interface resulting in a unstable ellipticity reading. For this reason, the flows were limited to 15 $mL.h^{-1}$ corresponding to a linear velocity of 840 $\mu m.s^{-1}$. One direct consequence of this limitation was that large ratio between the flow rates of the aqueous solution and of the surfactant solution were not accessible. Such large flow-rate ratios (typically of 100) allows the restriction of the surfactant solution to about half of the channel height [Curwen et al., 2007]. Once the flows are turned off, the surfactant diffuses evenly across the second half of the channel to the interface. There are two main interests in preventing the adsorption when the flows are turned on. First, the adsorption is recorded on a still,

more stable interface. Second, the adsorption occurs uniformly across the entire liquid-liquid interfacial area, avoiding non-uniform emulsification of the interface. In order to improve the stability of the liquid-liquid interface, the area of contact between the two liquids could be reduced to a disk of less than 1-cm diameter. The oil cavity could be a conic recess and the cell could be sealed by a hemisphere. Figure 6.19 proposes an alternative design to the existing top plate of the flow cell, limiting the volume of oil and the contact area between oil and water. It is worth noting that focussing optics for the laser would be needed if using a hemisphere.

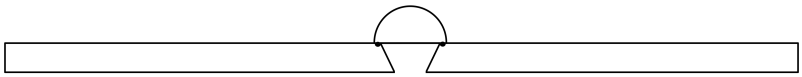

Figure 6.19: To-scale schematic representation of an alternative design to the existing top plate of the flow cell. The area of contact between the two liquids is limited to a disk of 9-mm diameter. The flow cell is sealed by a 10-mm hemisphere pushed onto an O-ring.

A second complication encountered during this study was the difficulty to obtain a clear reflection from the laser on the liquid-liquid interface. Due to the limited height of the aqueous channel below the oil (aqueous channel was 0.5-mm deep), it was easy to unintentionally make the oil touch the ND filter when adjusting the curvature of the interface or its height if the interface did not pin. After such an incident, it was difficult to form a distinguishable liquid-liquid interface and the cell had to be, in the worst case, re-dismantled and cleaned. The height of the aqueous channel was set to 0.5 mm in the original work of Curwen et al. to have a large width-to-height ratio for computational approximations and because the diffusion of surfactant across a 0.5-mm deep channel took hundreds of seconds, which was deemed a reasonable experimental time. However, in the flow cell used in the chapter, not only the limited height complicated the set-up of the experiments, it also affected the ellipticity absolute value because the reflection from the ND filter placed at the bottom of the recess could not be separated from that of the liquid-liquid interface. Furthermore, the measured ellipticity may result from interference between these two interfaces. This superposition thus complicated the interpretation of results. Based on the experience built throughout this study, it

is suggested that the thickness of the aqueous channel is increased to separate the two reflections. The larger depth of the channel will increase the diffusion time across the channel and thus the experimental time; however this drawback can be mitigated by using flow-rate ratios which may be chosen to limit the distance that the surfactant will still need to diffuse through, once the flows are stopped.

Both diffusion and convection transports are relevant in surfactant EOR. By implementing the simple modification proposed to the flow cell, both scenarios could be investigated. In this chapter, the flow rates used in the flow cell corresponded to velocities ranging from 56 to 840 $\mu m.s^{-1}$ which were comparable to reservoir flows, typically a pore per second. The conditions of formation of microemulsion in the flow cell presented in this chapter are thus relevant to surfactant EOR.

6.6.4. Conclusion

The chapter proposed a methodology development for the study of the microemulsion formation and evolution at the oil-water interface by ellipsometry. The flow cell of Curwen et al. ([Curwen et al., 2007]) was adapted to study the liquid-liquid interface. The pinning of the interface was promoted by tapering the base of the oil cavity to provide sharper pinning points and by differentiating the wettabilities of the aqueous channel and the oil cavity. The flow characteristics were relevant to surfactant EOR. The design of the cell led however to too many uncertainties to interpret the measured ellipsometry signals in terms of physical parameters such as adsorption and interface thickness. A number of design alterations were proposed to mitigate these issues.

Chapter 7

Summary and conclusion

This thesis focused on dynamic and local aspects of an oil-brine-surfactant system relevant to EOR. The work set out to aid the description of the displacement of oil during surfactant EOR by looking at non-equilibrium scenarios and designing a tool capable of analysing dynamically the formation of a microemulsion at the oil-water interface. Local concentrations, phase behaviours and flows near the oil-water interface during oil recovery differ from equilibrium and may depend on local surfactant depletion, local oil-brine ratio and local geometry. This work took a multi-scale approach to reflect the diversity of environments and scenarios encountered in a rock during surfactant flooding. In addition, experiments were carried out under convection and diffusion as both transports are relevant to surfactant EOR.

The continuum approach in modelling in the petroleum chemistry often keeps the surfactant concentration at high concentration (e.g. 2% of surfactant mixtures for EOR provided by Chevron Oronite [Dwarakanath et al., 2008]; 1% ENORDET, a surfactant blend of Shell Chemicals for surfactant EOR [Howe et al., 2015]), to account for surfactant loss during the flood caused by adsorption on the walls of the reservoir, partitioning into the oil or association with a microemulsion. Additionally, a large amount of surfactant leads to a large volume of middle phase, which is easily measured in the test tubes where the phase behaviour is assessed. However, significantly lower surfactant concentrations may be more representative of the

composition at the moving oil front where the flood solution may be depleted in surfactant.

In this thesis, the phase behaviour and oil displacement in pore network were investigated at low surfactant concentrations ($\approx 0.1\%$). First, the study at the reservoir scale (continuum approach) showed a power-law relationship between the SDS in the formulation and the minimum butan-1-ol concentration needed to present an L3 behaviour. The amount of cosurfactant needed to form L3 microemulsions at the moving front, which can be depleted in surfactant because of loss by adsorption, may thus be overestimated when based on phase behaviours studies with more concentrated surfactant solutions. Here, the use of NMR tubes allowed the visualisation of middle phase with volume down to 2 µL, permitting the study of phase behaviour by eye, which aided studies potentially down to 0.02 wt% SDS.

At the pore scale, nearly as much oil was recovered from a hydrophobic network of pores with the flood of a brine solution of 0.5 mM SDS (five times above cmc) and 5.3 wt% butan-1-ol, as with the flood of a brine solution of 137 mM SDS (more than 1000 times the cmc) and 6.3 wt% butan-1-ol. The floods recovered respectively 72% and 74% of the oil originally in place. The accessibility of butan-1-ol to partition to the oil phase was reduced in the SDS-rich brine solution because butan-1-ol co-adsorbed, and was solubilised, in SDS micelles. The interfacial tensions of the flood solutions with dodecane were very similar, respectively 0.28 ± 0.03 and 0.34 ± 0.03 mN.m^{-1}. The increased solubility of butan-1-ol in SDS-rich brines did not provide enough butan-1-ol to those systems to form L3 microemulsions with pure dodecane. This result indicates that the cost of a surfactant flood could be reduced by decreasing the amount of surfactant while maintaining the flood performance.

Surfactant screening in petroleum chemistry is based on the criterion that the surfactant mixture suitable to recover left-behind oil blobs after a water flood can form a bicontinuous microemulsion with the oil. The pore-scale study of this thesis showed however that a pore network was completely desaturated in oil (i.e. no oil blobs remaining) without the solubilisation of the oil phase in a middle phase. A second micromodel filled with a more polar oil (dodecane enriched in butan-1-ol) was

also eventually completely desaturated in oil, with the formation of a middle phase. However, in the latter example, the oil recovery took longer (higher flood volume) to reach a complete oil desaturation when the middle phase developed. Thus, solubilisation of oil in a middle phase is not essential for complete oil desaturation from a pore network. A limitation of this study however is that micromodels were initially completely saturated in oil. However, surfactant EOR is typically designed and used to recover oil from reservoirs after water-flooding and hence where the residual oil consists of by-passed zones and oil blobs that snapped-off from the oil bank during displacement through pore throats by the pore throats. The critical capillary number to displace a single oil blob may be larger than to displace an oil bank.

This thesis brought attention to flows arising at the fracture and pore scales near the oil-brine interface as a consequence of non-uniform concentration of surfactant and cosurfactant. The flows were observed in the representations of a hydrophilic millimetric fracture and a hydrophilic pore network. In the fracture-scale study, an interfacial-tension gradient along the oil-water interface, estimated to be less than 1% of the equilibrated interfacial tension, led to substantial fluid motion, at $300\,\mu m.s^{-1}$. The top of the oil drop was depleted in cosurfactant because of the limited amount of butan-1-ol available in the aqueous wetting film between the top of the oil drop and the pore wall. On the other hand, the lower interface of the oil drop was in contact with the bulk of the aqueous phase which represented an infinite reservoir of butan-1-ol. The asymmetry created Marangoni stress estimated by particle tracking in the aqueous bulk phase to be about 0.6 $mN.m^{-2}$. The resultant complex flow behaviour delayed the equilibration time between the flood solution and the oil. In the context of surfactant EOR, these flows may displace an oil drop over a few millimetres along a fracture but the pressure exerted by the flows on the drop would be too small to displace the drop through a constriction. More generally, this study showed a novel and captivating phenomenon of the "dripping droplets" where a small interfacial tension gradient led to long lasting self-induced convective flows. During the flood of a brine solution of surfactant and cosurfactant of a

hydrophilic pore network, the pore-scale study showed that oil blobs were displaced in the direction opposite to the flood direction. This unanticipated oil displacement has not been reported. A shortcoming of this study was that the potential to use these flows to dislodge oil from dead-end pores during surfactant flooding was not evaluated.

Finally, this thesis proposed ellipsometry as a tool to monitor, at the molecular level the evolution of the oil-water interface during surfactant flooding. Transport to the liquid-liquid interface by convection or diffusion, both relevant to surfactant EOR, could be followed. The design of the cell complicated the interpretations of experiments. Solutions were suggested to overcome these problems and to enable the interpretation of the measured signal variation in terms of adsorption and thickness of the interface.

To further the findings of the multi-scale investigation of dynamic events at the oil-water interface presented this thesis, chemically specific techniques could be coupled to the experiments. For example, at the pore scale, the presence of microemulsion at the interface, which was assessed visually or indirectly from contact angle, could be evaluated using a solvatochromic dye under fluorescent dye, as presented by Unsal et al. [Unsal et al., 2016]. At the molecular scale, evanescent-wave Raman scattering could be a suitable chemically specific technique to study the kinetics of adsorption at the oil-water interface. Another option would be to study a thin film of oil on a surfactant solution with external reflection FTIR. Finally, the composition of the third phase could be evaluated by transferring the interfacial film to a flat solid sample. Molecular specific study would provide new insights into the observed phenomena.

Finally, it would be valuable to compare the findings of this multi-scale approach using SDS and butan-1-ol with those using a combination of commercial surfactant/cosurfactant system employed for EOR in the petroleum industry. The commercial systems are designed to present high solubilisation factors at low surfactant concentration. Solubilisation factors are defined as ratios by volume of water (or oil) to surfactant in the microemulsion phase. High solubilisation

factors are correlated with ultra-low interfacial tensions that are sought after for oil mobilisation. In this thesis, the chosen surfactant mixture, at 6% w/v NaCl salinity, had a solubilisation factor of about 4. Surfactants specifically designed for surfactant EOR have solubilisation factors of 10 or more at the optimal salinity. However, a key drawback of using commercially available industrial surfactants, such as EDORNET, in academic research, is that they are rarely pure compounds. One solution would be to use pure chemical compounds available for research purposes with similar chemistry, although it is often thought that the blend of components within the commercial surfactant provide an enhanced performance over a wider range of compositions/conditions than a pure surfactant.

To conclude, this thesis presented a novel, multi-scale, approach to aid the description of the displacement of oil during surfactant EOR. Unexpected and previously unreported oil displacements were observed: the complete oil desaturation of a hydrophobic pore networks without the solubilisation of the oil bank into a third phase and the displacement of oil in the direction opposite to the flood direction in hydrophilic pore networks. Finally, the multi-scale approach highlighted the value of investigating low surfactant concentration which can lead to similar oil recoveries as highly-concentrated surfactant flood solutions.

Appendix

Note on brine solution of surfactant saturated with butan-1-ol.

Butan-1-ol was added to three 10 mL 6% w/v NaCl solutions of 137 mM SDS to 6.4, 8.4 and 18.5 wt% of the formulation (0.73 g, 0.79 g and 2.43 g of butan-1-ol respectively). The brine solution of surfactant and alcohol at the lowest concentration was a monophasic mixture. The 8.4-wt%-butan-1-ol solution was prepared by adding just enough butan-1-ol for the solution to separate into two phases. In the 18.5-wt%-butan-1-ol solution, alcohol was added in large excess of the amount required to observe the mono-to-biphasic transition. The mass ratios of butan-1-ol to SDS were respectively 1.8:1, 2.0:1 and 6.2:1. The dry contents (minimum three repeats) of upper and lower phases were measured on 500-μL samples which were dried at 60^{o}C for three hours and stored in a dessicator for cooling. The denser phases of the aqueous solutions were studied by Raman spectroscopy. Measurements were made on capillaries filled with the solutions to reduce the evaporation of butan-1-ol. Excitation was provided at 532 nm by a Laser Quantum Opus 532. Spectra were acquired by focusing the laser (power circa 100 mW in focus) in the bulk of the capillary where maximal signal was obtained. Spectra were obtained with incident light polarised parallel with respect to the plane of incidence. The angle of incidence was circa 73^o. Each spectrum was acquired with ten-second integration time. Spectra were normalised relative to the peak at 3245 cm^{-1}. Raman spectra of a 6% w/v NaCl brine solution saturated with butan-1-ol and of a solution of 6 wt% SDS in water were recorded

under the same conditions. The shapes of the CH-stretches bands of the aqueous solutions between 2800 and 3100 cm^{-1} were matched to linear combinations of the spectra of butan-1-ol-saturated brine, and of SDS. Figure 7.1 compares the spectra of the three aqueous solutions (green, red and black lines) to the corresponding linear-combination spectra (green, red and black dotted lines). The concentrations of butan-1-ol and SDS in the aqueous solutions were calculated from the coefficients of the linear combinations used for the mixed spectra. The differences between the prepared and calculated concentrations of SDS and butan-1-ol in the 6% w/v NaCl brine solution of 137 mM SDS and 6.4 wt% butan-1-ol were approximately 5%.

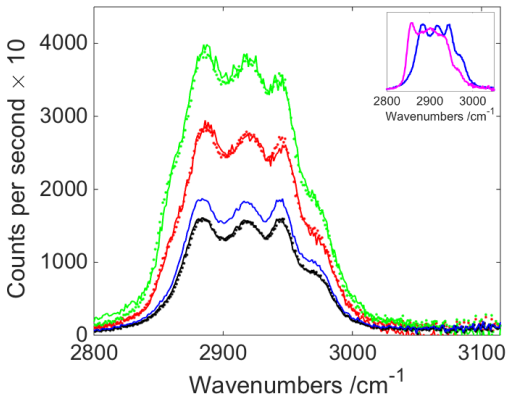

Figure 7.1: CH stretches of the 6% w/v NaCl brine solution of 137 mM SDS and 6.4 wt% butan-1-ol (green line) and denser phases of 6% w/v NaCl brine solutions of 137 mM SDS and 8.4 and 18.5 wt% butan-1-ol (red and black lines, respectively). Dotted lines are the corresponding mixed spectra obtained from linear combinations of the CH stretches in a 6% w/v NaCl brine solution saturated with butan-1-ol (blue line, in main figure and top-right corner figure) and in a solution of 6 wt% SDS in water (magenta line in top-right corner figure).

The quantity of butan-1-ol and SDS is proportional to the area below the CH-stretch bands. The top-right corner plot in Figure 7.1 shows that the shoulders centred around 2860 cm^{-1} in the aqueous phases spectra were due to the presence of SDS. This shoulder was observed in the mono-phasic brine solution of butan-1-ol prepared at 137 mM SDS (green line) and in the denser phase of the 6% w/v NaCl brine solution of 137 mM SDS and 8.4 wt% butan-1-ol (red line). On the other hand, there was no SDS shoulder in the spectrum of the 6% w/v NaCl brine solution of 137 mM SDS and 18.5 wt% butan-1-ol (black line). In addition, the

butan-1-ol concentration in this solution was smaller than the butan-1-ol saturation concentration in 6% w/v NaCl brine free of SDS (blue line). The more butan-1-ol was added in the aqueous phase preparation, the more surfactant partitioned into the lighter butan-1-ol-rich phase. In the 18.5 wt% butan-1-ol aqueous preparation, all the SDS was in the lighter phase as reversed micelles. The uptake of butan-1-ol within a brine solution of surfactant can be significantly higher than in brine solutions free of SDS. If one molecule of SDS contributes to the solubilisation of six molecules of butan-1-ol, the quantity of solubilised butan-1-ol in a brine solution of 137 mM SDS doubles compared to the quantity of butan-1-ol found in a surfactant-free 6% w/v NaCl brine solution saturated with butan-1-ol. The absence of micelles in the denser water-rich phase of the 18.5 wt% butan-1-ol aqueous preparation capped the butan-1-ol concentration to its solubility limit in absence of surfactant.

Salt and surfactant partitioned in favour of the lighter aqueous phase, with a dry-content ratio of lighter to denser phase of 1.70 $\pm$ 0.09 and 1.76 $\pm$ 0.04 for the formulations at 8.4 and 18.5 wt% butan-1-ol, respectively. Butan-1-ol concentrations in the heavier phases were estimated at 0.79 and 0.51 M for the formulations at 8.4 and 18.5 wt% butan-1-ol respectively, corresponding of a partition coefficient of butan-1-ol of 2.0 and 19.4 expressed as molar-concentration ratio of butan-1-ol in the lighter to the denser phase.

To summarise, a 6% w/v NaCl brine solution of 137 mM SDS containing 6.4 wt% butan-1-ol formed a single phase. When more butan-1-ol was added to the solution and its solubility limit was exceeded, the solution phase-separated into a water-rich phase and a butan-1-ol-rich phase. Both phases consisted of water, NaCl, butan-1-ol and SDS but in different proportion and with a different molecular arrangement. The lower phase of such a system contained less surfactant and alcohol than a brine solution of surfactant containing the maximum amount of butan-1-ol allowed to maintain a single phase.

Bibliography

[Afsharpoor et al., 2014] Afsharpoor, A., Ma, K., Duboin, A., Mateen, K., Jouenne, S., and Cordelier, P. (2014). Micro-scale experiment and CFD modeling of viscoelastic polymer; trapped oil displacement and deformation at the dead-end. Number SPE-169037-MS. SPE Improved Oil Recovery Symposium, 12-16 April, Tulsa, Oklahoma, USA, Society of Petroleum Engineers.

[Al-Adasani and Bai, 2010] Al-Adasani, A. and Bai, B. (2010). Recent developements and updated screening criteria of enhnaced oil recovery techniques. Number 130726.

[Al-Mjeni et al., 2010] Al-Mjeni, R., Arora, S., Cherukupalli, P., van Wunnik, J., Edwards, J., Felber, B., Gurpinar, O., Hirasaki, G., Miller, C., Jackson, C., Kristensen, M., Lim, F., and Ramamoorthy, R. (2010). Has the time come for EOR? *Oilfield Review*, 22(4):16–35.

[Alvarez et al., 2014] Alvarez, J., Neog, A., Jais, A., and Schechter, D. (2014). Impact of surfactants for wettability alteration in stimulation fluids and the potential for surfactant eor in unconventional liquid reservoirs. Number 169001, SPE Unconventional Resources Conference, 1-3 April, The Woodlands, Texas, USA.

[Andrade et al., 1999] Andrade, J., Costa, U., Almeida, M., Makse, H., and Stanley, H. (1999). *Physical Review Letters*, 82:5249–5252.

[Armstrong and Berg, 2013] Armstrong, R. and Berg, S. (2013). Interfacial velocities and capillary pressure gradients during haines jumps. *Physical Review*

E: Statistical Physics, Plasmas, Fluids, and Related Interdisciplinary Topics, 88(043010).

[Armstrong and Dorthe, 2012] Armstrong, R. and Dorthe, W. (2012). Microbial enhanced oil recovery in fractional-wet systems: A pore-scale investigation. *Transport in Porous Media*, 92(3):2012. 819-835.

[Armstrong et al., 2014] Armstrong, R., Georgiadis, A., Ott, H., Klemin, D., and Berg, S. (2014). Critical capillary number: Desaturation studied with fast X-raycomputed microtomography. *Geophysical Research Letters*, 41:55–60.

[Aveyard et al., 1986] Aveyard, R., Binks, B., Clark, S., and Mead, J. (1986). Interfacial tension minima in oil-water-surfactant systems. behaviour of alkane-aqueous NaCl systems containing aerosol OT. *Journal of the Chemical Society, Faraday Transactions 1*, 82:125–142.

[Azzam and Bashara, 1977] Azzam, R. and Bashara, N. (1977). *Ellipsometry and polarized light*. North-Holland Pub. Co.

[Bashforth and Adams, 1883] Bashforth, F. and Adams, J. (1883). *An attempt to test the theories of capillary action*. Cambridge University Press, London.

[Bataweel et al., 2011] Bataweel, M., Nasr-El-Din, H., and Schechter, D. (2011). Fluid flow characterization of chemical EOR flooding: A computerized tomography (CT) scan study. Number 149066, SPE/DGS Saudi Arabia Section Technical Symposium and Exhibition, 15-18 May, Al-Khobar, Saudi Arabia.

[Beaglehole, 1980] Beaglehole, D. (1980). Ellipsometric study of the surface of simple liquids. *Physica B+C*, 100(2):163 – 174.

[Berg et al., 2013] Berg, S., Ott, H., Klapp, S., Schwing, A., Neiteler, R., Brussee, N., Makurat, A., Leu, L., Enzmann, F., Schwarz, J., Kersten, M., Irvine, S., and Stampanoni, M. (2013). Real-time 3D imaging of haines jumps in porous media flow. *PNAS*, 110(10):3755–3759.

[Biais et al., 1981] Biais, J., Bothorel, P., Clin, B., and Lalanne, P. (1981). Theoretical behaviour of microemulsions geometrical aspects, dilution properties and role of alcohol. comparison with experimental results. *Journal of Dispersion Science and Technology*, 2(1):67–95.

[Bidyut and Debdurlav, 2007] Bidyut, K. and Debdurlav, N. (2007). Dilution method study on the interfacial composition, thermodynamic properties and structural parameters of w/o microemulsions stabilized by 1-pentanol and surfactants in absence and presence of sodium chloride. *Journal of Colloid and Interface Science*, 316(2):751 – 761.

[Botana et al., 2011] Botana, A., Aguilar, J., Nilsson, M., and Morris, G. (2011). J-modulation effects in DOSY experiments and their suppression: The Oneshot45 experiment. *Journal of Magnetic Resonance*, 208(2):270 – 278.

[Bourrel and Chambu, 1983] Bourrel, M. and Chambu, C. (1983). The rules for achieving high solubilization of brine and oil by amphiphilic molecules. *Society of Petroleum Engineers Journal*, 23:327–338. SPE-10676-PA.

[Bowcott and Schulman, 1955] Bowcott, J. and Schulman, J. (1955). Emulsions control of droplet size and phase continuity in transparent oil-water dispersions stabilized with soap and alcohol. *Zeitschrift für Elektrochemie, Berichte der Bunsengesellschaft für physikalische Chemie*, 59(4):283–290.

[Buchgraber et al., 2012] Buchgraber, M., Al-Dossary, M., Ross, C., and Kovscek, A. (2012). Creation of a dual-porosity micromodel for pore-level visualization of multiphase flow. *Journal of Petroleum Science & Engineering*, 86-87:27–38.

[Buijse et al., 2012] Buijse, M., Tandon, K., Jain, S., Handgraaf, J., and Fraaije, J. (2012). Surfactant optimization for EOR using advanced chemical computational methods. Number SPE-154212-MS, SPE Improved Oil Recovery Symposium, 14-18 April, Tulsa, Oklahoma, USA. Society of Petroleum Engineers.

[Cazabat et al., 1982] Cazabat, A., Langevin, D., Meunier, J., and Pouchelon, A. (1982). Critical behaviour in microemulsions. *Journal de Physique Lettres*, 43(3):89–95.

[Cense and Berg, 2009] Cense, A. and Berg, S. (2009). The viscous-capillary paradox in 2-phase flow in porous media. In *International Symposium of the Society of Core Analysts*, pages 27–30, Noordwijk, The Netherlands.

[Chun, 1979] Chun, H. (1979). Interfacial tensions and solubilizing ability of a microemulsion phase that coexists with oil and brine. *Journal of Colloid and Interface Science*, 71(408):408–426.

[Clarke et al., 2015] Clarke, A., Howe, A., Mitchell, J., Staniland, J., Hawkes, L., and Leeper, K. (2015). Mechanism of anomalously increased oil displacement with aqueous viscoelastic polymer solutions. *Soft Matter Communication*, 11:3536–3541.

[Cuenca et al., 2012] Cuenca, A., Chabert, M., Morvan, M., and Bodiguel, H. (2012). Axisymmetric drainage in hydrophobic porous media micromodels. *Oil and Gas Science Technology*, 67(6):953–962.

[Curwen et al., 2007] Curwen, T., Warner, J., Bain, C., Compton, R., and Eve, J. (2007). Adsorption kinetics in a dual-inlet channel flow cell: I. cetyl pyridinium chloride on hydrophilic silica. *The Journal of Physical Chemistry C*, 111(33):12289–12304.

[Day and Bain, 2007] Day, J. and Bain, C. (2007). Ellipsometric study of depletion at oil-water interfaces. *Physical Review E*, 76:041601.

[de Bruyn et al., 1989] de Bruyn, P., Overbeek, J., and Verhoeckx, G. (1989). On understanding microemulsions: III. phase equilibria in systems composed of water, sodium chloride, cyclohexane, sds, and n-pentanol. *Journal of Colloid and Interface Science*, 127(1):244 – 255.

[Drelich et al., 2002] Drelich, J., Fang, C., and White, C. (2002). *Encyclopedia of surface and colloid science*, chapter Measurement of Interfacial Tension in Fluid/Fluid Systems, pages 3152–3166. Marcel Dekker Press.

[Drude, 1891] Drude, P. (1891). Ueber die reflexion und brechung ebener lichtwellen beim durchgang durch eine mit oberfl chenschichten behaftete planparallele platte. *Annalen der Physik*, 279:126–157.

[Dwarakanath et al., 2008] Dwarakanath, V., Chaturvedi, T., Jackson, A., Malik, T., Siregar, A., and Zhao, P. (2008). Using co-solvents to provide gradients and improve oil recovery during chemical flooding in a light oil reservoir. Number SPE 113965-MS. Society of Petroleum Engineers.

[Fulmer et al., 2010] Fulmer, G., Miller, A., Sherden, N., Gottlieb, H., Nudelman, A., Stoltz, B., Bercaw, J., and Goldberg, K. (2010). NMR chemical shifts of trace impurities: common laboratory solvents, organics, and gases in deuterated solvents relevant to the organometallic chemist. *Organometallics*, 29(9):2176–2179.

[Garcia-Caurel et al., 2013] Garcia-Caurel, E., Ossikovski, R., Foldyna, M., Pierangelo, A., Drévillon, b., and De Martino, A. (2013). *Advanced Mueller Ellipsometry Instrumentation and Data Analysis*, pages 31–143. Springer Berlin Heidelberg, Berlin, Heidelberg.

[Graciaa et al., 1993a] Graciaa, A., Lachaise, J., Cucuphat, C., Bourrel, M., and Salager, J. (1993a). Improving solubilization in microemulsions with additives. 1. the lipophilic linker role. *Langmuir*, 9(3):669–672.

[Graciaa et al., 1993b] Graciaa, A., Lachaise, J., Cucuphat, C., Bourrel, M., and Salager, J. (1993b). Interfacial segregation of an ethyl oleate/hexadecane oil mixture in microemulsion systems. *Langmuir*, 9(6):1473–1478.

[Guering and Lindman, 1985] Guering, P. and Lindman, B. (1985). Droplet and bicontinuous structures in microemulsions from multicomponent self-diffusion measurements. *Langmuir*, 1(4):464–468.

[Hammond and Pearson, 2010] Hammond, P. and Pearson, J. (2010). Pore-scale flow in surfactant flooding. *Transport in Porous Media*, 83:127–149.

[He et al., 2014] He, K., Xu, L., Gao, Y., Neeves, K. B., Yin, X., Bai, B., and Smith, J. (2014). Validating surfactant performance in the Eagle Ford shale: A correlation between the reservoir-on-a-chip approach and enhanced well productivity. Number SPE-169147-MS. SPE Improved Oil Recovery Symposium, 12-16 April, Tulsa, Oklahoma, USA, Society of Petroleum Engineers.

[He et al., 2015] He, K., Xu, L., Gao, Y., Yin, X., and Neeves, K. (2015). Evaluation of surfactant performance in fracturing fluids for enhanced well productivity in unconventional reservoirs using Rock-on-a-Chip approach. *Journal of Petroleum Science and Engineering*, 135:531âĂŞ541.

[Herráez, 2006] Herráez, J.and Belda, R. (2006). Refractive indices, densities and excess molar volumes of monoalcohols + water. *Journal of solution chemistry*, 35(9):1315–1328.

[Hirasaki and Zhang, 2004] Hirasaki, G. and Zhang, D. (2004). Surface chemistry of oil recovery from fractured, oil-wet, carbonate formations. *Society of Petroleum Engineers*, 9(2):151–162.

[Howe et al., 2015] Howe, A., Clarke, A., Mitchell, J., Staniland, J., Hawkes, L., and Whalan, C. (2015). Visualising surfactant enhanced oil recovery. *Colloids and Surfaces A: Physicochemical and Engineering Aspects*, 480:449 – 461.

[Kegel et al., 1993] Kegel, W., van Aken, G., Bouts, M., Lekkerkerker, H., Overbeek, J., and de Bruyn, P. (1993). Adsorption of sodium dodecyl sulfate and cosurfactant at the planar cyclohexane-brine interface. validity of the saturation adsorption approximation and effects of the cosurfactant chain length. *Langmuir*, 9:252–256.

[Kokal, 2005] Kokal, S. (2005). Crude oil emulsions: A state-of-the-art review. *Society of Petroleum Engineers*, 20:01.

[Langevin et al., 1992] Langevin, D., Meunier, J., Eanrshaw, J., Cummins, H., Williams, L., Miyano, K., Schlossman, M., Persham, P., Rondelez, F., and Maystre, D. (1992). *Light scattering by liquid surfaces and complementary techniques*, volume 41 of *Surfactant science series*. M. Dekker, New York.

[Li et al., 2015] Li, H., Dawson, M., and Standnes, D. (2015). Multi-scale rock characterization and modeling for surfactant EOR in the Bakken. Number 175960, SPE/CSUR Unconventional Resources Conference, 20-22 October, Calgary, Alberta, Canada.

[Lide, 1993] Lide, D. (1993). *CRC Handbook of Chemistry and Physics*. CRC Press, 74^{th} edition.

[Lifton, 2016] Lifton, V. (2016). Microfluidics: an enabling screening technology for enhanced oil recovery (EOR). *Lab Chip*, 16:1777–1796.

[Liu et al., 2008] Liu, S., Zhang, D., Yan, W., Puerto, M., Hirasaki, G., and Miller, C. (2008). Favorable attributes of alkaline-surfactant-polymer flooding. *SPE Journal*, 13(1):5–16.

[Manning-Benson et al., 1997] Manning-Benson, S., Bain, C., and Darton, R. (1997). Measurement of dynamic interfacial properties in an overflowing cylinder by ellipsometry. *Journal of Colloid and Interface Science*, 189(1):109 – 116.

[Mazer et al., 1976] Mazer, N., Benedek, G., and Carey, M. (1976). An investigation of the micellar phase of sodium dodecyl sulfate in aqueous sodium chloride solutions using quasielastic light scattering spectroscopy. *The Journal of Physical Chemistry*, 80(10):1075–1085.

[Meunier, 1987] Meunier, J. (1987). Liquid interfaces : role of the fluctuations and analysis of ellipsometry and reflectivity measurements. *Journal de Physique*, 48:1819 – 1831.

[Misselyn-Bauduin et al., 2001] Misselyn-Bauduin, A., Thibaut, A., Grandjean, J., Broze, G., and Jérôme, R. (2001). Investigation of the interactions of

polyvinylpyrrolidone with mixtures of anionic and nonionic surfactants or anionic and zwitterionic surfactants by pulsed field gradient nmr. *Journal of Colloid and Interface Science*, 238(1):1 – 7.

[Mitchell et al., 2013] Mitchell, J., Chandrasekera, T., Holland, D., Gladden, L., and Fordham, E. (2013). Magnetic resonance imaging in laboratory petrophysical core analysis. *Physics Reports*, 526(3):165–225.

[Mitchell et al., 2015] Mitchell, J., Howe, A., and Clarke, A. (2015). Real-time oil-saturation monitoring in rock cores with low-field NMR. *Journal of Magnetic Resonance*, 256:34–42.

[Mitchell et al., 2012] Mitchell, J., Staniland, J., Wilson, A., Howe, A., Clarke, A., Fordham, E., Edwards, J., Faber, R., and Bouwmeester, R. (2012). Magnetic resonance imaging of chemical EOR in core to complement field pilot studies. In *International Symposium of the Society of Core Analysts*, Aberdeen, UK, 27-30 August.

[Mokso et al., 2011] Mokso, R., Marone, F., HaberthÃijr, D., Schittny, J., Mikuljan, G., Isenegger, A., and Stampanoni, M. (2011). Following dynamic processes by XâĂŘray tomographic microscopy with subâĂŘsecond temporal resolution. *AIP conference proceedings*, 1365(1):38–41.

[Moulik et al., 2000] Moulik, S., Digout, L., Aylward, W., and Palepu, R. (2000). Studies on the interfacial composition and thermodynamic properties of w/o microemulsions. *Langmuir*, 16(7):3101–3106.

[Mumtaz et al., 2015] Mumtaz, M., Tan, I., and Mushtaq, M. (2015). Synergistic effects of surfactants mixture for foam stability measurements for enhanced oil recovery applications. Number SPE-178475-MS, SPE Saudi Arabia Section Annual Technical Symposium and Exhibition, 21-23 April, Al-Khobar, Saudi Arabia. Society of Petroleum Engineers.

[Mysels and Princen, 1959] Mysels, K. J. and Princen, L. (1959). Light scattering by some laurylsulfate solutions. *The Journal of Physical Chemistry*, 63(10):1696–1700.

[Najjar and Stubenrauch, 2009] Najjar, R. and Stubenrauch, C. (2009). Phase diagrams of microemulsions containing reducing agents and metal salts as bases for the synthesis of metallic nanoparticles. *Journal of Colloid and Interface Science*, 331(1):214 – 220.

[Orsi et al., 1994] Orsi, T., Edwards, C., and Anderson, A. (1994). X-ray computed tomography: A nondestructive method for quantitative analysis of sediment cores. *Journal of Sedimentary Research, Section A: Sedimentary Petrology and Processes*, 64A(3):690–693.

[Piroird et al., 2011] Piroird, K., Clanet, C., and Quéré, D. (2011). Detergency in a tube. *Soft Matter*, 7:7498–7503.

[Salager et al., 2013] Salager, J., Forgiarini, A., and Bullón, J. (2013). How to attain ultralow interfacial tension and three-phase behavior with surfactant formulation for enhanced oil recovery: a review. part 1. optimum formulation for simple surfactant–oil–water ternary systems. *Journal of Surfactants and Detergents*, 16(4):449–472.

[Salter, 1977] Salter, S. (1977). The influence of type and amount of alcohol on surfactant-oil-brine phase behavior and properties. Number SPE-6843-MS, SPE Annual Fall Technical Conference and Exhibition, 9-12 October, Denver, Colorado. Society of Petroleum Engineers.

[Scanziani et al., 2017] Scanziani, A., Singh, K., Blunt, M., and Guadagnini, A. (2017). Automatic method for estimation of in situ effective contact angle from X-ray micro tomography images of two-phase flow in porous media. *Journal of Colloid and Interface Science*, 496:51–59.

[Sheng, 2010] Sheng, J. (2010). *Modern Chemical Enhanced Oil Recovery: Theory and Practice*, chapter Surfactant flooding, pages 239–336. Gulf Professional Publishing.

[Shih and Williams, 1986] Shih, L. and Williams, R. (1986). Raman spectroscopic determination of solubilization equilibria in surfactant solutions. *The Journal of Physical Chemistry*, 90(8):1615–1620.

[Singh et al., 2016] Singh, K., Bijeljic, B., and Blunt, M. (2016). Imaging of oil layers, curvature and contact angle in a mixed-wet and a water-wet carbonate rock. *Water Resources Research*, 52(3):1716–1728.

[Sinz et al., 2013] Sinz, D., Hanyak, M., and Darhuber, A. (2013). Self-induced surfactant transport along discontinuous liquidâĂŞliquid interfaces. *Journal of Physical Chemistry Letters*, 4(6):1039–1043.

[Song et al., 2013] Song, S., Koelsch, P., Weidner, T., Wagner, M., and Castner, D. (2013). Sodium dodecyl sulfate adsorption onto positively charged surfaces: Monolayer formation with opposing headgroup orientations. *The ACS Journal of Surfaces and Colloids*, 29(41).

[Song et al., 2014] Song, W., Fadaei, H., and Sinton, D. (2014). Determination of dew point conditions for CO_2 with impurities using microfluidics. *Environmental Science Technology*, 48(6):3567âĂŞ3574.

[Stigter et al., 1955] Stigter, D., Williams, R., and Mysels, K. (1955). Micellar self diffusion of sodium lauryl sulfate. *The Journal of Physical Chemistry*, 59(4):330–335.

[Tajima et al., 1970] Tajima, K., Muramatsu, M., and Sasaki, T. (1970). Radiotracer studies on adsorption of surface active substance at aqueous surface. i. accurate measurement of adsorption of tritiated sodium dodecylsulfate. *Bulletin of the Chemical Society of Japan*, 43(7):1991–1998.

[Tan et al., 2010] Tan, C., Huang, Z., and Huang, X. (2010). Rapid determination of surfactant critical micelle concentration in aqueous solutions using fiber-optic refractive index sensing. *Analytical Biochemistry*, 401(1):144 – 147.

[Unsal et al., 2016] Unsal, E., Broens, M., and Armstrong, R. (2016). Pore scale dynamics of microemulsion formation. *Langmuir*, 32(28):7096–7108.

[Van Geet et al., 2000] Van Geet, M., Swennen, R., and Wevers, M. (2000). Quantitative analysis of reservoir rocks by microfocus X-ray computerised tomography. *Sedimentary Geology*, 132(1âĂŞ2):25–36.

[van Nieuwkoop and Snoei, 1985] van Nieuwkoop, J. and Snoei, G. (1985). Phase diagrams and composition analyses in the system sodium dodecyl sulfate/butanol/water/sodium chloride/heptane. *Journal of Colloid and Interface Science*, 103(2):400 – 416.

[Varela et al., 1995] Varela, A., Macho, M., and González, A. (1995). The size of sodium dodecyl sulfate micelles in the presence of n-alcohols as determined by fluorescence quenching measurements. *Colloid & Polymer Science*, 273(9):876–880.

[Verhoeckx et al., 1987] Verhoeckx, G., de Bruyn, P., and Overbeek, J. (1987). On understanding microemulsions: I. interfacial tensions and adsorptions of SDS and pentanol at the cyclohexane/water interface. *Journal of Colloid and Interface Science*, 119(2):409 – 421.

[Viades-Trejo and Gracia-Fadrique, 2007] Viades-Trejo, J. and Gracia-Fadrique, J. (2007). Spinning drop method: From youngâĂŞlaplace to vonnegut. *Colloids and Surfaces A: Physicochemical and Engineering Aspects*, 302(1âĂŞ3):549 – 552.

[Vonnegut, 1942] Vonnegut, B. (1942). Rotating bubble method for the determination of surface and interfacial tensions. *Review of Scientific Instruments*, 13(1):6–9.

[Walther et al., 2010] Walther, F., Drobek, T., Gigler, A., Hennemeyer, M., Kaiser, M., Herberg, H., Shimitsu, T., Morfill, G., and Stark, R. (2010). Surface hydrophilization of SU-8 by plasma and wet chemical processes. *Surface and Interface Analysis*, 42(12-13):1735–1744.

[Wellington and Vinegar, 1987] Wellington, S. and Vinegar, H. (1987). X-ray computerized tomography. *Journal of Petroleum Technology*, 39(8).

[Wilkinson, 1984] Wilkinson, D. (1984). Percolation model of immiscible displacement in the presence of buoyancy forces. *Physical Review A*, 30(1):520 – 531.

[Winsor, 1948] Winsor, P. (1948). Hydrotropy, solubilisation and related emulsification processes. *Transactions of the Faraday Society*, 44:376–398.

[Xu et al., 2014] Xu, W., Ok, T., Xiao, F., Neeves, K., and Yin, X. (2014). Effect of pore geometry and interfacial tension on water-oil displacement efficiency in oil-wet microfluidic porous media analogs. *Physics of Fluids*, 26(093102):1–16.

[Youssef et al., 2014] Youssef, S., Rosenberg, E., Deschamps, H., Oughanem, R., Maire, E., and Mosko, R. (2014). Oil ganglia dynamics in natural porous media during surfactant flooding captured by ultra-fast X-ray microtomography. In *International Symposium of the Society of Core Analysts*, Avignon, France, 11-18 Septembre.

[Zangi et al., 2007] Zangi, R., Hagen, M., and Berne, B. (2007). Effect of ions on the hydrophobic interaction between two plates. *Journal of the American Chemical Society*, 129(15):4678–4686.

[Zhou and Dupeyrat, 1990] Zhou, J. and Dupeyrat, M. (1990). Alcohol effect on interfacial tension in oil-water-sodium dodecyl sulphate systems. *Journal of Colloid and Interface Science*, 134(2):320 – 335.

[Zhou and Rhue, 2000] Zhou, M. and Rhue, R. (2000). Effect of interfacial alcohol concentrations on oil solubilization by sodium dodecyl sulfate micelles. *Journal of Colloid and Interface Science*, 228(1):18 – 23.

[Zielinska et al., 1981] Zielinska, B., Bedeaux, D., and Vlieger, J. (1981). Electric and magnetic susceptibilities for a fluid-fluid interface; the ellipsometric coefficient. *Physica A: Statistical and Theoretical Physics*, 107(1):91–108.